ABSTRACT

Title of dissertation: Aero-Assisted Spacecraft Missions
Using Hypersonic Waverider Aeroshells

Jeremy Knittel, Doctor of Philosophy, 2015

Dissertation directed by: Dr. Mark J. Lewis
Professor
Department of Aerospace Engineering

Dr. Kenneth H. Yu
Associate Professor
Department of Aerospace Engineering

This work examines the use of high-lift, low drag vehicles which perform orbital transfers within a planet's atmosphere to reduce propulsive requirements. For the foreseeable future, spacecraft mission design will include the objective of limiting the mass of fuel required. One means of accomplishing this is using aerodynamics as a supplemental force, with what is termed an aero-assist maneuver. Further, the use of a lifting body enables a mission designer to explore candidate trajectory types wholly unavailable to non-lifting analogs. Examples include missions to outer planets by way of an aero-gravity assist, aero-assisted plane change, aero-capture, and steady atmospheric periapsis probing missions. Engineering level models are created in order to simulate both atmospheric and extra-atmospheric space flight. Each mission is parameterized using discrete variables which control multiple areas of design. This work combines the areas of hypersonic aerodynamics, re-entry

aerothermodynamics, spacecraft orbital mechanics, and vehicle shape optimization. In particular, emphasis is given to the parametric design of vehicles known as "waveriders" which are inversely designed from known shock flowfields. An entirely novel means of generating a class of waveriders known as "starbodies" is presented. A complete analysis is performed of asymmetric starbody forms and compared to a better understood parameterization, "osculating cone" waveriders. This analysis includes characterization of stability behavior, a critical discipline within hypersonic flight. It is shown that asymmetric starbodies have significant stability improvement with only a 10% reduction in the lift-to-drag ratio. By combining the optimization of both the shape of the vehicle and the trajectory it flies, much is learned about the benefit that can be expected from lifting aero-assist missions. While previous studies have conceptually proven the viability, this work provides thorough quantification of the optimized outcome. In examining an aero-capture of Mars, it was found that with a lifting body, the increased maneuverability can allow completion of multiple mission objectives along with the aero-capture, such as atmospheric profiling or up to 80° of orbital plane change. Completing a combined orbital plane change and aero-capture might save as much as 4.5 km/s of velocity increment while increasing the feasible entry corridor by an order of magnitude. Analyzing a higher energy mission type, a database of maximum aero-gravity assist performance is developed at Mars, Earth and Venus. Finally, a methodology is presented for designing end-to-end interplanetary missions using aero-gravity assists. As a means of demonstrating the method, promising trajectories are propagated which reduce the time of flight of an interstellar probe mission by up to 50%.

Aero-Assisted Spacecraft Missions Using Hypersonic Waverider Aeroshells

by

Jeremy Knittel

Dissertation submitted to the Faculty of the Graduate School of the
University of Maryland, College Park in partial fulfillment
of the requirements for the degree of
Doctor of Philosophy
2015

Advisory Committee:
Professor Kenneth Yu, Chair/Advisor
Dr. Mark Lewis, Co-Advisor
Professor Chris Cadou
Professor Dave Akin
Professor Shapour Azarm

Acknowledgments

First and foremost, I would like to thank my advisors Dr. Mark Lewis and Dr. Kenneth Yu for their support throughout my graduate career. I am incredibly appreciative of the opportunity Dr. Lewis gave me by bringing me to the University of Maryland and guiding me into and leading me through a research topic that I find fascinating, challenging and intellectually rewarding. I would also like to thank Dr. Yu for graciously welcoming me into his research group and allowing me to continue pursuing my own research interests. I am incredibly appreciative of the patience, advice and encouragement that both have given me.

I would also like to thank the rest of my dissertation committee, Dr. Shapour Azarm, Dr. Chris Cadou, and Dr. David Akin for their comments and considered review of my work. I appreciate the time and effort they were willing to dedicate to me.

I am grateful for the honor of being a member of the inaugural class of NASA's Space Technology Research Fellowship. My thanks go to those in NASA's Office of the Chief Technologist for bestowing this honor upon me. This financial support allowed me to focus exclusively on my research area, and connected me with many influential and leading researchers at a number of NASA centers.

I would like to thank the many people that have assisted me in the UMD Aero department offices including Otto Fandino, Tom Hurst, Rebecca Sarni, Michael Jones, LaVita Williams and Erika Aparakakankanange. They all were incredibly kind and make the department operate smoothly and efficiently.

I am greatly appreciative for the assistance of John Theisinger for his frequent technical advice, reviewing a number of my conference papers and his help in arranging my work at NASA Ames and NASA Langley. Further, I am grateful for his generosity in sharing his office with me for three months while I worked from NASA Langley.

I would like to express my appreciation to Dr. Dan Lyons for his mentorship during my time at JPL. He was constantly looking for opportunities for me to reach out and connect with others at JPL and greatly increased the value of my experience there. He also went above and beyond in reviewing my work and giving valuable comments and feedback.

I thank Joseph Garcia (NASA Ames) and Dr. Roby Wilson (JPL) for their hospitality in accepting and welcoming me into their groups for my fellowship on-site research experiences. These short work assignments were invaluable in the completion of my degree and will continue to guide me as I move forward in my career.

I have had the privilege of working with many esteemed colleagues during my time at UMD. In particular, I would like to acknowledge Dr. Kevin Ryan, Dr. Neal Smith, Dr. Adam Beerman, Vijay Ramasubramanian, Jonathon Geerts, Jason Burr, Rob Fievisohn and Nathan Shumway. Each of whom helped in their own way, whether it was thoughtful discussions about research, advice for dealing with the rigors of graduate school, or simply conversations to provide mental breaks during the work day.

I would like to thank the members of the Advanced Propulsion Research Lab

for welcoming me as one of their own. Despite a lack of overlap between our research areas, they were always able to pick apart my work and provide invaluable suggestions and comments.

I cannot possibly express how grateful I am for my family, Julia Maki, Greg Maki, Leila Maki, Nellie Knittel, and my parents Mark Knittel and Joanne Knittel. I am grateful to Julia for living a lofty standard that constantly challenges me to be better. Leila and Nellie helped brighten my day throughout the past year. And lastly, I can't begin to express how humbled I am by my parents. They have provided for me, sacrificed for me, loved me unconditionally, and been the consummate role models.

Finally, I would like to thank Aria. Her unwavering belief in me has been instrumental in completing this degree. She was willing to take my struggles and challenges as her own and has shown me limitless compassion and understanding.

Table of Contents

List of Tables

List of Figures

List of Symbols

a	acceleration
a	speed of sound
a	Runge-Kutta constant
a	semi-major axis of starbody's center-body ellipse
a	semi-major axis of spacecraft orbit
A	osculating cone waverider power law coefficient
A	area
α	angle-of-attack
α_0	vertical nose offset of starbody's center-body
b	semi-minor axis of starbody's center-body ellipse
b	Runge-Kutta constant
b	tine width
β	shock angle
β	yaw angle
c_A	axial force coefficient
c_D	drag coefficient
c_f	skin friction coefficient
c_l	roll moment coefficient
c_L	lift coefficient
c_m	pitch moment coefficient
c_n	yaw moment coefficient
c_N	normal force coefficient
c_P	pressure coefficient
c_Y	side force coefficient
$c_{n,\beta}$	yaw moment directional stability derivative
$c_{l,\beta}$	roll moment directional stability derivative
C_3	hyperbolic characteristic energy
C_3^+	hyperbolic characteristic escape energy
C_3^-	hyperbolic characteristic approach energy
D	starbody tine distribution parameter
ΔS	shock stand-off distance
e	starbody eccentricity
e	orbital eccentricity

ϵ	obliquity of the ecliptic
ϵ	orbital energy
ϵ	maximum allowable error
ϵ	radiative emissivity
f	objective function
f	set of ordinary differential equations
g	constraint function
γ	ratio of specific heats
γ	flight path angle
H	shock intersection height
H	scale height
h	altitude
h	enthalpy
h_a	orbital apoapse altitude
h_p	orbital apoapse altitude
i	orbital inclination
k	Runge-Kutta intermediary equation
κ	wing angle of a caret-wing
L	vehicle length
L/D	lift-to-drag ratio
l	length of a surface triangle
λ	latitude
M	Mach number
M	planetary mass
m	mass
μ	standard gravitational parameter
n	number of starbody tines
n	power law exponent
$\hat{n}$	normal unit vector
η_V	volumetric efficiency
ϕ	flow disturbance orientation angle
ϕ	bank angle
Φ	orbital angle
Ψ	vehicle heading angle
Ψ	inertial azimuth angle
Ψ	planetary approach angle
$\dot{q}$	heat rate
P	pressure
p	roll rate
Q	dynamic pressure
q	heat rate
q	pitch rate
θ	wedge angle
Θ	gravity or aero-gravity assist turning angle
r	orbital radius

r_a	orbital apoapse radius
r_p	orbital apoapse radius
R	radial distance
R	leading edge radius
R	local radius of curvature
R	gas constant
R_e	Reynolds number
ρ	atmospheric density
S	surface area
SM	static margin
St	Stanton number
σ	longitude
T	temperature
T_w	wall temperature
$\hat{t}$	tangent unit vector
t	time
τ	shear stress
v	velocity
v_∞	hyperbolic excess velocity
v_∞^+	hyperbolic excess escape velocity
v_∞^-	hyperbolic excess approach velocity
V	volume
w	width
x	axes coordinate
x	control system input
ξ	hyperbolic excess velocity ratio
y	axes coordinate
y	ODE state vector
y_0	caret-wing wedge width
z	axes coordinate

AGA	aero-gravity assist
AU	astronomical units
CBAero	Configuration Based Aerodynamics
CEA	Chemical Equilibrium with Applications
CFD	Computational Fluid Dynamics
CG	center of gravity
DSMC	direct simulation Monte Carlo
GA	genetic algorithm
GA	gravity assist
GMST	Greenwich mean sidereal time
GRAM	Global Reference Atmosphere Models
JPL	Jet Propulsion Lab
MATLAB	Matrix Laboratory software
MAXWARP	Maryland axisymmetric waverider program

NASA	National Aeronautics and Space Administration
NASP	National Aerospace Plane
ODE	ordinary differential equation
ODE23	ordinary differential equation solver in MATLAB
ODE45	ordinary differential equation solver in MATLAB
SLS	Space Launch System
SQP	Sequential Quadratic Programming
UMD	University of Maryland
USNO	United States Naval Observatory

Chapter 1

Introduction

1.1 Motivation

In 2010, NASA released a set of grand challenges addressing roadblocks to mankind's long term exploration and operation in space. Among these was a need for more efficient space transportation, as maneuvering is limited by the performance of current day propulsion systems.[1] This work seeks to address that important technology area without the need for an improved propellant system. Payload mass fractions on interplanetary missions are often less than 1%, and can be even worse for deep space missions. For example, the New Horizons spacecraft, currently en route to Pluto, had a payload fraction of only .14% at launch.[2] This leaves precious little mass budget for the scientific equipment which drives the mission.

Whereas a spacecraft must expel rocket propellant when maneuvering in the vacuum of space, flight in an atmosphere introduces the ability to use aerodynamic forces to modify an orbit. Orbital transfers conducted within a planetary atmosphere, known as aero-assist, can reduce the propellant requirements of a spacecraft mission and therefore increase the payload mass delivered. The benefits of aero-assist could go beyond reduced propellant requirements as well. For example, aero-assist can be used to increase heliocentric flight velocity. If the time required to reach the fly-by aero-assist planet is not too great, then the overall mission time

to the final destination can be reduced. In other cases, aero-assist can introduce completely new mission objectives, addressing different technical challenges, such as atmospheric profiling or probe deployment.

Favorable aero-assisted maneuvering force does not come free, as a candidate mission would require flight in some of the most extreme environments imaginable. For example. the fastest man-made entry into the Martian atmosphere to date was the Pathfinder spacecraft. On it's trajectory, it entered at 7.470 km/s and within 3 minutes decelerated to .37 km/s.[3] On the other hand, an aero-assist fly-by of Mars might require up to 5 minutes of flight in excess of 30 km/s. Atmospheric entry and sustained flight at hypersonic speeds would likely challenge the performance limits of thermal protection, control system, and possibly even structural technology. These performance metrics and the design of hypersonic vehicles are highly coupled. Generating design methodologies which are capable of multi-disciplinary analysis is necessary to encapsulate the linked design environment.

1.2 Objective

The primary objective of this work is to use optimization methodology to characterize and improve the design of spacecraft missions using hypersonic vehicles in planetary atmospheres. Specifically, the methodology that has been developed will be used to answer questions about: 1) the trade-offs between different performance metrics of vehicles designed for orbital flight speeds, 2) the potential delta-v savings for various orbital transfers using planetary atmospheres, and 3) the trends in trajectory design for interplanetary missions using aero-gravity assist.

This work uses mathematical models to describe the shape of hypersonic vehicles, calculate their performance, and propagate their trajectory. The models will encompass the geometry of the vehicle, aerodynamics, aerothermodynamics, stability behavior, atmospheric properties, and trajectory dynamics. The resulting

simulations are then put into an optimization routine in order to determine the trade-offs and trends in optimal aero-assist vehicles and trajectories.

Genetic algorithms are used in order to parse a wide set of non-continuous design variables with many non-linearities. In some cases, multi-objective genetic algorithms allow comparisons of different pareto optimal solutions. In other cases, a gradient based optimizer ensures that the genetic algorithm results reach a local optima satisfying necessary and sufficient conditions.

This research also attempts to design trajectories through and out of the solar system, using aero-assisted fly-bys. A phase-free method first selects a route in the form of a planetary fly-by sequence, and subsequently an iterative lambert solver is employed along with real ephemeris data to find launch opportunities. Finally, the entire trajectory is optimized using a so-called n-body simulator. Importantly, this work will demonstrate the major differences in aero-assisted trajectories with those that use more conventional gravity assists alone. As a means of demonstrating the method and the examining the wider design space, an example mission design is performed of an interstellar probe.

In specific, this work will include the following:

- A method of generating asymmetric starbody waveriders will be described and a thorough analysis of their forms will be performed.
- This work will consider the stability of waveriders.
- This work will present the first conceptual study of a combined aero-capture and orbital plane change maneuver, quantifying the potential delta-v savings.
- Analytical aero-gravity assist performance will be compared with simulated maneuver performance.
- Optimal aero-gravity assist departure geometry will be determined.

- A method for conceptual and preliminary design of interplanetary missions using optimized simulation data will be described.
- An optimization and simulation framework capable of propagating interplanetary trajectories from launch to destination using both gravity and aero-gravity assists will be detailed.
- This work will be the first to complete a detailed analysis of the benefit of using an aero-gravity assist maneuver for an interstellar probe.

Chapter 2

Background

This chapter presents the context in which the subsequent chapters exist. Summaries will be provided of the important concept areas, discussing relevant, previously published work. Topics include hypersonic waveriders, aero-assisted maneuver design, and interstellar missions.

2.1 Waveriders

2.1.1 Concept Development

A promising class of vehicle for hypersonic flight is the waverider. These vehicles are designed to have leading edges attached to a forebody shock, hence they can be thought of as riding a shockwave. The concept was first presented in 1959 by Nonweiler[4] as a means of studying the heat load on a manned re-entry vehicle. At the time, it was understood that a gliding vehicle could use lift to decelerate from orbital speeds at a slower rate than blunt bodies in exchange for worsening the heat rate at the leading edges. Nonweiler was looking into means of reducing both the high g-forces as well as the high heat rates. He theorized that if the leading edges were attached to a planar shock, then the heating problem would be simpler to study. His first paper in 1959 suggested multiple vehicle configurations, including a caret-wing waverider (see Fig. 2.1). Caret-wings are designed from a

two dimensional planar shock emanating from a wedge. Nonweiler later published a paper looking exclusively at caret-wings.[5]

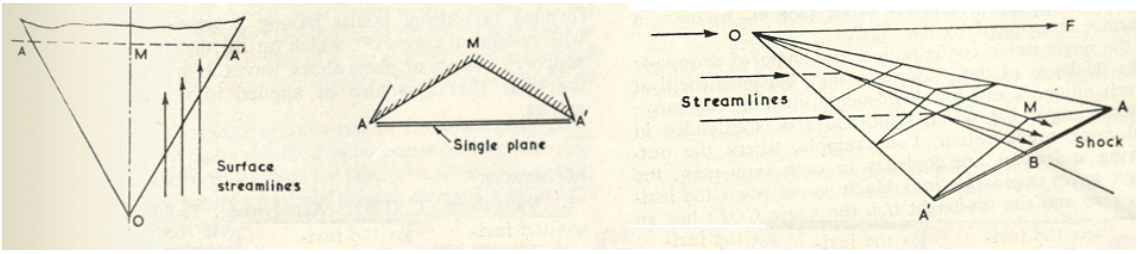

Figure 2.1: Nonweiler Caret-Wing. From Ref. [5]

Waverider design is not limited to 2-D planar shocks, as they can be designed from any known shock structure. In the immediate years following Nonweiler's first publication, additional research in the United Kingdom extended the waverider concept to other inviscid flowfields. Townend[6] looked into using isentropic compression, while Jones examined non-lifting conical[7] and general axisymmetric flows.[8] If a caret-wing section is replicated and multiple are attached leading edge-to-leading edge, then a symmetric starbody waverider is formed. The first study of starbody waveriders was by Gonor et al.[9] in the Soviet Union (see Figure 2.2).

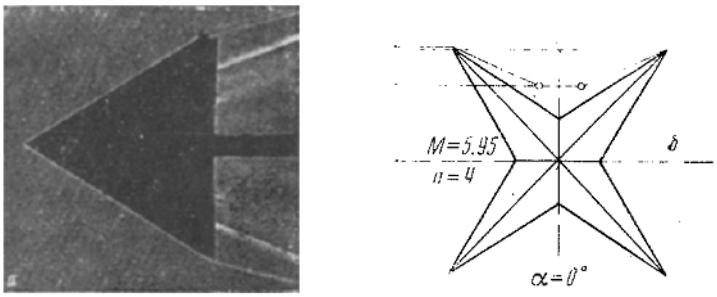

Figure 2.2: Schlieren image of a starbody waverider in Mach 5.95 flow and a front view schematic. From Ref. [9]

With the waverider gaining notoriety, studies validated and advanced the theoretical work done in concept development. Pennelegion and Cash,[10] Pike,[11] and Kipke[12] used hypersonic wind tunnels to demonstrate that the flowfields around waveriders were as predicted. These experimental studies were also useful for analyzing

the flowfield as the angle-of-attack or the flight Mach number varies (see Figure 2.3). This is known as the off-design performance of the waverider. Using experimental data for comparison, Squire[13] used an analytic method to model off-design waverider aerodynamics.

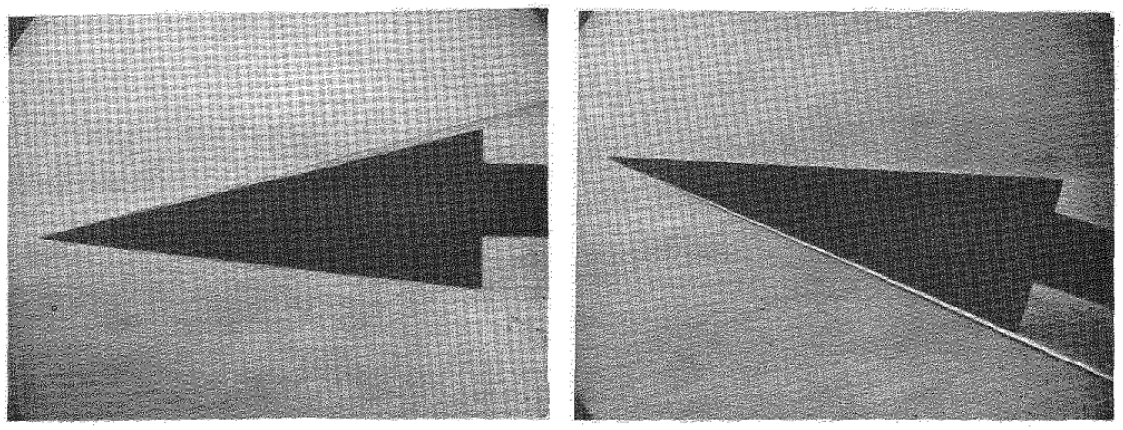

Figure 2.3: Schlieren image of a caret-wing in Mach 8.8 flow at $\alpha = 0°$ and $\alpha = 16°$. The shock on the underside of the vehicle has detached from the leading edges at the higher angle-of-attack. From Ref. [10]

Research picked up considerably in the 1980s, particularly in the United States, where interest in hypersonics was stimulated by the National Aerospace Plane (NASP). The remainder of Section 2.1 will provide a sampling of the extensive advances made in waverider study since the early 1980s, but is certainly not exhaustive.

2.1.2 Advanced Designs

As computational power has advanced, so has the complexity of the methods applied to designing waveriders. Rasmussen used analytic small disturbance theory to develop waveriders from inclined cones,[14] cones with elliptic cross-sections,[14] and ogive bodies.[15] Sobieczky et al.[16] conceived of an approach which uses a proscribed 3d shock shape described by a power law equation (see Figure 2.4). Their so-called "osculating cone" design methodology will be used extensively in the present work.

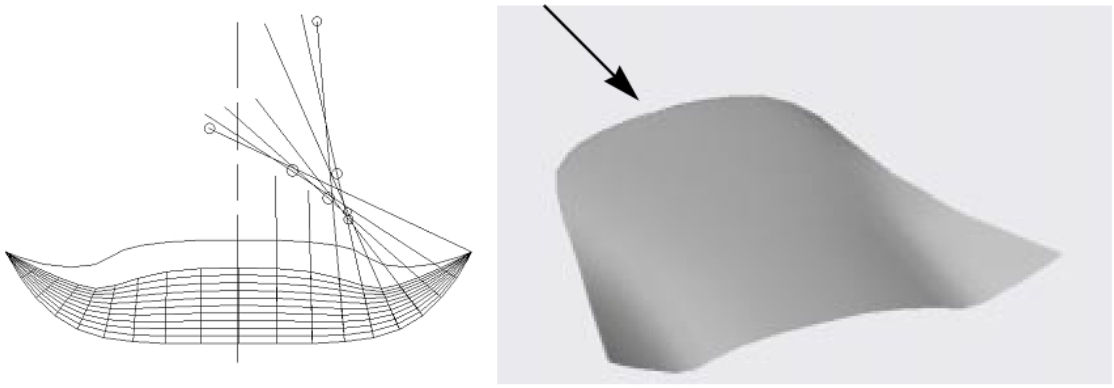

Figure 2.4: Modeling of an osculating cone waverider and the resulting waverider stream surface. From Ref. [16]

The waverider methods described thus far are all inverse design, as a vehicle is "carved" from a known or assumed flow field. Starkey and Lewis[17] developed a means of generating shapes in the forward direction, named the "variable-wedge-angle" method. Using power law equations to define the upper and lower surfaces of the waverider, the resulting shock shape and flowfield is calculated. Their method allowed a much simpler means of parameterizing the waverider shape, allowing optimization, while maintaining less than 2% error from higher-order methods. Starkey and Lewis[18] also used the forward design method to analyze off design effects.

Starbody waveriders have seen advances since their inception as well. Sabean et al.[19] conducted tests on starbodies with non-linear leading edges. They found roughly 20% drag reduction at $M = 6.4$ over cones with identical volumes and lengths. Corda[20] determined that each caret wing section of the starbody could be given its own design conditions, allowing starbodies to generate lift, even at zero angle-of-attack. It was shown that even with the additional lift generation, starbodies have favorable drag profiles as compared to equivalent cones. Asymmetric and non-linear starbodies will be heavily considered in this work, furthering the concepts presented by Corda and Sabean et al.

2.1.3 Optimization

The study of waveriders has often been concerned with finding vehicles with the greatest possible value of L/D. Naturally, many different optimization methods have been used in the waverider design process.

While Kim et al.[21] looked into the viscous effects on waveriders, Bowcutt[22] and Bowcutt et al.[23] published the first studies including skin friction drag in vehicle shape optimization (see Figure 2.5). The development of viscous optimized waveriders was a vital step in demonstrating the viability of producing high lift-to-drag ratios at hypersonic flight speeds. Many inverse design methods and optimization codes were compiled into a software program developed at the University of Maryland called MAXWARP[24] (Maryland AXisymmetric WAveRider Program).

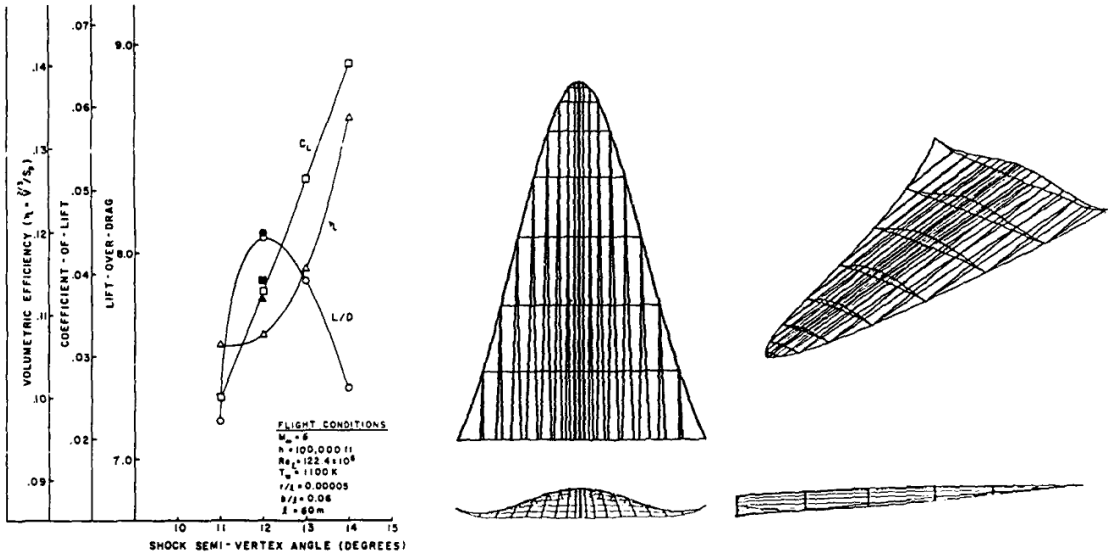

Figure 2.5: Data for viscous optimized waverider derived from right cones at Mach = 6 and three-view of the waverider. From Ref. [23]

The present work will use non-gradient and gradient based optimization methods to generate vehicle geometries, both of which have heritage in waverider design. Mangin et al.[25] used a simplex, gradient scheme to form waveriders from blunt blody flows. They found they could increase the volume of the waverider with-

out decreasing L/D. Foster et al.[26] demonstrated that evolutionary algorithms have comparable convergence to differential algorithms while avoiding local minima when optimizing aerospace vehicle shapes. Starkey et al.[27] and Armellin et al.[28] used an evolutionary algorithm to design optimal waverider shape and hypersonic trajectory pairs. Burt et al.[29] used simulated annealing of 3d direct simulation Monte Carlo (DSMC) calculations. Ryan[30] developed robust optimization techniques and applied them to hypersonic waveriders. He showed that this allows post-optimization analysis and insight which could be lost by more traditional schemes. Neville and Candler[31] incorporated CFD results inside of the optimization loop.

2.1.4 Validation

Experimental and advanced computational studies have been conducted to validate the expected performance of waveriders. Takashima and Lewis[32] used a Navier-Stokes solver to analyze off-design and skin friction effects of viscous optimized waveriders. The Naval Surface Warfare Center used their Hypervelocity Wind Tunnel 9 to experimentally test a waverider[33,34] developed in MAXWARP by Burnett and Lewis.[35] The study by Sabean et al.,[19] referenced earlier, used wind tunnel testing to validate an analytic waverider design method. A joint study between the Hypervelocity Wind Tunnel 9 (now part of the Arnold Engineering Development Center) and the University of Minnesota demonstrated the performance of a waverider test article (see Figure 2.6). Drayna et al.[36] published the computational results using a CFD code, US3D. Norris[37] presented the Mach 8 experimental data. Chauffour and Lewis[38] used CFD to determine the accuracy of the flowfield around osculating cone waveriders. Numerous other pure experimental[39–42] and pure CFD[43,44] studies also help to validate waverider performance.

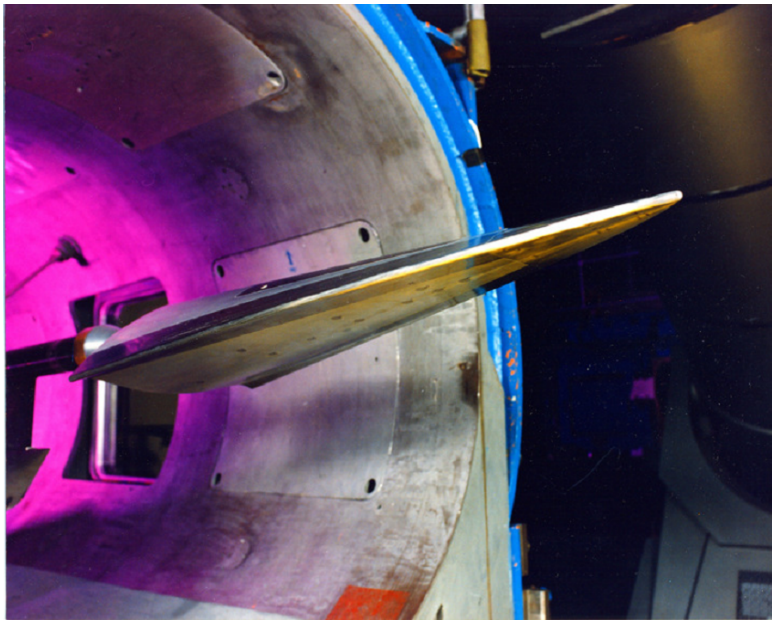

Figure 2.6: A Mach 14 Waverider installed in the Wind Tunnel 9 Test Cell. From Ref. [37]

2.1.5 Hypersonic Dynamics and Stability

An important aspect of the present work is the quantification of the stability of waverider vehicles. Stability analysis dates as far back as 1969, when Hui[45] derived closed form solutions for the pitch stability derivative of a caret wing using perturbation theory. He found that the derivative is a function of Mach number and leading edge incidence angle, but is independent of the wing's aspect ratio. More recently, Rasumussen[46] used Newtonian theory to determine stability derivatives for conically derived waveriders.

Piston theory was proposed for use at hypersonic speeds by Lighthill.[47] This method assumes that for high Mach number flows, the pressure of a disturbance is proportional to the normal surface velocity. This greatly simplifies the calculations of off-design waverider conditions, as analytic expressions are possible. Tarpley and Lewis[48] used piston theory to derive a complete set of lateral and longitudinal stability derivatives for caret-wings. Good agreement is shown between piston theory and

experimental data presented by Kipke.[12] Rudd and Pines[49] calculated propulsion related longitudinal stability derivatives on an engine integrated waverider using both piston theory and finite differencing. They found the effects of velocity changes on the flow through a scramjet combuster were too strong to be accurately modeled by piston theory. Finite differencing was much more accurate when portions of the flow reach lower Mach numbers.

With the end goal of developing control algorithms, linearized dynamics models have been presented for generic hypersonic vehicles.[50,51] With a linear dynamics model, eigenvalues can be calculated to analyze characteristic motion.[52,53] Mooij[52] studied characteristic motion of a blunted capsule and a lifting re-entry body and found that coupling of lateral and longitudinal motion can be of extreme importance in the hypersonic regime. This was observed less for his lifting shapes, but he was looking at vehicles with wings rather than waveriders.

2.1.6 Leading Edge Bluntness

From the very first days of the waverider, there have been concerns over the heating associated with sharp leading edges.[4] As the leading edge radius of a vehicle increases, the heating rate drops precipitously.[54] Van Mol and Anderson[55] performed the first complete analysis of waverider heating using a geometry with leading edge bluntness. Blosser et al.[56] performed a thorough trade study to create conceptual leading edge designs considering structural materials and thermal loads.

Mason and Lee[57] used Newtonian theory and CFD to develop a distinction between aerodynamic and geometric sharpness. They defined a waverider leading edge with a power law curve, and then measured the pressure coefficient. It was found that there was a considerable difference between leading edges with a power law exponent less than or greater than 2/3. The increased leading edge radius might have favorable impact on heating, but aerodynamically, it still behaved "sharp" (see

Figure 2.7). O'Brien and Lewis[58] confirmed this result in a numerical study in which they quantified the relationship between shock standoff and the leading edge power law exponent (see Figure 2.8). They concluded however, that for comparable heat loads and drag reduction, circular leading edges performed as well or better than power law leading edges. Santos and Lewis[59] showed a similar result for heating on waverider leading edges.

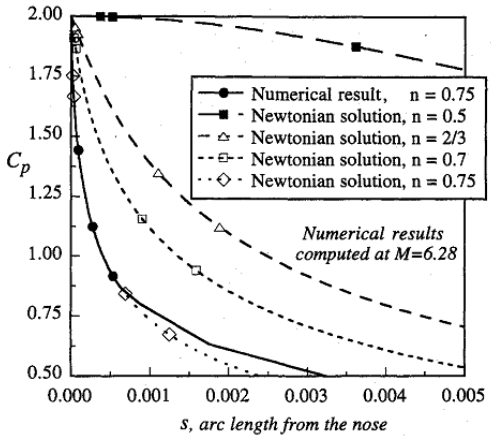

Figure 2.7: Variation of pressure coefficient for various leading edge power law coefficients, n. Note the change in inflection for n < 2/3. From Ref. [57]

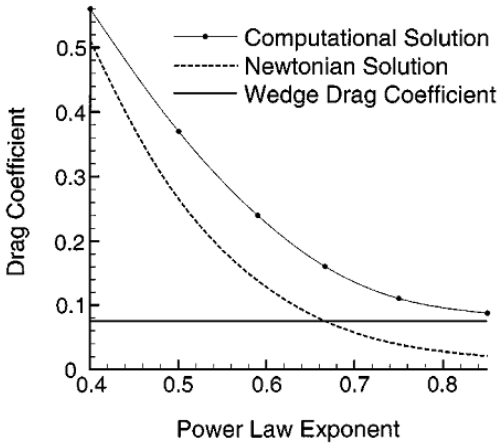

Figure 2.8: Variation of drag coefficient with power law exponent. Note the power-law Newtonian solution matches a comparable wedge angle for n ≈ 2/3. From Ref. [58]

Gillum and Lewis[33] presented data from a Mach 14 test in the Hypervelocity Wind Tunnel 9 (referenced previously in Section 2.1.4) on a waverider with blunted leading edges. While they showed favorable off-design behavior, a .25 inch leading edge radius resulted in flow spillage and increased wave drag. The sharp leading edge vehicle was predicted to have an L/D = 4.61. Leading edge bluntness decreased this value by 20% to L/D = 3.7. Silvester and Morgan[60] ran CFD and wind tunnel tests to compare a sharp and blunted caret-wing waverider. They found roughly 25% reduction in lift-to-drag ratio, which was attributed to flow spillage and viscous interaction. The greater pressure on the upper and lower surfaces of the caret-wing caused the boundary layer to grow faster and increase skin friction.

2.2 Aero-Assisted Spacecraft Missions

2.2.1 Aero-Assisted Orbital Transfers

The use of aerodynamic forces to alter the orbit of a spacecraft was first presented by London[61] with a paper examining orbital plane change. He noted that using an extra-atmospheric propellant burn to change the inclination of a spacecraft's orbit by 60° would require almost as much velocity change as the initial launch. He hypothesized that if aerodynamic lift could instead be used to complete the change of plane, then the propellant required to de-orbit and once again re-orbit might be minimal by comparison. He reduced the problem to an analytical form and found that for L/D = 2, propellant savings would be achieved for turns between 10° and 70° and up to orbital altitudes of 400 miles. Roessler[62] updated the method allowing for additional impulsive maneuvers during the atmospheric turn. He showed that the rotation and oblateness of the Earth had a considerable effect as an inclination change of +15° and -15° required different propellant velocity increments (turning towards Earth's ecliptic plane was less costly).

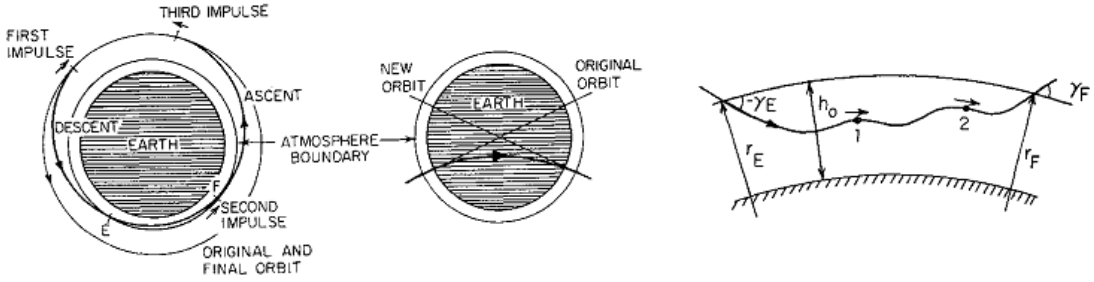

Figure 2.9: Schematic of aero-assisted plane change. Third image shows additional impulsive rocket burns inside of the atmosphere. From Ref. [62]

Early conceptual studies made simplifying assumptions about the atmospheric trajectory flown during an aero-assisted orbital transfer. Algorithms had not yet been developed to govern the flight profile by way of manipulation of the vehicle's lift vector. In the 1980s, research turned to developing control schemes which would

vary angle-of-attack and bank angle in order to use aerodynamics as efficiently as possible. This is important, as there will be losses due to varying lift and flying at some $L/D < L/D_{\mathbf{max}}$. These guidance laws were created with different objectives: minimizing energy loss,[63,64] minimizing fuel consumption,[65,66] or minimizing the heating rate.[67–69] A thorough summary of the relative merits of those algorithms published before 1996 is provided in a lecture by Miele.[70] While the specifics vary, the conclusion reached by all of these studies is that a well designed guidance law can result in aero-assisted orbital transfers which deliver fuel savings over entirely extra-atmospheric maneuvers and between 80%-99% of the expected savings from a simplified analytical model "optimum."

2.2.2 Aero-Gravity Assist

An aero-assist planet fly-by in which aerodynamic lift is used to supplement gravitational acceleration is named an aero-gravity assist. As the hyperbolic approach speed of a spacecraft increases, the achievable gravity assisted turning angle decreases. If the spacecraft enters the atmosphere during the maneuver, however, it can use aerodynamic forces to remain in the gravity well of the planet for a longer period of time. Aero-gravity assist (see Figure 2.10) was first proposed as a means of reducing propellant requirements for a solar probe by Randolph[71] at the Jet Propulsion Lab (JPL) in 1982. This initial investigation found promise for the maneuver itself, but skepticism for the vehicle requirements. He estimated a lift-to-drag ratio on the order of 10 would be needed. It was not until the introduction of viscous optimized waveriders by researchers at the University of Maryland[22] (UMD) in the late 1980's, that it was thought that the required lift-to-drag ratios would be attainable. This section attempts to summarize the flood of published studies that directly followed collaboration between JPL and UMD and the advancement of the combined concept in more recent years.

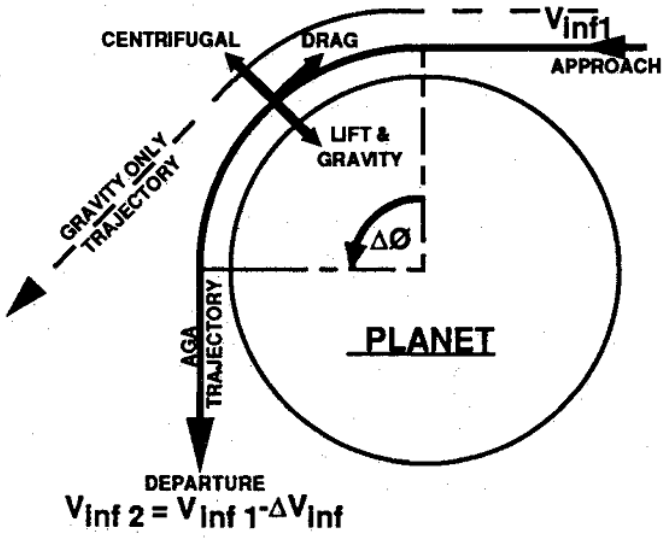

Figure 2.10: A general sketch of the aero-gravity assist concept. From Ref. [71]

Many of the studies mentioned in Section 2.1 were created with terrestrial applications in mind. One important aspect of extending waveriders for aero-gravity assist was to quantify their shapes for high altitude applications. Although the cruise for an AGA would be much lower, reentry would require transiting the upper atmosphere. Anderson et al.[72] used continuum flow analysis to consider waveriders above 90 km in Earth's atmosphere, and then applied corrections for low density effects. They found that as altitude increased, so did viscous drag associated with decreasing Reynolds number. While this lowered the maximum L/D, low density effects mitigated the decrease to a small degree. Rault[73] used DSMC for waveriders at altitudes between 97 km and 140 km in Earth's atmosphere and concluded that the very concept of a waverider might not be accurate in this flight regime, as the shock layers are broad and largely unattached to the leading edge. The effects of leading edge shock detachment resulted in L/D values well below 1 for this flight condition. An aero-assisted spacecraft would not be able to cruise with such poor aerodynamic performance.

Anderson et al.[74] extended the design space by designing viscous optimized waveriders for atmospheres beyond Earth. This study was extremely promising for

aero-gravity assist, as they calculated potential L/D values at Mars and Venus which were well above the range of requirements for the maneuver. For example, at 30 km altitude above Venus, a waverider with L/D = 14.96 was designed! While Mars was also able to support promising L/D ratios (between 5 and 10), Venus was found to be the most promising in L/D magnitude. Lewis and McRonald[75] analyzed trends in waverider design with specific AGA trajectories in mind. They showed curves relating L/D to leading edge radius, and L/D to overall waverider length. They also described a few sample trajectories including vehicle dimensions, maximum stagnation point heating, length of the required atmospheric turn, and all relevant velocities and velocity increments.

A trajectory based approach considers the aero-gravity assist maneuver independent of the design of the waverider vehicle. By assuming some vehicle L/D ratio, and a constant atmospheric flight altitude (ignoring the entry and ascent), analytical equations can be derived.[75] Simplifying the approach even more, an energy based method looks at semi-major axis, perihelion distance, and orbital period without consideration of where the planets lie along their orbits. Similarly, the energy of heliocentric transfer orbits which would be needed to reach the fly-by planet(s) and the final destination are easily computed. Finally, the needed performance of a gravity or aero-gravity assist is simply the change in direction and orbital elements between adjacent heliocentric transfer orbits. Using this approach, McRonald and Randolph[76,77] generated trends relating important parameters to the hyperbolic excess approach velocity: atmospheric flight time, bending angle, maximum aerodynamic g-load, and velocity loss. Analyzing their data, they found that Mars was a more promising candidate for AGA than Venus, because the atmospheric flight speeds would be lower. Overall, the best trajectories were found when an aero-gravity assist was used at both Mars and Venus. This would significantly reduce the required launch energy from Earth. Johnson and Longuski[78] developed a graphical

Table 2.1: Fastest potential AGA trajectories to the outer planets with L/D = 7 (ignoring phasing). All flybys of Earth (E), Mars (M), and Venus (V) represent aero-gravity assists. Time of flight (TOF) given in years. From Ref. [78]

v_∞,	Jupiter (J)		Saturn (S)		Uranus (U)		Neptune (N)		Pluto (P)	
km/s	Path	TOF	Path	TOF	Path	TOF	Path	TOF	Path	TOF
3	EVEMJ	1.99	EVEMS	3.53	EVEMU	8.21	EVEMN	15.33	EVEMP	23.08
3	EVEVMJ	1.64	EVEVMS	2.43	EVEVMU	4.24	EVEVMN	6.35	EVEVMP	8.21
3	EVEVEMJ	1.56	EVEVMVS	2.20	EVEVMVU	3.46	EVEVMVN	4.91	EVEVMVP	6.18
4	EVMJ	2.20	EVMS	5.61	—		—		—	
4	EVEMJ	1.43	EVEMS	2.44	EVMVU	4.71	EVMVN	7.21	EVMVP	9.44
4	EVEMVJ	1.36	EVEMVS	1.92	EVEMVU	3.20	EVEMVN	4.65	EVEMVP	5.93
4	EVEMVEJ	1.32	EVEMVES	1.87	EVEMVEU	3.14	EVEMVEN	4.58	EVEMVEP	5.85
5	EMJ	2.46	—		—		—		—	
5	EVMJ	1.46	EVMS	2.61	EVMU	5.52	EVMN	9.14	EVMP	12.45
5	EVEMJ	1.24	EVMVS	2.08	EVMVU	3.53	EVMVN	5.18	EVMVP	6.63
5	EVEMVJ	1.23	EVEMVS	1.78	EVEMVU	3.04	EVEMVN	4.49	EVEMVP	5.76
6	EMJ	1.68	EMS	3.64	EMU	14.16	—		—	
6	EVMJ	1.27	EVMS	2.21	EMVU	4.41	EMVN	6.96	EMVP	9.23
6	EVEMJ	1.11	EVMVS	1.74	EVMVU	3.00	EVMVN	4.45	EVMVP	5.72

method of viewing this energy based method. They then created tables of minimum time of flight to the outer planets with an L/D = 7 (see Table 2.1). These serve as theoretical minimums for the time of flight from Earth to a destination planet with a given launch energy.

As mentioned, the energy based method does not account for planet phasing. Many studies have also conducted searches of launch opportunities over decade long ranges maintaining the constant altitude and L/D assumptions. Sims et al.[79,80] generated a comprehensive set of tables showing mission opportunities to Jupiter, Saturn, Uranus, Neptune and Pluto. They allowed for an infinite lift-to-drag ratio, as needed. Bonfiglio et al.[81] generated similar trajectory tables, but now using L/D = 5, 7, or 10.

The trajectory based approaches described thus far focus on the interplanetary AGA trajectory, with only an analytic equation to describe the atmospheric flight. Lohar et al.[82] used the equations of motion, an estimate for the maximum L/D ratio, and a Newtonian theory based drag polar to integrate the atmospheric trajectory. They introduced a limited amount of control in allowing the spacecraft to vary its pitch, and therefore its L/D. They then put the simulation into an optimization routine and attempted to maximize the heliocentric velocity. They demonstrated that even without the simplifying assumptions of constant lift-to-drag ratio and ignoring ascent/descent, the AGA maneuver is superior to the gravity assist maneuver. They later demonstrated that the same is true, even with the introduction of a heat rate constraint[83] and especially when heliocentric plane change is desired.[84]

Lavagna et al.[85] modelled the atmospheric AGA manuever with an increased number of degrees of freedom in pitch control, thus complicating the design space. By optimizing for planetocentric velocity loss and time of maneuver, they demonstrated that a genetic algorithm was the most effective at parsing the atmospheric trajectory design space, due to the extreme nonlinearity and number of local optima.

The pitch angle is not the only the means of varying a vehicle's lift vector and controlling the atmospheric trajectory. Armellin et al.[86] introduced a bank angle control law and compared it to the pitch controller, once again using a genetic optimizer. More advanced control systems have also been proposed using contemporary control theories.[87–89]

Two hypersonic vehicles and their associated aerodynamic performance likely vary sufficiently that they would not have identical optimal flight profiles. Armellin et al.[28] published a study in which they developed an algorithm to optimize the atmospheric trajectory being flown concurrently with the vehicle shape (see Figure 2.11). They used the variable wedge angle method of describing waveriders introduced by Starkey and Lewis[17] including leading edge bluntness. The study is both a proof of concept of the multi-faceted optimization approach, as well as a useful validation that AGA would be more effective than gravity assist alone, even with strong heating constraints which increase the leading edge radius and reduce L/D.

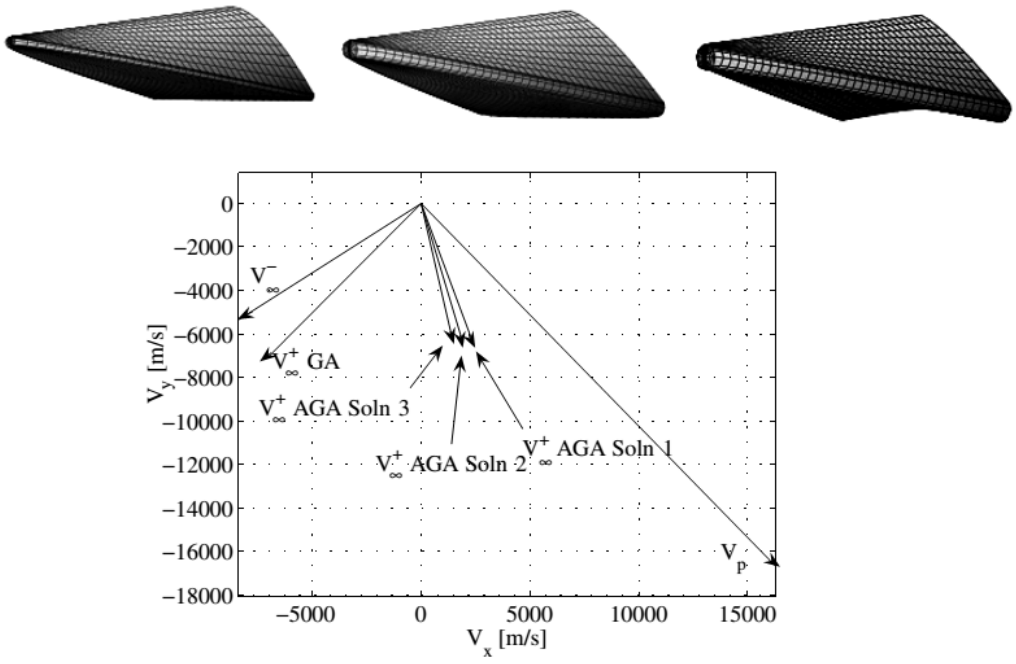

Figure 2.11: The three optimal waveriders corresponding to the three optimal trajectory solutions 1, 2, 3. Note the varying degrees of turning from the approach velocity vector towards the planet's velocity vector. From Ref. [28]

2.2.3 Aero-capture

When on an interplanetary trajectory, a force must be applied to slow a spacecraft in order to enter a captured orbit around a planet. Aero-assist can be used in this scenario as well, by entering the destination planet's atmosphere on a hyperbolic orbit. This aero-capture concept was first described by Cruz in 1979.[90] It was theorized using a moderate lift-to-drag shape in order to allow sufficient control authority to overcome uncertainties in atmospheric chemistry. As the concept has evolved, our understanding of destination planets has improved, and technology heritage has been prioritized. This has steered mission designers towards low-lift (L/D $<$ .4) and medium-lift (.4 $<$ L/D $<$ 1) forms. In fact, the authors are the first to present results of an aero-capture using a high lift-to-drag waverider (in this work and in Ref. [91]).

Section 2.2.3 will not exhaustively cover the state of the art in blunt body aero-capture, as the maneuver is of limited similarity to the high-lift analog. Control algorithms presented for medium- and low-lift aero-capture[92,93] have little applicability to waveriders. The increased strength of the lift force and reduced deceleration force greatly change the dynamics. These studies can sometimes be used for comparison, however. For example, Armellin and Lavagna[94] have published a multi-objective optimization of medium to low-lift aero-capture. The pareto-optimal solutions they generated will be compared to pareto-optimal solutions for high-lift waveriders.

For a more complete analysis, Lockwood provides a thorough overview of aero-capture concepts for Titan[95] and Neptune,[96] while Wright et al.[97] presented a comparable study for Mars.

2.3 Interstellar Probes

As of this writing, the Voyager 1 probe is the only man-made object to reach interstellar space. It was launched from Earth in the 1970s with a primary mission of studying the Jovian and Saturnian systems. Exiting the solar system was only a secondary mission objective, so it has limited capability for science in interstellar space. The suggestion of a mission with the primary purpose of reaching interstellar space was presented in 1987 by Nock[98] and Etchegaray.[99] At the time, the mission concept was called the "Thousand Astronomical Units (TAU) Mission" (interstellar space begins around 125 AU). This ambitious endeavor would use a nuclear powered electric propulsion system in order to attempt to reach the TAU mark in 50 years. The TAU mission suggested three main scientific objectives:[99]

1. Stellar Parallax. The confidence intervals of measurements at astronomical scales are relatively large, as we are able to observe only from Earth or very nearby. Sending a spacecraft to interstellar space could dramatically improve the measurement accuracy. This has practical applications for our understanding of the expansion rate of the Universe and thereby its history and evolution.

2. Astronomy. A unique vantage point would allow new observations of the Universe, possibly revealing never before seen galaxies and star clusters.

3. Space Physics. A spacecraft sent to interstellar space could make better measurements of the heliopause, interstellar medium and make tests of gravity lensing with signals sent to Earth.

The TAU mission was never funded, but it has been revised and updated. In 1999, NASA started an interstellar program, headquartered at JPL. Three studies highlight their scientific goals,[100] the engineering design,[101] and the propulsion options

in specific.[102] The stated mission objective was to reach 200 AU in under 15 years with sufficient consumables to last until at least 400 AU. Using a solar sail, the necessary velocity was theorized to be achievable, but the mission was once again never funded.

A thorough set of direct and gravity assist trajectory options to interstellar space was presented by Fiehler and McNutt.[103] They found a minimum time to 200 AU of 23.7 years by performing a gravity assist around Jupiter and then Saturn. The baseline trajectories presented by Fiehler and McNutt will be heavily leveraged for comparison with the aero-gravity assist trajectory options presented in this work (these trajectory options are summarized in Fig. 2.12).

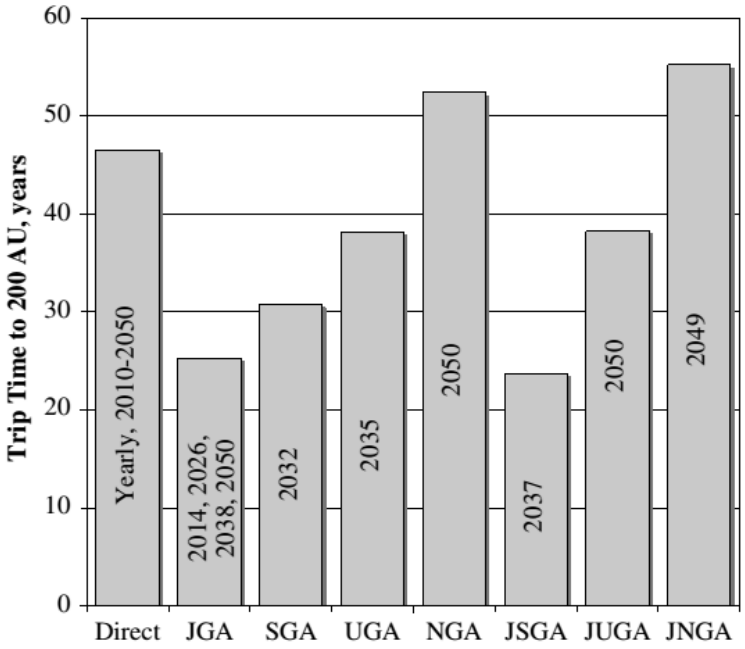

Figure 2.12: Performance of different trajectory options to reach 200 astronomical units using single or double gravity assists around the outer planets. From Ref. [103]

Chapter 3

Geometric Modeling

This chapter will discuss the nature of hypersonic waveriders and various methods of generating their forms. Discrete inputs are used to describe compressible shock structures and to create matching aerospace shapes. By modifying the inputs, a great variety of vehicle geometries are possible, with different expected aerodynamic, aerothermal, and structural characteristics. Optimization methodologies can be used to modify the inputs and maximize one or multiple performance qualities. The applied studies presented in the later chapters of this work use one or more of the waverider models discussed in this chapter.

3.1 General Comments

Any aerospace vehicle traveling greater than the speed of sound will develop shockwaves, greatly increasing the gaseous pressure over its surface area. As the flight speed of the vehicle increases, so too does the pressure behind these shockwaves. Any vehicular surface which lies at a nonzero angle relative to the velocity experiences a deceleration force due to the increased pressure known as wave drag. This is an unavoidable result, and at best, wave drag can only be mitigated by changing the flight conditions or by reducing the frontal profile of the vehicle.

While wave drag is a penalty of the shockwaves present at supersonic and hy-

personic speeds, the increased gas pressure surrounding the vehicle can be exploited for a beneficial purpose: generating lift. If the shockwaves create stronger pressure in the flow below the vehicle than the pressure in the flow above the vehicle, then a net vertical force is created. This phenomena is known as compression lift, and it serves as a fundamental principle behind the design of hypersonic waveriders. The design objective is to exploit this behavior as efficiently as possible. Highly compressed post-shock gas should be confined to the underside of the vehicle, and the upper surface should be exposed to a less compressed flowfield. This is made possible by designing the waverider such that its leading edges are attached to the shock structures. If there is any detachment, or a gap between the shockwave and the leading edge of the vehicle, highly compressed gas can 'leak' around the leading edge to the upper surfaces of the vehicle. This is known as flow spillage.

The design process of a hypersonic waverider can be the derivative of a known flowfield, can be conducted in concert with a flowfield construction, or can result in a defined flowfield. Regardless, the final product of a waverider design includes the shape of a vehicle, and an estimate of the compressible flow around it. This implies an important detail of the waverider concept, they are designed for one specific free-stream flight condition. For geometry definition, shock geometries must be calculated, which can only be done with a fixed free-stream value for both the Mach number, M, and the ratio of specific heats, γ. The values chosen typically correspond to a relevant flight condition during the trajectory being designed (often peak dynamic pressure).

During a real hypersonic trajectory both M and γ will likely vary, and in those cases, the vehicle is said to be 'off-design'. In many cases, the performance of the waverider will suffer when flying in an off-design condition. As the flight speed changes, the geometry of the shock structures will change as well, which can result in leading edge detachment and flow spillage.

In order to produce attached shockwaves, each waverider shape is first created with sharp leading edges. This allows relatively simple shock geometry calculation and makes high speed geometry generation more tractable. Unfortunately, a realistic hypersonic design requires the leading edges of the vehicle to be slightly blunted for realistic survival of heating loads. The waverider modeling conducted in this work similarly uses blunted leading edges. The sharp vehicle designs are modified after the initial design to add bluntness. Various methods of blunting leading edges have been proposed in the past,[56,58] however this work will use a volume addition methodology. Upper and lower surfaces are moved perpendicularly outward a distance R, and a cylindrical leading edge is created in the resulting gap (see Figure 3.1). This volume addition procedure was preferred over numerically "polishing" the leading edges because that can result in significant volume reduction.

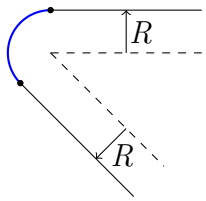

Figure 3.1: Waverider leading edge before (dashed) and after (solid) adding blunted leading edge (blue).

Finally, the aerodynamic model which will be discussed in the next chapter requires the numeric description of each waverider to be in a consistent format, regardless of the geometry model used to generate it. In specific, that format is an unstructured triangular mesh of the surface (see Figure 3.2). The greater the number of triangles used to describe the surface, the more accurate the aerodynamic model will be, in exchange for increased computation time. For each triangle in the surface mesh, the following parameters are required:

1. Coordinates (x,y,z) of the three vertices
2. Coordinates of the geometric center
3. Direction of the surface outward normal, $\hat{n}$
4. Direction of the surface streamwise direction, $\hat{t}$

5. Length of the triangle in the streamwise direction

6. Area

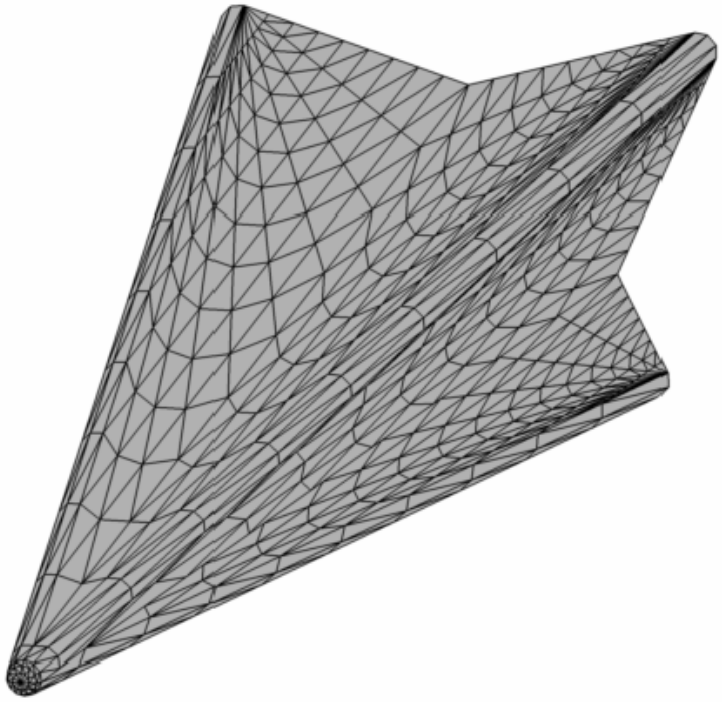

Figure 3.2: Example of an unstructured triangular mesh grid of a waverider surface.

3.2 Caret-Wing Waveriders

Caret-wing waveriders will not be used in any of the case studies of the later chapters of this work, however, they are a relatively simple to understand concept which make subsequent sections easier to grasp. The caret-wing design was first proposed by Terrence Nonweiler in 1959,[4] and is the first documented waverider concept. They are so named, because each lateral cross Section resembles the keyboard caret character, ˆ.

A caret-wing is formed from a basic compressible flow structure, a planar shockwave, emanating from a wedge flow disturbance (see Figure 3.3). The leading edges are drawn along the shock plane in the downstream direction. Designing the

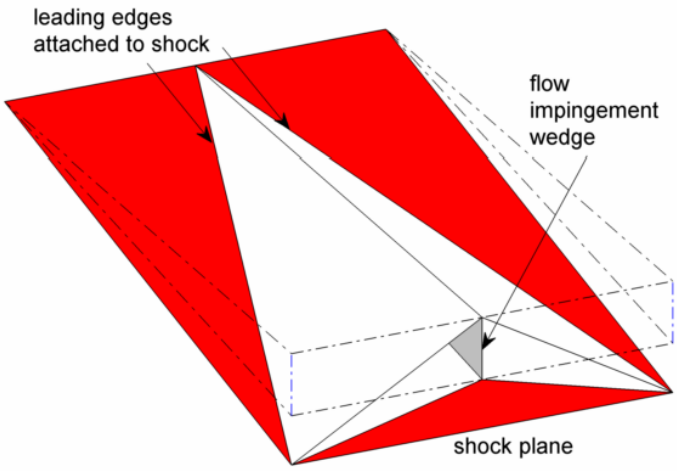

Figure 3.3: Caret-wing waverider

leading edges to be directly attached to the shockwave will prevent flow spillage and improve the compression lift effect. The upper surface of a caret-wing is parallel to oncoming flow (at zero angle-of-attack). The shock compresses the gas that flows past the lower surface of the vehicle, while the gas flowing over the upper surface will be at or near free-stream pressure.

3.2.1 Parameterization

There are relatively few variables required to design a caret-wing waverider (see Figure 3.4):

1. Wedge angle, θ
2. Wedge width, y_0
3. Wing angle, κ
4. Length, L, or Volume, V
5. Free-stream flight variables (likely M and γ)

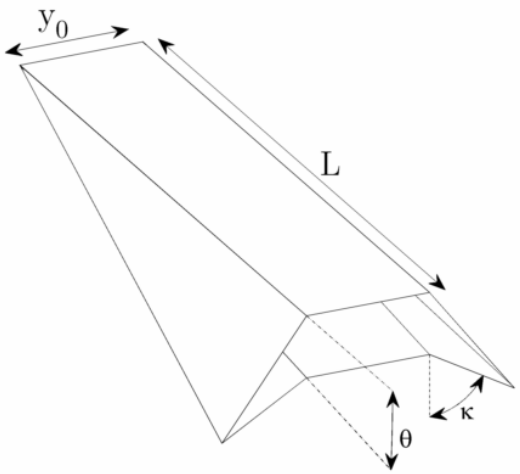

Figure 3.4: Caret-wing waverider design variables

The wedge width can be zero, as shown in Figure 3.3, however, it needn't be, as shown in Figure 3.4. There are practical reasons why a finite wedge width would be desirable; the wedge section of a caret-wing could contain additional payload or it has been considered for the placement of a propulsion system such as a scramjet.[49]

The wing angle, κ, can vary between 0° and 90°, however, designs yielded from a value chosen near either of these endpoints is unlikely to be desirable. As κ approaches 90°, the width of the caret-wing increases rapidly, and the compression lift effect is dampened. As κ decreases towards 0°, wall effects become increasingly important, and simple 2-d flow assumptions are not sufficient to capture the aerodynamics involved. The flow inside of the caret-wing section is assumed to be entirely 2-dimensional and parallel to the surfaces (no lateral flow). Near the walls of the caret-wing, boundary layer effects decrease the validity of that simplifying assumption.

3.3 Starbody Waveriders

Starbody waveriders consist of multiple caret-wing sections attached leading edge to leading edge and upper surface to upper surface (see Figures 3.5 and 3.6).

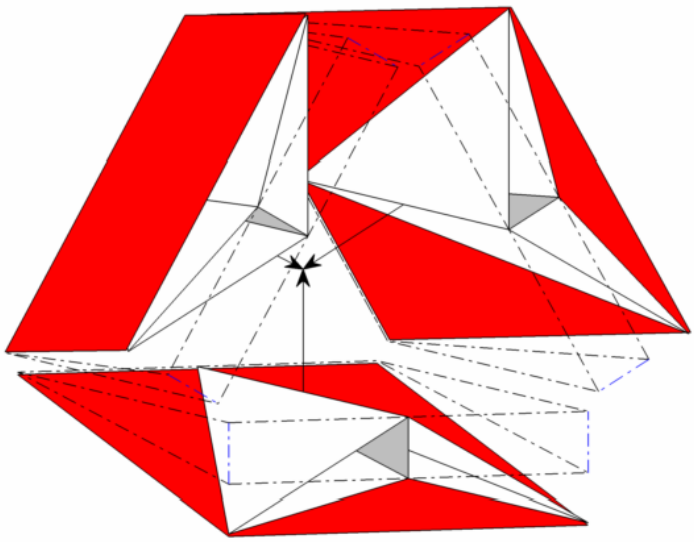

Figure 3.5: Three caret-wings combine to form a star-body

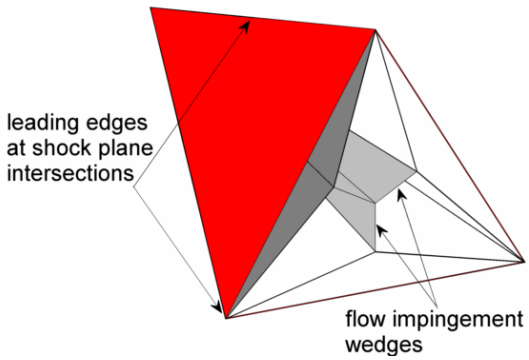

Figure 3.6: Three-tine Starbody

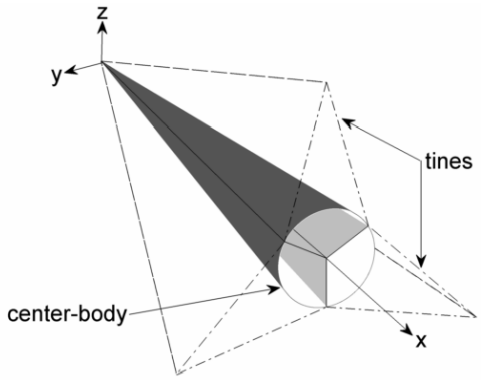

Figure 3.7: Starbody terminology and axes

The number of caret-wing sections which are combined dictate the number of wing protrusions, or so called tines (see Figure 3.7). In order to practically complete the design, a minimum of three caret-wing sections are required. There is no maximum, however, as increasingly thinner caret-wing sections could be combined. For this work, a maximum of six-tine starbodies are considered. As the number of tines increases, the associated value of κ (see Figure 3.4) for each caret-wing section necessarily trends closer and closer to 0°. As discussed in the previous section, the assumption of a simple two dimensional flowfield within the caret-wing sections

becomes less accurate in this case. The boundary layers from the vehicle walls comprise a larger and larger percentage of the flowfield as κ decreases.

The most basic starbodies are both vertically and horizontally symmetric. Regardless of the number of tines, or the roll angle, these vehicles always produce zero net side force and zero net lift. Varying the angle-of-attack of a symmetric starbody could produce a net lift force, however, this changes the strength of the shockwave structures surrounding the vehicle, resulting in off-design behavior.

Starbodies do not need to be symmetric, so long as their leading edges are located at adjacent shock planes. Breaking the symmetry about the x-y plane (see Figure 3.7 for coordinate system) can result in vehicle shapes which use compression lift to generate a net force in the vertical direction, even at zero angle-of-attack. It is unlikely that asymmetry would be desired about the x-z plane, as a net side force is undesirable for an aerospace vehicle.

3.3.1 Parameterization

The asymmetric starbody design methodology first creates a conical center-body containing the 2-d flow impingement wedges of each caret-wing section (see Figure 3.7). Each 2-d wedge corresponds to the base of a caret-wing. The dimensions of the center-body are allowed to vary within certain limits, as are the locations of the flow impingement wedges.

In this work, four parameters are used to describe the shape of the center-body: number of flow impingement wedges and tines (n), eccentricity (e), distribution of tines (D) and the vertical nose offset (α_0). Two additional parameters are used to scale the vehicle: volume (V) or length (L) and slenderness ratio of the center-body (a/L). Next, the sharp leading edged starbody is fully defined using a shock strength calculator (these will be described in Chapter 4). The shock calculator requires an additional two or three variables, often altitude in the atmosphere of

a specified planet (h) giving standard day free-stream properties, and flight Mach number (M). Finally, a value for the leading edge radius (R) is required to add bluntness.

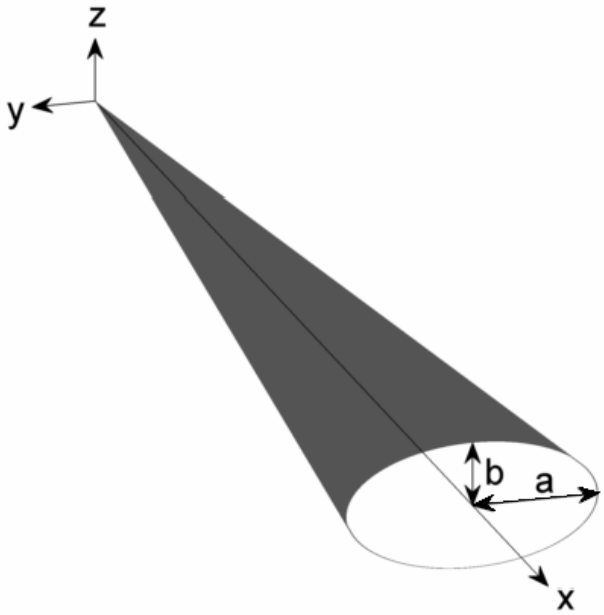

Figure 3.8: Center-body dimensions and coordinate system.

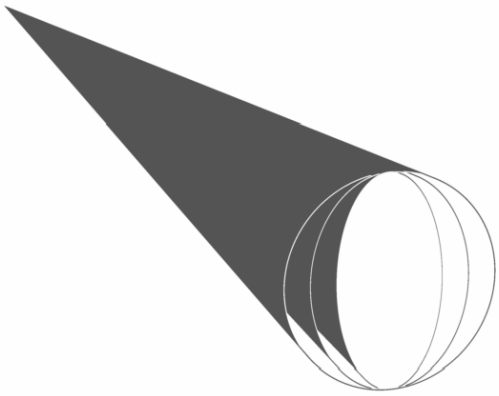

Figure 3.9: Center-bodies with $e = 0$, $e < 0$, and $e << 0$

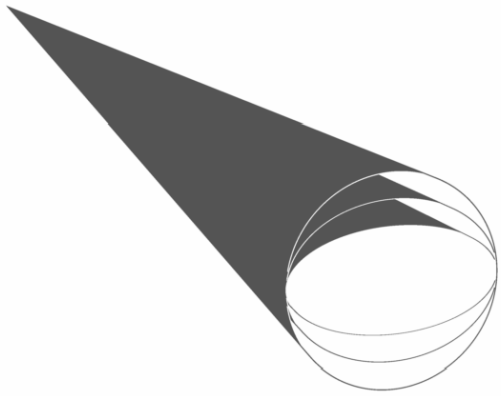

Figure 3.10: Center-bodies with $e = 0$, $e > 0$, and $e >> 0$

The eccentricity of the center-body, e, is a ratio between -1.0 and 1.0 which compares the longer and shorter sides of an elliptical cross-section of the conical

center-body. It is calculated as:

$$e = \frac{a - b}{a + b} \tag{3.1}$$

where a is the semi-major axis and b is the semi-minor axis (see Figure 3.8). As e increases from zero, the center-body becomes more elliptical. In order to model an ellipse elongated in either the spanwise or vertical axis, negative values of eccentricity can be used. The absolute value of any $e < 0$ is used to represent eccentricity with stretching along the z axis rather than along the y axis. Figures 3.9 and 3.10 show center-bodies with various values of e.

The D parameter is a fraction between -1.0 and 1.0 that weights asymmetric tine placement on the top (maximum at $D = +1$) or bottom (maximum at $D =$ -1) of the vehicle. In order to connect all shocks, there are limits to the location of the tines on one side of the center-body. For example, a value of $D =$ - .35 indicates that each tine has rotated 35% from its initial, axisymmetric location towards its bottom-most location. Figures 3.11 and 3.12 show five-tine center-bodies with various values of D. Note that as D varies, the relative size of each tine will vary as the intersection of adjacent shock planes occurs in different locations in space.

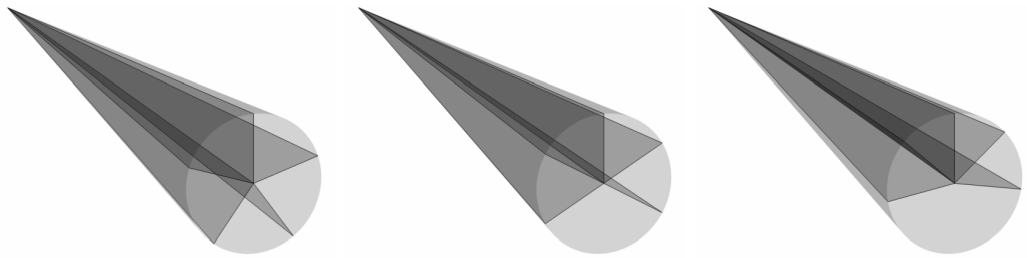

Figure 3.11: Center-bodies with D = 0, D > 0, and D >> 0

In the calculation of the center-body slenderness ratio, the semi-major axis of the ellipse in the base plane is scaled by the length of the vehicle, L. This is similar to specifying the half-angle of the center-body:

$$\theta_{\text{center-body}} = \tan^{-1}(\frac{a}{L}) \tag{3.2}$$

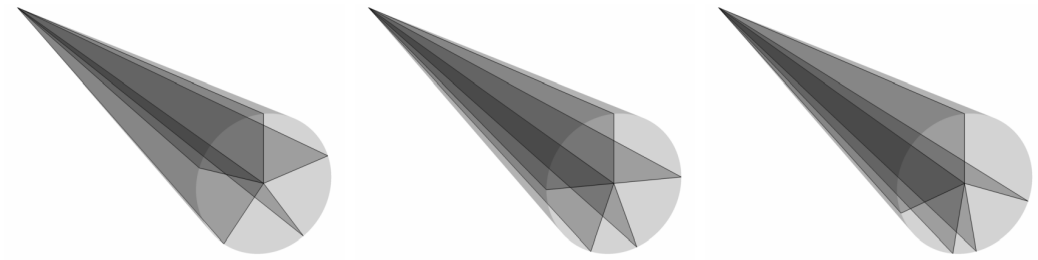

Figure 3.12: Center-bodies with $D = 0$, $D < 0$, and $D << 0$

The slenderness ratio is preferred to a half-angle as it is more explicit about the dimensions being compared when the center-body is non-circular.

The vertical nose offset, α_0, moves the location of the nose of the cone, making the center-body an oblique, rather than right, cone. The nose of the center-body is only able to move vertically in the $\pm z$ direction, using a value of α_0 as a fraction between -1.0 and 1.0. Figure 3.13 shows five-tine centerbodies with various values of α_0. In terms of geometry generation, this changes the flow impingement wedge angles and the resulting shock strengths. It is scaled by the semi-major axis (when $e > 0$) or the semi-minor axis (when $e < 0$) in order to give the parameter units of length. This method prevents the nose from creating negative flow impingement angles. Typically a positive α_0 is desired, as it will create larger flow impingement angles on the lower half of the starbody and weaker shocks on the upper half of the starbody, thus amplifying the compression lift effect.

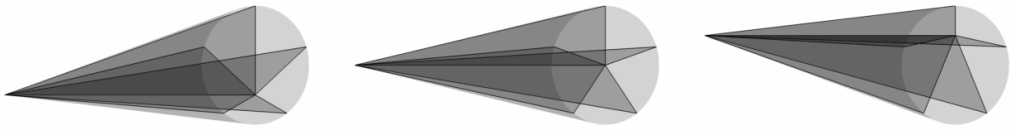

Figure 3.13: Centerbodies with $\alpha_0 < 0$, $\alpha_0 = 0$, and $\alpha_0 > 0$

The center-body and final starbody can be scaled up or down to match a proscribed overall length or volume. Only one can be used, however, or else the geometry is overdefined.

3.3.2 Creation Method

The steps to create the star shape are as follows:

1. Using $L = 1$, determine a from a/L.

2. At $x = L$, create the center-body ellipse using e and Equation 3.1 to determine the semi-minor axis. See Figure 3.8.

3. Using α_0, determine the location of the center-body nose, along the $x,y = 0$ line. See Figure 3.14.

4. Determine locations around ellipse of flow disturbances (using n and D). By connecting the locations at $x = L$ to the vehicle nose at $x = 0$, the flow disturbance wedges are created. See Figure 3.15.

5. Calculate the resulting flow disturbance angle, θ, for each wedge. This is the angle between the x-axis and the flow disturbance line along the edge of the center-body. See Figure 3.16.

6. Calculate shock-angles, β, using a shock geometry solver such as the θ-β-M relation or a high temperature iterative solver.

7. Using the β angle for each wedge, draw the shock planes. See Figure 3.17.

8. Find intersection lines of adjacent shock planes (these will be the sharp leading edges). See Figure 3.18.

9. Connect lines found in step 8 to the lines on the surface of the center-body found in step 4. This closes the vehicle. See Figures 3.19 and 3.20..

10. Move each surface a distance R in a direction perpendicular to that surface. See Figure 3.21.

11. Draw a circular leading edge in each resulting gap, ensuring tangency to both surfaces.

12. Calculate a normalized volume, V_0.

13. Scale the vehicle to the desired absolute volume, V, or length, L.

    See Figure 3.22 for the final waverider!

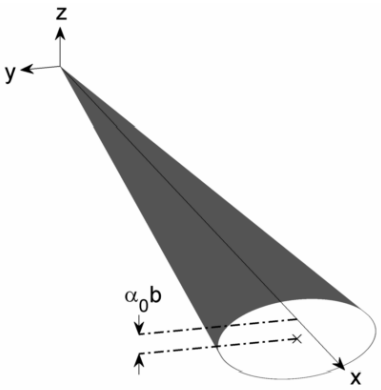

Figure 3.14: Step 3. Move center-body nose using semi-minor or semi-major axis, and input variable, α_0.

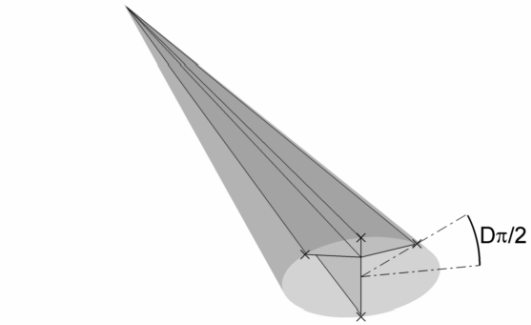

Figure 3.15: Step 4. Determine flow impingement locations around center-body using D.

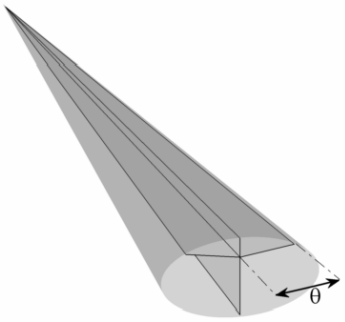

Figure 3.16: Step 5. Determine the flow impingement angles, θ.

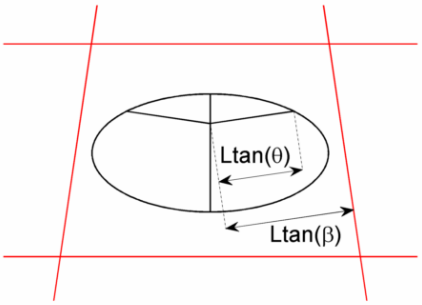

Figure 3.17: Step 7. Determine the locations of the shock planes. This image is in the base plane of the center-body.

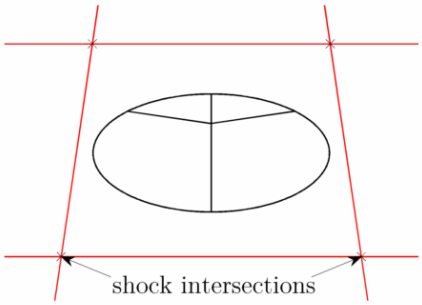

Figure 3.18: Step 8. Find the intersections of the shock planes. Again, this image is shown in the base plane of the center-body.

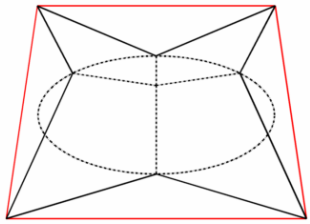

Figure 3.19: Step 9. Connect the shock intersections with the flow impingement wedges. This image is in the base plane of the center-body.

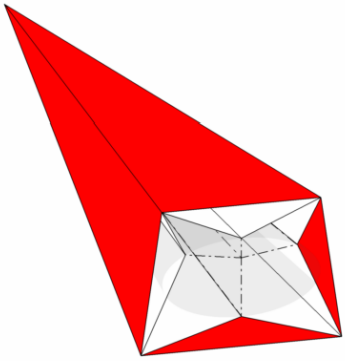

Figure 3.20: Step 9. Connect the shock intersections with the flow impingement angles and with the nose of the center-body.

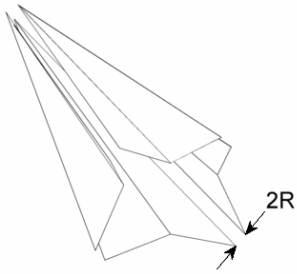

Figure 3.21: Step 10. Move each surface out by a distance R

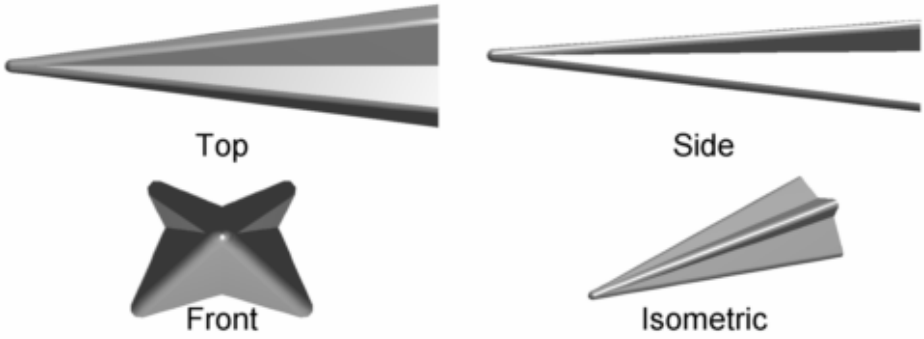

Figure 3.22: The example four-tine starbody waverider.

3.3.3 Feasibility

Certain combinations of D, e, α_0 and flight conditions result in designs for which adjacent shock planes either don't cross, or more often, intersect a different shock plane first. The former condition can only be reached when adjacent shock planes are parallel. The latter condition becomes more and more likely as D, e, and α_0 increase in magnitude.

As a demonstration, consider the generation of a four-tine starbody using the center-body shown in Figure 3.23. The inputs will be infeasible if the shock planes from the lateral flow impingement wedges intersect before either intersect the planar shock from the flow impingement wedge in the -z direction. With the given configuration, this condition is closely reached with a Mach number of 10 as shown in Figure 3.24. With the exact same geometry inputs, but an increased design flight speed of $M = 100$, the design is no longer feasible, and the shocks from the lateral flow impingement wedges cross eachother before crossing the bottom most shock (see Figure 3.25).

To consider the conditions which result in an infeasible design, the intersection of lateral shocks must occur lower than the shockwave from the bottom flow impingement wedge. That is, as shown in Figure 3.26:

$$H_2 < H_1 \tag{3.3}$$

The value for these heights are dependent on shock strengths and the parameters depicted in Figure 3.27. The heights are defined as:

$$H_1 = \frac{\Delta S_1}{\cos(\phi)} = \frac{L\tan(\beta_1)}{\cos(\phi)} \tag{3.4}$$

$$H_2 = \Delta S_2 = L\tan(\beta_2) \tag{3.5}$$

where β_1 and β_2 are the shockwave angles, calculated as in step 7 above. The angle, ϕ is calculated from the geometry input variables using the law of cosines (Equation 3.6) and law of sines (Equation 3.7):

$$R_1^2 = (\alpha_0 a)^2 + R_0^2 - 2\alpha_0 a R_0 \cos(\frac{\pi}{2} + \frac{D\pi}{2}) \tag{3.6}$$

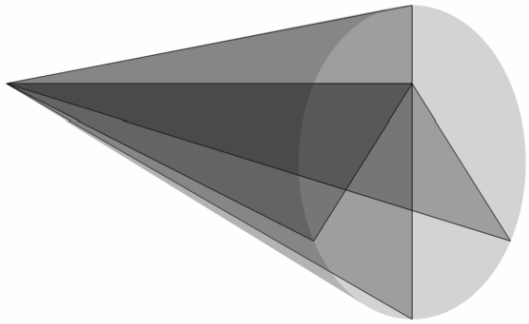

Figure 3.23: Center-body of a starbody waverider with $e = .15$, $\alpha_0 = \frac{1}{2}$, and $D = -\frac{1}{3}$.

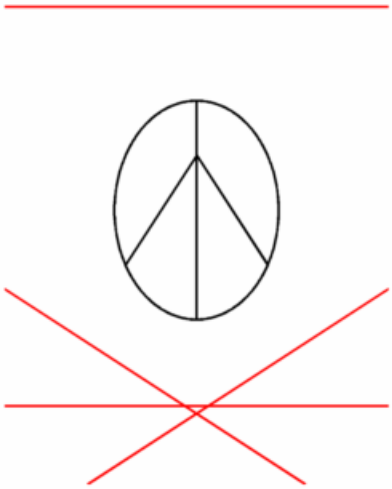

Figure 3.24: Base plane of the example center-body with shock planes drawn in for $M = 10$, $\gamma = 1.4$. Design is feasible.

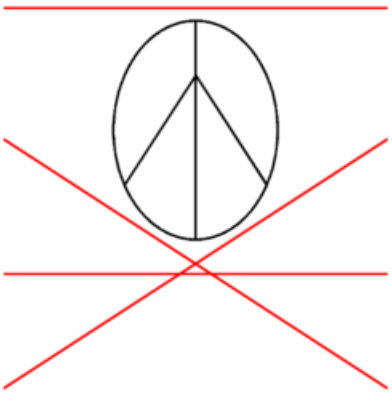

Figure 3.25: Base plane of the example center-body with shock planes drawn in for $M = 100$, $\gamma = 1.4$. Design is infeasible.

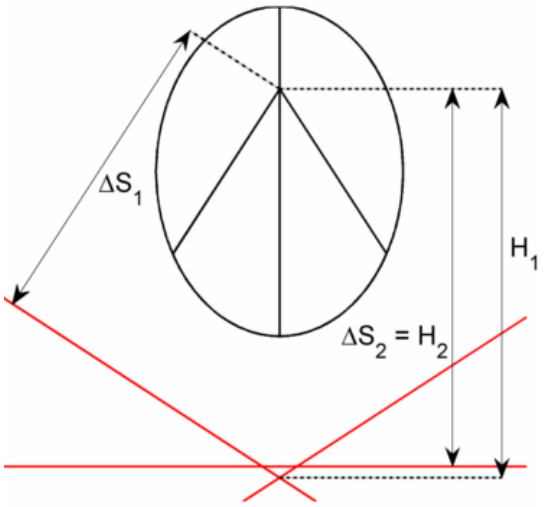

Figure 3.26: Dimensionality of shock plane intersections.

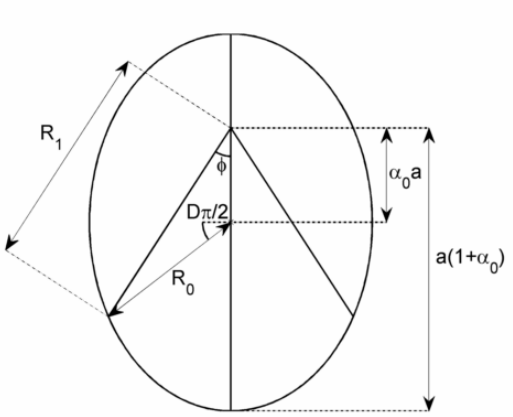

Figure 3.27: Relationship between input variables and base plane geometry.

$$\frac{\sin(\frac{\pi}{2} + \frac{D\pi}{2})}{R_1} = \frac{\sin(\phi)}{R_0} \tag{3.7}$$

Finally, when the center-body is not circular and D does not equal 0 or 1, the value of R_0 is not equal to the semi-major or semi-minor axes. Therefore, the value of this distance is determined using the following equation describing an ellipse:

$$R_0 = \frac{ab}{\sqrt{(b\cos(\frac{\pi}{2} + \frac{D\pi}{2}))^2 + (a\sin(\frac{\pi}{2} + \frac{D\pi}{2}))^2}} \tag{3.8}$$

Depending on the method used to determine β as a function of the flow impingement angles, the set of Equations 3.4 through 3.8 can either be solved in closed form or must be solved using an iterative numerical root finder for the values of H_1 and H_2. With these values, feasibility is checked using the inequality presented in Equation 3.3.

3.4 Osculating Cone Waveriders

Gottfried Wilhelm von Leibniz coined the phrase 'kissing circle' or 'osculating circle' (circulus osculans in the original latin) to refer to a circle which is exactly tangent to a curve with circular radius matching the curve's local radius of curvature.[104] An osculating cone is therefore one which contains an osculating circle in some relevant plane.

In the osculating cone waverider generation method, a flowfield is first determined as one axisymmetric slice of the flow about a conical body. This is determined by integrating the classic Taylor-Maccoll equations.[54] The waverider shape is carved from an imagined flowfield which is an amalgamation of multiples of these cross sections stacked side-by-side. All cross sections are generated from a cone with the same half angle; however, each cone has a different local radius in the waverider's base plane. Given that multiple cones are theoretically joined together, each is referred to as "osculating" or just "kissing" the net shockwave.

The radial conical sections are translated forward and backward relative to the oncoming flow, thereby requiring only one Taylor-Maccoll solution per waverider, while allowing variation in the shockwave's local radius of curvature. This is only an approximate solution, but previous studies of osculating cone waveriders using CFD have validated that the method produces well-defined waverider shapes, so long as there is smooth variation in shock radii.[38] If the radii vary too rapidly, the Taylor-Maccoll solution increasingly underpredicts the rate of lateral flow expansion. This inaccuracy can also be mitigated by increasing the number of osculating cones used to model the shockwave shape.

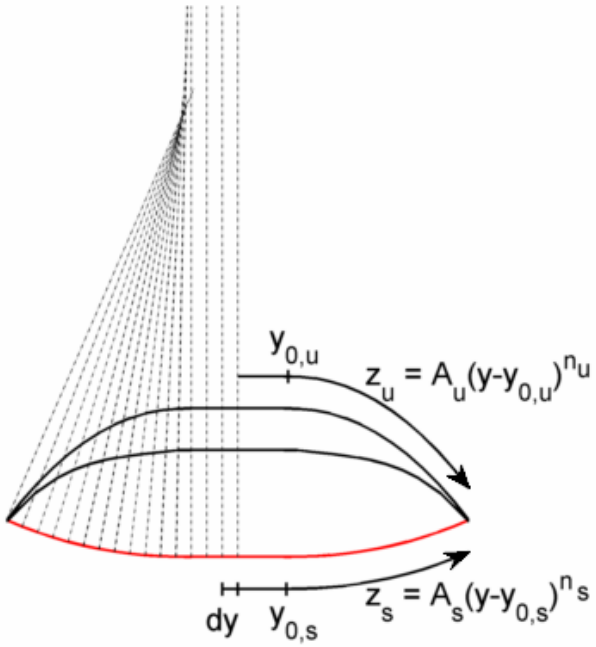

Figure 3.28: Base plane of osculating cone waverider. Dashed lines indicate radii of individual osculating cones. Red line indicates shock surface.

3.4.1 Parameterization

The parameterization of osculating cone waveriders follows the so-called dual power law approach described by Chauffour (see Figure 3.28).[38] An equation of the form shown in Equation. 3.9 defines both the vehicle's upper surface, as well as the arbitary shock shape in the base plane (with different values for A, y_0, and n for each surface):

$$z = A(y - y_0)^n \tag{3.9}$$

Note that y_0 is the half-width of a flat section of the respective surface, A is a scalar coefficient, and n is a scalar exponent.

In addition to these variables, additional inputs are needed to scale the vehicle, describe the cone used in the Taylor-Maccoll integration, to quantify the flight

condition, and to specify the bluntness of the waverider's leading edge.

As with starbody waveriders, a value for either the volume, V, of the final vehicle or the length, L, of the final vehicle is required. The vehicle is designed using a unit length, and a baseline volume is calculated. The final vehicle is simply scaled up so that the final length or volume matches the input.

As mentioned, each osculating cone has the same half-angle, θ, in order to greatly increase the calculation efficiency, as the Taylor-Maccoll equations are integrated only once. The value of the half-angle is a required input to the shape generation process.

The final variables are the same as those of starbody waveriders: two or three inputs to define the flight condition, and one additional value indicating the leading edge radius, R.

3.4.2 Creation Method

The steps to create a waverider using the osculating cones methodology are as follows:

1. Solve the Taylor-Maccoll equations for the flowfield in one axisymmetric slice around a cone with half angle, θ. For simplicity, assume that the cone increases in radius in the $+x$ direction, and has its nose located at the origin.

2. Generate points for the shockwave shape and upper surface shape using the inputs A_s, $y_{0,s}$, n_s, A_u, $y_{0,u}$, and n_u at an even interval dy. See Figure 3.29.

3. Use those points to numerically calculate the first and second derivative at each point. The end points will require a forward or backward numerical scheme, but the intermediary points can use any method. For example, the central difference method calculates the derivatives as:

Figure 3.29: Points for the upper surface and the shock surface as seen in a 2d view in the waverider's base plane.

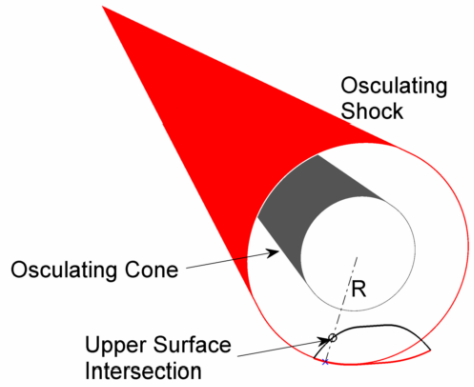

Figure 3.30: One of the osculating shocks and osculating cones. The back radius of the shock, shown as R, is the same length as the radius of curvature at the point marked by the x. The intersection with the upper surface is also noted.

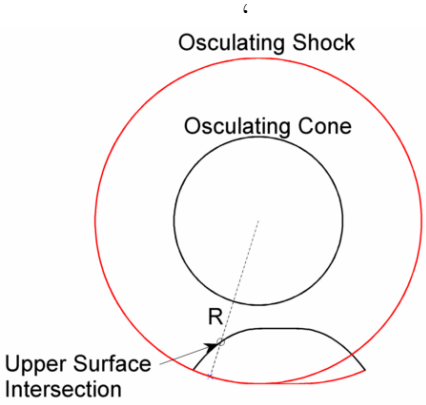

Figure 3.31: 2d view in the waverider's base plane showing one of the osculating shocks and osculating cones. The back radius of the shock, shown as R, is the same length as the radius of curvature at the point marked by the x. The intersection with the upper surface is also noted.

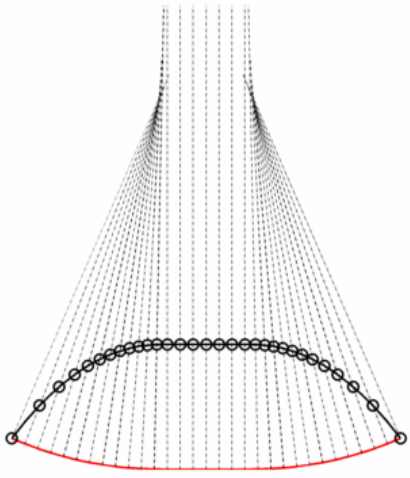

Figure 3.32: A 2d view in the waverider's base plane of the radii of all osculating shocks and their intersections with the upper waverider surface.

$$z' = \frac{z(y+dy) - z(y-dy)}{2dy} \tag{3.10}$$

$$z'' = \frac{z(y+dy) - 2z(y) + z(y-dy)}{dy^2} \tag{3.11}$$

4. Use the first and second derivatives to calculate the radius of curvature of the shockwave at each location. At each discretized location, the flow solution will be solved using a cone with half angle, θ, and resulting shockwave radius in the base plane of the waverider equal to the radius of curvature (see Figures 3.30-3.32). Local radius of curvature is calculated as:

$$R = \frac{(1 + z'^2)^{3/2}}{z''} \tag{3.12}$$

5. Moving along lines perpendicular to the local shock tangents, find intersections with the upper surface. The lines being followed are the back radii of the osculating shocks. See Figures 3.30-3.32.

6. Moving in the -x direction, upstream from the intersection points, trace the upper surface until reaching the edge of the osculating cones. Connecting all of these intersections forms the overall waverider leading edge. A triangle is formed by connecting the original shockwave point (found in step 2), the upper surface intersection (found in step 5) and the leading edge point (found in this step). See Figures 3.33 - 3.35.

7. Translate each triangle along with the respective osculating cone such that the nose of the osculating cone is at the origin. See Figure 3.36.

8. Rotate each triangle such that it is in the *x-(-z)* plane. See Figure 3.36.

9. Using the conical flowfield solution found in step 1, trace streamlines from the leading edge locations until they reach the waverider base plane. In the

Figure 3.33: Moving directly upstream, in the -x direction, the upper surface is traced until it reaches its respective osculating shock.

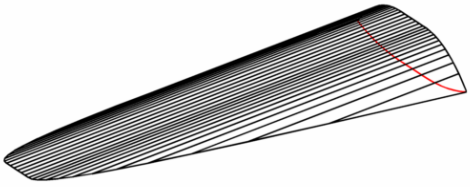

Figure 3.34: Performing the upper surface tracing until each osculating shock intersection, the leading edge of the waverider is created.

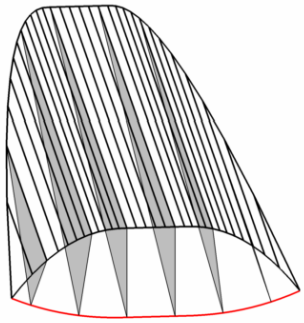

Figure 3.35: Depiction of the upper surface traces, the waverider leading edge and a few triangles described in step 6.

Figure 3.36: Trace of one streamline which will form the bottom waverider surface. Note that the waverider upper surface and shock have been translated and rotated so that the triangle formed in step 6 is entirely in the x-z plane.

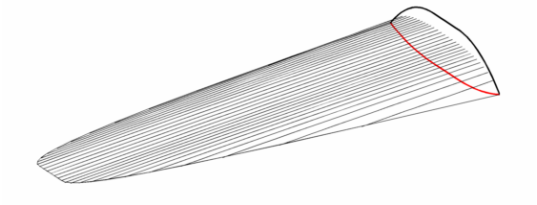

Figure 3.37: The lower surface of the waverider formed from the stream traces translated back into the original waverider reference frame.

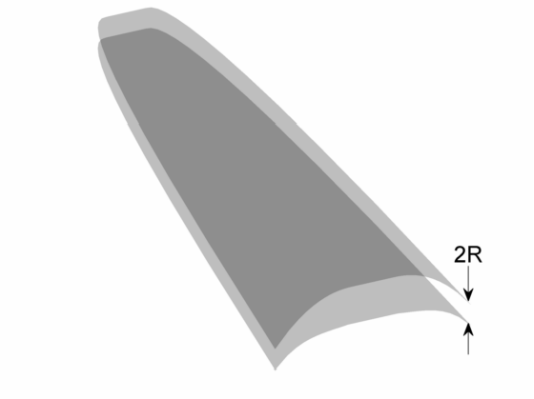

Figure 3.38: The waverider upper and lower surfaces moved about to facilitate drawing a circular leading edge in between.

rotated and translated frame, follow streamlines until the x-location matches the x-location of the translated and rotated shockwave point and upper surface intersection. See Figure 3.36.

10. Rotate the points found along the streamlines by the same magnitude but opposite direction as in step 8.

11. Translate the streamline points by the negative displacement as performed in step 7. The resulting points form the lower surface of the waverider. See Figure 3.37.

12. Move the upper surface a distance R in the $+z$ direction and the lower surface a distance R in the -z. See Figure 3.38.

13. Draw a circular leading edge between the two surfaces.

14. Calculate a normalized volume, V_0.

15. Scale the vehicle to the desired absolute volume, V, or to the desired length, L.

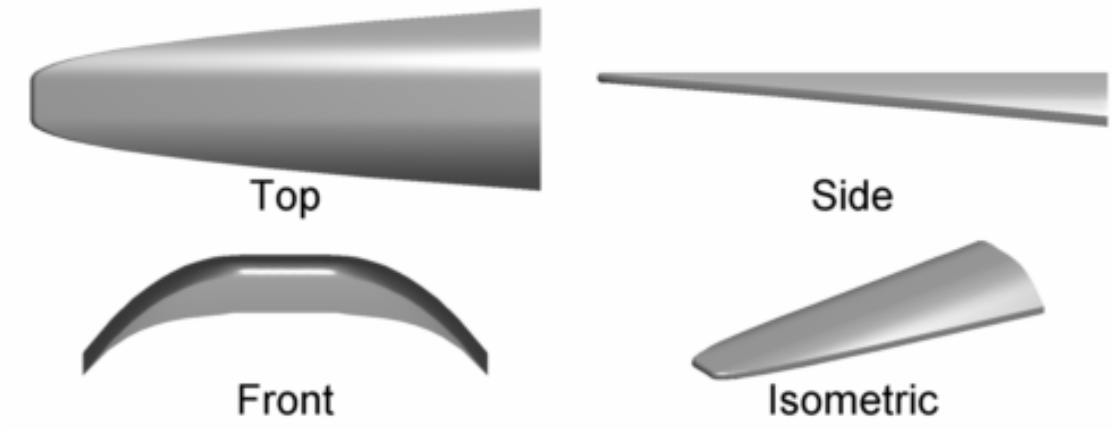

Figure 3.39: The fully constructed example osculating cone waverider.

3.4.3 Feasibility

There are certain combinations of shockwave and upper surface power law inputs which yield infeasible geometric designs. These can be categorized into two main scenarios.

The most common issue arising from the osculating cones methodology is that the shockwave curvature changes too rapidly. This causes the osculating shock radii to be at high angles relative to each other, and they cross below the upper surface

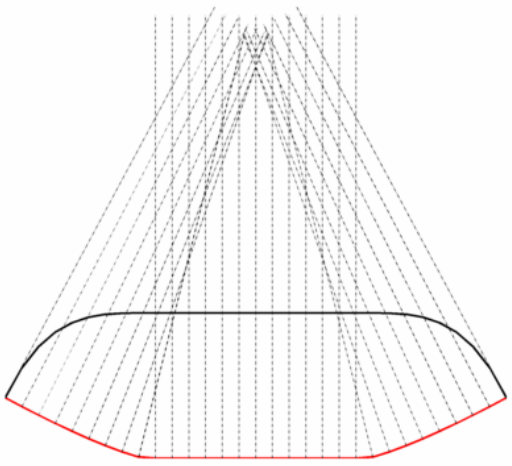

Figure 3.40: The osculating shock radii cross before reaching the upper surface.

(see Figure 3.40). If the methodology was continued past step 5 for such a design, it would be found that the streamlines cross, and a non-physical bottom surface would have been numerically created.

Another common problem arising from this methodology is that the upper surface and shockwave meet at too extreme of an angle (see Figure 3.41). In fact, the angle between the two should be less than 90°, or else the sides of the waverider will be open (see Figure 3.42). When step 5 of the waverider generation process is completed, the upper surface intersections for $y = \pm y_{max}$, should be coincident with the shockwave. If the angle between the shockwave and the upper surface is greater than 90°, this will not be the case, and the vehicle will not be closed on the sides!

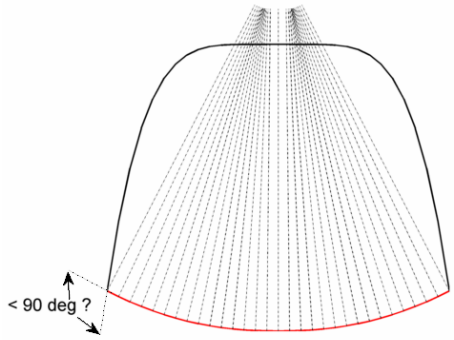

Figure 3.41: The angle between the shock and the upper surface is too extreme.

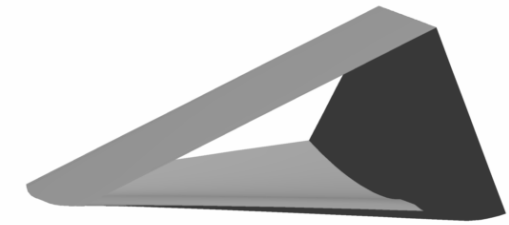

Figure 3.42: Infeasible waverider, as its sides are open.

Chapter 4

Aerodynamic Modeling

In this chapter, a description is given for methods of estimating the aerodynamic forces and moments acting on a waverider. The flowfield is first assumed to be inviscid, and a prediction of the velocity and gaseous properties is made, solving for the temperature and pressure as a function of position over the body. Multiple methods of calculating this pressure will be described as will the relative merits. Next, the inviscid flowfield is used as an estimate of the flow properties at the edge of the vehicle's viscous boundary layers. Then, the viscous stresses on the vehicle are determined. Finally, the pressure and shear stresses are integrated over the surface area of the vehicle in order to generate net aerodynamic forces and moments.

4.1 Shock Calculations

The first step in determining the aerodynamic forces around the vehicle is to calculate the strength and geometry of the compressible flow structures. The equations and methods in this section describe the means of calculating shock geometries as well as the change in flow properties across the discontinuity.

Because waveriders are designed to be attached to shocks emanating from their leading edges, many of these tools are used during the vehicle shape generation. They also must be sufficiently robust to be used during trajectory propagation,

when the free-stream flight conditions will change, as will the vehicle's orientation to the oncoming flow (due to varying angle-of-attack, α).

4.1.1 Constant γ Shocks

The first shock structure under consideration is the 2-d, attached, planar shock in a non-reacting gas. In this scenario, a shockwave forms at an angle, β, relative to the free-stream gas, turning the flow parallel to a compression corner with angle, θ. Further, the gas has a constant ratio of specific heats, γ, which holds both upstream and downstream of the shockwave.

Using the three conservation laws (mass, momentum, energy) and the perfect gas law, the shock geometry and changes in flow properties and the shock geometry can be found in closed form:

$$\tan(\theta) = \frac{2M_1^2 \sin^2(\beta) - 2}{M_1^2(\gamma + cos(2\beta)) + 2} \cot(\beta) \tag{4.1}$$

$$M_2 = \frac{\sqrt{\frac{M_1^2 \sin^2\beta + \frac{2}{\gamma-1}}{\frac{2\gamma}{\gamma-1} M_1^2 \sin^2\beta - 1}}}{\sin(\beta - \theta)} \tag{4.2}$$

$$P_2 = P_1 \left[1 + \frac{2\gamma}{\gamma+1}\left(M_{n,1}^2 - 1\right)\right] \tag{4.3}$$

$$\rho_2 = \rho_1 \left[\frac{(\gamma+1)M_{n,1}^2}{(\gamma-1)M_{n,1}^2 + 2}\right] \tag{4.4}$$

$$T_2 = T_1 \left[\frac{P_2}{P_1}\frac{\rho_1}{\rho_2}\right] \tag{4.5}$$

$$a_2 = \sqrt{\gamma R T_2} \tag{4.6}$$

$$v_2 = M_2 a_2 \tag{4.7}$$

where the subscript (1) refers to flow properties upstream of the shock, and (2) refers to downstream conditions. A full derivation for equations 4.1 - 4.7 will not be provided in this work, but is available from any fundamental aerodynamic textbook, including Ref [105].

One important note is that in most cases, the disturbance angle θ is known, and β is an unknown to be solved for. Unfortunately, Equation 4.1 is only closed form in the inverse scenario, when β is known and θ is not. In this case, numerical iteration can be used to converge on a value for β. Alternatively, a closed form approximation is available from Mascitti:[106]

$$B = -\frac{M_1^2 + 2}{M_1^2} - \gamma \sin^2(\theta) \tag{4.8}$$

$$C = \frac{2M_1^2 + 1}{M_1^4} + \left(\frac{(\gamma+1)^2}{4} + \frac{\gamma - 1}{M_1^2} \right) \sin^2(\theta) \tag{4.9}$$

$$D = -\frac{\cos^2(\theta)}{M_1^4} \tag{4.10}$$

$$\Phi = \cos^{-1}\left(\frac{4.5BC - B^3 - 13.5D}{(B^2 - 3C)^{1.5}} \right) \tag{4.11}$$

$$\beta = \sin^{-1}\left(\sqrt{-\frac{B}{3} + \frac{2}{3}\sqrt{B^2 - 3C}\cos\left(\frac{\Phi + 4\pi}{3} \right)} \right) \tag{4.12}$$

In the case of a waverider with sharp leading edges, the pressure found with Equation 4.3 can be used to calculate forces on the vehicle. With no leading edge bluntness, the flowfield is assumed to be uniform behind the shockwave, therefore, no additional steps are required to estimate the flowfield at the surface of the waverider. This would be the case within any caret-wing section of a starbody (with $R_{LE} = 0$), or on the top-surface of an osculating cone waverider (with $R_{LE} = 0$) at some non-zero angle-of-attack. It does not apply to the lower surface of even a sharp leading edge osculating cone waverider, as the surface is not linear and the post-shock flow properties are never assumed to be constant (see Section 4.1.3).

4.1.2 Shocks with Local Equilibrium, Reacting Gas

At orbital flight speeds, non-ideal gas behavior can be extremely important. At the high post-shock temperatures found in this flight regime, some energy is absorbed into chemical reactions which change the composition of the gas and its

thermodynamic properties. Recall that a primary assumption made in deriving the oblique shock relations (Equations 4.1 - 4.7) is that γ is constant. If the shockwave causes the chemical makeup of the gas to change, then the oblique shock relations cannot be used as before.

In order to allow reasonable calculation time, it is assumed that all chemical reactions are coincident with the shockwave. In reality, chemical reactions can occur downstream of the shockwave. In this work, the gas downstream of the shock is assumed to be in equilibrium. Similarly, it is assumed that the gas is calorically perfect within the regions up and downstream of the shockwave, but not across the discontinuity.

4.1.2.1 Iterative Calculation

In order to solve for the shockwave angle, β, relative to the free-stream flow due to some disturbance angle, θ, a dual layered iteration is required. These steps are adapted from the method outlined by Anderson.[54] Even if the shock angle was known, iteration would be required to determine the correct post shock chemical composition. The shock angle is not known though, so it must be iterated as well before the correct overall solution is found. The procedure is as follows:

1. Guess a value for the shock angle, β'. 90% of the value predicted by the θ-β-M relation (Equation 4.1) is a good guess.

2. Using β', calculate the component of velocity normal to the shock:

$$v_{1,n} = v_1 \sin \beta' \tag{4.13}$$

3. Guess a value for the post-shock density, ρ_2'. $4\rho_1$ is a suitable starting guess.

4. Calculate the post-shock pressure and enthalpy using the conservation of mo-

mentum and energy:

$$P_2 = P_1 + \rho_1 v_{1,n}^2 \left(1 - \frac{\rho_1}{\rho_2'}\right) \tag{4.14}$$

$$h_2 = h_1 + \frac{v_{1,n}^2}{2} \left(1 - \frac{\rho_1^2}{\rho_2'^2}\right) \tag{4.15}$$

5. Use a chemical equilibrium solver to determine the equilibrium density, temperature and specific heat ratio for a gas with the specified enthalpy and pressure. In this work, NASA's Chemical Equilibrium with Applications (CEA)[107] is used.

$$[\rho_2, T_2, \gamma_2] = \text{CEA}(P_2, h_2) \tag{4.16}$$

6. Compare the density obtained from the chemical equilibrium solver with the guessed value from step 3:

$$\epsilon_\rho \overset{?}{>} \left|1 - \frac{\rho_2'}{\rho_2}\right| \tag{4.17}$$

   If the difference between ρ_2 and ρ_2' is greater than some predetermined acceptable error ($\epsilon_\rho = 10^{-5}$ was used in this work), then update $\rho_2' = \rho_2$, and return to step 4. If the difference is less than ϵ_ρ, move on to the next step.

7. Calculate the ratio of normal flow velocities up and downstream of the shock, using the conservation of mass:

$$\frac{v_{2,n}}{v_{1,n}} = \frac{\rho_1}{\rho_2} \tag{4.18}$$

8. Calculate the shock angle which would generate this ratio of flow velocities. From the shock geometry:

$$\tan(\beta - \theta) = \frac{v_{2,n}}{v_{1,n}} \tan(\beta) \tag{4.19}$$

In order to develop an expression for $\beta = f\left(\theta, \frac{v_{2,n}}{v_{1,n}}\right)$, the following trigonometric identity is required:

$$\tan(\beta - \theta) = \frac{\tan(\beta) - \tan(\theta)}{1 + \tan(\beta)\tan(\theta)} \tag{4.20}$$

By setting the right hand side of Equation 4.19 equal to the right hand side of Equation 4.20, and simplifying, the following expression is developed:

$$\frac{v_{2,n}}{v_{1,n}}\tan(\theta)\tan^2(\beta) + \left(\frac{v_{2,n}}{v_{1,n}} - 1\right)\tan(\beta) + \tan(\theta) = 0 \tag{4.21}$$

This is simply the quadratic equation with $\tan(\beta)$ as the only unknown. Therefore, the shock angle can be calculated as:

$$\tan(\beta) = \frac{\frac{v_{2,n}}{v_{1,n}} - 1 \pm \sqrt{\left(\frac{v_{2,n}}{v_{1,n}} - 1\right)^2 - 4\frac{v_{2,n}}{v_{1,n}}\tan^2(\theta)}}{2\frac{v_{2,n}}{v_{1,n}}\tan(\theta)} \tag{4.22}$$

9. Compare the value of β' and β:

$$\epsilon_\beta \overset{?}{>} \left|1 - \frac{\beta'}{\beta}\right| \tag{4.23}$$

If the difference between β and β' is greater than some predetermined acceptable error ($\epsilon_\beta = 10^{-5}$ was used in this work), then update $\beta' = \beta$, and return to step 2. If the difference is less than ϵ_β, then the process is complete!

With the value of β found, the individual post-shock flow properties were found as steps within the most recent iteration.

In practice, the inner iteration loop is complete within 8 iterations, however the outer loop might require 20 iterations in order to converge. Typically, the most computationally challenging step is solving for chemical equilibrium. In fact, CEA

requires iterations itself in order to reach a solution. Requiring CEA to run up to 160 times in order to find the shock properties makes this a much more time consuming process than using the standard shock strength calculations outlined in Section 4.1.1.

4.1.2.2 Database Generation

It was found to be advantageous to create a database of post shock values which could be interpolated during trajectory propagation. The process outlined above was repeated for discretized values of $0° < \theta < \theta_{\max}$, $10 < M < 210$, and 0 km $< h < h_{\text{atmos}}$ for Mars, Earth and Venus. $\theta_{\max}$ was the value for which shock separation occurs, and h_{atmos} is the maximum altitude of the relevant atmosphere.

A variable grid size was used in order to limit the calculation time required to generate the database, and speed up the interpolation process. Different regions of the 3d space are more linear than other regions, allowing fewer data points.

In order to develop the database, the following steps are used:

1. A fixed initial discretization, or grid spacing value, is determined for each variable ($d\theta = 8°$, $dM = 40$, $dh = 25$ km). Let this be grid 1.

2. At each node in grid 1, the post shock properties are calculated using the steps in the previous section. Let this be database 1.

3. Each grid spacing value is cut in half ($d\theta = 4°$, $dM = 10$, $dh = 12.5$ km) creating a new 3d grid, called grid 2.

4. At each **new** node in grid 2, the post shock properties are calculated using interpolation of database 1. The new nodes are those which are in grid 2, but not in grid 1. This is roughly half of the nodes.

5. At all nodes in grid 2, the post shock properties are determined. At any node

not in grid 1, the properties are calculated using Section 4.1.2.1. At any node which is in grid 1, the properties are known and simply copied. This creates database 2.

6. For each new node in grid 2, the value of β from step 4, β_I, is compared with the value from step 5, β_C:

$$\epsilon_\beta \overset{?}{>} \left| 1 - \frac{\beta_I}{\beta_C} \right| \tag{4.24}$$

   If the difference between β_I and β_C is greater than some predetermined acceptable error ($\epsilon_\beta = 10^{-5}$ was used in this work), then this node is marked as not converged. If the value is converged, then the node is marked as such. If all nodes are converged, then the database is complete!

7. Each grid spacing value is cut in half ($d\theta = 2°$, $dM = 5$, $dh = 6.25$ km).

8. Grid 3 is created by adding up to 26 points around all unconverged nodes of grid 2. Assume that b corresponds to an unconverged node in grid 2 with $M = M_b$, $\theta = \theta_b$, and $h = h_b$. In 3d space, there are 26 points surrounding b, which correspond to all unique combinations of $M = \{M_b - dM, M_b, M_b + dM\}$, $\theta = \{\theta_b - d\theta, \theta_b, \theta_b + d\theta\}$, and $h = \{h_b - dh, h_b, h_b + dh\}$, but are not b itself (see Figure 4.1). If b is located at one edge of the 3d design space, then there will only be 17 new nodes. If b is located at the intersection of two edges of the 3d design space, there will only be 11 new points. If b is located at one of the eight corners of the 3d design space, there will only be 7 new nodes.

9. Return to step 4, but now using the two most recent grids throughout, until all values are converged in step 6.

In this manner, the final grid will be much more dense in regions of great nonlinearity, and less dense where fewer data points are suitable. Figure 4.2 shows the final grid for Mars.

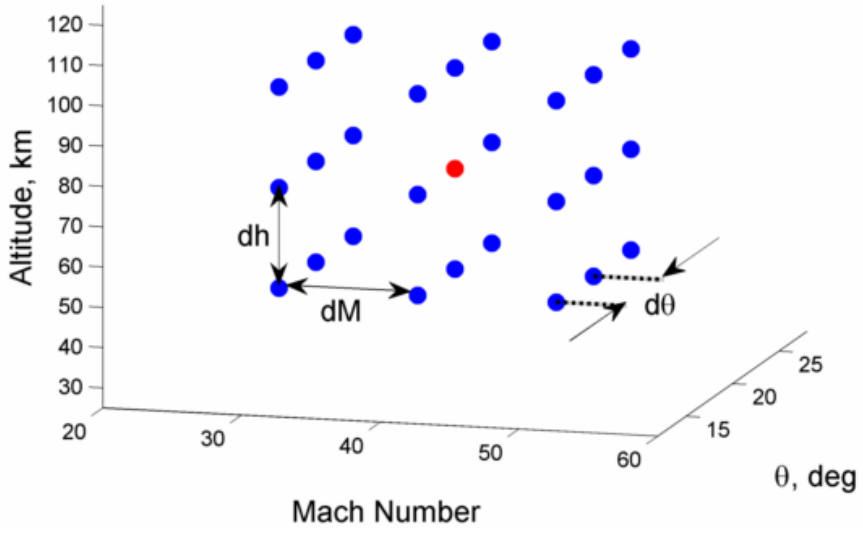

Figure 4.1: Red dot is point b. Blue dots are the new nodes.

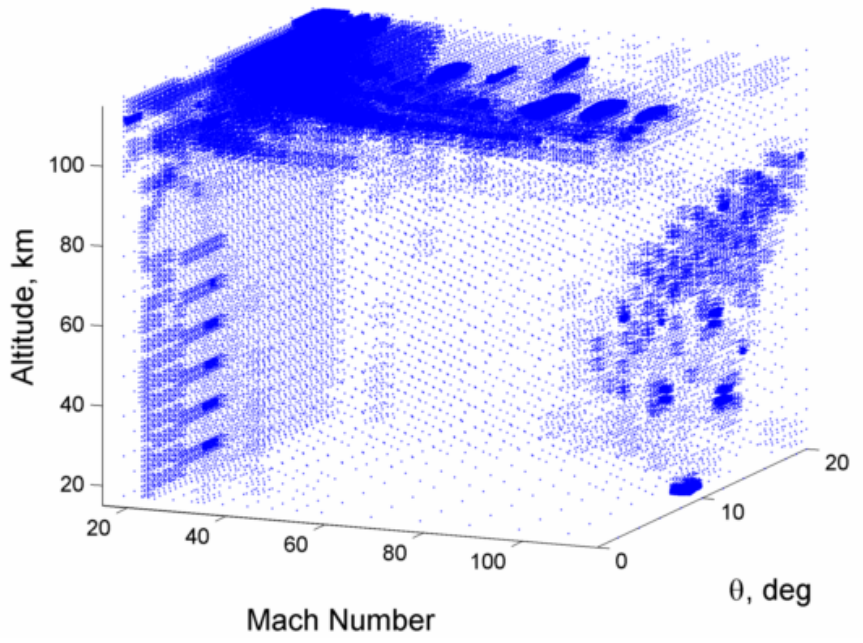

Figure 4.2: Martian high temperature database data points. 288879 nodes were required to obtain less than a 10^{-4}% error in prediction of the shock angle at all tested midpoints. Note that some regions of the design space require more densely packed data points.

Note that upon returning to step 4, a non-uniform database must be interpolated. MATLAB's scattered interpolant class is used to accomplish the complicated process efficiently.

4.1.3 Conical Shocks

The differential equation describing the flow around a right circular cone was first worked out by Taylor and Maccoll[108] in 1933. Even though a 2d view of a cross-section of the scenario looks similar to the 2d planar shock, the flow is inherently non-linear in this case, due to 3d expansion. This 3d relieving effect tends to accelerate the supersonic flow, and curve the streamlines away from the surface of the cone. The initial shock angle is therefore less than the equivalent wedge.

Despite the 3d relieving effect, the analysis can be completed in only two dimensions, by making a reasonable assumption that the shockwave and flow about the cone are axisymmetric. Using polar coordinates, where $\hat{r}$ is a location radially outward from the nose of the cone, and $\hat{\theta}$ is a positive angular direction away from the cone, the total velocity is:

$$v = \sqrt{v_r^2 + v_\theta^2} \tag{4.25}$$

It can be shown that if the shockwave about the cone is straight, then there is no entropy gradient in the post-shock flow and the flow must be irrotational. In axisymmetric polar coordinates, constraining the vorticity of the flow to be zero yields the following relation between the flow directions:

$$\frac{dv_r}{d\theta} = v_\theta \tag{4.26}$$

This will be extremely important in applying the boundary conditions when solving for the flowfield about a cone. The Taylor-Maccoll Equation is a second order,

ordinary differential Equation:

$$\frac{\gamma-1}{2}\left(v_{\max}-v_r^2-\left(\frac{dv_r}{d\theta}\right)^2\right)\left(2v_r+\frac{dv_r}{d\theta}\cot(\theta)+\frac{d^2v_r}{d\theta^2}\right) - \frac{dv_r}{d\theta}\left(v_r\frac{dv_r}{d\theta}+\frac{dv_r}{d\theta}\frac{d^2v_r}{d\theta^2}\right)=0 \quad (4.27)$$

where $v_{\max}$ is the theoretical speed if all enthalpy was converted into kinetic energy:

$$v_{\max}=\sqrt{2h_0}=\sqrt{2h+v^2} \quad (4.28)$$

where h and h_0 are the static and total enthalpy of the flow, respectively. Equation 4.27 is simpler to integrate if in non-dimensional form. It is therefore helpful to create a non-dimensional variable, v', by scaling the flow velocity by $v_{\max}$. Reworking Equation 4.28, it is found that:

$$\frac{v}{v_{\max}}=v'=\left(\frac{2}{(\gamma-1)M^2}+1\right)^{-\frac{1}{2}} \quad (4.29)$$

Finally, by dividing the Taylor-Maccoll Equation by $v_{\max}$, the non-dimensional form is:

$$\frac{\gamma-1}{2}\left(1-v_r'^2-\left(\frac{dv_r'}{d\theta}\right)^2\right)\left(2v_r'+\frac{dv_r'}{d\theta}\cot(\theta)+\frac{d^2v_r'}{d\theta^2}\right) - \frac{dv_r'}{d\theta}\left(v_r'\frac{dv_r'}{d\theta}+\frac{dv_r'}{d\theta}\frac{d^2v_r'}{d\theta^2}\right)=0 \quad (4.30)$$

Unfortunately, Equation 4.30 cannot be solved in closed form, instead requiring numerical integration. In order to do so, the boundary conditions are defined to be the flow velocity directly behind the shockwave. The total velocity is:

$$v_0'=\left(\frac{2}{(\gamma-1)M_2^2}+1\right)^{-\frac{1}{2}}\Bigg|_{\text{behind shock}} \quad (4.31)$$

where M_2 is the Mach number directly behind the shock. It can be found using Equation 4.2. Recalling Equation 4.25, the initial flow velocities in polar form are:

$$v'_{r,0} = v'_0 \cos(\beta - \theta_{\text{cone}}) \tag{4.32}$$

$$v'_{\theta,0} = v'_0 \sin(\beta - \theta_{\text{cone}}) \tag{4.33}$$

The first derivative of v'_r is known from the irrotational condition mentioned previously (see Equation 4.26). The second derivative of v'_r is determined by solving Equation 4.30 for $\frac{d^2 v'_r}{d\theta^2}$. The system of equations is:

$$\frac{dv'_r}{d\theta} = v'_\theta \tag{4.34}$$

$$\frac{d^2 v'_r}{d\theta^2} = \frac{v'^2_\theta v'_r - \frac{\gamma-1}{2}(1 - v'^2_r - v'^2_\theta)(2v'_r + v'_\theta \cot(\theta))}{\frac{\gamma-1}{2}(1 - v'^2_r - v'^2_\theta) - v'^2_\theta} \tag{4.35}$$

With the initial conditions, and the system of ordinary differential equations, an ODE solver such as MATLAB's ode23s can be used to find the entire flowfield (v_r,v_θ) for any position (r,θ).

The flow properties within the flowfield are typically of more use than the flow velocity. In order to find the thermodynamic properties of the gas, the Mach number is first found by inverting Equation 4.29:

$$M^2 = \frac{2v'^2}{(\gamma - 1)(1 - v'^2)} \tag{4.36}$$

As mentioned, the flow is assumed to be isentropic behind the shockwave. The isentropic relations can therefore be used to find the temperature, pressure and

density at any location, by simply using the Mach number:

$$T = T_0 \left[1 + \frac{\gamma - 1}{2} M^2\right]^{-1} \tag{4.37}$$

$$P = P_0 \left[1 + \frac{\gamma - 1}{2} M^2\right]^{\frac{-\gamma}{\gamma - 1}} \tag{4.38}$$

$$\rho = \rho_0 \left[1 + \frac{\gamma - 1}{2} M^2\right]^{\frac{-1}{\gamma - 1}} \tag{4.39}$$

where the total conditions are behind the shockwave, and not necessarily in the free-stream. The total conditions behind the shockwave (subscript 2) are found relative to the free-stream total conditions (subscript 1) using the following equations:

$$\frac{P_{0,2}}{P_{0,1}} = \frac{\rho_{0,2}}{\rho_{0,1}} = \left(\frac{\frac{\gamma+1}{2} M_1^2}{1 + \frac{\gamma-1}{2} M_1^2}\right)^{\frac{\gamma}{\gamma-1}} \left(\frac{1}{\frac{2\gamma}{\gamma+1} M_1^2 - \frac{\gamma-1}{\gamma+1}}\right)^{\frac{1}{\gamma-1}} \tag{4.40}$$

$$\frac{T_{0,2}}{T_{0,1}} = 1 \tag{4.41}$$

4.2 Surface Inclination Methods

Surface inclination methods can be used to estimate the inviscid flowfield around a body. These techniques approximate the variation in pressure as primarily a function of the angle between the free-stream and the local body.

While a waverider shape may have complex geometry, determining the local body angle is a relatively simple calculation. This section describes two different categories of surface inclination methods and their use in this study.

4.2.1 Newtonian and Modified Newtonian Method

Classic Newtonian flow theory is the simplest method of estimating the pressure distribution over a blunted vehicle in hypersonic flow. The theory was worked out with the incorrect assumption that fluid particles have no interactions with each

other, but instead interact with the body using inelastic collisions. While the physical explanation was misguided, the resulting theory is quite useful for hypersonic flow.

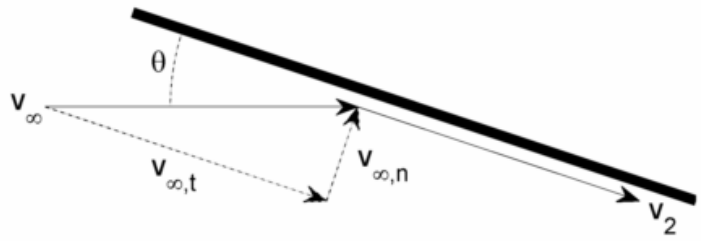

Figure 4.3: Schematic of Newtonian Hypersonic Theory.

A uniform flow of fluid particle is assumed to move towards a rigid body which is locally inclined at an angle of θ relative to each fluid particle's linear motion (see Figure 4.3). After striking the surface, the fluid particles lose their momentum normal to the wall and move tangentially to the surface. The time rate of change of the fluid's normal momentum (per area) is then:

$$\frac{\Delta(\text{momentum})}{\Delta(\text{time})} = \rho_\infty v_\infty \sin^2(\theta) \tag{4.42}$$

Of course, change in momentum is equal to force, in this case exerted on the body by the fluid flow. If the force per area is considered to be a pressure in excess of the static pressure of the flow, then the pressure coefficient and pressure are expressed as:

$$P = \rho_\infty v_\infty^2 \sin^2(\theta) + P_\infty \tag{4.43}$$

$$c_P = 2\sin^2(\theta) \tag{4.44}$$

Note that any surface area which is not directly incident to oncoming flow is assigned a pressure coefficient of zero, rather than using a negative incident angle.

While Newtonian theory is extremely simple to apply, it has limited applicability due to the lack of dependence on flight speed. An improved version was worked out by Lester Lees[109] and is referred to as the modified Newtonian method:

$$c_P = c_{P,\max} \sin^2(\theta) \tag{4.45}$$

$$P = \frac{1}{2}\rho_\infty v_\infty^2 c_{P,\max} \sin^2(\theta) + P_\infty \tag{4.46}$$

where $c_{P,\max}$ refers to the pressure coefficient at a stagnation point behind a normal shock at the given flight speed:

$$c_{P,\max} = \frac{2}{\gamma M^2}\left[\left(\frac{(\gamma+1)^2 M^2}{4\gamma M^2 - 2(\gamma-1)}\right)^{\frac{\gamma}{\gamma-1}}\left(\frac{1-\gamma+2\gamma M^2}{\gamma+1}\right) - 1\right] \tag{4.47}$$

The geometry dependence of the modified method is the same as the classic Newtonian theory, however the coefficient is now dependent on flight Mach number, which improves accuracy. In particular, the flight speed dependence improves the accuracy of pressure estimation at lower Mach numbers. As $M \to \infty$, if it is assumed that the value of γ goes to 1 (a good assumption), then the value of $c_{P,\max} \to 2$ and the original Newtonian theory is recovered.

4.2.2 Tangent Cone/Wedge

The tangent-cone/tangent-wedge methods are so-named as the thermodynamic properties at a given location on a hypersonic body are assumed to be the same as those on a cone/wedge which has an equivalent angle with the free-stream (see Figure 4.4). A body with a blunted leading edge will create a curved shockwave behind it. Moving from a point on the body to a point on the shockwave, the pres-

sure decreases. Studies have shown that a good estimate of the amount of decrease, is the pressure behind a shock that would result from a wedge or cone with the same local half angle.[54,110,111]

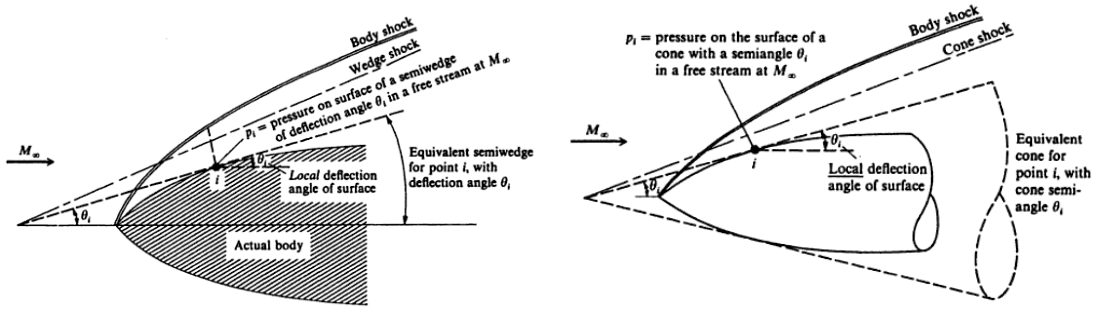

Figure 4.4: Schematic of the tangent wedge and tangent cone methods of estimating surface pressure. From Ref. [54]

The method was empirically developed, so there is no derivation to present nor are there any new equations. The shock calculations described in Section 4.1 are simply made using the inclination of each local region of the vehicle.

4.2.3 Application to Waveriders

In practice, the modified Newtonian method is most useful and accurate at estimating the pressure coefficient over blunt bodies.[54,110] This is important as any waverider with a finite leading edge radius is blunt, at least in this region.

The tangent methods are most useful for bodies which have attached, but curved shockwaves. As shown by Mason and Lee[57] the immediate presence of geometric bluntness does not translate to aerodynamic bluntness. That is, waveriders with very small leading edge radii will still have attached shockwaves. For these waveriders, the tangent methods are most accurate at predicting the pressure at the surface.

In this work, a distinction is made between aerodynamically sharp and blunt bodies using the criteria of the critical attached inclination angle. For a given Mach

number, there is a maximum disturbance angle, θ_c, which yields a solution to the θ-β-M relation. In the case of a shock with constant γ, the critical angle can be found by solving the following equation for β_c and using it in Equation 4.1:[104]

$$\sin^2 \beta_c = \frac{1}{4\gamma M^2} \left((\gamma+1)M^2 - 4\sqrt{(\gamma+1)\left[(\gamma+1)M^4 | 8(\gamma-1)M^2 + 16\right]} \right) \quad (4.48)$$

If the local inclination angle for a given region of the waverider is greater than or equal to θ_c, the modified Newtonian method is used. If the local inclination angle for a given region of the waverider is less than θ_c, one of the tangent methods predicts the local surface properties.

In the case of starbody waveriders, when a local θ is less than θ_c, the tangent wedge method is used. On the other hand, when a local θ is less than θ_c on an osculating cone waverider, the tangent cone method is employed. As the leading edge radius on either waverider model decreases towards zero, the local inclination angles are the same as those that were used for shape generation of the sharp leading edge vehicle. In this case, when using the respective tangent method, the sharp leading edge solution is recovered. Thus, the aerodynamic calculations are continuous from a sharp leading edge vehicle to a highly blunted waverider.

Using the local surface inclination methods allows one single aerodynamic model to predict consistent pressure calculations as the vehicle experiences an angle-of-attack, for any geometry type. The only requirement is a mesh of the surface area of the vehicle into small regions with known area. With the edge points of each meshed surface area, the determination of the local inclination is trivially simple. The remaining pressure prediction only requires Equation 4.46 or one of the shock strength calculators described in Section 4.1.

4.3 Viscous Methodology

The reference temperature method estimates shear stress on vehicles flying at hypersonic speeds.[112] In order to account for the effects of compressibility, the fluid properties relating to skin friction are estimated at a reference temperature, T^*, which is a function of the Mach number and vehicle wall temperature, T_{wall}:

$$T^* = T_2 \left(1.28 + .023 M_2^2 + .58 (\frac{T_{\text{wall}}}{T_2} - 1) \right) \tag{4.49}$$

$$\mu^* = \mu_0 \left(\frac{T^*}{T_0} \right)^{1.5} \left(\frac{T_0 + S}{T^* + S} \right) \tag{4.50}$$

$$\rho^* = \frac{P_2}{R T^*} \tag{4.51}$$

$$\left(\frac{\text{Re}}{x} \right)^* = \frac{\rho^* v_2}{\mu^*} \tag{4.52}$$

where T_0, μ_0, and S are gas specific constants (see Table 4.1). The wall temperature depends on the application, but for an aero-assist application, a very high value is warranted ($T_{\text{wall}} = 1900$ K is used in this work).

Table 4.1: Gas constants for terrestial planets

	T_0 [K]	S [K]	$\mu_0 \left[\frac{\text{Ns}}{\text{m}^2}\right]$
Mars	231	293.15	1.480 x 10^{-5}
Earth	291.15	120	1.827 x 10^{-5}
Venus	231	293.15	1.480 x 10^{-5}

Calculations are made assuming turbulent flow over the entire vehicle. In reality, portions of the vehicle would have laminar boundary layers, and therefore lower skin friction. Hypersonic boundary layer transition is an extremely active area of current day research, with a conclusive model still under development. Rather than introduce a relatively unvalidated estimation method, requiring significant calculation complexity, a conservative estimate was used instead. For a turbulent boundary

layer, the shear stress is estimated using the following correlation:

$$\tau^* = \frac{.0592\rho^* v_2^2}{2x^{.2}(\left(\frac{\mathrm{Re}}{x}\right)^*)^{.2}} \tag{4.53}$$

4.4 Force and Moment Calculations

Thus far, this chapter has discussed estimations of inviscid and viscous flowfields. In this section, the gaseous properties which have been determined previously are summed into resultant forces and moments acting on the vehicle. These forces and moments will be fed into a flight simulator in later chapters.

As mentioned in the previous chapter, the vehicle models in this study were developed with an aerodynamic panel code in mind. The surface of each waverider was broken up into many triangles (see Figure 3.2). The aerodynamic environment is calculated on each triangle, converted into a force, and finally the forces are summed over the entire triangular mesh. This yields the resultant forces and moments acting on the vehicle.

When within a planetary atmosphere, the exterior of a waverider is assumed to be entirely surrounded by gaseous atmosphere. The pressure this gas exerts on the surface of the vehicle has been solved for as a thermodynamic property in the previous sections. Because the vehicle is moving, and is not entirely symmetric, the pressure distribution is not uniform and there is likely a net pressure force. Over a given region of the vehicle, the force due to aerodynamic pressure is:

$$\mathbf{F_P} = -P_2 A\hat{n} \tag{4.54}$$

where A is the area of the surface over which P_2 exists and F_P acts. Also, $\hat{n}$ is oriented outwardly normal to the surface.

The expression developed to determine the shear stress acting over a given

region of vehicle surface (Equation 4.53) is written as a function of x, or the stream-wise distance from the leading edge of the vehicle. Therefore, the shear stress must be integrated over each surface, rather than simply multiplying by area. Assuming that each surface is triangular, as is the case in the unstructured grids generated for the previous Chapter's waveriders, the skin friction force on a given region is:

$$\mathbf{F}_\tau = \frac{25}{18}\frac{A}{l^{.2}}\tau^* \cos^2(\theta)\hat{t} \tag{4.55}$$

where A is the area of the surface over which F_τ acts, l is the length of that surface, $\hat{t}$ is oriented parallel to the local streamlines at the surface, and θ is the angle the surface makes relative to the free-stream flow.

Finally, the inviscid and viscous aerodynamic forces are integrated over the vehicle surface yielding the resultant force and moments. Assuming that there are k triangles in a given waverider mesh, the axial and normal force coefficients are:

$$c_A = \frac{1}{\frac{1}{2}\rho_\infty |\mathbf{v}|^2 S}\left\{\sum_m^k (\mathbf{F}_{\mathbf{P},\mathbf{m}} \cdot \hat{\mathbf{x}}) + \sum_m^k (\mathbf{F}_{\tau,\mathbf{m}} \cdot \hat{\mathbf{x}})\right\} \tag{4.56}$$

$$c_N = \frac{1}{\frac{1}{2}\rho_\infty |\mathbf{v}|^2 S}\left\{\sum_m^k (\mathbf{F}_{\mathbf{P},\mathbf{m}} \cdot \hat{\mathbf{z}}) + \sum_m^k (\mathbf{F}_{\tau,\mathbf{m}} \cdot \hat{\mathbf{z}})\right\} \tag{4.57}$$

where $\hat{\mathbf{x}}$ and $\hat{\mathbf{z}}$ are in body axis coordinates (the origin is at the nose, and the centerline of the vehicle is the $+x$ axis). The angle-of-attack converts the axial and normal forces into the more useful lift and drag coefficients which are related to the free-stream flow direction:

$$c_L = c_N \cos(\alpha) - c_A \sin(\alpha) \tag{4.58}$$

$$c_D = c_N \sin(\alpha) + c_A \cos(\alpha) \tag{4.59}$$

Note that bank angle is not included here, and lift is assumed to be the entirety of

the resultant force which is normal to the velocity vector. The magnitude will be converted into planetary axes using the bank angle during trajectory propagation in the next chapter.

Finally, similar to the summations performed to develop the resultant forces, the location and moment arms of each triangular surface can be included in order to develop expressions for the net moment coefficients:

$$c_l = \frac{1}{\frac{1}{2}\rho_\infty |\mathbf{v}|^2 SL} \left\{ \sum_m^k r_{yz,m} (\mathbf{F}_{\mathbf{P},\mathbf{m}} \cdot \hat{\phi}) - \sum_m^k r_{yz,m} (\mathbf{F}_{\tau,\mathbf{m}} \cdot \hat{\phi}) \right\} \tag{4.60}$$

$$c_m = \frac{1}{\frac{1}{2}\rho_\infty |\mathbf{v}|^2 SL} \left\{ \sum_m^k r_{xz,m} (\mathbf{F}_{\mathbf{P},\mathbf{m}} \cdot \hat{\alpha}) - \sum_m^k r_{xz,m} (\mathbf{F}_{\tau,\mathbf{m}} \cdot \hat{\alpha}) \right\} \tag{4.61}$$

$$c_n = \frac{1}{\frac{1}{2}\rho_\infty |\mathbf{v}|^2 SL} \left\{ \sum_m^k r_{xy,m} (\mathbf{F}_{\mathbf{P},\mathbf{m}} \cdot \hat{\beta}) - \sum_m^k r_{xy,m} (\mathbf{F}_{\tau,\mathbf{m}} \cdot \hat{\beta}) \right\} \tag{4.62}$$

where $\hat{\phi}$ is a bank angle rotation about the vehicle's x-axis, $\hat{\alpha}$ is an angle-of-attack rotation about the vehicle's y-axis, $\hat{\beta}$ is a yaw angle rotation about the vehicle's z-axis, and r is the distance from the relevant axis of rotation:

$$r_{xy,m} = \sqrt{(x_m - x_{\text{cg}})^2 + (y_m - y_{\text{cg}})^2} \tag{4.63}$$

$$r_{xz,m} = \sqrt{(x_m - x_{\text{cg}})^2 + (z_m - z_{\text{cg}})^2} \tag{4.64}$$

$$r_{yz,m} = \sqrt{(y_m - y_{\text{cg}})^2 + (z_m - z_{\text{cg}})^2} \tag{4.65}$$

4.5 Stability Derivatives

To date, flight experience in the hypersonic regime has suggested that stability of waverider forms presents a pressing challenge. Analysis of the effect of control surfaces is not included at this stage of work, so stability has been considered without a focus on controllability.

In this study, stability of waverider designs is determined using the magnitude

of stability derivatives. This is a first order method which models aircraft behavior around a specific flight condition as a linear system. Five point central differencing is used to calculate the following numerical derivatives:

$$c_{m\alpha}(\alpha) = \frac{-c_m(\alpha + 2\Delta\alpha) + 8c_m(\alpha + \Delta\alpha) - 8c_m(\alpha - \Delta\alpha) + c_m(\alpha - 2\Delta\alpha)}{12\Delta\alpha} \quad (4.66)$$

$$c_{l\beta}(\beta) = \frac{-c_l(\beta + 2\Delta\beta) + 8c_l(\beta + \Delta\beta) - 8c_l(\beta - \Delta\beta) + c_l(\beta - 2\Delta\beta)}{12\Delta\beta} \quad (4.67)$$

$$c_{n\beta}(\beta) = \frac{-c_n(\beta + 2\Delta\beta) + 8c_n(\beta + \Delta\beta) - 8c_n(\beta - \Delta\beta) + c_n(\beta - 2\Delta\beta)}{12\Delta\beta} \quad (4.68)$$

where $\Delta\alpha$, $\Delta\phi$, and $\Delta\beta$ are small disturbance angles.

For all stability calculations, the center of gravity (CG) is placed at the trim location. Symmetry enforced by the parameterization of the geometry guarantees trim in yaw and roll if the CG is along the centerline. Static longitudinal stability is assessed using the static margin:

$$SM = \frac{x_{NP} - x_{CG}}{L} \quad (4.69)$$

where x_{NP} is the vehicle's neutral point. The neutral point is the location of the center of gravity which would make $c_{m\alpha} = 0$. Determining the neutral point requires calculating one additional stability derivative, the change in $c_{m\alpha}$ with changes in x_{CG}. That is:

$$c_{m\alpha,xCG}(\alpha, x_{CG}) = \frac{1}{12\Delta x_{CG}}[-c_{m\alpha}(\alpha, x_{CG} + 2\Delta x_{CG}) + 8c_{m\alpha}(\alpha, x_{CG} + \Delta x_{CG}) - 8c_{m\alpha}(\alpha, x_{CG} - \Delta x_{CG}) + c_{m\alpha}(\alpha, x_{CG} - 2\Delta x_{CG})] \quad (4.70)$$

Then, the neutral point is calculated as:

$$x_{NP} = x_{CG} - \frac{c_{m\alpha}(\alpha, x_{CG})}{c_{m\alpha,xCG}(\alpha, x_{CG})} \quad (4.71)$$

Physically speaking, the neutral point is where the center of gravity would need to be for changes in the vehicle's angle-of-attack to not produce any pitching moment. When the center of gravity is forward of the neutral point, then the value of $c_{m\alpha}$ is negative. This is the essence of stability. When $c_{m\alpha}$ is negative, any angle-of-attack disturbance causes a moment which acts acts to restore the pitch to zero. On the other hand, if the neutral point is behind the CG, then pitch disturbances create moments which tend to exacerbate the rotation. The static longitudinal stability and distance away from neutral stability is summarized by the sign and magnitude of the static margin.

Chapter 5

Trajectory Simulation

In this work, aero-assisted trajectories are directly simulated. This allows a more detailed consideration than a purely analytic approach. A simulation was written in MATLAB utilizing dynamic integration capabilities. The equations and models used to create a flight path through outer space and planetary atmospheres are the subject of this chapter, along with other topics related to simulating aerospace trajectories.

5.1 Methodology and Simplifying Assumptions

The code was written so that the simulation framework can continuously propagate a trajectory anywhere in the solar system, including into and out of a terrestrial planetary atmosphere (Mars, Earth, Venus). When the position of the vehicle is calculated to be inside of an atmosphere, aerodynamic forces are determined as an acceleration on the vehicle along with gravitational accelerations. Outside of the atmosphere, gravitational forces are considered alone.

Depending on the nature of the simulation, gravitational force is either calculated for all major solar system bodies (a so called, 'n-body' simulation) or only calculated for one main planetary body (2-body simulation). This methodology is similar to the 'patched conics' approach of studying spacecraft trajectories. When in

the near vicinity of a planet, the motion of a spacecraft is dominated by that planet, and the gravitational acceleration due to other bodies can be neglected. The criteria for defining the region around a celestial object for which it's gravitational attraction is dominant is referred to as its 'sphere of influence'. This radial distance is calculated using Equation 5.1:

$$R_{SOI} = a\left(\frac{m}{M_{Sun}}\right)^{\frac{2}{5}} \tag{5.1}$$

where a refers to the semi-major axis of the planet's orbit around the Sun, and m is the mass of the planet. In any case study where the trajectory of an aero-assist vehicle is entirely within a planet's sphere of influence, a 2-body simulation is used. This method is extremely common in satellite and spacecraft simulations and yields sufficiently accurate results to justify the computational simplification.

Where this work differs from the patched conic approach is the use of a full n-body simulation when trajectories are propagated through multiple planetary spheres of influence. The distance calculated in Equation 5.1 corresponds to points in space where the gravitational acceleration due to the Sun is roughly the same magnitude as the gravitational acceleration due to the relevant planet. It is therefore an approximation of the transition between when either body's attractive force is most influential on spacecraft motion. In that transition region, the force due to both the planet and the Sun are both kinematically significant. While the patched conic method provides an excellent first order trajectory approximation, better results are achieved by considering the gravity of all planetary bodies. For example, when considering an aero-gravity assist mission, the trajectory might be propagated from Earth, through a series of gravity assist and aero-gravity assist fly-bys before reaching some final destination. During each fly-by, the spacecraft is within the sphere of influence of that planetary body. The patched conic approach

says that the fly-by should be propagated using 2-body dynamics until the sphere of influence is reached, and then a 2-body simulation should be run with the Sun as the central body. The n-body simulation method instead calculates the acceleration of all planets at every time step. This avoids the necessity of setting criteria for when each gravitational acceleration is statistically relevant. When going through the computational effort of numerically integrating the equations of motion of a spacecraft, using a full n-body simulation is justified. A simpler approach such as Keplerian orbit propagation is better suited for use with a patched conic method.

When calculating gravitational accelerations, spherical harmonics are ignored, and each planet is treated as a point mass. Of course, this is only in terms of calculating the direction and magnitude of the gravitational force, and the surface of the planet is still a rigid boundary. The oblateness of each planet is not considered, but the simulation is stopped with error if the radial distance between the aero-assist vehicle and any planet is equal to or less than the approximate spherical radius of the body. In most cases, a buffer altitude is added to the rigid boundary of the planet in order to ensure that there is no contact with any surface features such as mountains. Any time a buffer altitude is used in a case study, it will be specifically mentioned in the later chapters.

Within an atmosphere, the accelerations due to aerodynamic lift and drag are dependent on the vehicle's design and must be calculated at each time step. As was described in the previous chapter, compressible flow calculations were summed over the waverider. The aerodynamic calculators require an estimate of the atmospheric conditions (pressure, temperature, density, composition), and an atmospheric model determines these based on the vehicle position.

The simulation created has 5-degrees of freedom: 3 translational directions, as well as pitch angle and bank angle. Given that all of the waveriders developed using the Chapter 3 methods are symmetric in the yaw direction, no yaw force would be

expected using the aerodynamic models described. Further, waveriders operate in an 'off-design' condition when they fly with a non-zero yaw angle, so there is no motivation to induce a yaw angle. Thus, a yaw angle is neither desired nor possible to generate unintentionally, so it was omitted from the simulation.

It must be noted that while the simulations account for changes in two of the waverider's euler angles, this study does not include modeling of control devices. Admittedly, these would impact the aerodynamic and aerothermal environments and slightly increase both drag and heating. The performance estimates obtained herein would be slightly negatively impacted by these control devices. On the other hand, as will be shown, the control scheme used is significantly more simplistic than an actual flight vehicle would have. A more rigorous flight controller would likely be able to recover some performance when it is designed for a specific flight platform.

5.2 Control Algorithms

The intent of the control scheme is to manipulate the vehicle's aerodynamics to guide the vehicle from atmospheric entry to atmospheric exit. The vehicle's path through the atmosphere is determined by manipulation of both its angle-of-attack and bank angle.

These control schemes were created with two main principles in mind, simplicity and breadth. First, because each simulation would be run inside of an optimization loop, a significantly high number of trajectories would be run. From a given set of initial conditions, the optimization routine might need to run over 10000 times to reach a converged solution. For this reason, the vehicle controller could not be a computationally heavy, real time system. In fact, trajectory simulations several orders of magnitude faster than real-time were strongly desired.

Second, the same control scheme will be used for all waverider shapes, therefore the control law equations must be sufficiently robust to control vehicles with

potentially drastically different aerodynamic behavior by simply manipulating the gains and exponents. These gains and exponents are discrete inputs which can be varied manually, or by an external numerical optimization algorithm.

Neither control surfaces nor reaction control thrusters are modeled; however it is assumed that the vehicle has some method of either aerodynamically or propulsively affecting 0.25° of pitch or 0.5° of roll per second. This ensures smooth transition of the vehicle's euler angles, while eliminating the need for detailed control system modeling.

In all three control algorithms that will be discussed, the flight was broken down into separate flight components. Control parameters are used to alternate between the different scenarios. All paths have three separate stages:

1. Initial descent (α fixed)
2. Cruise
3. Final ascent (α fixed, α and $c_L > 0$)

The initial entry stage is defined by two input parameters, the flight path angle of entry and the angle-of-attack. Both values are inputs to the control system from an external source (user or an optimization algorithm). In some cases, the lift vector augments gravity, so as to pull to the vehicle deeper into the atmosphere. In the upper atmosphere, there is insufficient density to fly at a constant altitude, therefore a descent is necessary, and is either more efficient or only possible if lift-augmented. In other cases, the vehicle has a steep entry flight path angle, and must use lift acting opposite to gravity. As the flight path angle of entry becomes steeper, the angle-of-attack must increase to prevent excessive heating and penetration too deep into the atmosphere, or worse reaching the planetary surface. Conversely, as the flight path angle of entry becomes more and more shallow, the vehicle must fly at

an increasingly negative angle-of-attack to prevent skipping out of the atmosphere without ever reaching trimmed flight.

The intermediary, cruise stage represents the great flexibility of a lifting body. Inertial forces are so great that without sufficient aerodynamic lifting force, the aero-assist vehicle would likely be ejected from the atmosphere. A blunt body might not be able to generate sufficient lift in order to hold itself in the atmosphere, unless it decelerated critically and was not able to exit the atmosphere at all. The three control methodologies created as part of this work differ in their handling of the cruise flight stage. The specific algorithms as well as the advantage and disadvantages of each will be discussed in the following sections.

The final ascent consists of applying the lift vector opposite to the gravitational acceleration, thus facilitating an exit from the atmosphere. This operation can be triggered by monitoring the orbital energy of the vehicle as it flies. When it nears the desired final condition, ϵ_{ascent}, which is supplied as an input to the control system, the vehicle pulls up and exits as quickly as possible. The final orbital energy is that which will allow the vehicle to successfully complete the mission under review. It is inexact, however, as it requires an understanding of the exact flight path used to reach atmospheric exit, before the ascent occurs. The exit trigger occurs when the predicted flight path would result in the desired atmospheric exit conditions.

5.2.1 Altitude Varied

The first control algorithm developed is the most simplistic. It was created primarily for use with aero-capture like mission scenarios, in order to allow comparisons with more conventional blunt entry vehicle types. It was also desired to create an algorithm which could analyze the wide range of entry flight paths possible with a high lift vehicle. The increased controllability of a waverider aero-shell over a conventional blunt atmospheric entry body enables a significantly larger flight envelope.

Blunt body atmospheric entry trajectories typically involve one single descent into more dense regions of atmosphere, however, a high lift waverider allows for more intricacy. While high lift designs were desired to facilitate the comparison, because deceleration was required of the trajectory, flying in a higher drag configuration was actually valued as well. For this reason, an angle-of-attack based controller was implemented.

Further, this control algorithm was designed so that it would immediately function without the need to specify inputs which are suitable for a given vehicle geometry. The trade-off is that this control system is more rudimentary and does not deliver as high of performance as the subsequent control algorithms.

Straightforward triggers were used to allow the vehicle to change angle-of-attack and fly at different orientations for relevant sections of the flight. These are:

1. Minimum altitude of negative lift, $h_{(-\alpha)}$
2. Maximum altitude of positive lift, $h_{(+\alpha)}$

With these two triggers, three zones are created, one with negative lift, one with positive lift, and one in between with near zero lift (these are depicted in Figure 5.1). In each region, the vehicle flies at a constant α, but of a different magnitude. As an example, assume that the two triggers are set to 25 km and 15 km. As the vehicle descends, it flies at negative α, until it crosses $h_{(-\alpha)} = 25$ km. At that point, it pitches to reach $\alpha = 0$, and holds there until a new trigger is reached. Assuming the vehicle has enough inertia (as in Figure 5.1), it continues to descend, and eventually passes $h_{(+\alpha)} = 15$ km altitude. In order to prevent an impact trajectory, the control scheme triggers a pitch to a positive angle-of-attack. Eventually the vehicle lifts up, and passes 15 km, and the same trigger sends the vehicle back to $\alpha = 0$. This process continues until the third flight segment is reached.

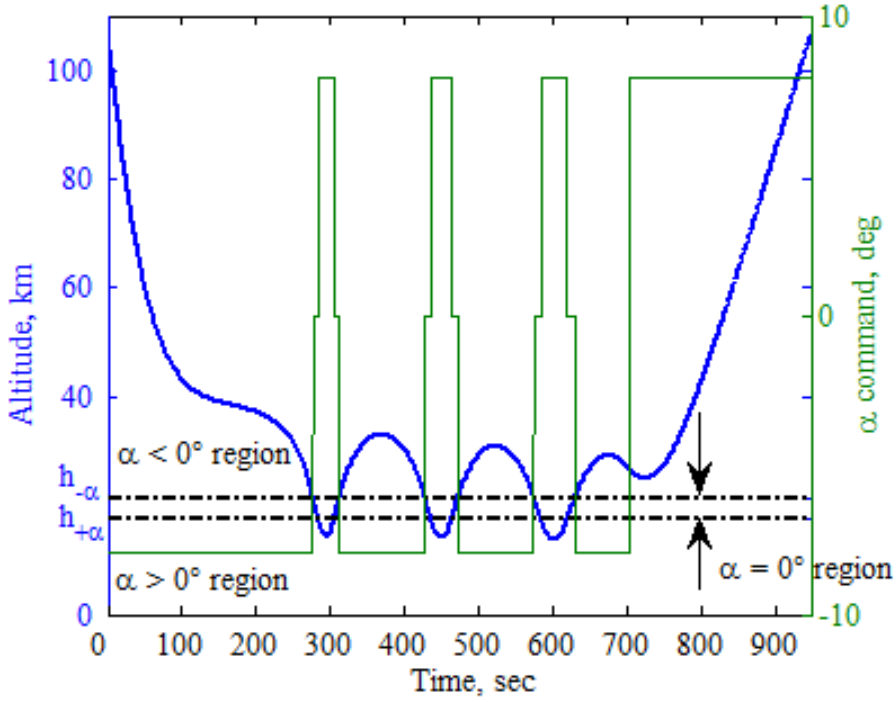

Figure 5.1: Altitude based control system. Dashed lines separate the three altitude control regions.

The specific angles used in the $\alpha > 0$ and $\alpha < 0$ regions are an input to the simulation, set by the user or the optimization routine.

The initial descent is considered complete, and the control system is triggered on when $h_{(-\alpha)}$ is first reached. If it is not reached at all, then the vehicle will exit the atmosphere and likely not complete its mission successfully. The input parameters controlling the initial descent (entry flight path angle, γ and the descent angle-of-attack) would then need to be modified.

The cruise stage is complete, and the vehicle begins its final ascent using the limiting orbital energy, ϵ_{ascent}, discussed above. When the vehicle's orbital energy crosses the limiting value, the vehicle will pitch up, to its maximum allowable magnitude and use aerodynamics to ascend and exit the atmosphere more efficiently.

5.2.2 Bank Modulation

Waverider vehicles can maintain higher lift-to-drag ratios when they limit their angle-of-attack close to zero. For this reason, this control system primarily varies the bank angle (ϕ) of the waverider, rather than its angle-of-attack. The on-design aerodynamic forces generated by the waverider should be greater than or equal to those required to maintain constant altitude flight. If the on-design aerodynamics of the vehicle have excess strength, then, in order to maintain cruise conditions, the vehicle will bank and rotate its lift vector slightly away from vertical until net vertical forces are roughly eliminated.

Using this control algorithm, the initial descent is completed once the vehicle reaches the nominal periapsis, marked by first having zero vertical velocity (shown by the first set of red arrows in Figure 5.2). When this occurs, the second flight stage is initiated and a trimming routine is executed to target constant altitude flight. Note that this is only a notional periapsis, as the vehicle may reach lower altitude during the controlled flight. The gains are sometimes marginally too large or too small for truly constant-altitude flight, and those vehicles slightly drift upward and downward, as seen in the blue altitude trajectory of Figure 5.2.

The gains and exponents ($\vec{x}_{\text{control}} = \{x_1, x_2, x_3, x_4, x_5, x_6\}$) are left as inputs, as the ideal parameters are a function of entry conditions and waverider performance characteristics. The overall system is represented by Equations 5.2 - 5.6:

$$(c_L)_{\text{goal}} = -(x_1(\vec{v} \cdot \hat{r}) + x_2 \Delta h)(|\vec{v}|/|v_{\text{entry}}|)^{x_3} \frac{m}{QS} \tag{5.2}$$

$$\phi_{\text{command}} = \cos\left(\frac{(c_L)_{\text{goal}}}{(c_L)_{\text{max}}}\right)^{-1} - \frac{\pi}{2} x_4 \tag{5.3}$$

$$\text{if} \quad ((c_L)_{\text{goal}} > (c_L)_{\text{max}}) \quad \text{then} \quad \alpha_{\text{command}} = \frac{((c_L)_{\text{goal}} - (c_L)_{\alpha=0}}{(c_L)_{\alpha,\text{max}} - (c_L)_{\alpha=0}} \alpha_{\text{max}} \tag{5.4}$$

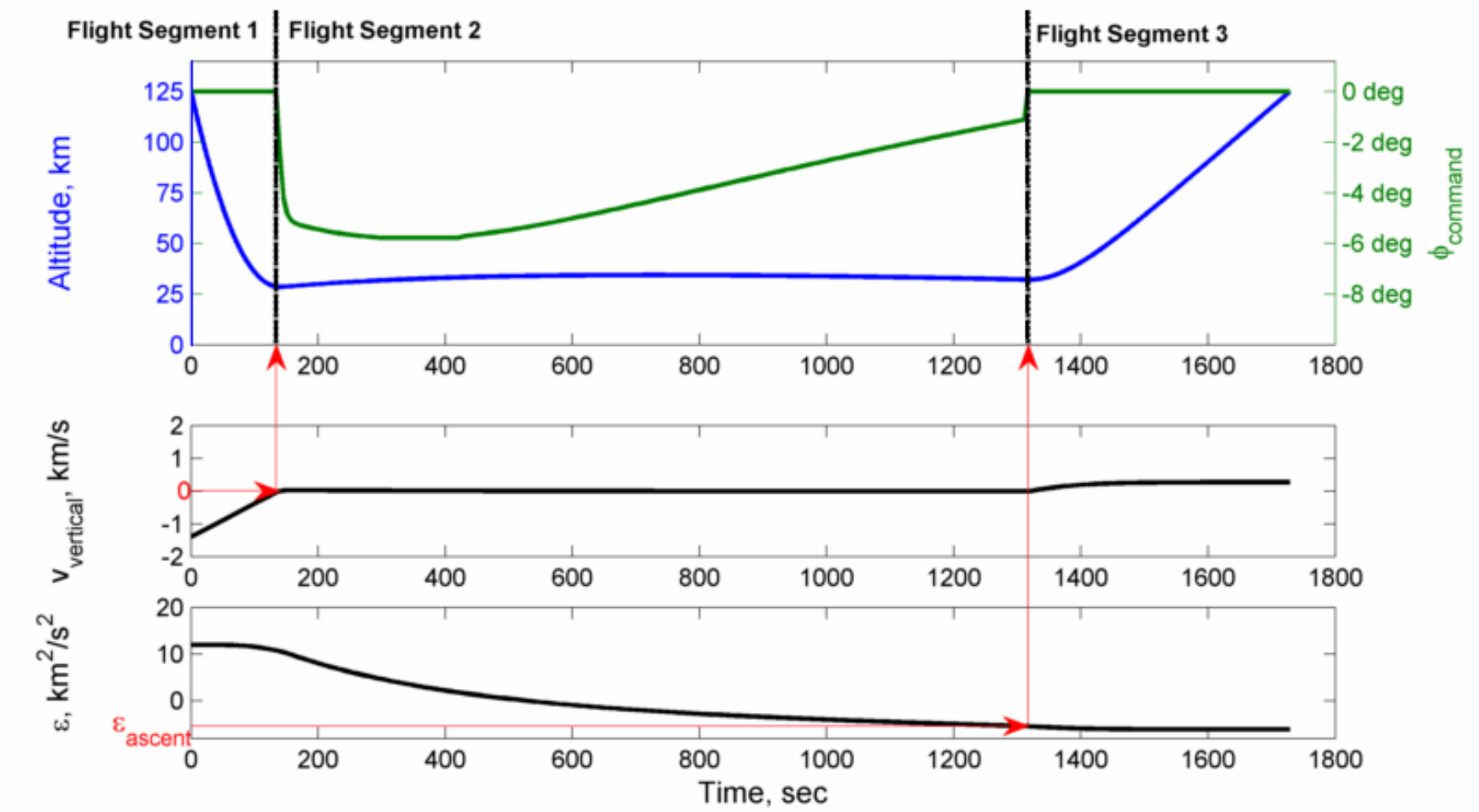

Figure 5.2: Example vehicle trajectory showing control scheme actions and flight segments. Red arrows point to limiting conditions being reached and subsequent flight segment transitions.

$$\dot{\phi} = q = x_5(\phi_{\text{command}} - \phi) \tag{5.5}$$

$$\dot{\alpha} = p = x_6(\alpha_{\text{command}} - \alpha) \tag{5.6}$$

The value of $(c_L)_{\max}$ is a function of the angle-of-attack (when $\phi = 0$), while $(c_L)_{\alpha=\max}$ is the lift coefficient at the maximum allowable angle-of-attack. For a given flight condition, if $(c_L)_{\max}$ is less than $(c_L)_{\text{goal}}$, only then is α allowed to vary. Similarly, the angle-of-attack is reduced back to zero degrees before bank angle is induced to reduce the vertical component of the lift vector. The maximum value of the angle-of-attack is specific to each waverider, but is small overall. Typically the value is restrained to less than ± 4 degrees. Within this small rotation range, the off-design effects are likely to be minimal.

In order to maintain constant altitude flight, the bank angle is smoothly varied and determined relative to both the vertical velocity as well as the vertical displacement from the target altitude. In both cases, the vertical direction is the outwardly normal vector relative to the local planetary surface. The two feedback parameters are inversely related to lift generation. For example, a positive vertical velocity (or positive altitude displacement) will command negative lift generation by way of a small bank angle. Conversely, negative vertical velocity (or negative altitude displacement) will command an increase in the bank angle to reduce the lift generation in the vertical direction.

Other logic exists in order to account for specific scenarios, such as constraining the roll and pitch rates to the maximums specified in the introduction to Section 5.2. At any given timestep, the value of $(c_L)_{\max}$ is determined from the waverider's flight condition. Then, the ODE solver is used on Equations 5.5 and 5.6 to determine the values of ϕ and α.

One concern related to roll-based control systems is the magnitude of the resulting plane change. Given the propulsive cost of inclination correction maneuvers,

a high degree of plane change would be costly. In order to minimize the effect, whenever the waverider returns to zero degrees, the direction of the bank is reversed to average out the displacement from the initial approach plane. Fortunately, only very small angles of bank are necessary for level flight, which keeps the inclination of the outbound path to a minimal value ($\Delta i < 3°$). However, as a precaution, additional control logic is used to vary the angle-of-attack in cases when bank would otherwise cause inclination to become too large.

5.2.3 Angle-of-Attack Modulation

In this final control scheme, the orientation of the waverider is once again determined as a function of vertical velocity, measured relative to the fly-by planet's surface ($\vec{v} \cdot \hat{r}$) and altitude relative to a desired cruise altitude (Δh). In this case however, the primary means of manipulating the aerodynamic lift force is by changing the vehicle's angle-of-attack, rather than its bank angle. This methodology was created in order to allow a test case in which cross-track distance was maximized. In such a scenario, bank angle was desired to remain at a relatively high and constant magnitude. Also, in some cases, a higher drag configuration might be desirable in order to increase deceleration, therefore a higher angle-of-attack would be allowable, despite some off-design waverider behavior.

The primary difference between this control system and the one described in Section 5.7 is that bank angle is held at a fixed value rather than varied. Once again, the cruise stage is triggered by the flight path's nominal periapsis, marked by zero vertical velocity. Once this occurs and the cruise stage begins, the gains and exponents of the system are input as a control vector. The control laws are represented by Equations 5.7 - 5.10:

$$(c_L)_{\text{goal}} = -(x_1(\vec{v} \cdot \hat{r}) + x_2 \Delta h)(|\vec{v}|/|v_{\text{entry}}|)^{x_3} \frac{m}{QS} \tag{5.7}$$

$$\alpha_{\text{command}} = \frac{((c_L)_{\text{goal}} - (c_L)_{\alpha=0}}{(c_L)_{\alpha=\max} - (c_L)_{\alpha=0}} \alpha_{\max} \cos\phi \tag{5.8}$$

$$\dot{\alpha} = p = x_4(\alpha_{\text{command}} - \alpha) \tag{5.9}$$

$$\dot{\phi} = p = 0 \tag{5.10}$$

Again the value for $(c_L)_{\alpha=\max}$ is the lift coefficient at the maximum allowable angle-of-attack, $\alpha_{\max}$. This value varies for each waverider, as do appropriate values for the control vector $\vec{x}_{\text{control}} = \{x_1, x_2, x_3, x_4\}$. In addition to the gains and exponents in the above system, the fixed bank angle exists as an input.

5.3 Equations of Motion

In this section, the movement of the aero-assist vehicle is described using the equations governing its dynamics. These are completely general, so the mission type being reviewed is of no importance. Modifying the initial and end conditions is sufficient to consider any aero-assist mission. At this stage, the specific aero-shell shape is of no importance either. The equations of motion will be written in terms of aerodynamic coefficients which could correspond to any of the waverider models described or any other vehicle shape.

The trajectory can be propagated in a number of different reference frames, each with its own advantages and disadvantages. Three separate reference frames will be considered here: planet-centered inertial, Sun-centered inertial, and a non-inertial, rotating planet coordinate frame. Each will be discussed, as will the manner in which positions and velocities can be transferred between them.

5.3.1 Planet-Centered Planet-Fixed

A planet-centered, planet-fixed non-intertial frame of reference rotates along with the surface of that planet. It is therefore fixed, relative to the planet. In the

case of Earth, which will be discussed as an example in this section, the coordinate system is known as the Earth-centered, Earth-Fixed (ECEF, see Figure 5.3) frame.

The greatest advantage of this coordinate system is that neither locations on the surface of the Earth, nor the bulk atmosphere are moving relative to the frame itself. Further, all atmospheric gas motion can be neglected if winds are ignored. This is a comfortable assumption given the low magnitude that atmospheric winds have relative to the hypersonic speeds at which aero-assist vehicles operate. Assuming an aero-assist vehicle would likely travel at or well over Mach 20, even a Category 5 hurricane force wind of 70 m/s would only constitute 1.75% of the flight speed.

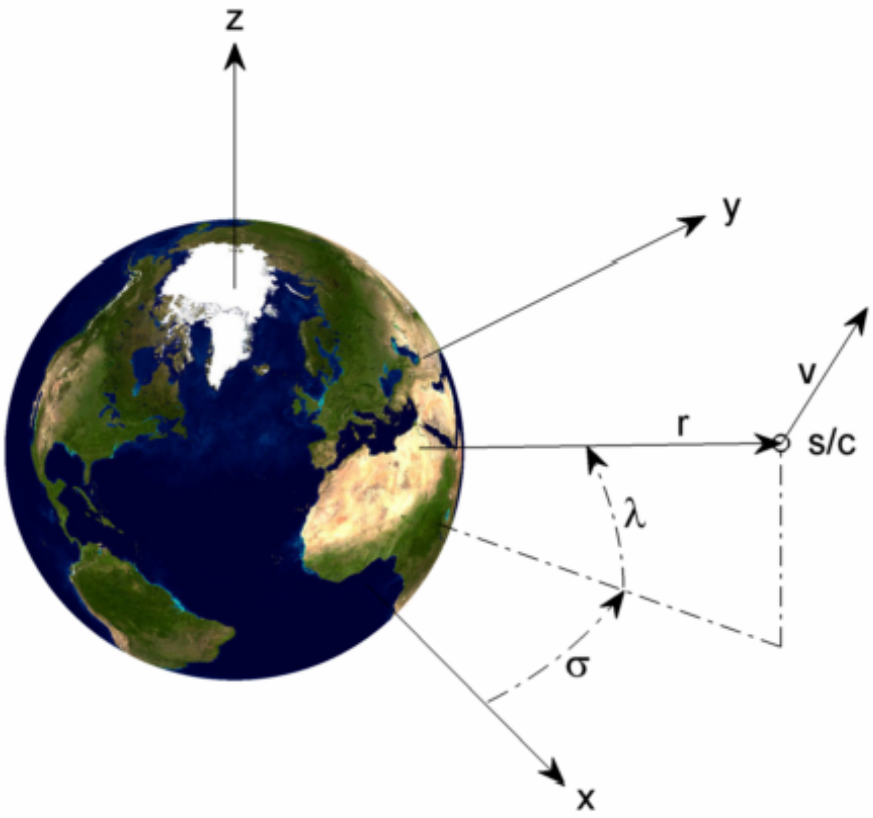

Figure 5.3: Earth-centered, Earth-fixed reference frame. Longitude, σ, and latitude, λ, of the spacecraft are as noted.

Further, the rotating coordinate system is most useful when considering the

state of the vehicle relative to locations on the surface of the planet. This is particularly relevant at Earth, as our own viewpoint is rotating along with the planet.

The z-axis of the rotating frame is defined to be the rotation axis of the planet, with positive direction out the north pole. In the case of Earth, the x-axis points from the center of the planet through the intersection of the equator and the prime meridian (in the ocean, just off the coast of Africa). The y-axis completes the basis, and points through the equator and the 90° longitude line.

The equations of motion in this non-inertial frame must include centripetal acceleration in order to account for the movement of the frame itself. The set of ordinary differential equations are as follows:

$$\dot{r} = v \sin\gamma \tag{5.11}$$

$$\dot{\sigma} = \frac{v \sin\gamma \cos\psi}{r \cos(\phi)} \tag{5.12}$$

$$\dot{\lambda} = \frac{v \cos\gamma \sin\psi}{r} \tag{5.13}$$

$$\dot{v} = \frac{1}{2}\rho_\infty v^2 \frac{S}{m} c_D - \frac{\mu \sin\gamma}{r^2} \tag{5.14}$$

$$\dot{\gamma} = \frac{1}{2}\rho_\infty v \frac{S}{m} c_L \cos(\phi) - \frac{\mu \cos\gamma}{v r^2} + \frac{v \cos(\gamma)}{r} \tag{5.15}$$

$$\dot{\psi} = \frac{1}{2}\rho_\infty v \frac{S}{m} c_L \frac{\sin(\phi)}{\cos\gamma} - \frac{v \tan\lambda \cos(\gamma) \cos\psi}{r} \tag{5.16}$$

where r is the radial distance from the center of the planet, v is the flight speed, σ is the longitude, λ is the latitude, γ is the flight path angle relative to the planet's local horizontal, ψ is the heading angle of the vehicle relative to due east, ϕ is the bank angle, S is the reference surface area of the aero-shell, m is the mass of the vehicle, c_L and c_D are the aerodynamic coefficients and ρ_∞ is the atmospheric density, determined from an atmospheric model. See Figures 5.3 and 5.4 for depictions of the coordinate system variables.

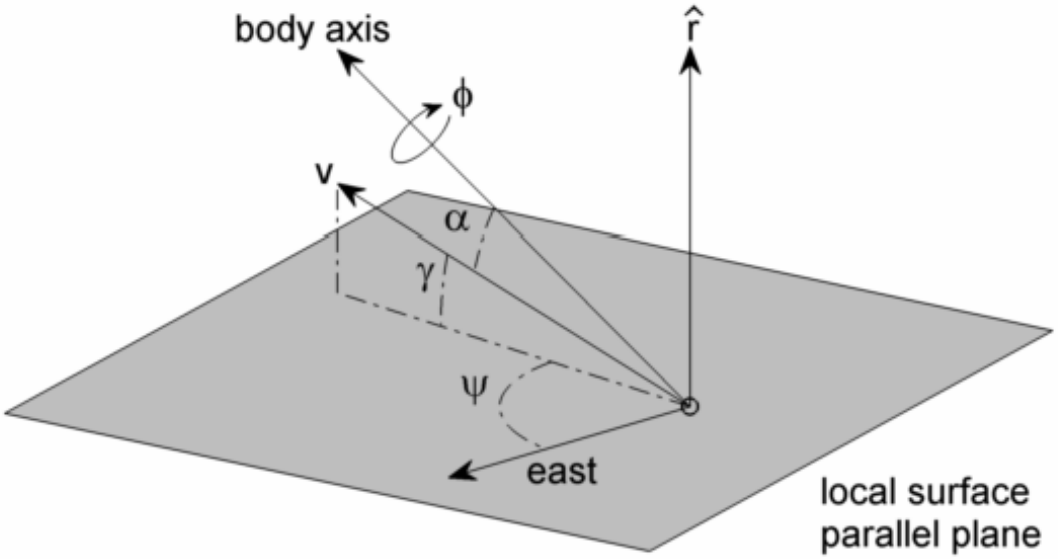

Figure 5.4: Schematic of the local body axis system. The gray plane is tangent to the local surface of the planet, and perpendicular to the position vector, $\boldsymbol{r}$.

5.3.2 Planet-Centered Inertial

Inertial coordinates are the simplest to conceptualize. The motion of all spacecraft and planetary bodies are determined relative to some fixed observation point. When inside of a planet's sphere of influence, the center of that body is a natural selection. The frame is oriented such that even if the planet is rotating, the coordinate frame is fixed.

Inertial coordinate frames can be defined for any planetary body, but for the purposes of discussion, this section is written with reference to Earth, and its inertial coordinate system (Earth-Centered Inertial, ECI, see Figure 5.5). Inertial coordinates around any other planet can be defined using the same method as the ECI frame.

First, the x-vector is commonly selected to be the vernal equinox at the J2000 epoch (12:00, January 1st, 2000). The vernal equinox is a vector starting from the center of the Earth, and pointing through Earth's equator, directly at the center

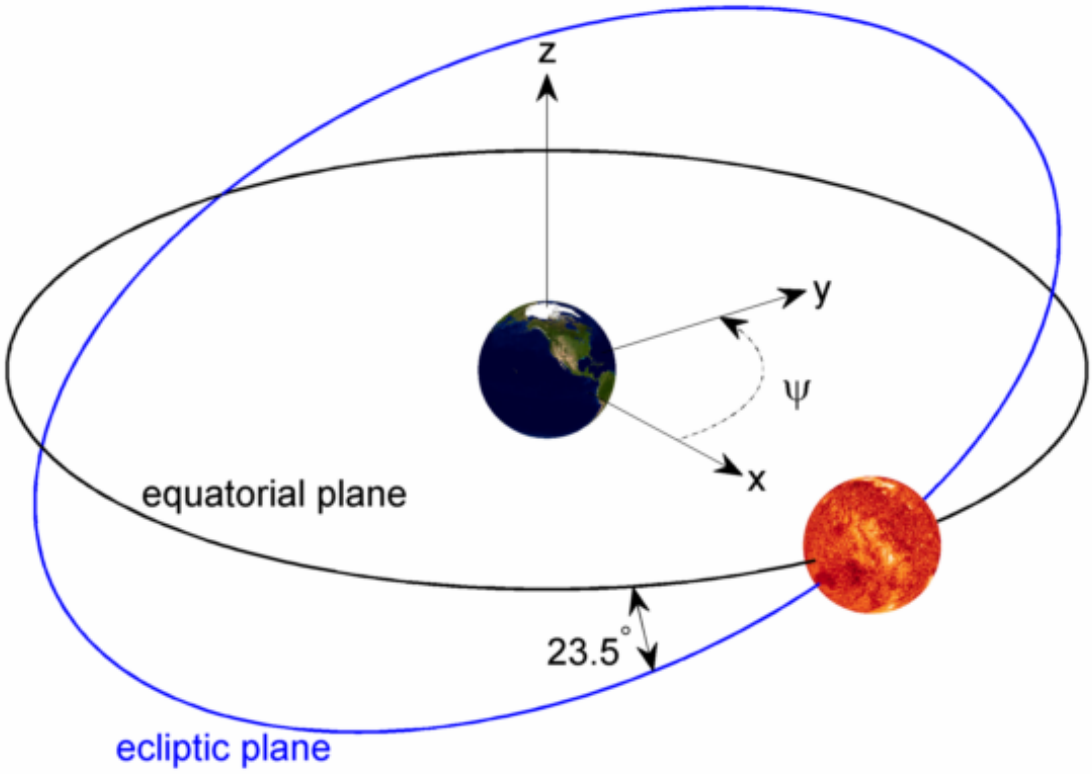

Figure 5.5: ECI coordinate system. With Earth fixed, the Sun rotates around Earth in the ecliptic plane. The x-direction, or vernal equinox vector, is fixed in the direction of the position where the Sun crosses the equatorial plane from north to south. ψ is the azimuth angle of a location around the Earth.

of the Sun as the Sun (traveling along the ecliptic plane relative to a fixed Earth) cross the Earth's equatorial plane from south to north. Because of the precession of Earth's rotation, the south to north Sun vector crossing does not occur at the exact same location year after year. In order to fully define the vernal equinox, it is referenced with a specified epoch, in this case J2000.

The z-vector is defined to be pointing directly out the north pole, matching the axis of rotation. The y-axis is the cross product of the two other vectors, which completes the basis. The x,y plane is the equatorial plane, and is at roughly a 23.5° relative to Earth's orbital, or ecliptic plane.

One main advantage of propagating the orbit in inertial coordinates is the

simplicity of the equations of motion. There is no need to include the centrifugal and Coriolis accelerations. The state vector of the spacecraft is able to provide directionality for the aerodynamic forces. The calculations are performed in each of the $\hat{x}$, $\hat{y}$, $\hat{z}$ planet-centered inertial directions. Using the radius and velocity vectors, $\mathbf{r}$ and $\mathbf{v}$, the acceleration equations are:

$$a_x = -\mu\frac{r_x}{|\mathbf{r}|^3} + \frac{1}{2}\rho_\infty|\mathbf{v}_\infty|^2\frac{S}{m}\left\{\frac{r_x}{|\mathbf{r}|}c_L\cos(\phi) - \frac{v_x}{|\mathbf{v}|}c_D\right\} \tag{5.17}$$

$$a_y = -\mu\frac{r_y}{|\mathbf{r}|^3} + \frac{1}{2}\rho_\infty|\mathbf{v}_\infty|^2\frac{S}{m}\left\{\frac{r_y}{|\mathbf{r}|}c_L\cos(\phi) - \frac{v_y}{|\mathbf{v}|}c_D\right\} \tag{5.18}$$

$$a_z = -\mu\frac{r_z}{|\mathbf{r}|^3} + 3\frac{1}{2}\rho_\infty|\mathbf{v}_\infty|^2\frac{S}{m}\left\{\frac{r_z}{|\mathbf{r}|}c_L\cos(\phi) - \frac{v_z}{|\mathbf{v}|}c_D\right\} \tag{5.19}$$

The free-stream density, ρ_∞ is determined using an atmosphere model (discussed in Section 5.4) at the current altitude ($|\mathbf{r}| - R_E$) above the surface. The states, $\mathbf{r}$, and $\mathbf{v}$, are known from previous time steps, or initial conditions.

Due to the simplifying assumptions made about the control system's ability to impart moments about the vehicle, the equations of motion for the euler angles of the vehicle are less fundamental. As discussed in Section 5.2 for each algorithm, the assumptions vary, and in some cases, the bank rate is fixed to be zero. Also, the yaw angle and yaw angle rate are always fixed to zero. The equations used to integrate rotation rates into rotation angles are repeated here for completeness:

$$\dot{\phi} = p = c_1(\phi_{command} - \phi) \tag{5.20}$$

$$\dot{\alpha} = q = c_2(\alpha_{command} - \alpha) \tag{5.21}$$

where c_1 and c_2 are scalar inputs to the control system.

The main disadvantage of inertial coordinates is that the atmosphere of the planet is moving relative to the coordinate system. Therefore, in order to correctly

calculate the aerodynamic forces, the velocity of the atmosphere relative to the spacecraft must be accounted for. Similar to the rotating frame, it is assumed that the atmosphere is quiescent relative to the surface of the planet. The linear velocity relative to the inertial frame is therefore:

$$|\mathbf{v}_{\text{wind}}| = \frac{2\pi|\mathbf{r}|}{T} \tag{5.22}$$

where T is the rotational period of the planet. In the case of Earth, $T = 23$ hours, 56 minutes, 4 seconds. Earth's 24 hour sidereal period is relative to the Sun. Because Earth is rotating in the same direction as its orbit, it must rotate slightly further than 360° each day. Relative to a fixed inertial observer, the Earth completes a 360° revolution 56 seconds less than a 24 hour sidereal day. Note that the speed of the atmosphere is not the same as an orbital speed. While gravitational force does keep the planet's atmosphere attached, the primary force which keeps the atmosphere rotating at roughly the same speed as the surface is friction, hence the rigid body rotation form of Equation 5.22.

Further complicating the use of inertial coordinates is the need to book-keep the direction of the relative wind velocity. Aerodynamic forces are typically calculated in airframe coordinates. Therefore the velocity of the free-stream atmosphere is needed relative to the vehicle. In order to determine the relative atmospheric wind speed, first determine the azimuth angle, ψ, of the spacecraft in the ECI system:

$$\psi = \tan^{-1}\left(\frac{r_y}{r_x}\right) \tag{5.23}$$

Note that ψ is similar to the longitudinal angle in a rotational coordinate system, but it is symbolized differently here to avoid confusion, as it does not refer to locations

on the surface of the Earth. With the azimuth angle, the direction of the wind is:

$$\hat{\mathbf{v}}_{\text{wind}} = -\sin(\psi)\,\hat{x} + \cos(\psi)\,\hat{y} + 0\hat{z} \tag{5.24}$$

Using equations 5.22 - 5.24, the free-stream wind velocity relative to the vehicle, v_∞, is defined as:

$$\mathbf{v}_\infty = \mathbf{v} - \mathbf{v}_{\text{wind}} = \begin{bmatrix} v_x \\ v_y \\ v_z \end{bmatrix} - \begin{bmatrix} -\frac{2\pi|\mathbf{r}|}{T}\sin(\psi) \\ \frac{2\pi|\mathbf{r}|}{T}\cos(\psi) \\ 0 \end{bmatrix} \tag{5.25}$$

The magnitude of $\mathbf{v}_\infty$ is the airspeed of the vehicle, and the direction is used in calculating the euler angles. Similarly the air speed Mach number, M_∞, for which all aerodynamic calculations are made, is determined using the magnitude of $\mathbf{v}_\infty$, not $\mathbf{v}$.

5.3.3 Sun-Centered Inertial

An inertial coordinate frame relative to the Sun is the most common means of propagating an interplanetary spacecraft trajectory. Positions of each planet relative to the Sun are readily available, possibly most notably from JPL's HORIZONS system.[113] Therefore, propagation of individual planet's orbits is not necessary, and the relative position of the spacecraft to each planet is a simple vector subtraction.

In the Sun-centered inertial, or heliocentric inertial (HCI, see Figure 5.6) frame, the x-vector is the same as the ECI x-axis, except that it points in the opposite direction, from the Sun to the Earth. The z-vector is typically defined to be perpendicular to Earth's ecliptic plane. It is therefore a unit vector in the direction of Earth's orbital angular momentum. Again, the y-vector is simply the cross product of the other two principle directions in order to complete the basis.

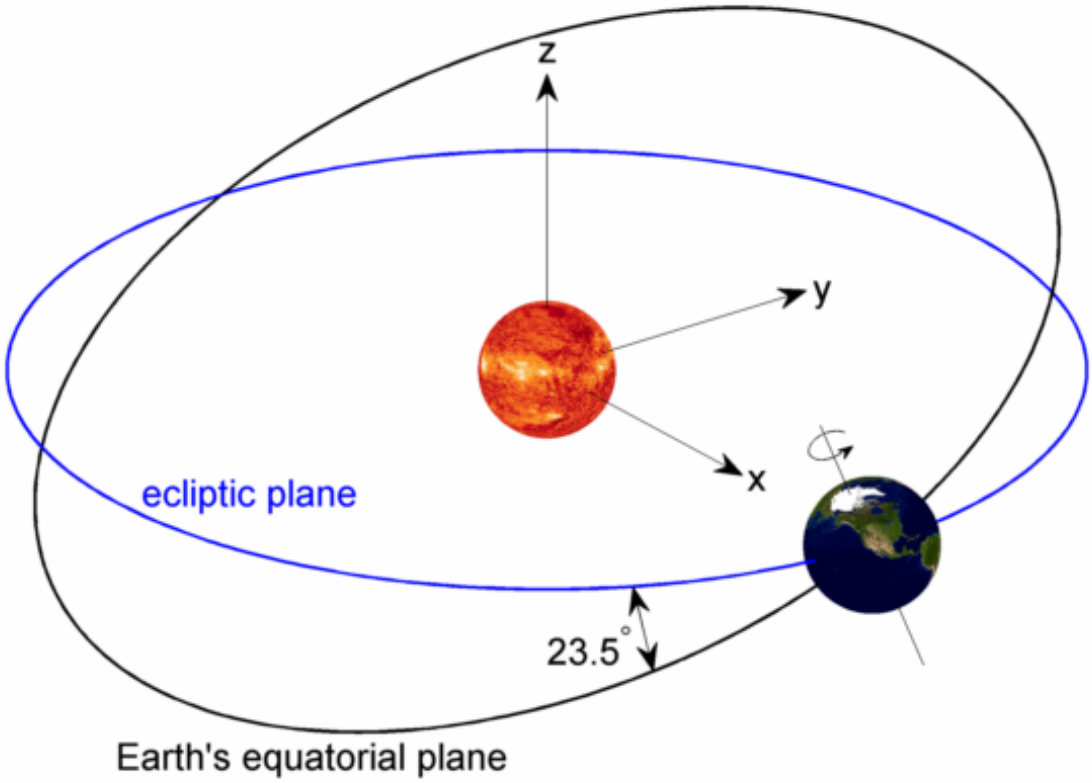

Figure 5.6: HCI coordinate system. Earth orbits around the Sun in the ecliptic plane. The x-direction, or the negative of the vernal equinox vector, is fixed in the direction of the position where the Earth's equatorial plane crosses the ecliptic plane from south to north.

For simplicity, this frame is not used when the aero-assist vehicle is inside of a planetary atmosphere. For that reason, the equations of motion are extremely simple and reduce to Newton's law of gravitation:

$$a_x = -\mu \frac{r_x}{|\mathbf{r}|^3} \tag{5.26}$$

$$a_y = -\mu \frac{r_y}{|\mathbf{r}|^3} \tag{5.27}$$

$$a_z = -\mu \frac{r_z}{|\mathbf{r}|^3} \tag{5.28}$$

Other forces could be added in, such as solar radiation pressure, but for the purposes

of this work, gravity was the only force assumed to act on the vehicle when in deep space.

The rotation rates of the vehicle are not mentioned here, as the rotation rates are set to zero when not in an atmosphere. It is assumed that the final vehicle would have some manner of orientation control, but again, these systems are not modeled. Further, the orientation of the vehicle in deep space is not of particular relevance at this stage of design, as parameters such as viewing angles are not considered. The only instance that orientation of the vehicle is important is at an atmospheric entry point. These initial conditions are manually set when switching between coordinate systems.

5.3.4 Coordinate Transformations

When certain relevant conditions are reached, it is useful to change coordinate systems amongst the three presented. For example, when a spacecraft enters the sphere of influence of a planet, it is often useful to use equations of motion in a frame of reference centered at that planet, rather than at the Sun. Further, when the spacecraft enters the atmosphere, if positions relative to a location on the surface of the planet are of interest, then inertial coordinates might be transfered into a planet-fixed coordinate frame.

5.3.4.1 HCI to ECI

First, consider a transformation from heliocentric inertial coordinates into Earth-centered inertial coordinates. Again, the ECI system will be used as an example, but conversion into another planet's inertial coordinates follows the same principle. At the instant in time that the conversion is made, the spacecraft and

Earth have heliocentric positions, $\mathbf{r}_{HCI}$ and $\mathbf{r}_{E,HCI}$, respectively:

$$\mathbf{r}_{HCI} = \begin{bmatrix} r_x \\ r_y \\ r_z \end{bmatrix}_{HCI} \tag{5.29}$$

$$\mathbf{r}_{E,HCI} = \begin{bmatrix} r_{E,x} \\ r_{E,y} \\ r_{E,z} \end{bmatrix}_{HCI} \tag{5.30}$$

Positions of planets in heliocentric coordinates can be obtained from an ephemeris database such as JPL's HORIZONS.[113] The transformation into the position of the spacecraft in ECI coordinates is then:

$$\mathbf{r}_{ECI} = \begin{bmatrix} r_z \\ r_y \\ r_z \end{bmatrix}_{ECI} = \begin{bmatrix} 1 & 0 & 0 \\ 0 & \cos(\epsilon) & -\sin(\epsilon) \\ 0 & \sin(\epsilon) & \cos(\epsilon) \end{bmatrix} \left(\begin{bmatrix} r_x \\ r_y \\ r_z \end{bmatrix}_{HCI} - \begin{bmatrix} r_{E,x} \\ r_{E,y} \\ r_{E,z} \end{bmatrix}_{HCI} \right) \tag{5.31}$$

The only needed variable is the angle between the ecliptic plane of Earth's orbit and Earth's equatorial plane, ϵ. This is often called the obliquity of the ecliptic. As mentioned previously, it has a value of roughly 23.5°, but it varies slightly due to the precession in Earth's rotation. To calculate the exact value at a given Julian date, Lasker[114] presented a model, repeated here:

$$\begin{aligned} \epsilon = 0.409092802283074 \quad &- \quad 0.0002269661065878 \left(\frac{JD - 2451545.0}{36525} \right) \\ &- \quad 2.8623399732707 \cdot 10^{-9} \left(\frac{JD - 2451545.0}{36525} \right) \\ &+ \quad .79645943005142 \cdot 10^{-9} \left(\frac{JD - 2451545.0}{36525} \right) \end{aligned} \tag{5.32}$$

5.3.4.2 ECI to HCI

The inverse conversion, from the ECI system into the HCI system, can be conducted using the same set of equations reworked. In particular, Equation 5.31 can be written:

$$\mathbf{r}_{HCI} = \begin{bmatrix} r_z \\ r_y \\ r_z \end{bmatrix}_{HCI} = \begin{bmatrix} 1 & 0 & 0 \\ 0 & \cos(\epsilon) & -\sin(\epsilon) \\ 0 & \sin(\epsilon) & \cos(\epsilon) \end{bmatrix}^{-1} \begin{bmatrix} r_x \\ r_y \\ r_z \end{bmatrix}_{ECI} + \begin{bmatrix} r_{E,x} \\ r_{E,y} \\ r_{E,z} \end{bmatrix}_{HCI} \tag{5.33}$$

where ϵ is calculated using Equation 5.32.

5.3.4.3 ECI to ECEF

Because the z-axes of the ECI and ECEF frame are parallel, and the x-y planes are co-planar, there are only two steps to convert between the two: 1) Find the rotation angle about the z-axis to line up the x and y axes; and 2) Convert Cartesian coordinates to spherical.

The x-axis in the ECEF frame points through the prime meridian, which was placed based on the location of Greenwich, England. Using the model presented by the United States Naval Observatory (USNO),[115] the angle between the vernal equinox and the prime meridian can be calculated as:

$$\sigma_{VE} = \frac{2\pi}{24} GMST \tag{5.34}$$

where GMST is the Greenwich mean sidereal time in hours. This signifies the number of hours since the prime meridian passed the vernal equinox. It is typically reduced by a value of $24k$ such that it has a range from 0 hours to 24 hours (k is any positive integer that satisfies the 0-24 hour condition). Alternatively, GMST can be

used in full form and σ can be reduced by $2\pi k$ to only signify an angle between 0 and 2π. In order to calculate GMST, Equation 5.35 is also provided by the USNO:

$$GMST = 18.697374558 \quad + \quad 24.06570982441908 \left(\frac{JD - 2451545.0}{36525} \right) \tag{5.35}$$

To complete step 1 of the conversion, the ECI position is simply rotated about the z-axis:

$$\mathbf{r}_{ECEF} = \begin{bmatrix} r_z \\ r_y \\ r_z \end{bmatrix}_{ECEF} = \begin{bmatrix} \cos(-\sigma_{VE}) & -\sin(-\sigma_{VE}) & 0 \\ \sin(-\sigma_{VE}) & \cos(-\sigma_{VE}) & 0 \\ 0 & 0 & 1 \end{bmatrix} \begin{bmatrix} r_z \\ r_y \\ r_z \end{bmatrix}_{ECI} \tag{5.36}$$

The ECEF frame typically uses spherical coordinates, not Cartesian, similar to the equations of motion presented in Section 5.3.1. A standard conversion between the coordinate systems will complete the ECI to ECEF conversion (all variables are in the ECEF frame):

$$r = \sqrt{r_x^2 + r_y^2 + r_z^2} \tag{5.37}$$

$$\sigma = \tan^{-1} \left(\frac{r_y}{r_x} \right) \tag{5.38}$$

$$\lambda = \sin^{-1} \left(\frac{r_z}{\sqrt{r_x^2 + r_y^2 + r_z^2}} \right) \tag{5.39}$$

5.3.4.4 ECEF to ECI

Equations 5.34 through 5.39 can simply be inverted in order to obtain positions in a planet centered inertial coordinate system, such as ECI, from a planet fixed coordinate system, such as ECEF. For completeness, the equations are inverted

here:

$$\mathbf{r}_{ECEF} = \begin{bmatrix} r_z \\ r_y \\ r_z \end{bmatrix}_{ECEF} = \begin{bmatrix} r\cos(\lambda)\cos(\sigma) \\ r\cos(\lambda)\sin(\sigma) \\ r\sin(\lambda) \end{bmatrix} \tag{5.40}$$

$$GMST = 18.697374558 \quad + \quad 24.06570982441908\left(\frac{JD - 2451545.0}{36525}\right) \tag{5.41}$$

$$\sigma_{VE} = \frac{2\pi}{24} GMST \tag{5.42}$$

$$\mathbf{r}_{ECI} = \begin{bmatrix} r_z \\ r_y \\ r_z \end{bmatrix}_{ECI} = \begin{bmatrix} \cos(\sigma_{VE}) & -\sin(\sigma_{VE}) & 0 \\ \sin(\sigma_{VE}) & \cos(\sigma_{VE}) & 0 \\ 0 & 0 & 1 \end{bmatrix} \begin{bmatrix} r_z \\ r_y \\ r_z \end{bmatrix}_{ECEF} \tag{5.43}$$

5.4 Atmospheric Modeling

An atmospheric model is an essential component of a trajectory simulation. The model is used to determine the temperature, pressure, and density of the atmospheric gas through which the aero-assist vehicle is flying at any time step in the flight path. This has bearing on the aerodynamic forces and the aerothermal environment surrounding the vehicle.

Earth's atmosphere is relatively well understood and quantified. Our understanding of the atmospheres of Mars and Venus is less well known, and is based primarily on a limited set of flight data. Each interplanetary spacecraft sent to these planets has been equipped with scientific instruments capable of sampling and quantifying the atmospheric properties as they descended towards the surface. Any model of the gas properties at these planets is certainly less precise than a model of Earth.

Many meteorological factors will determine the atmospheric conditions on any given day, and these are hard, if not impossible to predict. Many simplifying assump-

tions are necessary in order to run a trajectory simulation. First, as was mentioned above, it was assumed that all atmospheres have zero wind velocity.

Other simplifying assumptions are made, but they vary depending on the atmosphere model employed. Two different sets of atmosphere models were used: exponential height profiles and the Global Reference Atmosphere Models (GRAM) developed at the NASA Marshall Space Flight Center. Depending on the study, either model could have been used, resulting in a slightly varied level of fidelity and execution time.

5.4.1 Global Reference Atmosphere Models

The Global Reference Atmosphere Models[116] are a set of applications which provide engineering-level estimates of the properties of atmospheres at solar system bodies. There is an application available for Earth (Earth-GRAM), Mars (Mars-GRAM), and Venus (Venus-GRAM), as well as other destinations which might be able to support an aero-assist mission (Titan and Neptune). They are the definitive set of tools to determine atmospheric conditions for engineering applications. Beyond the standard functionality, they also have useful features such as a realistic dispersion algorithm in order to do perturbation Monte-Carlo analysis.

Earth-GRAM[117] uses data from a number of sources, including sounding rockets, weather balloons, aircraft, ground based observations and satellite remote sensing. Earth-GRAM has geographic longitude and latitude variability, as well as seasonal and monthly variations. Rather than using a standard atmospheric composition, Earth-GRAM has estimates of the concentration of different gaseous species at each altitude location. These are used in this study in order to improve the estimate of the air's ratio of specific heats, γ. The value of γ has great importance on the aerodynamic forces generated by the aero-assist vehicle. Finally, while they are not used in this work, Earth-GRAM also provides detailed wind estimates.

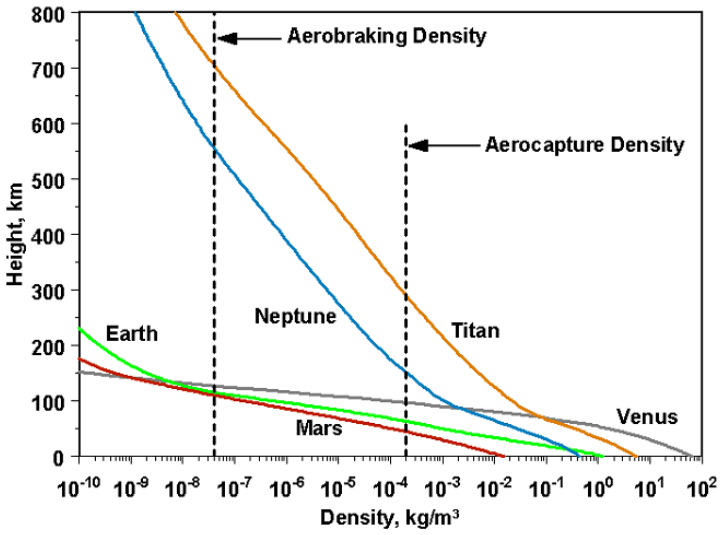

Figure 5.7: Atmospheric Density Comparisons using the GRAM suite of tools. From Ref. [116]

Mars-GRAM[118] compiles Martian atmospheric measurements from the Mariner missions, the Viking missions, Mars Pathfinder, and Mars Global Surveyor. These create a relatively comprehensive data set capable of characterizing atmospheric conditions in the Martian atmosphere as a function of latitude, longitude and epoch (which determines the position of the planet in its orbit).

Venus-GRAM[119] is based primarily on the Venus International Reference Atmosphere (VIRA).[120] In turn, VIRA is based on the VEGA 1 and 2 missions, the Galileo mission, the Pioneer and Magellan Venus orbiters, and the Venera 11, 13, 15 and 16 missions. The application is able to produce standard atmospheric values, including realistic variations for time of day, solar viewing angle, and latitude/longitude position.

5.4.2 Scale Height

The simplest means of approximating the atmospheric conditions in the atmosphere of a planet can be done using a set of exponential decay equations. As altitude increases, pressure and density tend to decrease exponentially.

An exponential model for an atmosphere uses the principle of scale height, H, or the altitude distance over which a thermodynamic property changes by one exponential order, e^1. In the simplest form, one single scale height can be used for the entire altitude range of an atmosphere. Improved performance is found if the scale height is instead a function of altitude as well. In order to scale the exponential relationship, at least one value for pressure and density at a reference altitude is required. At any other altitude, pressure and density are calculated as:

$$\rho = \rho_{\text{Ref}} \exp \frac{h_{\text{Ref}} - h}{H} \tag{5.44}$$

$$P = P_{\text{Ref}} \exp \frac{h_{\text{Ref}} - h}{H} \tag{5.45}$$

With two thermodynamic properties known, atmospheric temperature can be calculated using either an iterative gas composition calculator such as NASA's Chemical Equilibrium with Applications[107] (CEA) or more simply, the ideal gas law:

$$T = \frac{P}{\rho R} \tag{5.46}$$

Similarly, the gas constant, R, can be assumed as a constant throughout the atmosphere, or updated at each altitude using CEA.

Justus and Braun[121] compiled a set of exponential atmospheric data. The models used in this work are exclusively taken from that publication. The data sources for the exponential models are the same as the GRAM tools, however averages are used instead, in order facilitate much quicker implementation and much faster calculation. The atmospheric data for Venus, Earth and Mars is presented in Tables 5.2, 5.3, 5.4 respectively. Between each altitude range supplied, equations 5.44 and 5.45 are used to find the current value. If not using CEA to estimate gas composition, Justus and Braun recommend using the values specified in Table 5.1.

Table 5.1: Constants for Exponential Models

	γ	R J/(Kg-K)
Venus	1.286	190.22
Earth	1.400	287.12
Mars	1.330	191.38

Table 5.2: Atmospheric Properties of Venus

Altitude km	Scale Height km	Density kg/m^3	Pressure kPa	Temperature K
0	18.46	6.48E+01	9.09E+01	735.3
10	17.30	3.77E+01	4.68E+01	658.2
20	15.30	2.04E+01	2.22E+01	580.7
30	13.04	1.02E+01	9.50E+00	496.9
40	10.76	4.40E+00	3.45E+00	417.6
50	8.93	1.59E+00	1.05E+00	350.5
60	6.80	4.69E-01	2.32E-01	262.8
70	5.44	8.39E-02	3.64E-02	229.8
80	4.66	1.19E-02	4.43E-03	197.1
90	4.00	1.15E-03	3.68E-04	169.4
100	3.78	7.99E-05	2.63E-05	173.9
110	3.62	5.81E-06	1.73E-06	158.0
120	3.48	3.20E-07	9.74E-08	159.0
130	3.68	1.85E-08	6.21E-09	166.8
140	4.22	1.39E-09	5.84E-10	176.2
150	4.64	1.61E-10	9.41E-11	194.2

Table 5.3: Atmospheric Properties of Earth

Altitude km	Scale Height km	Density kg/m^3	Pressure kPa	Temperature K
0	10.20	1.225E+00	1.09E+00	288.1
10	7.66	4.135E-01	2.85E-01	223.3
20	6.31	8.891E-02	5.94E-02	216.6
30	6.50	1.841E-02	1.29E-02	226.5
40	6.86	3.996E-03	3.09E-03	250.3
50	8.14	1.027E-03	8.57E-04	270.6
60	8.02	3.097E-04	2.36E-04	247.0
70	7.14	8.283E-05	4.95E-05	219.6
80	6.33	1.846E-05	1.13E-05	198.6
90	5.62	3.416E-06	1.97E-06	186.9
100	5.57	5.604E-07	3.37E-07	195.1
110	5.69	9.708E-08	7.19E-08	240.0
120	8.38	2.222E-08	2.47E-08	360.0
130	11.71	8.152E-09	1.18E-08	469.3
140	14.86	3.831E-09	6.61E-09	559.6
150	17.70	2.076E-09	4.06E-09	634.4

Table 5.4: Atmospheric Properties of Mars

Altitude km	Scale Height km	Density kg/m^3	Pressure kPa	Temperature K
0	11.60	1.550E-02	6.49E-03	214.0
10	11.73	6.470E-03	2.59E-03	205.0
20	10.68	2.630E-03	9.66E-04	188.3
30	9.77	9.800E-04	3.35E-04	175.0
40	9.06	3.400E-04	1.08E-04	162.4
50	8.42	1.080E-04	3.22E-05	152.2
60	7.93	3.180E-05	8.96E-06	144.2
70	7.53	8.730E-06	2.38E-06	139.5
80	7.47	2.290E-06	6.20E-07	139.0
90	7.51	6.010E-07	1.63E-07	139.0
100	7.38	1.590E-07	4.32E-08	139.0
110	7.75	4.140E-07	1.21E-07	149.4
120	8.34	1.190E-08	3.74E-09	159.7
130	9.58	3.760E-09	1.26E-09	170.0
140	9.65	1.090E-09	5.31E-10	245.1
150	9.70	4.730E-11	2.76E-11	288.6

5.5 Aerothermal Modeling

The surface integrated heat load as well as the stagnation point heating are of critical importance to the feasibility of aero-assisted missions. To limit leading edge heating rates, geometries will tend to have relatively large leading edge radii. This necessary trade-off decreases aerodynamic performance.

5.5.1 CBAero

A software package developed at NASA Ames, Configuration Based Aerodynamics[122] (CBAero), quantifies the aerothermodynamic environment at the surface of the vehicle. The principle of CBAero is similar to this work: conceptual and preliminary design must use rapid, engineering level solutions in favor of computationally heavy CFD. It uses proven and understood analysis methods to determine aero-heating for arbitrary body shapes and is not limited in flight speed or free-stream condition. It has been validated for use with subsonic, supersonic, and hypersonic applications both at Earth and other planetary destinations.[123]

CBAero requires vehicle models to be input using a triangular surface grid (see Figure 3.2). The exterior of every waverider generated in this study was meshed into an unstructured triangular grid upon generation. This was chosen in order to facilitate aerodynamic panel codes, but the specifics were selected in order to allow the use of CBAero.

In order to determine the aero-heating environment, CBAero first assesses the inviscid surface flow field, and estimates the streamline patterns. It then determines whether the surface flowfield is laminar or turbulent based on the attachment distance of a given streamline. The user is allowed to specify a transition criteria of Re_θ/M. The local Reynold's number and the reference enthalpy method (similar to the reference temperature method discussed in Section 4.3) is used to estimate the

local skin friction. Then, using Reynold's analogy, the Stanton number is calculated:

$$St = \frac{c_f}{2} \tag{5.47}$$

The definition of the Stanton number can be used to develop an expression for the convective heat rate as a function of wall temperature:

$$\dot{q}_{\text{conv}} = St\rho_\infty c_P(T_w - T_\infty)v_\infty \tag{5.48}$$

Finally, assuming that the vehicle wall does not absorb any heat, the radiative heat rate is set equal to the convective, and can be solved for the wall temperature:

$$\dot{q}_{\text{conv}} = \dot{q}_{\text{rad}} = \sigma\epsilon T_{\text{wall}}^4 \tag{5.49}$$

where ϵ is the wall emissivity.

5.5.2 Waverider Validation

CBAero is a highly validated tool, however it has no documented use with hypersonic waveriders. The closest known analog is its use studying the HL-20 at hypersonic entry speeds.[122] As a relatively quick validation, the waveriders presented in Reference [124] were reproduced as best as possible using the osculating cone methodology discussed in Section 3.4. The geometries produced are not identical, because full dimensions were not provided, and because the method of blunting the leading edge is different. In this work, the waverider is given a constant circular leading edge over the full span of the vehicle. Vanmol instead allowed his leading edges to vary spanwise. For the reproduced waveriders, the constant value was chosen to be the leading edge radius at the nose of Vanmol's waveriders.

Vanmol used a set of analytic relations in order to analyze the aerodynamic

and aerothermal environment about his waveriders. Importantly, when he calculated heat transfer rates, similar to CBAero, he assumed that the wall temperature was such that the heat transfer losses by radiation equal the heat transfer from convection. Vanmol, however, capped the equilibrium wall temperature to be 1900 K, in line with estimates for material performance of carbon-carbon composites of the time. If a wall temperature of 1900 K was not sufficient to radiate all energy, then the structure was assumed to absorb the excess heat. CBAero does not assume a maximum radiative equilibrium temperature.

The results of the comparison are presented in Figures 5.8 through 5.23. Convective heat transfer and wall temperature are presented along the leading edge for Vanmol's waveriders (black data points) and the waverider reproductions solved in CBAero (blue data points). The stagnation points at each spanwise location are plotted for Vanmol. CBAero data points represent every value along the triangulated leading edge mesh. The blue data locations with the maximum heat transfer and wall temperature are the triangles which lie closest to the stagnation point, and likely contain the stagnation point. As mentioned, CBAero averages the expected heating value at each triangular node to provide a value for the whole triangle area. This will tend to lower the heating value at the stagnation points slightly.

The data matches particularly well along the centerline of the vehicles (normalized distance = 0, in each chart). This is a promising result, as this is where the geometry of the waveriders is most similar. As the spanwise location increases, both the convective heat transfer and the wall temperature differ more and more. They do however differ in the expected manner, given the geometry differences. Moving towards the edge of the vehicle, the waverider reproductions have constant leading edge radius, whereas Vanmol's waveriders have sharper and sharper leading edges. It would be expected that Vanmol's waverider would have higher heating and wall temperatures near the vehicle edges, and this is universally found.

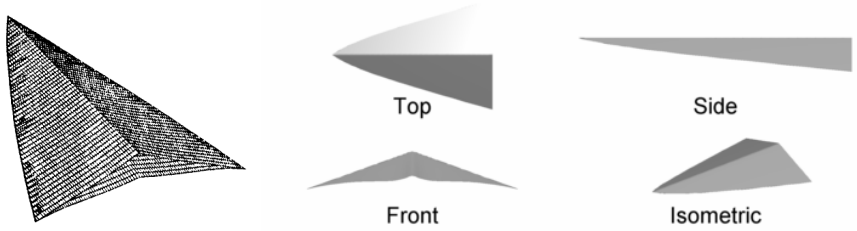

Figure 5.8: $M = 5$, Q = .2 atm waverider. Left image from Ref. [124]

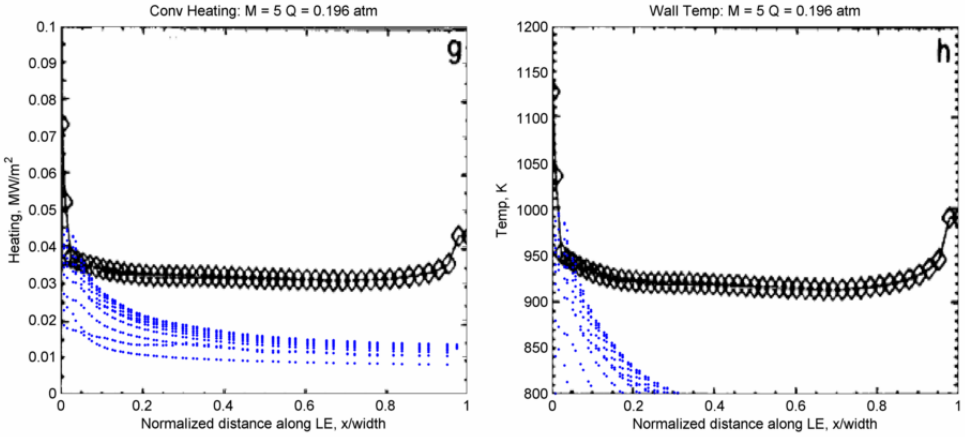

Figure 5.9: Comparison of CBAero and analytical model for $M = 5$, Q = .2 atm waverider. Background data from Ref. [124]

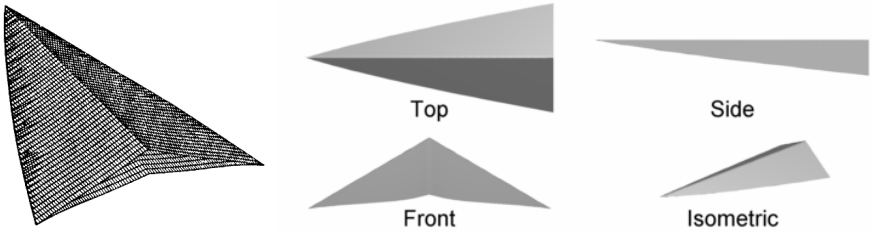

Figure 5.10: $M = 5$, Q = 1 atm waverider. Left image from Ref. [124]

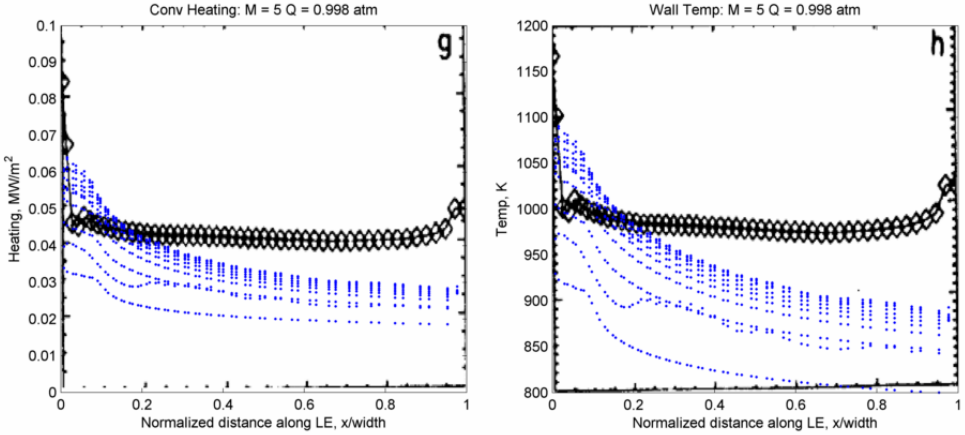

Figure 5.11: Comparison of CBAero and analytical model for $M = 5$, Q = 1 atm waverider. Background data from Ref. [124]

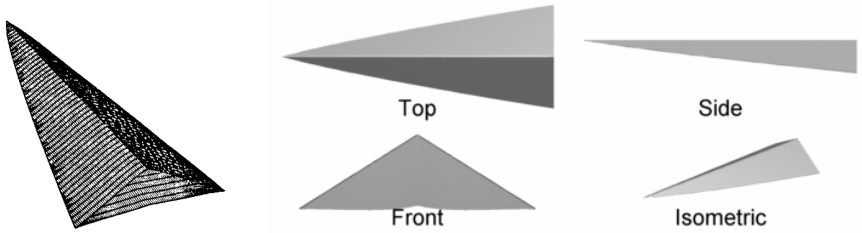

Figure 5.12: $M = 10$, Q = .2 atm waverider. Left image from Ref. [124]

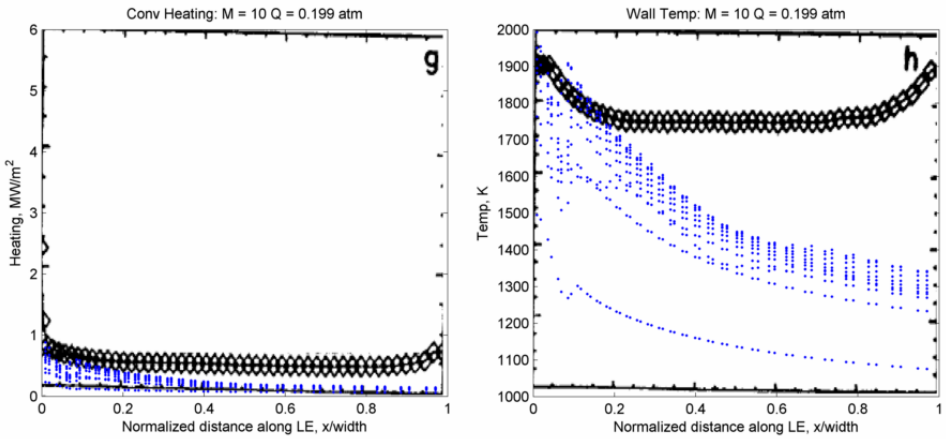

Figure 5.13: Comparison of CBAero and analytical model for $M = 10$, Q = .2 atm waverider. Background data from Ref. [124]

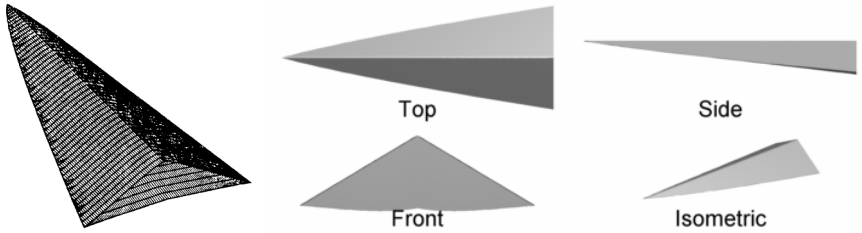

Figure 5.14: $M = 10$, Q = 1 atm waverider. Left image from Ref. [124]

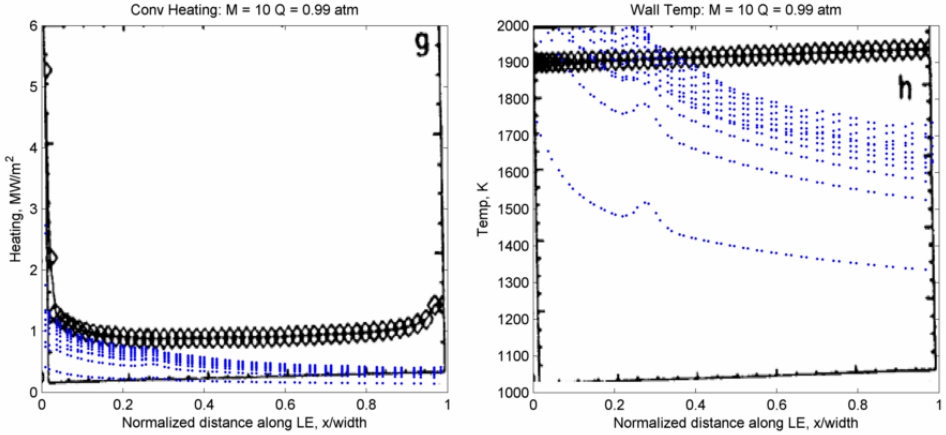

Figure 5.15: Comparison of CBAero and analytical model for $M = 10$, Q = 1 atm waverider. Background data from Ref. [124]

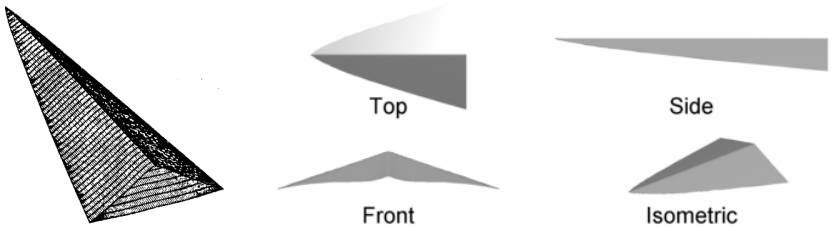

Figure 5.16: $M = 15$, Q = .2 atm waverider. Left image from Ref. [124]

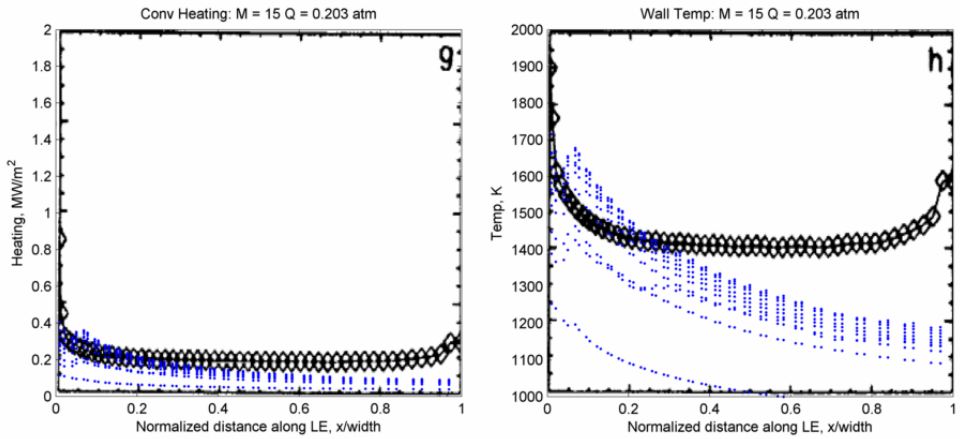

Figure 5.17: Comparison of CBAero and analytical model for $M = 15$, Q = .2 atm waverider. Background data from Ref. [124]

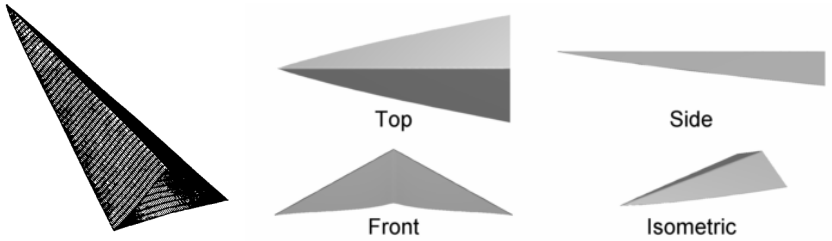

Figure 5.18: $M = 15$, Q = 1 atm waverider. Left image from Ref. [124]

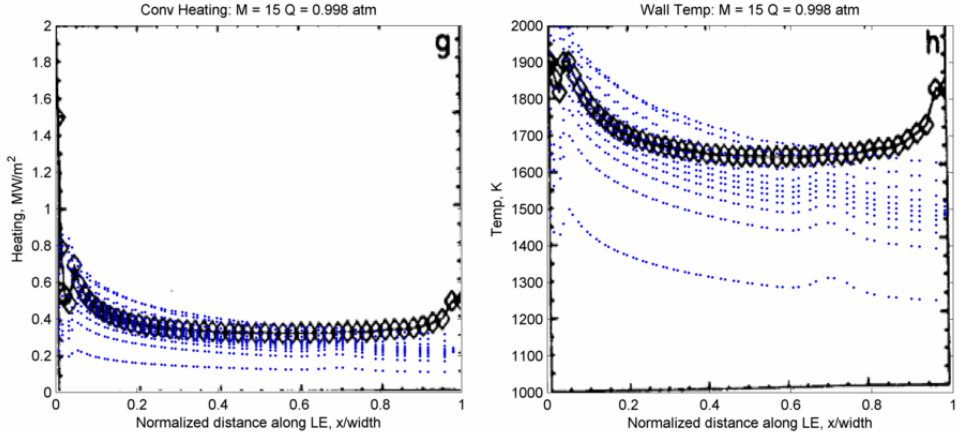

Figure 5.19: Comparison of CBAero and analytical model for $M = 15$, Q = 1 atm waverider. Background data from Ref. [124]

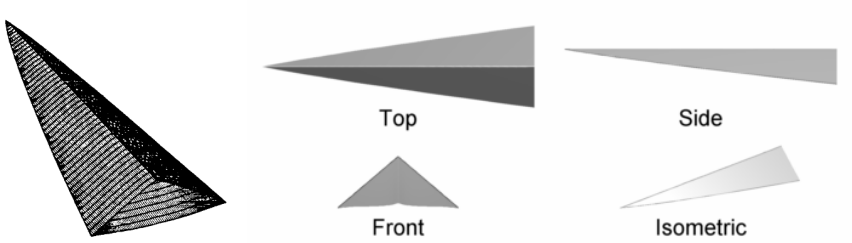

Figure 5.20: $M = 20$, Q = .2 atm waverider. Left image from Ref. [124]

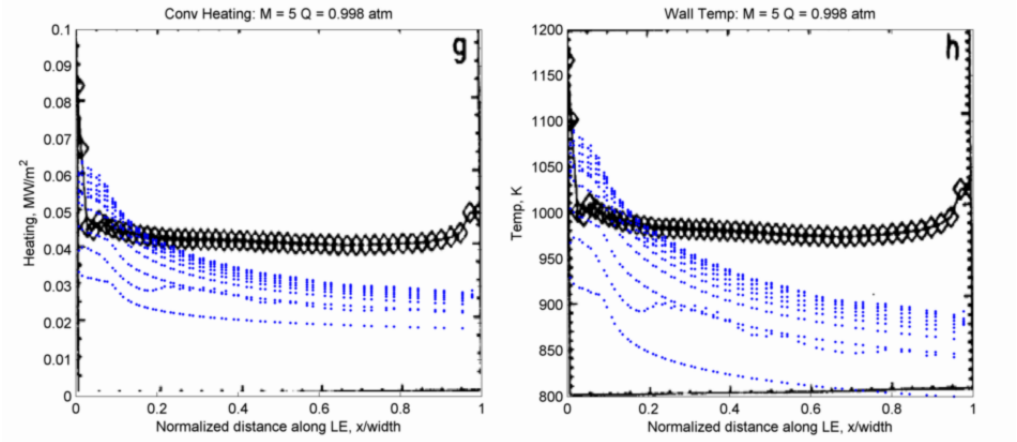

Figure 5.21: Comparison of CBAero and analytical model for $M = 20$, Q = .2 atm waverider. Background data from Ref. [124]

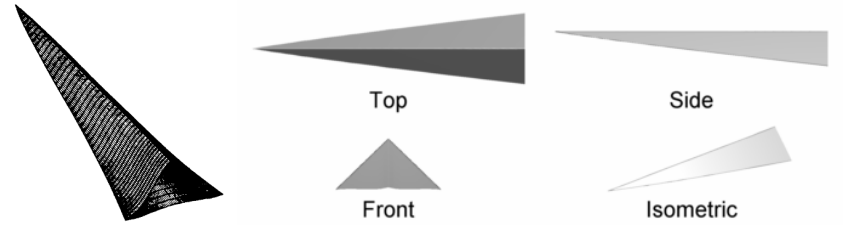

Figure 5.22: $M = 20$, Q = 1 atm waverider. Left image from Ref. [124]

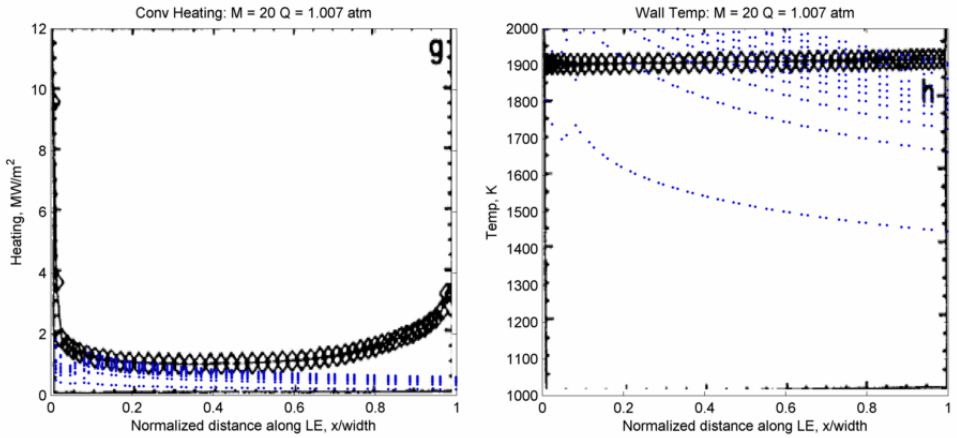

Figure 5.23: Comparison of CBAero and analytical model for $M = 20$, Q = 1 atm waverider. Background data from Ref. [124]

Further, given the damping of the stagnation point heating using CBAero, it would also be expected that the heating values would tend to be slightly lower than what Vanmol found when performing calculation at the exact stagnation points along the leading edge. This is also observed in many cases.

The largest data discrepancy occurs when Vanmol limits the wall temperature to 1900 K (see Figures 5.15 and 5.23). Again, CBAero does not manually limit the maximum radiative heat transfer, and for these cases, the wall temperatures do not match well, even at the waverider root.

5.6 Integration Method

A MATLAB built-in ordinary differential Equation solver, ODE23, is used for time integration of the equations of motion. ODE23 is an implementation of the Bogacki-Shampine[125] method. It uses a pair of third and second order Runge-Kutta solvers using variable time steps.

The equations of motion represent a set of ordinary differential equations of the form:

$$y'(t) = f(t, y(t)), \qquad t_0 < t < t_{\text{final}} \tag{5.50}$$

where $y(t_0)$ is a known initial condition. In specific to the trajectory problem, $y(t)$ is a vector containing the states of the spacecraft, and $y'(t)$ is a vector containing

the state variable derivatives:

$$y(t) = \begin{bmatrix} r_x(t) \\ r_y(t) \\ r_z(t) \\ v_x(t) \\ v_y(t) \\ v_z(t) \\ \alpha(t) \\ \phi(t) \end{bmatrix} \tag{5.51}$$

$$y'(t) = \begin{bmatrix} v_x(t) \\ v_y(t) \\ v_z(t) \\ a_x(t) \\ a_y(t) \\ a_z(t) \\ \dot{\alpha}(t) \\ \dot{\phi}(t) \end{bmatrix} \tag{5.52}$$

The Runge-Kutta formula of order s, approximates the function value at the next time step as:

$$\hat{y}(t + \Delta t) = y(t) + \Delta t \sum_{i=1}^{s} b_i k_i \tag{5.53}$$

$$k_i = f(t + \Delta t \sum_{j=1}^{i-1} a_{i,j}, y(t) + \Delta t \sum_{j=1}^{i-1} a_{i,j} k_j), \quad i = 2, ..., s \tag{5.54}$$

where b_i, and $a_{i,j}$ are constants specific to the method. In the case of the Bogacki-Shampine method, $a_{2,1} = \frac{1}{2}$, $a_{3,1} = 0$, $a_{3,2} = \frac{3}{4}$, $b_1 = \frac{2}{9}$, $b_2 = \frac{1}{3}$, and $b_3 = \frac{4}{9}$. Carrying

out the summations, the equations become:

$$k_1 = f(t, y(t)) \tag{5.55}$$

$$k_2 = f(t + \frac{1}{2}\Delta t, y(t) + \frac{1}{2}\Delta t k_1) \tag{5.56}$$

$$k_3 = f(t + \frac{3}{4}\Delta t, y(t) + \frac{3}{4}\Delta t k_2) \tag{5.57}$$

$$\hat{y}(t + \Delta t) = y(t) + \frac{2}{9}\Delta t k_1 + \frac{1}{3}\Delta t k_2 + \frac{4}{9}\Delta t k_3 \tag{5.58}$$

The Bogacki-Shampine method also includes a second order approximation to the solution in order to improve accuracy and refine the time step if necessary. The refinement uses the following equations:

$$k_4 = f(t + \Delta t, \hat{y}(t + \Delta t)) \tag{5.59}$$

$$y(t + \Delta t) = y_n + \frac{7}{24}\Delta t k_1 + \frac{1}{4}\Delta t k_2 + \frac{1}{3}\Delta t k_3 + \frac{1}{8}\Delta t k_4. \tag{5.60}$$

If the error between $\hat{y}(t + \Delta t)$ and $y(t + \Delta t)$ is too great, then the time step is decreased.

Note that the value of k_1, given by Equation 5.55 is simply the value of k_4 calculated at the previous timestep using Equation 5.59. The method therefore only requires three function evaluations per time step (equations 5.56, 5.57, and 5.59). Further, the values of $y(t)$ and $y'(t)$ is required only at the time step, t, in order to determine the value at the next time step, $t + \Delta t$.

The error tolerance determines the execution speed as well as the precision of the final answer. In order to select a suitable value, a trade study was performed. Four random initial conditions were chosen corresponding to an aero-gravity assist at Mars, an aero-capture at Mars, an aero-gravity assist at Earth and an aero-gravity assist at Venus. For completeness, the trajectories were also propagated

using ODE45, another popular ODE solver in MATLAB.

The relative tolerance was incrementally decreased from 10^{-1} to the minimum acceptable value in MATLAB, 10^{-13}. The final positions of the spacecraft, at atmospheric exit, were used as the means for comparison. For each solver, the trajectory propagated using a tolerance of 10^{-13} was considered to be the accepted value. The results are presented in Figure 5.24.

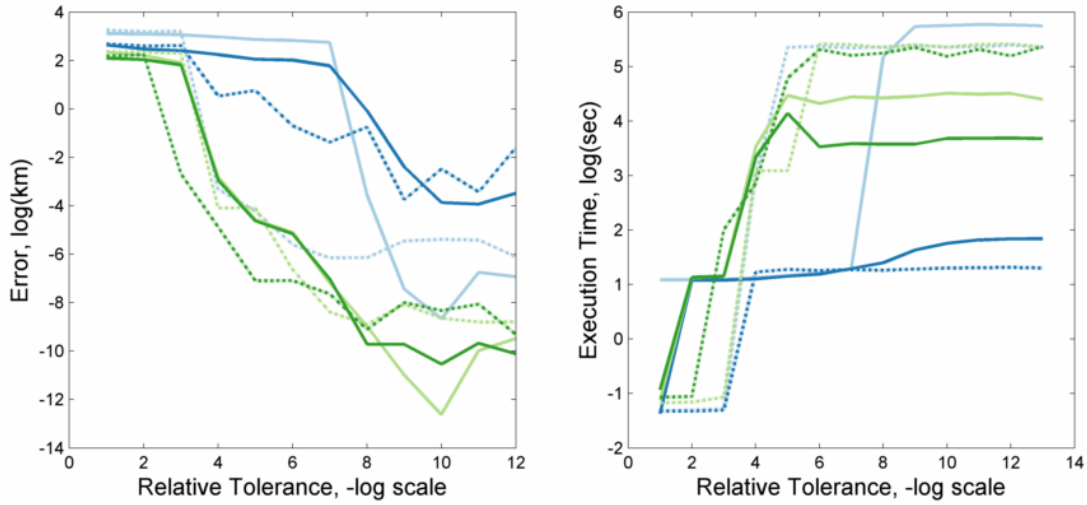

Figure 5.24: Comparison of trajectories propagated with ODE45 and ODE23. Dashed lines are for ODE45 and solid lines are for ODE23.

For most tolerance values, and for all four example trajectories, ODE23 outperformed ODE45 in terms of convergence. A maximum value for the relative tolerance was found to be roughly 10^{-8}. Any smaller, and the values seemed to show good convergence. ODE23 and ODE45 did not have a consistent relationship in terms of computational speed. In two of the cases, ODE23 was faster, and ODE45 was faster for the other two trajectories. As expected, good convergence came at the expense of execution time. Once the solution was within a kilometer of the final value, however, there was much less penalty to decreasing the tolerance.

By analyzing the data in these charts, ODE23 was selected as the integration method, using a relative tolerance of 10^{-10}.

Chapter 6

Waverider Shape Studies

A pair of studies were conducted in order to investigate the waverider models presented. In particular, a thorough analysis is performed of the method created for generating asymmetric starbodies. In these studies, there is no mission under review or trajectory propagated. A fixed design condition is presented, and then a number of waveriders are created. Then, the aerodynamic models presented in Chapter 4 and the aerothermodynamics code discussed in Section 5.5 are used to calculate relevant metrics of comparing different waverider shapes. This chapter discusses the results of these studies.

6.1 Starbody Asymmetry

First, the design space of asymmetric waveriders is investigated. Recall that there are three input parameters which determine the asymmetry of the resulting waverider shape: D, e, and α_0. See Section 3.3 for a description of these variables.

As e and D increase in magnitude, the length of the tines tend to increase as well. As each approach unity, the length can increase dramatically, as the connection point between the shock on the underside and the nearest on the topside moves towards infinity. The result is a flying wing-type vehicle.

As α_0 increases in magnitude, the vertical symmetry of the starbody breaks,

Table 6.1: Test conditions for asymmetric starbody study

n	3, 4, 5, 6
e	-1:.01:1
D	-1:.01:1
α_0	-.62, 0, .62
R	.01 m
w	9 m
Atmosphere	Mars
M	18
h	20 km

not in terms of tine placement, but in terms of shock strength. Therefore, extremes in this value do not tend to affect metrics such as volume and surface area as greatly as D and e. On the other hand, α_0 very directly changes the pressure distribution over the surface of the waverider and creates a huge range of aerodynamic performance as characterized by lift-to-drag ratio.

In order to quantify these trends, a numerical analysis was performed by creating a large database of waveriders. A flight condition was chosen and then waveriders were created for all unique combinations of e and D for three different values of α_0. The test conditions are summarized in Table 6.1. In order to keep the waveriders similar, all vehicles must be scaled to have a common length, volume or width. In this case, each was limited to a maximum diameter of extent of 9 meters. This means that each waverider would just fit into a 9 meter diameter launch fairing.

The waveriders were compared using lift-to drag ratio and static margin. Appendix A contains additional plots showing the range in the following vehicle shape metrics: length, volume, surface area, and volumetric efficiency.

Figures 6.1 - 6.12 show the lift-to-drag results and Figures 6.13 - 6.24 show the stability results. Each plot is displayed in a group of three corresponding to the number of tines and the three different values of α_0. All figures are contour plots showing the values over the $\leq$ 40000 waveriders generated for each unique

combination of e, D, and α_0.

Note that there are discontinuities in the plots due to the shape generation and variable definition method. In many cases, for a given value of e, D can only vary slightly and still create a feasible waverider design. For example, see Figure 6.6. For $e >$ -.5, the tines can be placed in a full down configuration, all the way through a full up configuration and still generate a feasible design. On the other hand, for $e <$ -.5, only a small rotation of the tines is possible by way of D, therefore $D =$ -1 and $D = +1$ map to similar rotations so as to be feasible for all values of D. This results in a skewing of the data from right to left (easily seen in the blue segment of the figure). Similar skewing is seen in other charts such as Figure 6.8 and Figure 6.9.

The centerpoint of each one of the lower left hand figures corresponds to the only values possible with a symmetric starbody. Introducing these three asymmetry parameters clearly allows for a hugely increased design space.

The lift-to-drag ratio values vary greatly with all three asymmetry variables. The most significant effect is in response to the effective angle-of-attack parameter, α_0. This is seen by comparing the relative magnitudes of the color scales in Figures 6.1 - 6.12. As α_0 increases in magnitude, so does the magnitude of the lift-to-drag ratio. For example, a 4-tined starbody with $\alpha_0 = \pm.62$ is capable of producing lift to drag ratios up to 4.5 or 5, whereas, with $\alpha_0 = 0$, the maximum magnitude of L/D is roughly 1.5. Note that in this context, the sign of the the lift-to-drag ratio is irrelevant, as the waverider can simply be inverted to produce the opposite aerodynamic behavior.

The relationship between D, e and lift-to-drag ratio is complex and must be considered on a case by case basis. In some instances (such as Figure 6.4) as eccentricity and tine distribution increase in magnitude, the lift-to-drag ratio decreases. In other cases (such as Figure 6.8), the exact opposite is true and the

maximum magnitudes of lift-to-drag are found in the corners of the chart.

The number of tines does not tend to have a qualitative effect on the aerodynamic performance of asymmetric starbodies. For example, by inspection of each chart corresponding to $\alpha_0 = \pm.62$, (Figures 6.1, 6.4, 6.7, and 6.10) it is seen that there are certain qualitative features in common, regardless of the number of tines. They are certainly not identical, but many of the regions of high L/D and low L/D are shared.

The most consistent and pronounced effect on static margin is seen by varying the value of α_0. Vehicle asymmetry tends to force the vehicle to be closer to neutrally stable. The magnitude of static margin for waveriders with α_0 is typically one to two orders of magnitude larger than the values found for vehicles with $\alpha_0 = \pm.62$. This is an important result. Breaking the symmetry of a starbody waverider results in a much more stable vehicle configuration, even in lateral pitch stability. Developing vehicle shapes which have greater aerodynamic performance appears to co-beneficial to improved stability behavior.

Except for the case when $n = 3$, there is little consistent correlation between e, D and static margin. In some cases, extreme values of e and D force the static margin closer to 0. In other cases, it causes the magnitude to increase both in the stable and unstable direction. Overall trends are difficult to determine, and unfortunately, each must be addressed on a case by case basis.

6.2 Asymmetric Starbody and Osculating Cone Comparisons

In this section, two different types of waveriders are compared: "osculating cone" waveriders and "starbody" waveriders. Each vehicle type has different benefits and drawbacks which will be qualitatively and quantitatively analyzed.

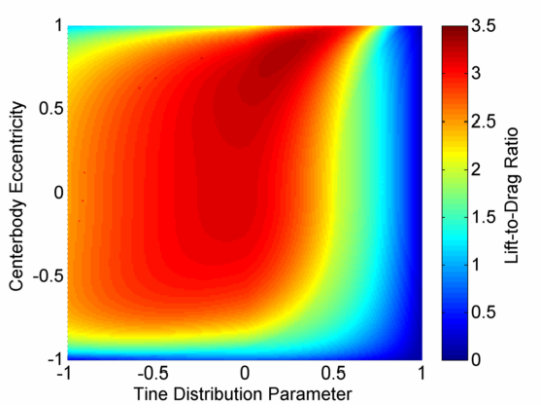

Figure 6.1: Range of lift-to-drag ratio for a 3-tined starbody with $\alpha_0 = 0.62$. $M = 18$, $h = 20$ km, in the Martian atmosphere.

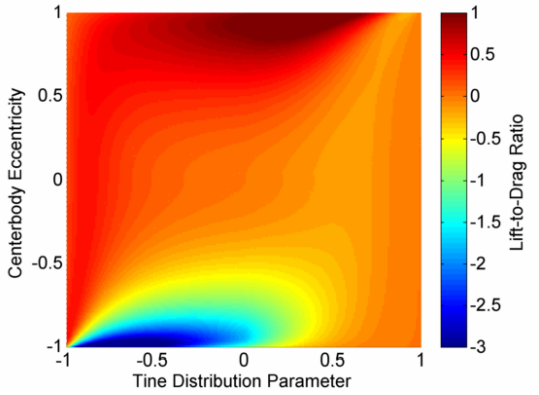

Figure 6.2: Range of lift-to-drag ratio for a 3-tined starbody with $\alpha_0 = 0$. $M = 18$, $h = 20$ km, in the Martian atmosphere.

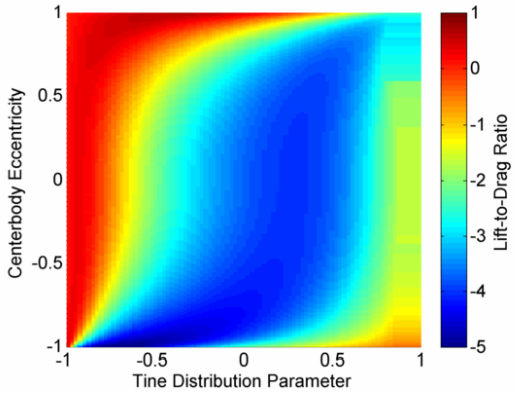

Figure 6.3: Range of lift-to-drag ratio for a 3-tined starbody with $\alpha_0 = -0.62$. $M = 18$, $h = 20$ km, in the Martian atmosphere.

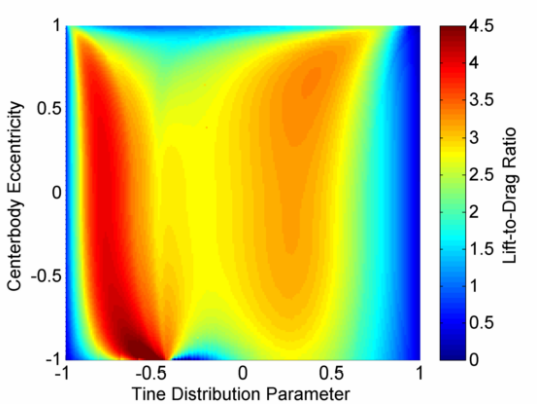

Figure 6.4: Range of lift-to-drag ratio for a 4-tined starbody with $\alpha_0 = 0.62$. $M = 18$, $h = 20$ km, in the Martian atmosphere.

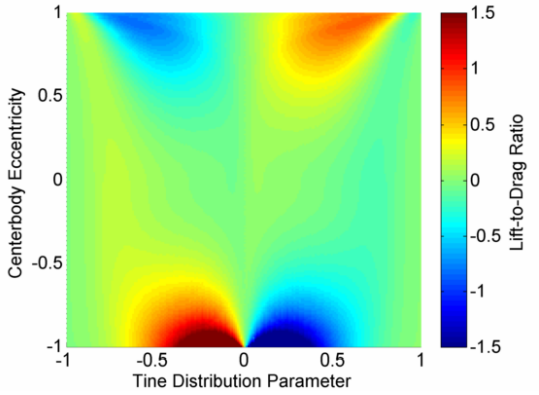

Figure 6.5: Range of lift-to-drag ratio for a 4-tined starbody with $\alpha_0 = 0$. $M = 18$, $h = 20$ km, in the Martian atmosphere.

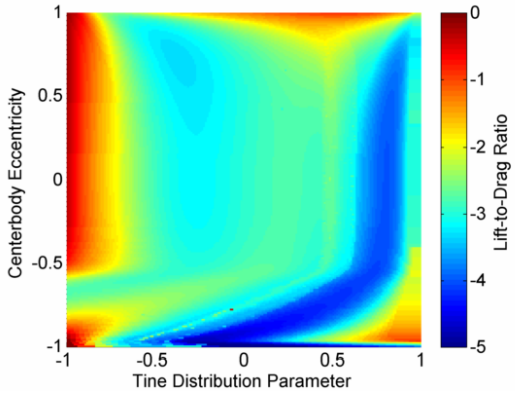

Figure 6.6: Range of lift-to-drag ratio for a 4-tined starbody with $\alpha_0 = -0.62$. $M = 18$, $h = 20$ km, in the Martian atmosphere.

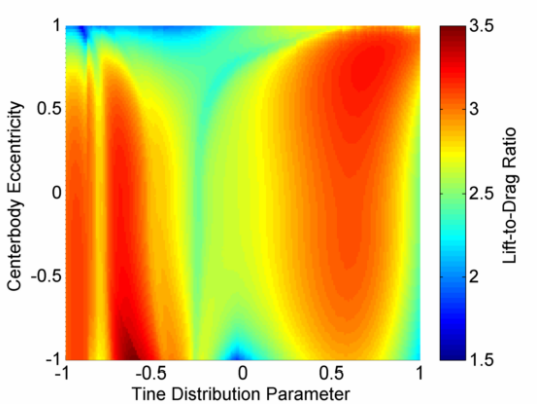

Figure 6.7: Range of lift-to-drag ratio for a 5-tined starbody with $\alpha_0 = 0.62$. $M = 18$, $h = 20$ km, in the Martian atmosphere.

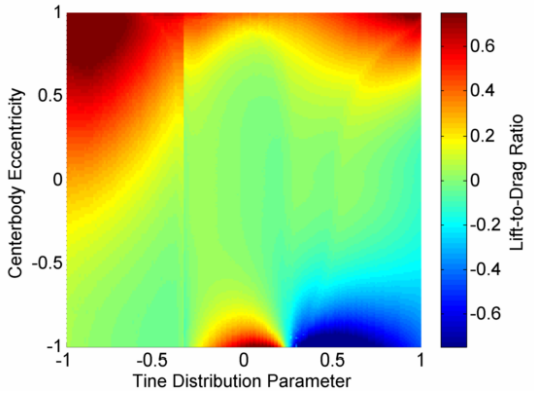

Figure 6.8: Range of lift-to-drag ratio for a 5-tined starbody with $\alpha_0 = 0$. $M = 18$, $h = 20$ km, in the Martian atmosphere.

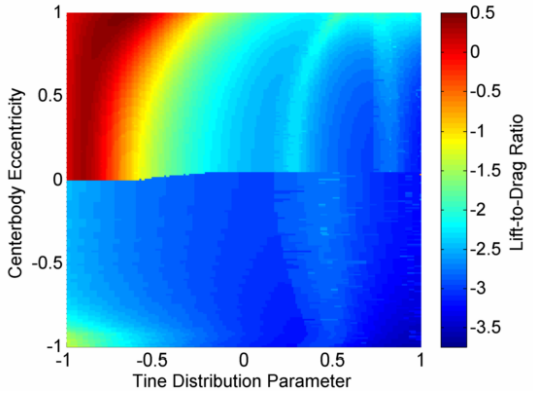

Figure 6.9: Range of lift-to-drag ratio for a 5-tined starbody with $\alpha_0 = -0.62$. $M = 18$, $h = 20$ km, in the Martian atmosphere.

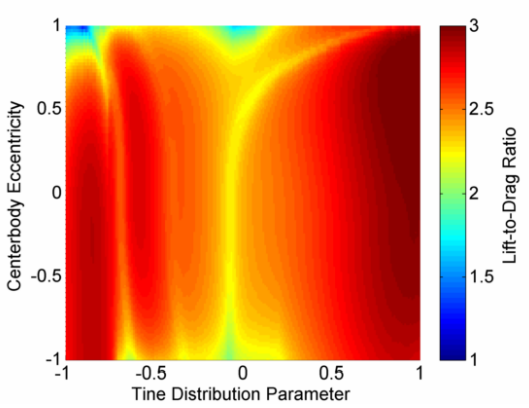

Figure 6.10: Range of lift-to-drag ratio for a 6-tined starbody with $\alpha_0 = 0.62$. $M = 18$, $h = 20$ km, in the Martian atmosphere.

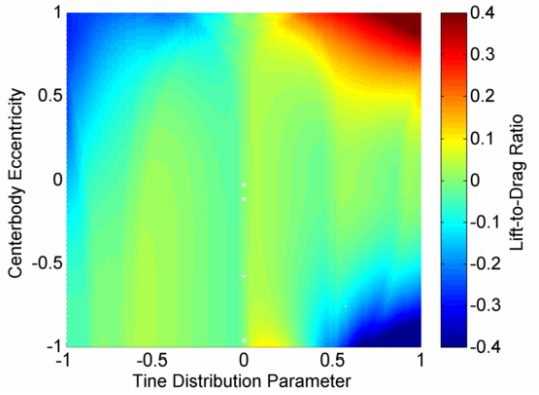

Figure 6.11: Range of lift-to-drag ratio for a 6-tined starbody with $\alpha_0 = 0$. $M = 18$, $h = 20$ km, in the Martian atmosphere.

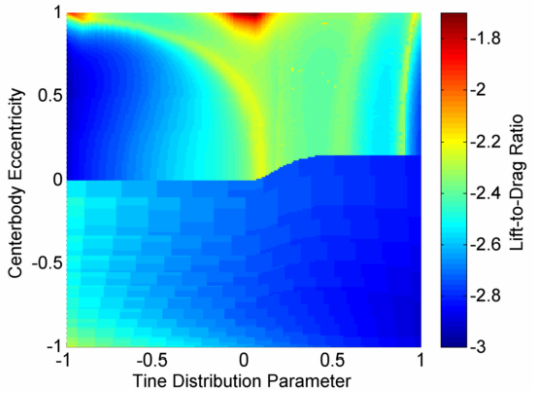

Figure 6.12: Range of lift-to-drag ratio for a 6-tined starbody with $\alpha_0 = -0.62$. $M = 18$, $h = 20$ km, in the Martian atmosphere.

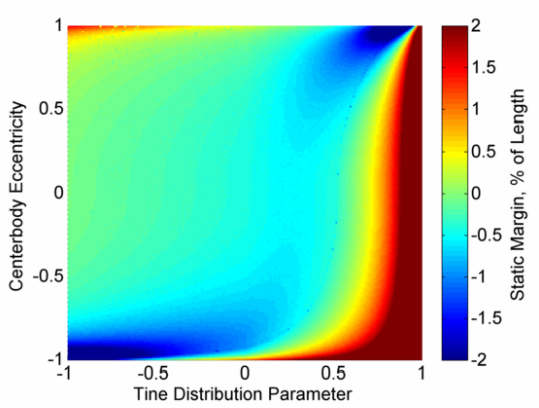

Figure 6.13: Range of static margin for a 3-tined starbody with $\alpha_0 = 0.62$. $M = 18$, $h = 20$ km, in the Martian atmosphere.

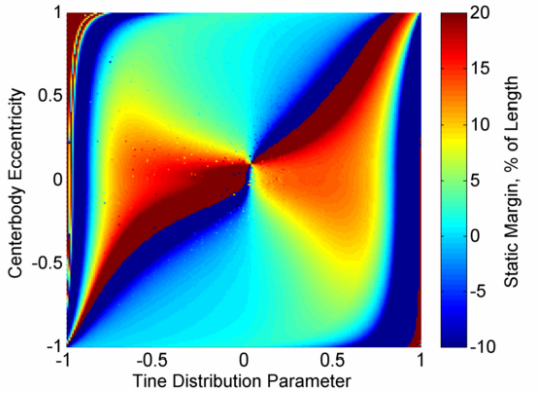

Figure 6.14: Range of static margin for a 3-tined starbody with $\alpha_0 = 0$. $M = 18$, $h = 20$ km, in the Martian atmosphere.

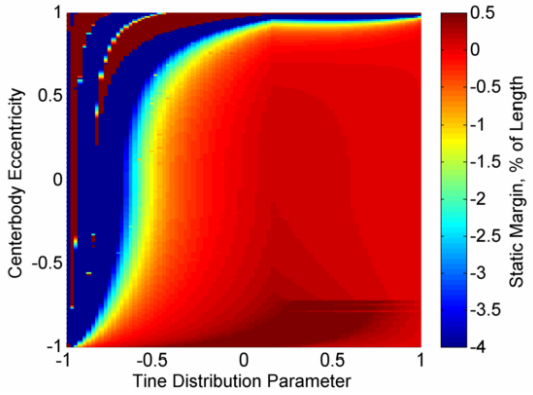

Figure 6.15: Range of static margin for a 3-tined starbody with $\alpha_0 = -0.62$. $M = 18$, $h = 20$ km, in the Martian atmosphere.

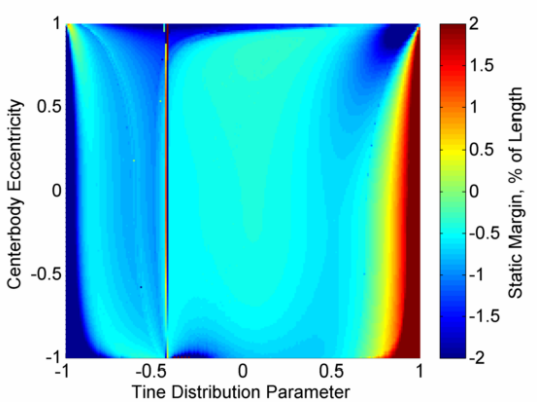

Figure 6.16: Range of static margin for a 4-tined starbody with $\alpha_0 = 0.62$. $M = 18$, $h = 20$ km, in the Martian atmosphere.

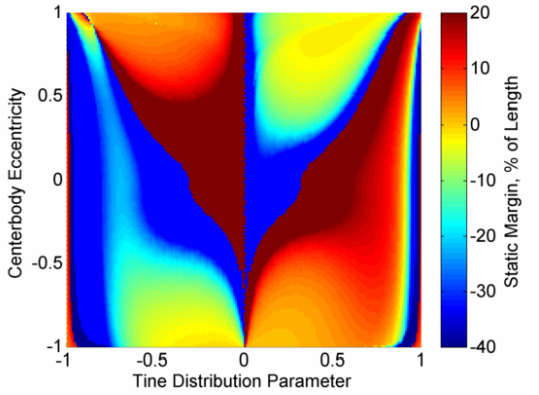

Figure 6.17: Range of static margin for a 4-tined starbody with $\alpha_0 = 0$. $M = 18$, $h = 20$ km, in the Martian atmosphere.

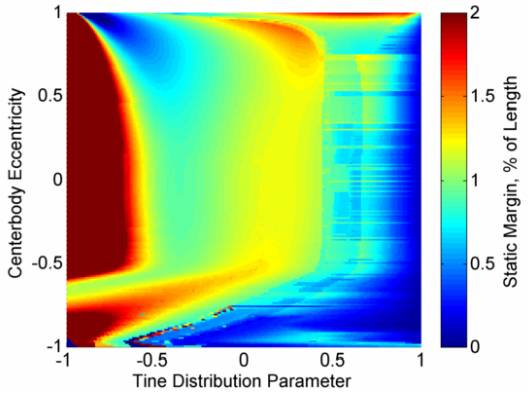

Figure 6.18: Range of static margin for a 4-tined starbody with $\alpha_0 = -0.62$. $M = 18$, $h = 20$ km, in the Martian atmosphere.

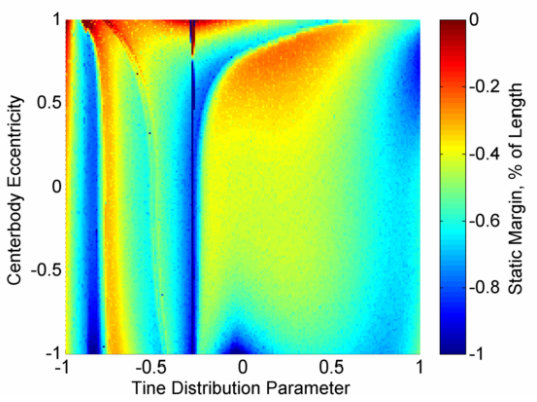

Figure 6.19: Range of static margin for a 5-tined starbody with $\alpha_0 = 0.62$. $M = 18$, $h = 20$ km, in the Martian atmosphere.

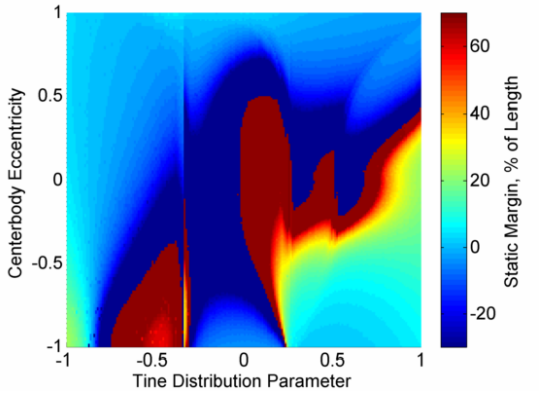

Figure 6.20: Range of static margin for a 5-tined starbody with $\alpha_0 = 0$. $M = 18$, $h = 20$ km, in the Martian atmosphere.

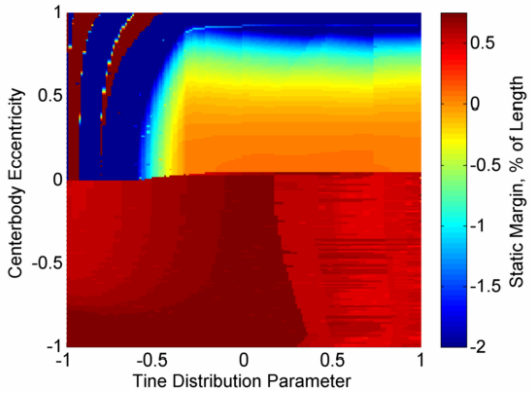

Figure 6.21: Range of static margin for a 5-tined starbody with $\alpha_0 = -0.62$. $M = 18$, $h = 20$ km, in the Martian atmosphere.

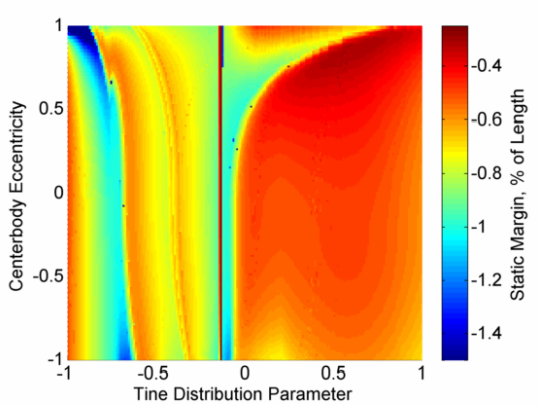

Figure 6.22: Range of static margin for a 6-tined starbody with $\alpha_0 = 0.62$. $M = 18$, $h = 20$ km, in the Martian atmosphere.

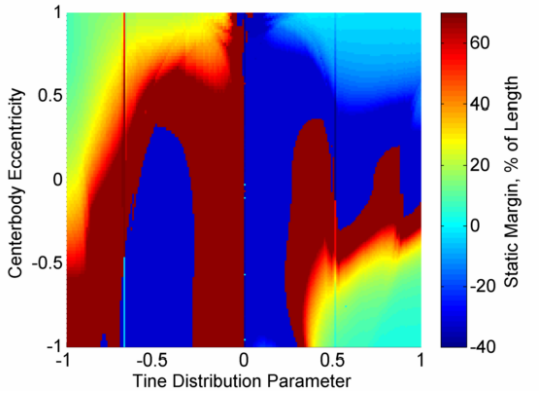

Figure 6.23: Range of static margin for a 6-tined starbody with $\alpha_0 = 0$. $M = 18$, $h = 20$ km, in the Martian atmosphere.

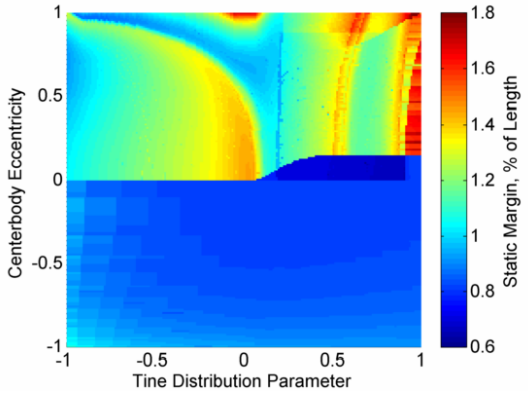

Figure 6.24: Range of static margin for a 6-tined starbody with $\alpha_0 = -0.62$. $M = 18$, $h = 20$ km, in the Martian atmosphere.

6.2.1 Optimization Methods

A genetic algorithm was used to optimize over the shape generating variables. Multi-objective methodology allows for comparison between designs with different strengths and weaknesses. Four objectives are considered which evaluate waverider performance over a range of important areas. These are summarized in Equations 6.1 - 6.4, written in the standard form as a minimization problem:

$$f_1 = -L/D \tag{6.1}$$

$$f_2 = \dot{q}_{\max} \tag{6.2}$$

$$f_3 = -\eta_V \tag{6.3}$$

$$f_4 = -R \tag{6.4}$$

The first objective function quantifies the aerodynamic performance of the vehicle. As the lift-to-drag ratio increases, the losses due to drag are reduced. While a higher ratio is not necessarily most efficient for aero-capture type missions, aero-gravity assist and aero-assisted plane change would certainly benefit. Aero-heating is certainly a crucial design limitation for any re-entry spacecraft. The heating rate over the entire vehicle is calculated, but only the maximum local heat rate is used as an objective. The surface integrated heat load is also an important design metric, but it was found to be correlated closely enough with the maximum heat rate (inversely) that it was unnecessary to include as an objective. In order to be a useful spacecraft re-entry forebody, a waverider shape must have sufficient volume in order to accommodate payload. The volumetric efficiency is used as a measure of the usable volume compared to surface area, as per Equation 6.5:

$$\eta_V = \frac{(36\pi)^{1/3} V^{2/3}}{S} \tag{6.5}$$

This parameter is scaled so that the maximum possible ratio is 1 (a sphere). The more slender a vehicle is, the lower this ratio will be, and the less volume it will have for payload. Further, as the vehicle slenderness increases, the structural bending will likely increase, requiring greater structural mass.

Both aero-heating and volumetric efficiency are positively correlated with each other and the final objective value, R. It is important to include all three nonetheless, as they each compete with aerodynamic performance differently. For example, an osculating cone waverider with a lift-to-drag ratio of 5 may have greater bluntness and a lower max heat rate than one with L/D = 4, if the power law equations were tuned accordingly. On the other hand, the three metrics are positively correlated, and increasing L/D decreases R and $\dot{q}_{max}$, if the power law equations are held constant. An accurate pareto curve is desired between all competing objective pairs, and this can only be obtained with inclusion into the genetic algorithm. The fourth objective function is not necessarily an isolated objective itself, however it is a primary goal of this study to quantify the effect of bluntness on waverider aerodynamics. While this final objective function increases the complexity of the genetic algorithm from an optimization standpoint, it will allow the generation of a unique and complete pareto curve.

Finally, the optimization routine includes a number of manually enforced constraints. The constraint shown in Equation 6.6 ensures that the vehicle is not too wide. While the vehicle length is used as an independent variable in the design process, the resulting width is a dependent variable. For the purposes of this study, it is constrained to a value which would optimistically fit inside of a launch vehicle payload fairing, $w_{\max} = 8$ meters. In the case of starbody waveriders, the width is defined as the smallest radius cylinder in which the vehicle could fit. Equations 6.7 and 6.8 constrain the leading edge bluntness to the desired range. It should be noted that there are a number of implicit constraints used to enforce realistic waverider

shapes which are not discussed here as they are not quantifiable. For example, certain combinations of geometry inputs could result in a starbody shape in which adjacent shock planes do not intersect, or adjacent osculating cone streamlines cross. Discussion of these feasibility scenarios were discussed in Chapter 3.

$$g_1 = w - w_{\max} \;=\; w - 8\,\text{m} \;\leq\; 0 \tag{6.6}$$

$$g_2 = R - R_{\max} \;=\; R - .2\,\text{m} \;\leq\; 0 \tag{6.7}$$

$$g_3 = R_{\min} - R \;=\; .001\,\text{m} - R \;\leq\; 0 \tag{6.8}$$

6.2.2 Design Conditions

The parameters used in this study are presented in Table 6.2. This includes the free-stream conditions, the vehicle design constants and the optimization design variables. Free-stream conditions are based on the exponential model presented in the previous chapter of Earth's atmosphere.

Table 6.2: Flight Conditions and Design Constants

h	25 km, 50 km, 75 km	
M	30, 60, 90	
L	10 m	
R	.001 m : .150 m	
$w_{\max}$	8 m	
θ	4° : 30°	Base vehicle half angle
$y_{0,u}$	.001 m : 2 m	Width of flat Section of osc. cone upper surface
A_u	-.001 : -1	Coefficient in osc. cone upper surface power law
n_u	1.001 : 10	Exponent in osc. cone upper surface power law
$y_{0,l}$	.001 m : 2 m	Width of flat Section of osc. cone shock shape
A_l	.001 : 1	Coefficient in osc. cone shock shape power law
n_l	1.001 : 10	Exponent in osc. cone shock shape power law
D	-1 : 1	Starbody tine distribution parameter
e	-1 : 1	Starbody centerbody eccentricity
α_0	-1 : 1	Starbody effective angle-of-attack

For each of the 9 unique flight conditions, an 800 generation genetic algorithm

was completed. Each generation consisted of a population of 800, meaning that the study comprised over 5.7 million unique waverider designs. The results are presented in the following sections.

6.2.3 Optimal Shapes

A selection of the most optimal waveriders found are discussed here. The first set of waveriders (Figures 6.25 and 6.26) were found to generate the greatest amount of lift relative to the drag that they create. Both the osculating cone waverider (Vehicle A) and the starbody waverider (Vehicle B) have almost negligible leading edge bluntness and are very slender in the vertical direction. Both of these qualities serve to minimize the strength of the forebody shock, thus yielding less pressure on the body. Further, the slenderness reduces the frontal area over which pressure drag acts. Vehicle A is also extremely slender in the lateral direction, reducing both frontal area and overall surface area. Conversely, Vehicle B is just shy of the maximum allowable width. This may not be intuitive, because the wider the vehicle, the greater skin friction it experiences over such large surface area. The design methodology of starbody waveriders precludes slenderness in both the lateral and

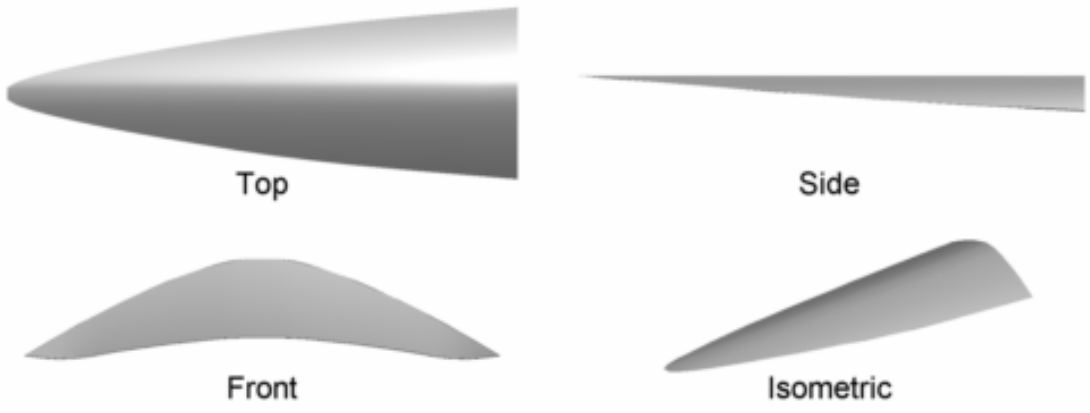

Figure 6.25: Vehicle A. Highest L/D osculating cone waverider for M = 30, Alt = 25 km. L/D = 7.31, R = .001 m, η_V = 29.4%, $\dot{q}_{max}$ = 27.3 KW/cm^2, $\dot{q}_{net}$ = 7.69 KW, SM = -8%

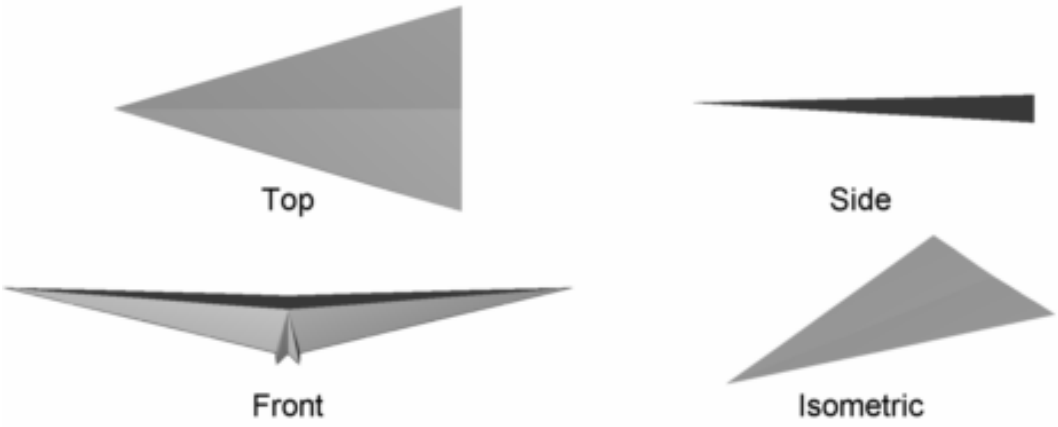

Figure 6.26: Vehicle B. Highest L/D starbody waverider for $M = 90$, Alt = 25 km. L/D = 6.33, $R = .001$ m, $\eta_V = 25.9\%$, $\dot{q}_{max} = 3.80$ MW/cm^2, $\dot{q}_{net} = 143$ KW, SM = -2%

vertical direction. This is due to the need to place leading edges at the intersection of adjacent shock planes. If the tines bunch on the underside, as is the case with Vehicle B, the intersection line moves further outward. Width does give greater lifting surface area, which benefits the lift-to-drag ratio. The trade-off is not entirely beneficial though, and Vehicle A has a greater value of L/D than Vehicle B. This trend is seen throughout the comparison study, and osculating cone waveriders tend to have better aerodynamic efficiency as measured by the lift-to-drag ratio.

The next set of waverider images (Figures 6.27 and 6.28) depict the osculating cone waverider (Vehicle C) and starbody waverider (Vehicle D) which have the minimum heating rates for their respective flight conditions. This metric is very dependent on flight speed and free-stream gas properties, so the magnitude of $\dot{q}_{\max}$ for Vehicles C and D relative to each other is not relevant. As expected, both vehicles have a leading edge radius as close to the maximum constraint as would be expected in a genetic algorithm. If a gradient based method was run with each of these waveriders as a starting point, and maximum local heating rate was the sole objective function, the design would almost certainly reach $R = .2$ m.

Vehicle C is one of the wider osculating cone waveriders returned by the op-

timization, and in general, width increased as the max heating decreased. When considering osculating cone waveriders, the relationship between R and $\dot{q}_{\max}$ is complicated by the lateral bluntness of the nose. This is determined by the power law equations, not just the choice of R. For example, even if Vehicle A had a larger value of R, there would still be very little effective lateral bluntness, as the power law equations dictated that the nose be relatively sharp in the horizontal direction.

Figures 6.29 and 6.30 depict waveriders with the best static longitudinal stability performance for their flight conditions. Recall that the center of gravity was assumed to be at the trim location, as no control surfaces are yet modeled. While the size and position of the control surfaces (or other control devices) could certainly allow the CG to be placed away from the trim location, keeping all waveriders trimmed allows consistent comparison. Pitch stability will be discussed further in Section 6.2.5, however note that in most cases, no longitudinally stable vehicles were found. The waveriders presented here were simply the least unstable.

The osculating cone waverider, Vehicle E, notably has a similar shape to Vehicle C, which has a worse static margin. The primary difference between the two is their design flight condition. Each were amongst the least statically unstable

Figure 6.27: Vehicle C. Minimum maximum heat rate osculating cone waverider for $M = 90$, Alt = 75 km. L/D = 1.76, $R = .198$ m, $\eta_V = 66.8\%$, $\dot{q}_{max} = 6.51$ KW/cm^2, $\dot{q}_{net} = 46.0$ KW, SM = -2.8%

Figure 6.28: Vehicle D. Minimum maximum heat rate starbody waverider for M = 60, Alt = 25 km. L/D = .122, R = .199 m, η_V = 68.8%, $\dot{q}_{max}$ = 73.3 KW/cm^2, $\dot{q}_{net}$ = 221.7 KW, SM = -29.5%

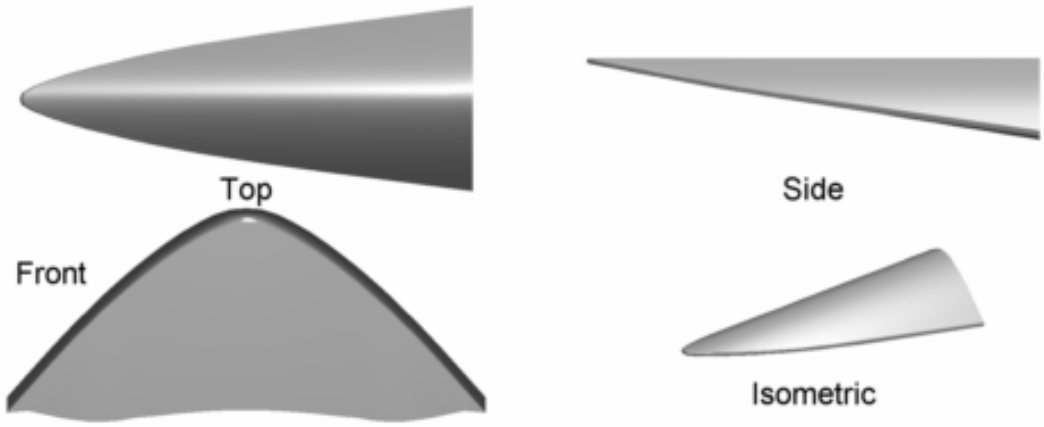

Figure 6.29: Vehicle E. Maximum static margin osculating cone waverider for M = 30, Alt = 50 km. L/D = 3.16, R = .065 m, η_V = 52.6%, $\dot{q}_{max}$ = 1.64 KW/cm^2, $\dot{q}_{net}$ = 1.8 KW, SM = -1.09%

designs for their respective flight speeds and altitudes, however the increased speed and altitude for which Vehicle C was designed causes its trimmed CG to be further from its neutral point.

Vehicle F has a combination of vehicle design parameters which allow its trimmed CG to be closest to pitch stability. The most noticeable geometric feature is its width. In this case, the waverider has much sharper leading edges, and is more vertically slender, rendering it slightly less volumetrically efficient. Inter-

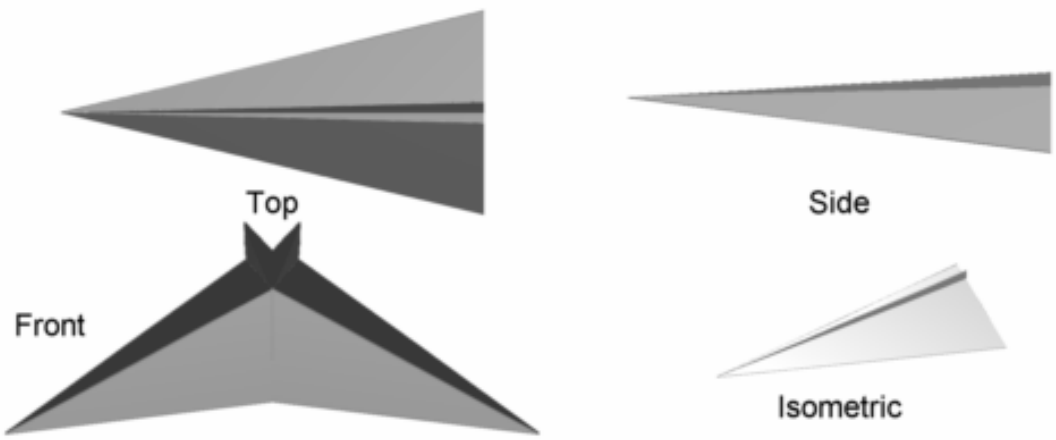

Figure 6.30: Vehicle F. Maximum static margin starbody waverider for $M = 30$, Alt = 75 km. L/D = 2.29, $R = .014$ m, $\eta_V = 41.8\%$, $\dot{q}_{max} = .732$ KW/cm^2, $\dot{q}_{net} = .178$ KW, $SM = -1.29\%$

estingly, the vehicle has a relatively high L/D ratio (for the given flight condition), even though the smaller tines are located on the underside, as opposed to Vehicle B. The effective angle-of-attack is positive in both cases, allowing the pressure to be greater on the underside regardless of the location of the tines.

6.2.4 Pareto Trade-offs

The competitive nature of the objective functions is seen in Figures 6.31 through 6.36 with each marker representing a waverider design. The utility of including all three objective functions is seen by quickly noticing the wide variation in the shapes of each pareto curve. Note that the legend shown in the first two plots applies to all remaining results in this section.

The first set of curves pertain to the effect of bluntness on osculating cone waveriders (Figure 6.31) and starbodies (Figure 6.32). Unfortunately, the trade-off lines are concave, indicating that the slope is steepest in the undesirable sections of the objective space. For example, the magnitude of $\partial(\text{L/D})/\partial R$ is the greatest where L/D is high. Near the maximum values of lift-to-drag, even small changes in R have a drastic impact on aerodynamic performance. Even slight blunting of

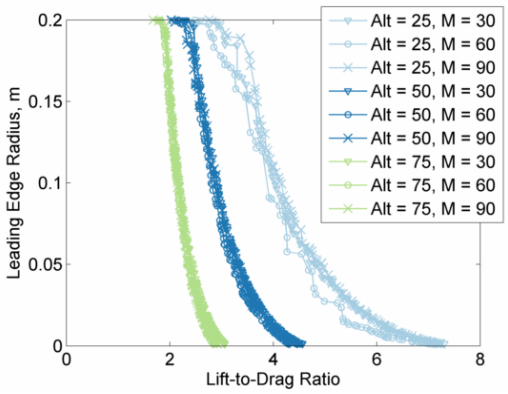

Figure 6.31: Osculating cone waverider trade-off for lift-to-drag ratio with leading edge bluntness.

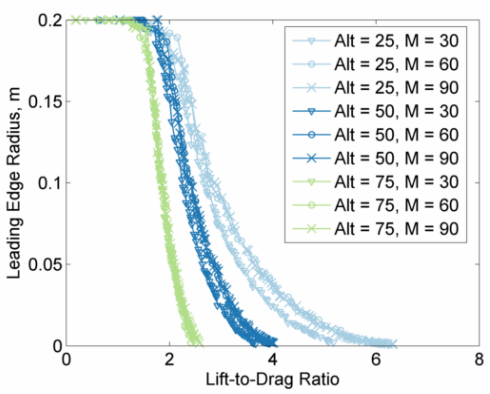

Figure 6.32: Starbody waverider trade-off for lift-to-drag ratio with leading edge bluntness.

leading edges can drastically reduce the vehicle's effectiveness in generating lift and limiting drag. This is in contrast to a convex pareto curve, in which modest values of both objectives are feasible.

While the shape of the curves is analogous, optimized osculating cone waveriders are capable of ∼10% L/D improvements over starbodies. In both Figures 6.31 and 6.32, the effect of Mach number independence is demonstrated. For a given flight altitude, accelerating the vehicle through the three sets of Mach numbers tested has little effect on optimized performance. This result has been demonstrated in many other studies of waveriders, however it is beneficial to reproduce it here.

Altitude effects are considerable when looking at L/D potential. This is observable when designing optimized aero-assist trajectories. Even without constraining the cruise flight conditions, trajectory optimization routines will often narrow in on a small range of altitudes. In this region of the atmosphere, the free-stream air is dense enough to sustain a sufficiently high lift-to-drag ratio, without being so dense that the magnitude of drag force decelerates the vehicle too rapidly.

The relationship between volumetric efficiency and lift-to-drag ratio is much closer to fully convex. Figures 6.33 and 6.34 show the trends for osculating cone waveriders and starbodies, respectively. Increasing the leading edge radius improves

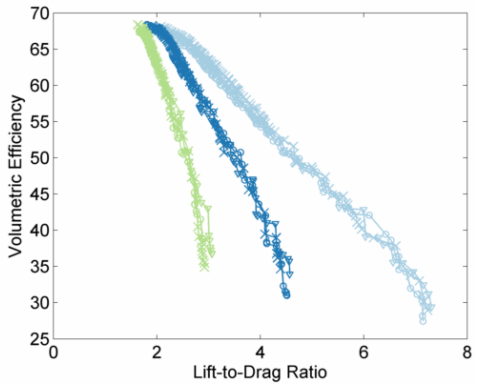

Figure 6.33: Osculating cone waverider trade-off for lift-to-drag ratio with volumetric efficiency.

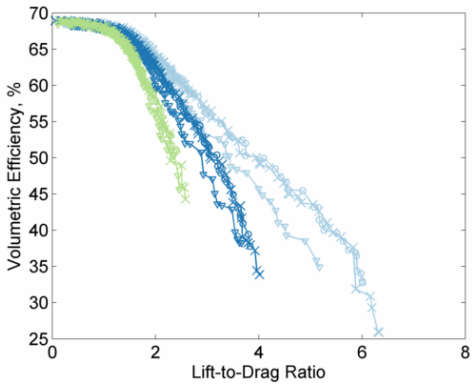

Figure 6.34: Starbody waverider trade-off for lift-to-drag ratio with volumetric efficiency.

the volumetric efficiency, but reduces the lift-to-drag ratio. Further, a high lift-to-drag ratio requires slenderness, in at least the vertical direction. Vertical slenderness reduces the interior volume, but does not dramatically affect the overall surface area.

Once again, the Mach number has only limited effect on the trade-off curves. The $M = 30$, Alt = 25 km line of the starbody optimization appears to be the only exception. There is no clear physical explanation for this, therefore it is assumed to be the result of a minorly stalled genetic algorithm. Re-running this flight condition would likely generate waveriders which match the other Alt = 25 km pareto curves.

One interesting result regarding volumetric efficiency is the similar magnitudes between the two waverider models. The increased slenderness of osculating cone waveriders suggested that they might have less volume relative to their surface areas. This is not the case however, and removes one potential benefit of starbodies. This does not suggest that the osculating cone waveriders in this study have comparable dimensional volumes, but that they could be scaled up with similar performance. Future study could use vehicle volume as a constant rather than vehicle length to make the needed comparison.

The effect of flight Mach number on waverider design is seen in the next set of pareto curves. These show the lift-to-drag ratio vs. maximum heating rate (see

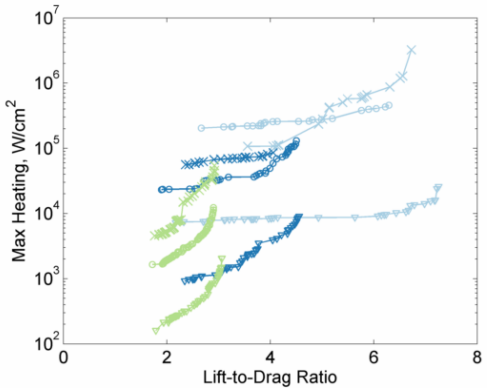

Figure 6.35: Osculating cone waverider trade-off for lift-to-drag ratio with maximum local heat rate.

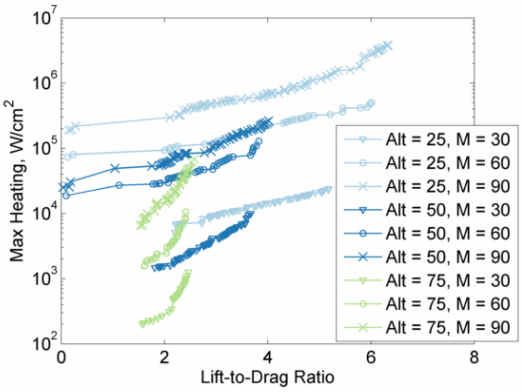

Figure 6.36: Starbody waverider trade-off for lift-to-drag ratio with maximum local heat rate.

Figures 6.35 and 6.36). Mach number independence does not occur with heating rate, and this presents a significant problem for aero-assist technology. Note that the pareto curves shown here are less full, due to the challenges of scaling the heat rate objective function (Equation 6.2). While volumetric efficiency will always be a value between 0% and 100%, and L/D is unlikely to exceed 10, the range of maximum heat rate is much less orderly. Optimization routines do not perform well when the objective functions have dissimilar magnitudes, and can result in pareto curves with grouping and gaps which Figures 6.35 and 6.36 show.

In terms of heating rate, there is little difference between the two waverider models. This is not entirely unexpected; the maximum heating rate occurs at the stagnation point of the vehicle's nose, and is primarily a function of the leading edge radius. Note that while it appears that there is a lesser gap between the $M = 30$ and $M = 60$ curves and the $M = 60$ and $M = 90$ curves, this is a by-product of the logarithmic scale of the heating axis. If plotted on an equal axis, the effect is reversed. The maximum heating rate rises exponentially with the flight Mach number.

Finally, Figures 6.37 and 6.38 are not pareto-curves, but show the positive correlation between lift-to-drag ratio and the surface integrated heat load. Blunt-

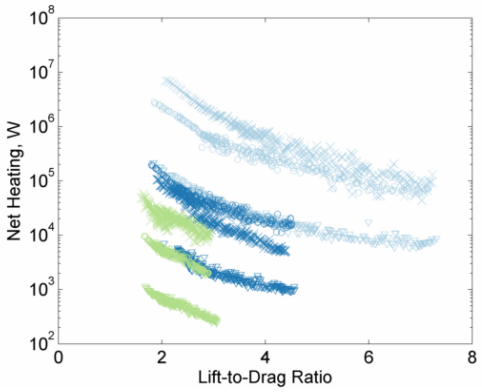

Figure 6.37: Osculating cone waverider trade-off for lift-to-drag ratio with surface integrated heat rate.

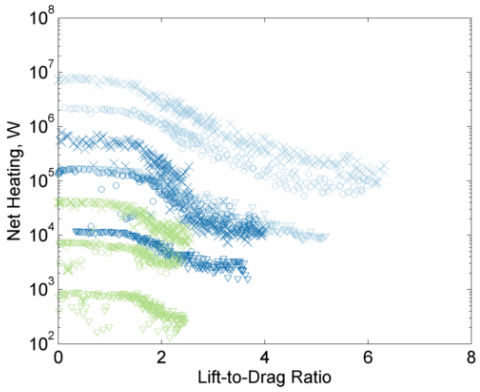

Figure 6.38: Starbody waverider trade-off for lift-to-drag ratio with surface integrated heat rate.

ness weakens the flowfield at the leading edge, but raises the temperature over the remaining vehicle. Relative to each other, the behavior of each trendline is similar to the maximum local heat rate, but they are inversely related to the aerodynamic performance.

6.2.5 Stability Optimized Waveriders

The stability of waverider designs is an extremely vital subject of study, and is considered here. The most basic feature of a vehicle's stability behavior is its static stability profile. Each design's static stability is considered in all 3 primary directions. All results are plotted against the volumetric efficiency, which was found to have the strongest correlation of the four objective functions.

Figures 6.39 and 6.40 show the relative degree of pitch instability of each waverider model. A positive value is desired, as it indicates that the CG has been placed forward of the neutral point. This would indicate that the vehicle could fly straight and level without needing any control surfaces to trim the aircraft, and any pitch disturbances would be damped out. Unfortunately, almost no such designs were found in this study. This is not to say that such designs do not exist, but they do not appear to be co-optimal with any of the objective functions used. Future

study could use a positive static margin as a constraint.

Starbody waveriders appear to have static margins slightly closer to stable, except at very high volumetric efficiencies. At high η_V, starbodies are near symmetric, with very large leading edge radii. Both of these negatively affect pitch stability, as predicted in Section 6.1. Unexpectedly, both the flight altitude and speed were crucially important in determining the static longitudinal stability. As altitude increased, or speed decreased, the vehicle's trimmed centers of gravity move further and further aft from their neutral points.

Next, directional stability is considered. If the waverider experiences a disturbance causing a slight sideslip, it is desirable that the vehicle naturally tend toward yawing to neutralize the disturbance. This means that a positive value is desired for $c_{n,\beta}$. A disturbance resulting in a positive sideslip equates to a negative yaw angle, therefore a positive yawing moment is required to return to a yaw angle of zero.

Figures 6.41 and 6.42 are plots of the waverider directional stability. The starbody designs and osculating cone designs have very different patterns. As starbodies increase in volumetric efficiency, they are better able to maintain a yaw heading. A more volumetric starbody is less vertically slender, and the design process dictates

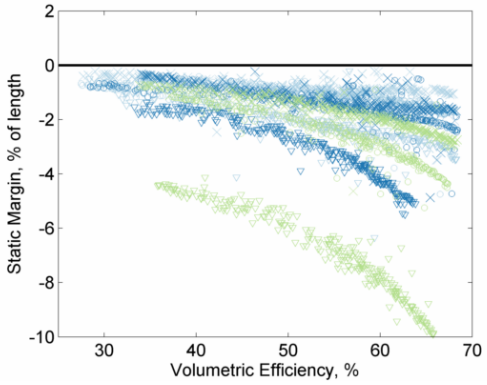

Figure 6.39: Static margin for osculating cone waveriders. Black line represents stability threshold. Positive values are desired.

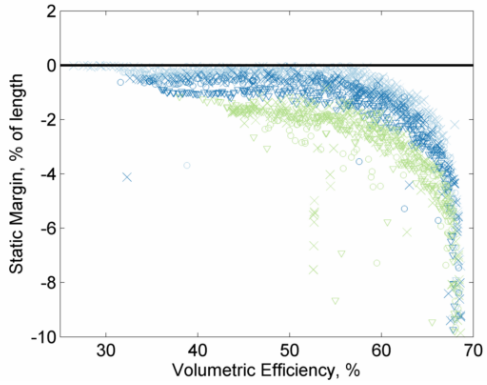

Figure 6.40: Static margin for starbody waveriders. Black line represents stability threshold. Positive values are desired.

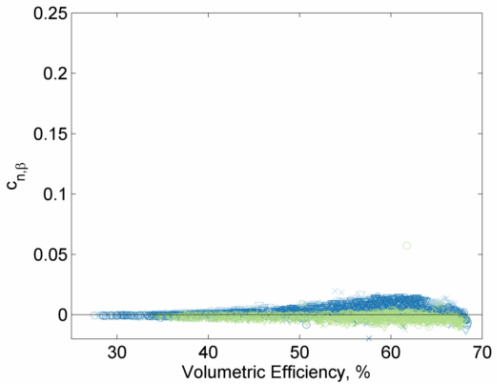

Figure 6.41: Directional static stability derivative for osculating cone waveriders. Black line represents stability threshold. Positive values desired.

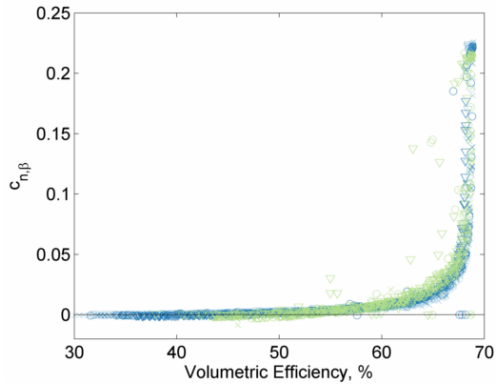

Figure 6.42: Directional static stability derivative for starbody waveriders. Black line represents stability threshold. Positive values desired.

that it is therefore closer to vertically symmetric (see Figure 6.28). This provides large surface area on the lateral sides of the vehicle with which to act as an effective rudder. Osculating cone waveriders do not have similar geometric features and the range of waverider behavior increases with η_V. Once again, design altitude and flight speed play a key role, and helps to determine where in the spread a given waverider design might fall.

Finally, the static stability of each waverider model in roll is analyzed using $c_{l,\beta}$. When an aircraft receives a positive sideslip disturbance, the result is an unequal free-stream condition on either side of the vehicle. This tends to create a rolling moment, named the dihedral effect. A stable vehicle will respond with a negative rolling moment in order to return the vehicle to zero sideslip. An unstable configuration would have a positive rolling moment, and this would exacerbate the sideslip disturbance.

The two waverider models in question have starkly different performance, and starbodies are seen to be far superior. In Figure 6.43, it is seen that almost all osculating cone waveriders found in this study are statically unstable in this mode. Further, as the vehicles became less slender, the behavior diverges even more. While

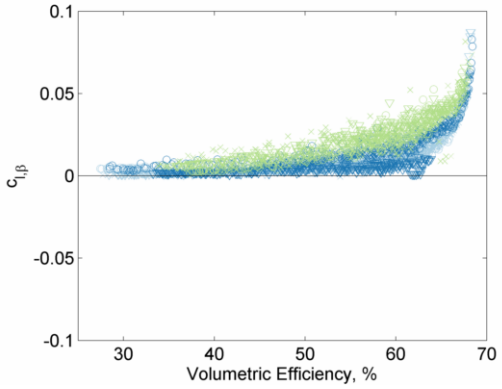

Figure 6.43: Roll static stability derivative for osculating cone waveriders. Black line represents stability threshold. Negative values are desired.

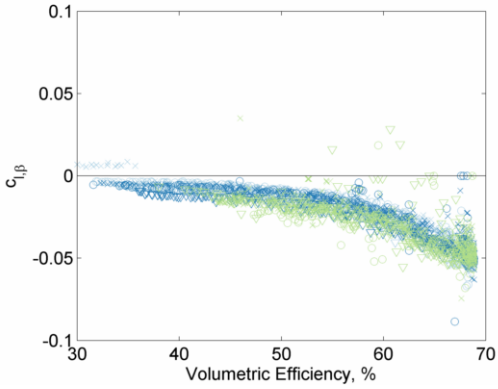

Figure 6.44: Roll static stability derivative for starbody waveriders. Black line represents stability threshold. Negative values are desired.

high-lift osculating cone waveriders tend to have effective dihedral due to the design methodology (see Figure 6.25), they can have effective anhedral as they become more oblate (see Figure 6.29). Further, in the thin atmosphere of high altitude flight, these waveriders perform even worse.

Conversely, the overwhelming majority of starbody waveriders perform admirably in static roll stability (see Figure 6.44). This behavior is traced to the additional lifting surfaces that they have around the circumference of the body. Vertically oriented caret-wing sections of the vehicle generate the majority of the lift. The lateral caret-wing sections, however, provide the majority of the restoring roll force in this stability mode. The larger the non-lifting caret-wing sections are, the more restorative moment they are capable of generating, as is the case with high η_V designs.

Chapter 7

Aero-Capture Design

7.1 Pure Mars Aero-Capture

Traditionally designed aero-capture maneuvers, using blunt capsules with limited lifting capability, are high risk, and require extremely precise control of vehicles operating at the very limit of their design margins. Performing an aero-capture with a lower drag, lift-generating body can reduce fuel requirements when used as an alternative to using propulsion.[74] Whereas the standard aero-capture sheds excess hyperbolic velocity in a quick periapsis fly-by, a vehicle of the type proposed would use lift to augment gravitational force, allowing it to remain in the atmosphere for a longer period of time, thereby decreasing the rate of energy dissipation through drag. The resulting lower heating rates and lower structural loads compared to those of a non-lifting trajectory can ease the requirements on both the thermal protection and structural systems.[126]

While the tools developed for this investigation could easily be applied to any reasonable aero-capture target, Mars was used as the destination planet due to the high availability of blunt body aero-capture studies.[97] The exponential profile of the Martian atmosphere described in Section 5.4.2 was used for free-stream properties.

7.1.1 Mission Profile

The objective of an aero-capture is to dissipate orbital energy, facilitating entry from a hyperbolic orbit into a final, closed orbit of a desired semi-major axis. In this study, two initial conditions were considered, one corresponding to a fast transfer orbit from Earth and a second corresponding to a more gradual Earth to Mars transfer. The former scenario results in relatively high entry velocity, while the latter scenario results in a lower entry velocity and energy. The details of these initial conditions are given in Table 7.1. Values matching those in Refs. 97 and 127 were selected for ease of comparison.

Table 7.1: Initial Conditions

	High Energy Initial Orbit	Low Energy Initial Orbit
r_a	< 0	< 0
ϵ	20 km^2/s^2	12 km^2/s^2
v_∞	6.32 km/s	4.89 km/s
v_{entry}	$\sim$ 8 km/s	$\sim$ 7 km/s
γ_{entry}	$\sim 10^\circ$	9°

Table 7.2 contains the details of the target and final orbits. The former takes the vehicle from the edge of the atmosphere to apoapsis where an impulsive rocket burn circularizes into the final orbit.

Table 7.2: Post Maneuver Conditions

	Target Orbit	Final Orbit
h_a	400 km	400 km
h_p	$<$ 125 km	400 km
ϵ	$\sim$(-5 km^2/s^2)	-5.64 km^2/s^2
e	$0 < e < 1$	0

7.1.2 Monte Carlo and Optimization

The design space of vehicle shape and trajectory optimization is often highly nonlinear, therefore finding globally optimal solutions is extremely difficult. Even

if globally optimal solutions were not achieved, it is still possible to analyze trends in locally optimal solutions. For this study, a large number of randomized initial inputs were uniformly distributed within the design space (see Table 7.3). The altitude based control system described in Section 5.2.1 was used. Asymmetric starbody waveriders were used as the shape model.

Table 7.3: Constraints

	Min	Max
n	3	6
D	-1	1
e	-1	1
γ_{entry}	-16°	-8°
$h_{-\alpha}$	$h_{+\alpha}$	55 km
$h_{+\alpha}$	0 km	$h_{-\alpha}$
$\alpha+$	0°	8°
$\alpha-$	-8°	0°
ϵ_{ascent}	-5.5 km^2/s^2	-3 km^2/s^2

At each initial set of inputs, a gradient based optimization method was used to find the nearest local solution. The overall scheme was therefore a combination of Monte Carlo simulation and gradient based methods. The design space consisted of nine inputs: three geometry and six trajectory variables (n varies, but is limited to one integer value whenever the optimization routine is called). In addition to the five control system variables, the trajectory simulation required an initial flight path angle, γ_{entry}. This parameter served as a means of varying the penetration into the atmosphere. Aerodynamic forces, and the direction of the lift vector during the initial descent affected the actual path flown, however γ_{entry} served to create the nominal path.

Each design was assessed with the objective function defined in Equation 7.1, written as a minimization problem:

$$f = \frac{-\left(t_{\text{exit}} - t_{\text{entry}}\right)}{\left|\epsilon_{\text{final}} - \epsilon_{\text{target}}\right|} \tag{7.1}$$

The optimization routine minimized the objective function for each initial condition, returning a local optimum. This function reaches a minimum as the denominator approached zero and as the magnitude of the time difference increased. The inclusion of the denominator was intended to ensure that exit occurred along the target orbit. Again, the target orbit was designed to take the vehicle to apoapsis at 400 km. If the final energy, ϵ_{final}, was far from the target energy, ϵ_{target}, the aero-capture maneuver did not succeed in reaching the final apoapsis, therefore the design variables were modified to adjust.

If it is assumed that the total dissipated energy is constant, as necessitated by the choice of denominator of the objective function, then the numerator can serve to increase the overall time of flight. The purpose of this is to favor lifting trajectories over flight paths usable with blunt bodies. It should be noted that as the time spent in the atmosphere increases, without the total energy fluctuating, the average dissipation rate decreases. However, the derivative of the energy was not included; therefore, this objective function did not have a bias towards a specific type of dissipation path.

7.1.3 Results

The Monte Carlo simulation was run with 4000 different initial inputs. With the use of a gradient based optimizer, not all of these returned optimal solutions. Almost three quarters, or 2931 of the cases did result in a locally optimal solution, further, 2020 resulted in a target orbit within 1% of the target energy. The other 911 cases may have been locally optimal, however insufficient energy dissipation took place during the atmospheric flight and therefore the target orbit was under shot. The results of the following sections represent the 2020 feasible cases as the remaining trajectories were filtered.

7.1.3.1 Trajectory Types

The chosen control system model allowed for the generation of a variety of flight paths. Each can be categorized into one of three categories: altitude hold, skipping, or single skip. Three example trajectories of each type are presented in Figure 7.1.

Altitude hold trajectories (Figure 7.1a) consist of a dive to a specific altitude, followed by level flight until sufficient energy has been dissipated. The altitude at which the glide occurs is dependent on the starbody's value of L/D. The higher the ratio, the higher the altitude at which the glide can occur, as the increase in c_L overcomes the lower free-stream density (and thus dynamic pressure). No altitude

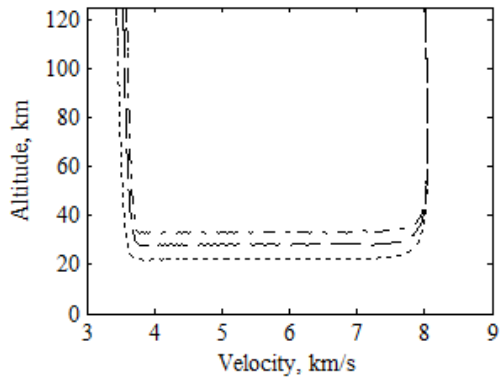

(a) Altitude Hold Trajectories

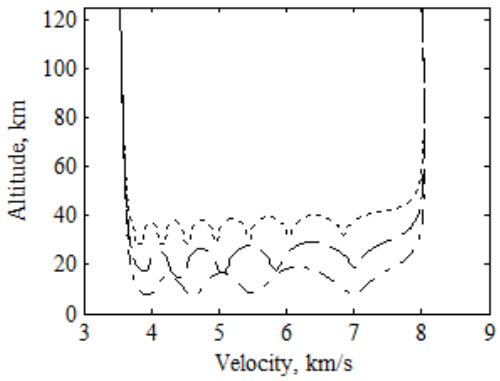

(b) Skipping Trajectories

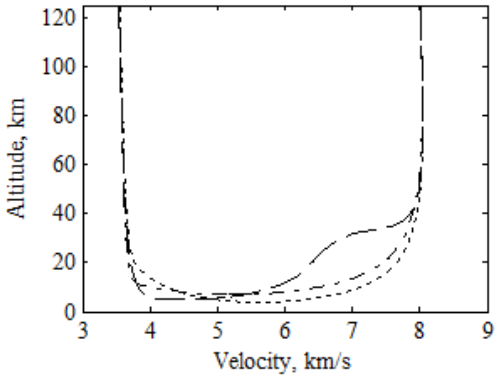

(c) Single Skip Trajectories

Figure 7.1: Different trajectory types

hold trajectory was found above $h = 40$ km, as the Martian atmosphere is not dense enough to sustain level flight for the chosen class of vehicle.

Skipping trajectories (Figure 7.1b) involve repeated dives into the denser atmosphere. They can be categorized by the number of skips, as shown in Figure. 7.2. As the number of skips increase, the minimum altitude of the skips generally increases as well. Repeated entry into the denser atmosphere will result in rapid energy dissipation, and the vehicle will exit after only a short number of skips.

Single skip trajectories (Figure 7.1c) involve very high deceleration, correspondingly high energy dissipation and heating rates, and a much more constrained entry corridor. They are primarily non-lifting trajectories, even though lift may be used to supplement gravity during the ascent and descent flight stages.

The overall frequency of occurrence of each trajectory type in this study is displayed in Figure 7.2. Skipping trajectories were the most frequent solution found in the Monte Carlo simulations. The number of single skip trajectories was quite small, as would be expected for lifting bodies. While the study was designed to allow single skip trajectories, it was understood that these would be far less frequent, as the objective function devalued them.

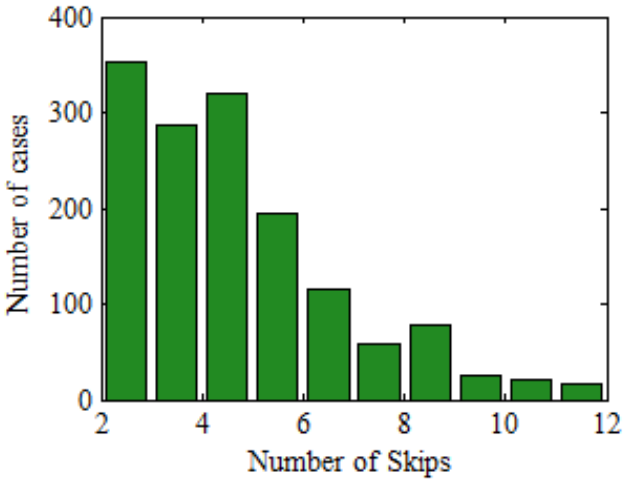

Figure 7.2: Number of skips per trajectory

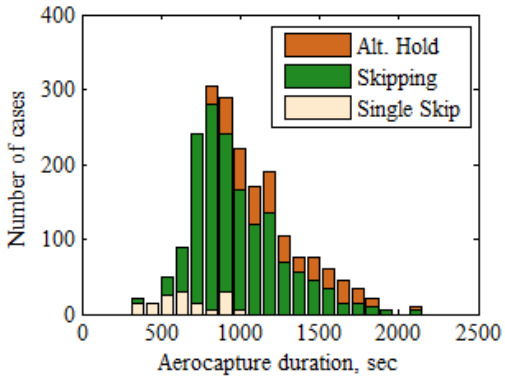

Figure 7.3: Frequency of Aero-capture Duration

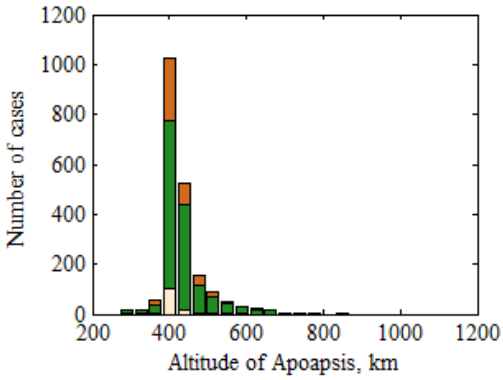

Figure 7.4: Altitude at apoapsis following aero-capture

There were more altitude hold solutions found than single skip, however the optimization routine did not select these nearly as often as skipping trajectories. While the control system allowed for altitude hold flight paths, the non-linearity of the problem, and the precision which is required to enter and fly an altitude hold decreased the frequency with which these solutions were found. By observing the trends of flight duration in Figure 7.3, it is not evident that altitude hold solutions are in fact more optimal than skipping for reducing the average energy dissipation rate. Skipping trajectories, on the other hand, could allow substantially more atmospheric profiling to be completed as a secondary mission objective.

In order to validate the methodology of the control system, the starbody trajectories were propagated past the edge of the atmosphere until they reached apoapsis. If apoapsis occurred at some altitude other than the chosen 400 km, the details of the trajectory path through the atmosphere are of little concern, as the aero-capture was not successful and the circularizing maneuver would require relatively large amounts of propellant. As shown in Figure 7.4, in the overwhelming majority of solutions, the control system was able to guide the vehicle to apoapse where the orbit could be circularized for the least energy, 400 km.

The limitations of the control system's exit energy method are amplified by

skipping trajectories. If the starbody is skipping, it is possible that when the limiting condition is reached, the vehicle may already be in a lift-up condition and unable to exit any quicker. For example, if the limiting condition is reached when the vehicle is in the $\alpha > 0$ region, the vehicle is already in a positive angle-of-attack configuration. If the resulting exit flight path angle is too shallow and overshoots apoapsis at h = 400 km, the only option is for the vehicle to begin the pull up operation before entering the $\alpha > 0$ region. This is likely to undershoot instead, as seen in Figure 7.4. On the other hand, if the vehicle is on an altitude hold, it is always capable of executing the ascending exit pitch.

7.1.3.2 Geometric Effects

The number of starbody tines, n plays a role in setting the volumetric efficiency of the starbody shape, as seen in Figure 7.5. The larger the number of tines, the more likely the starbody is to have a high ratio of volume to surface area. If n had been allowed to increase beyond 6, this trend likely would have reversed eventually. Extreme values of n would result in a starbody with very high surface area, with diminishing increases in volume.

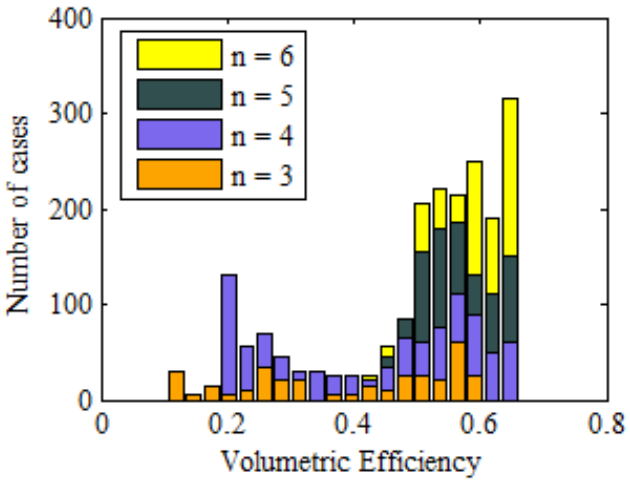

Figure 7.5: Effects of n on the vehicle's volumetric efficiency. Colors indicate different numbers of tines

For $n = 3$ and 4, there are two distinct peaks. The lower peak corresponds to flying wing type bodies (see Figure 6.26). In this case, two tines tend to dominate, as they are much larger than the other tine(s). The dominant tines are stretched considerably in the y-direction, resulting in a vehicle with very high lifting surface. Due to the extremely high surface areas in such cases, viscous drag will also be quite high.

The second peak ($\eta_v > .5$), matches the peak found for higher tine starbodies. For $n = 5$ and 6, the tendency towards more volumetrically efficient designs is a result of the inverse design process. There are more tines usable to connect shock planes on opposite sides of the center-body, therefore the tines do not need to drastically lengthen in order to make connections as e and D increase in magnitude. For $n = 3$ and 4, this peak corresponds instead to more blunt vehicle designs. These designs use trajectories with less lift; therefore, they need more drag to decelerate more quickly.

The behavior trends for peak acceleration illustrate one of the benefits of lifting aero-capture, that peak acceleration can be lower than non-lift trajectories, typically less than 4 g's (see Figure 7.6). The number of tines does not have a clear impact on this result, as the trend for each individual value of n follows the overall trend. This is significant, as the number of tines is likely to play a large role in the structural complexity of the vehicle. Three-tine designs tend to have more slender, higher aspect ratio shapes, and are therefore likely to have higher structural mass. If an $n = 6$ design is able to produce a trajectory with axial loads that are comparable to those of an $n = 3$ design, the higher-numbered tine design should be more desirable as the aspect ratio will be lower.

The value of L/D is not constant through a given trajectory. Accordingly, the value of both lift and drag are calculated at every time step. The relative amount of lift a given vehicle exhibits over the course of a trajectory is best characterized by

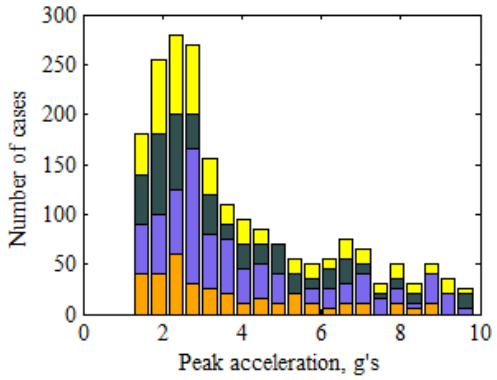

Figure 7.6: Maximum g-load experienced during entire trajectory (Earth g's)

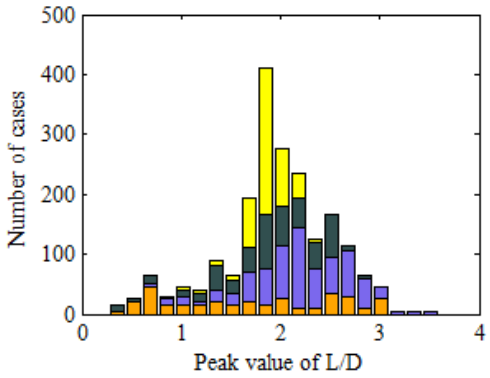

Figure 7.7: Maximum magnitude of lift-to-drag ratio during entire trajectory

the peak value of L/D rather than a trajectory average. The mean value is set not only by available aerodynamic performance, but by the type of trajectory flown. For example, L/D varies greatly during a skipping trajectory, but is relatively constant for an altitude hold.

The number of tines has an effect on the maximum magnitude of L/D as shown in Figure 7.7. Four- and six-tine starbodies have more obvious trends than three- and five-tine starbodies. This is due to the symmetry requirement imposed about the x-z plane. For a starbody with an odd number of tines, this actually enforces that one tine be located in the x-z plane. This generally results in less surface area perpendicular to the lift direction in either the $\alpha > 0$ or $\alpha < 0$ orientation. The design methodology does not enforce whether this odd tine is on the upper or lower surface. On whichever side it does reside, however, the area that is perpendicular to the lift direction will be less than on the opposite side. This tends to reduce the tendency to favor trajectories where higher L/D is vital. Overall the maximal value of L/D tends to decrease as n increases and the shapes become less wing-like.

7.1.3.3 Effects of entry velocity

Reducing the transfer velocity has a pronounced effect on the trajectory path chosen by the optimization routine. Figures 7.8 and 7.9 show the similar trend of the decreasing importance of the flight path for decreasing transfer velocity.

Figure 7.8 shows the distribution of minimum altitudes reached during flight for the two different entry velocities. Note that despite having less energy to dissipate, the lower entry velocities tend to yield lower minimum altitudes. This seems to have occurred because the gradient-based solver was more likely to settle on a single or low skip trajectory to successfully complete the aero-capture maneuver. In other words, the presence of locally optimal solutions in this regime may have biased the results. It should not be concluded that altitude hold solutions at higher altitudes do not exist, nor even that they are less prevalent than single skip trajectories. Increasing the number of Monte Carlo simulation runs would be useful in verifying that high lift solutions are just as widespread.

As was done in Figure 7.7, the distribution of values of maximum L/D is plotted in Figure 7.9, but now the colors indicate the effect of entry velocity. It should be noted that values of L/D greater than 3 are seldom optimal. An interme-

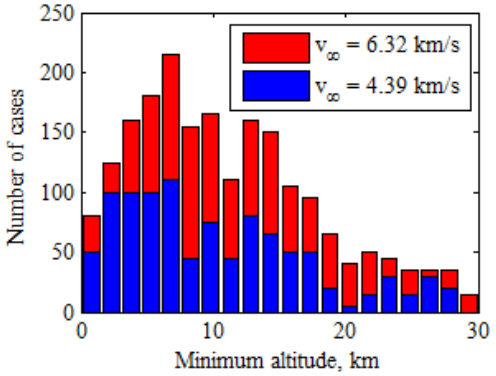

Figure 7.8: Altitude of closest approach during entire trajectory. Colors indicate entry energy

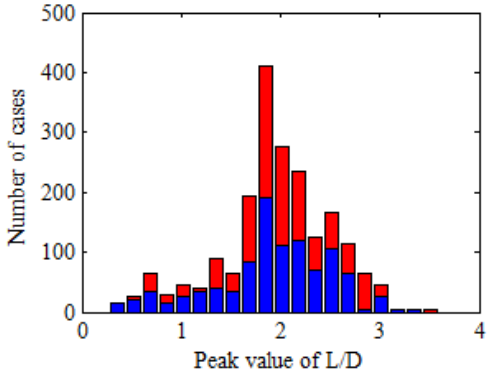

Figure 7.9: Maximum magnitude of lift-to-drag ratio during entire trajectory

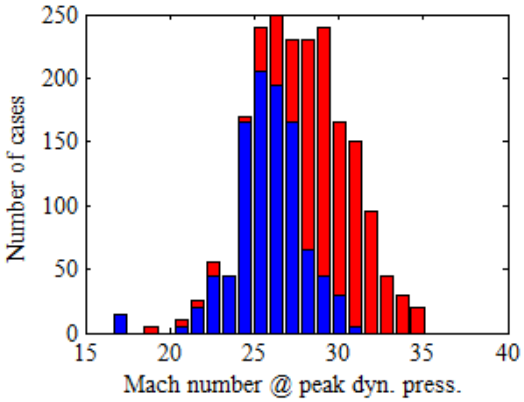

Figure 7.10: The flight Mach number as the vehicle experiences maximum dynamic pressure

diate magnitude is more frequently preferred by the Monte Carlo simulations, with a peak near L/D = 2. The peak at L/D = 2 is found for both values of the entry velocity shown. The lower energy condition does tend to create a wider distribution of solutions with L/D < 1.5; however, there is still a distinct peak near L/D = 2. Moderate values of L/D are likely favored because they strike a balance between desirable control behavior without the high drag of large surface areas.

As shown in Figure 7.10, the higher energy entries have a peak in the expected range of $28 < M < 30$. In order to take best advantage of the starbody's design point, the design M should actually be a function of the expected entry velocity. With lower v_∞, the peak value of Mach number tends to be more distinct and occurs at a lesser Mach number.

7.1.3.4 Optimal Starbody Shapes

The geometries with the most locally optimal trajectory solutions were found for each number of starbody tines, n. The resulting waveriders are displayed in Figure 7.11, and their parameters are displayed in Table 7.4. While many of the locally-optimal solutions tended to create the very large wing span shapes discussed previously, these optimal starbodies all have relatively high volumetric efficiency.

Table 7.4: Optimal Designs

n	3	4	5	6
V	40 m^3	40 m^3	40 m^3	40 m^3
m	8000 kg	8000 kg	8000 kg	8000 kg
D	.380	-.724	-.442	-.616
e	-.223	-.625	.031	-.742
L	11.0 m	9.8 m	11.7 m	13.9 m
$b_{\max}$	4.15 m	4.35 m	1.82 m	1.78 m
S	103.2 m^2	109.83 m^2	87.3 m^2	92.27 m^2
η_V	54.8%	51.5%	64.4%	61.3%
Max L/D	2.48	2.97	1.98	2.17

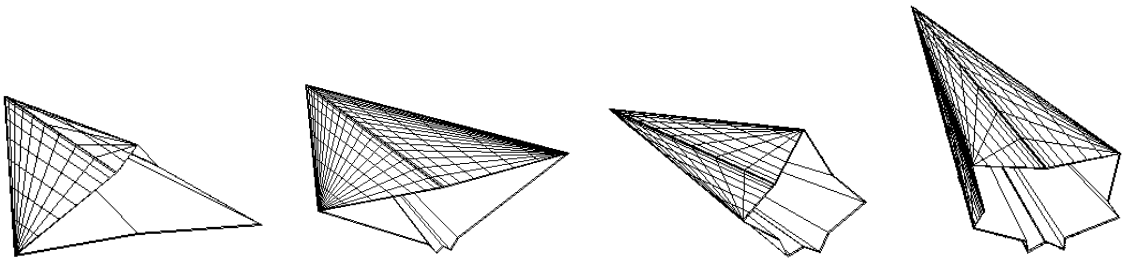

Figure 7.11: Optimal 3, 4, 5, and 6 tine starbodies

All but the five-tine starbody have large surface areas on the upper or lower surface, largely parallel to the vehicle's z-axis, providing area for the generation of lift. This trend found in the three-, four-, and six-tine starbodies suggests that the five-tine solution is simply an outlier.

The variable,$b_{\max}$, represents the widest tine. This value can therefore be used to determine the maximum dimension, for example, that might have to be contained in a faring or shroud. By this criteria, the six-tine solution is extremely favorable as it demonstrates high lift with a value of $b_{\max}$ that is only half as large as the four-tine solution.

7.1.3.5 Entry Corridors

Additional Monte Carlo trials were run over only the trajectory design space while the starbody shape was held constant. The three-, four-, five-, and six-tine

starbodies described in the previous section were used to characterize the entry corridor. In order to quantify the range of entry conditions that a vehicle can successfully use, the entry corridor, defined by the angle between the maximum entry flight path angle and the minimum entry flight path angle, is calculated.

A main concern for aero-capture trajectories is the sensitivity to deviations from the intended flight path. With a low value of L/D, a given vehicle has very little ability to mitigate under- or over-shoot during the course of a trajectory. In order to determine the entry corridor, approximately 500 Monte Carlo simulations were run per vehicle over the design space. In each case the entry corridor was calculated by identifying the two extrema of entry flight path angle, The results are dependent on the entry velocity, so the simulations were repeated for each entry condition. The results are presented in Table 7.5.

Table 7.5: Entry Corridors

	n	3	4	5	6
$v_\infty = 6.32$ km/s	$\gamma_{\max}$	-9.11°	-8.90°	-9.73°	-9.79°
	$\gamma_{\min}$	-14.14°	-15.24°	-15.61°	-14.73°
	Corridor	5.03°	6.34°	5.88°	4.95°
$v_\infty = 4.89$ km/s	$\gamma_{\max}$	-8.95°	-8.90°	-9.25°	-9.32°
	$\gamma_{\min}$	-14.15°	-13.64°	-14.64°	-14.65°
	Corridor	5.20°	4.74°	5.39°	5.27°

Each of the vehicles studied was capable of generating at least L/D = 1.98, so they all have similarly large entry corridors. This relatively large entry corridor is perhaps the principle advantage of lifting aero-capture trajectories. In two of the cases, the lower energy entry condition did not yield a larger entry corridor than the corresponding high energy case, but this is unrealistic and likely due to an insufficient number of trials being conducted.

7.2 Mars Aero-Capture with Inclination Change

Analyzing the results in the previous section, it is clear from the controllability evidenced by the large entry corridors that there is excess aerodynamic capability present in the waverider models. One potential use of this excess lifting force is to complete a secondary objective along with the aero-capture. One promising such mission goal is inclination change. Using propellant to change the inclination of a spacecraft's orbit is one of the most mass costly spacecraft maneuvers. If aerodynamics could be used rather than propellant, great savings are likely possible. In this section, the maximum possible inclination change that is possible in one aero-capture flight is investigated.

Identical initial conditions were considered as the previous section, one corresponding to a fast transfer orbit from Earth (∼160 days) and a second corresponding to a more gradual Earth to Mars transfer (∼250 days). The former scenario results in a higher entry velocity ($\mathbf{v}$ = 8.02 km/s), while the latter scenario results in a lower entry velocity ($\mathbf{v}$ = 6.95 km/s) and corresponding energy. The details of these initial conditions are given in Table 7.6. Once again, values matching those in 127 and 97 were selected for ease of comparison.

Table 7.7 contains the details of the target and final orbits. The target flight path takes the vehicle from the edge of the sensible atmosphere to apoapsis where

Table 7.6: Initial Conditions

	Low Energy Entry	High Energy Entry
r_a	< 0	< 0
ϵ	12 km^2/s^2	20 km^2/s^2
v_∞	4.89 km/s	6.32 km/s
v_{entry}	∼7 km/s	∼8 km/s
γ_{entry}	∼9°	∼9°
M_{design}	26	29
γ_{design}	1.34	1.32

Table 7.7: Post-Maneuver Conditions

	Target Orbit	Final Orbit
h_a	400 km	400 km
h_p	< 50 km	400 km
ϵ	$\sim$(-6 km^2/s^2)	-5.64 km^2/s^2
e	$0 < e < 1$	0
i	> 0	> 0

it is assumed an impulsive rocket burn circularizes into the final orbit.

For simplicity, the vehicle's initial inclination was assumed to be zero; without any side force, the vehicle would remain entirely in the Martian equatorial plane. The vehicle was then oriented to exert aerodynamic forces in the out of plane direction and affect an orbital plane change. A previous study[62] suggests that rotating away from the planet's equatorial plane is more costly than the reverse, so this is a conservative approach.

No limit was placed on the maximum amount of inclination the final orbit can have, even though a retrograde orbit ($i > 90°$) is unlikely to be desirable, let alone feasible, during only one periapsis fly-by. This was done as this work attempts to conceptually explore what is possible rather than assume a design point.

A buffer altitude of 15 km was used to prevent collision with the surface or any topographical features. This gives clearance above all locations on the Martian surface except the three highest peaks. If the trajectory of any vehicle crossed this 15 km threshold, the simulation was stopped as if the vehicle had struck the surface. In such cases the outputs were such that on the next function evaluation within the optimization routine, the vehicle would likely avoid penetration so deep into the atmosphere.

In order to manipulate the aerodynamics during the atmosphere, the angle-of-attack control system described in Section 5.2.3 was used. Of course, a bank angle controller would allow the waverider to remain on-design, however the bank angle was used as a design variable so as to achieve sufficient inclination change.

7.2.1 Optimization

There were two design parameters limited to integer values only, n and v_∞. The number of tines was limited to 3, 4, 5 or 6 and the initial v_∞ was set to either 6.32 km/s or 4.89 km/s. Each unique combination necessitated a separate optimization run, yielding eight total runs. All other variables were free to vary within the ranges shown in Table 7.8.

Table 7.8: Optimization Design Parameters

	Variable	Min	Max	Comments
Geometry	n	3	6	integer values only
	D	-1	1	
	e	-1	1	
Trajectory	v_∞	4.89 km/s	6.32 km/s	the min or max value only
	γ_{entry}	8°	20°	
	α_{entry}	-6°	6°	further constrained by geometry
	ϕ	0°	90°	
	ϵ_{ascent}	-5.5 km^2/s^2	-3 km^2/s^2	

7.2.1.1 Objective Function

An SQP gradient based optimization routine (built into MATLAB via the function 'fmincon') was used to determine the optimal combination of geometry and trajectory parameters. An initial guess was provided, the local derivatives were calculated and then the routine stepped in the direction of the local minima. The intent of this study was to determine the capability for plane change, therefore the objective function incorporated only the final inclination, i, scaled by $\pi/2$ radians as shown in Equation 7.2:

$$\min f = -\frac{i}{\pi/2} \tag{7.2}$$

7.2.1.2 Constraints

Constraint functions ensured that the aero-capture ran to completion. Doing so was complicated by the main figure of merit, the final altitude of apoapsis, h_f, being discontinuous as the vehicle decelerated. For hyperbolic orbits, the apoapsis altitude is negative. As the vehicle decelerates, the apoapsis altitude increases in magnitude towards negative infinity. When sufficient energy has been dissipated and the orbit is neutrally captured, the value becomes infinite. Finally, as the vehicle is more and more captured, the final apoapsis altitude decreases from positive infinity. It could therefore only be calculated once the orbital energy became negative. Otherwise the gradient would have pushed in the incorrect direction. In order to achieve this, an inequality constraint was created relative to the target apoapsis altitude h_T, which is shown in Equation 7.3. This constraint was multiplied by a logical statement, so that the gradient was not calculated when the orbital energy was greater than zero. This implied a need for a second constraint in order to provide a gradient at positive values of orbital energy. In fact, the final orbital energy, ϵ_f, itself was used and scaled by the initial orbital energy, ϵ_0.

The two inequality constraints are shown in Dquations 7.3 and 7.4. The constraint in Equation 7.3 has an extra term so that the apoapsis altitude target must be reached only within .01 km or 10 meters. It was deemed that saving many iterations was an acceptable trade-off for a 10 m accuracy, especially given the level of uncertainties in other parts of the simulation. Both constrained values were scaled to have similar magnitude.

$$c_1 = (\epsilon < 0)\frac{|h_f - h_T| - .01km}{h_f} \leq 0 \tag{7.3}$$

$$c_1 = \frac{\epsilon_f}{\epsilon_0} \leq 0 \tag{7.4}$$

7.2.2 Results

Fifteen random initial conditions were run for each of the eight sets of fixed parameters, resulting in 120 locally optimal trajectory and geometry solutions. While it is not certain that true global optima were found, extremely large magnitudes of plane change were found to be possible. All 120 cases were further analyzed to determine trends in certain figures of merit as inclination increased. Next, from the full set, eight optimal geometries were selected, one for each combination of tine number and initial energy. These eight shapes were then used to further examine the trajectory of the combined maneuver.

7.2.2.1 Optimization Trends

By combining the trajectory and geometry optimizations, the design space is sufficiently complex that there are many local extrema in the objective function. On the other hand, it was discovered that for a given starbody shape, there is in fact one globally optimal set of trajectory parameters. Therefore, far fewer extrema would be present if a dual layer optimization had been run, where the best trajectory was found for each geometry generated during the optimization, rather than varying both concurrently. This would have added dramatic increases in computation time however, so it is not clear that there would be great benefit to this strategy. The presence of so many extrema can be positive as well, as insight into the problem can be gleaned by analyzing trends in the locally optimal solutions.

Each data point in Figures 7.12a-7.12e represents one of the 120 locally optimal solutions. Note that the inclination of the final orbit was plotted inversely, as was the volumetric efficiency, so that the ideal result would then be in the lower left hand corner. In these plots, the results are parsed for the different atmospheric entry speeds.

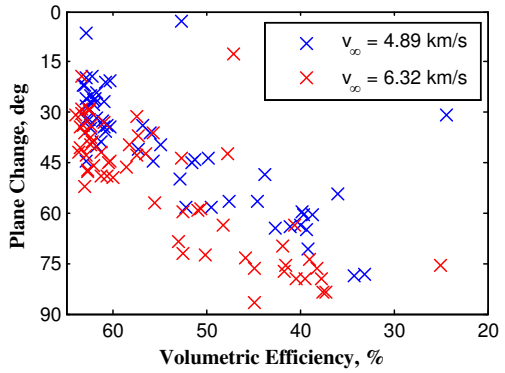

(a) Volumetric Efficiency

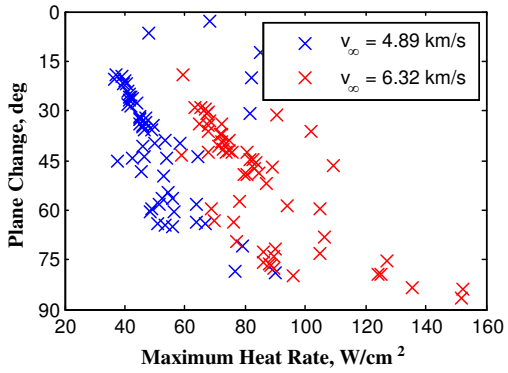

(b) Maximum Heat Rate

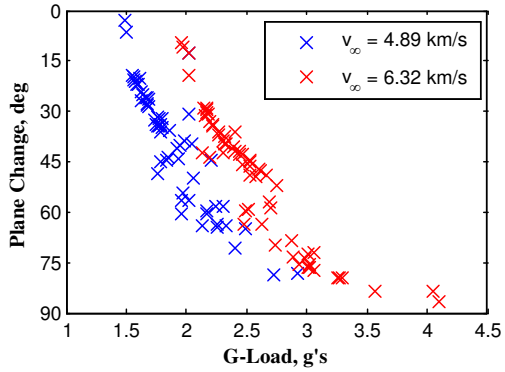

(c) G-load (Earth g's)

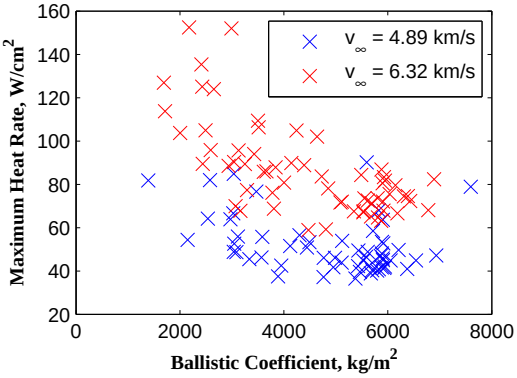

(d) Ballistic Coefficient

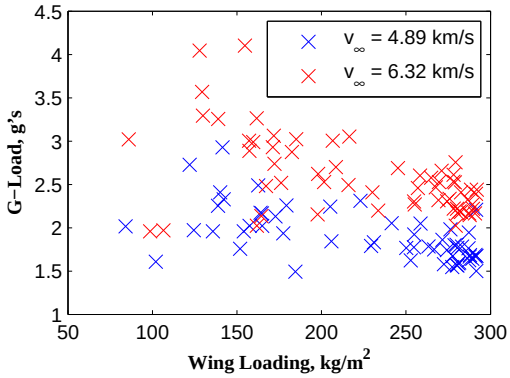

(e) Wing Loading

Figure 7.12: Trends in design metrics as inclination change increases. This study was conducted as a series of single objective optimizations, but these trends resemble multi-objective pareto curves.

In Figure 7.12a, one of the fundamental difficulties in designing hypersonic vehicles is seen. The more slender a vehicle shape and design, the less drag it will impart. In the case of starbodies, as a shape becomes more slender, its lifting area increases as well, so the lift-to-drag ratio can increase dramatically. At the same time, as the vehicle becomes more slender, it will have less usable volume. At a later stage of design, when more would presumably be known about the other required subsystems, a trade-off could be performed with a constraint placed on the volumetric efficiency and even the packaging density. While there were many designs found that were capable of greater than 70° of plane change, many would require a vehicle shape with less than 40% volumetric efficiency. In these cases, in order to fulfill the necessary cargo volume requirement, the vehicle cross-section would need to be extremely large, possibly impeding fit into a launch vehicle fairing unless deployment mechanisms were used.

The maximum heating rate experienced during the course of the trajectory is a vital metric for sizing the thermal protection system. As the plane change that can be realized from a given design increases, the maximum value of heat rate experienced over the course of the trajectory increases as well (see Figure 7.12b). As was expected, the higher energy entry condition shifts the results to higher heating rates and slightly lower to greater plane change. If the vehicle has greater energy to dissipate, then it must spend more time in the atmosphere decelerating, and there is more time for aerodynamics to be used to impart plane change. Once again, as the design process continues, constraints could be used to account for the maximum acceptable heating rate of the expected vehicle materials.

Also note that the maximum aerodynamic g-load increases as the plane change increases (Figure 7.12c). In order to achieve such high turning, the vehicle must use relatively high aerodynamic forces to change its course. The high forces clearly result in high aerodynamic g-loads on the vehicle. If the aero-shell had a 3g limit,

for example, there are a number of trajectories which would not be possible, as the vehicle could not withstand the g-load. Once again, the curve shifts to the right for the higher energy initial condition due to stronger accelerations being imparted to the vehicle. Increasing the sustainable g-load of a vehicle would likely undesirably increase the structural mass as well.

High lift reentry is a unique flight environment and typical figures of merit do not always accurately predict performance. This is the case with both the ballistic coefficient (see Figure 7.12d) and the wing loading (see Figure 7.12e, measured by total wetted area, as the entire surface area contributes to or impedes lifting force). These values are plotted against maximum heat rate and maximum acceleration as they have no discernable correlation to plane change acheivable. The former value is commonly used in estimating the heat load expected on a blunt re-entry vehicle, with higher drag (low ballistic coefficient) designs being favorable. While this trend is observed to a small degree in Figure 7.12d, the trend is reversed at high ballistic coefficients. Further, there appears to be a value of ballistic coefficient which would minimize the heat load required.

In the case of purely atmospheric vehicles, the wing loading is a vital metric for analyzing aircraft performance. In the high lift re-entry scenario, however, no correlation was observed linking the achievable plane change and wing loading. Only a slight trend was seen when comparing the wing loading to the maximum acceleration required to complete the maneuver. Generally, as wing loading increases, the required maximum acceleration decreases. This is due to the decreased turning capability associated with the decreased lifting potential of a high wing loading vehicle.

Table 7.9: Optimized Starbody Designs

n	3	4	5	6	3	4	5	6
v_∞	4.89 km/s	4.89 km/s	4.89 km/s	4.89 km/s	6.32 km/s	6.32 km/s	6.32 km/s	6.32 km/s
V	40 m^3	40 m^3	40 m^3	40 m^3	40 m^3	40 m^3	40 m^3	40 m^3
m	8000 kg	8000 kg	8000 kg	8000 kg	8000 kg	8000 kg	8000 kg	8000 kg
e	.785	.793	.686	.188	-.482	-.071	-.196	-.486
D	-.849	-.915	-.860	-.847	-.630	-.864	-.865	-.667
l	10.70 m	10.06 m	13.21 m	13.46 m	9.11 m	7.98 m	11.60 m	13.27 m
$b_{\max}$	7.56 m	8.23 m	3.44 m	2.15 m	6.75 m	8.81 m	3.88 m	2.66 m
S	164.9 m^2	170.7 m^2	107.0 m^2	90.0 m^2	125.8 m^2	143.5 m^2	101.8 m^2	93.6 m^2
η_V	34.3%	33.1%	52.9%	62.9%	44.9%	39.4%	55.5%	60.4%
Max L/D	2.63	2.47	2.07	1.83	2.18	2.25	2.03	1.77
$i_{\max}$	78.8°	78.5°	49.7°	44.5°	86.5°	79.7°	57.2°	45.0°

7.2.2.2 Optimal Vehicle Shapes

The details of the optimal geometries for each of the eight combinations of n and v_∞ are presented in Table 7.9 and the high initial energy optimal starbody designs are displayed in Figure 7.13 (at the bank angle for their respective optimal cruise trajectories). Several items are of importance in Table 7.9. First, all designs have negative values of D. Recall that this parameter controls the location of the starbody tines, and a negative value indicates that they have been shifted towards the bottom side. With the starbodies shown in Figure 7.13, notice that there is a grouping of small tines on the bottom side, and only larger tines on the top side of the vehicle. This creates large lifting surfaces on the topside of the vehicle, which is necessary for exerting strong aerodynamic forces. The vehicles are essentially flying upside down from a conventional hypersonic configuration, in order to use negative lift to overcome the strong orbital inertial forces which tend to push the waverider out of the atmosphere.

Changing the eccentricity of the center-body yields different trends for the two initial energy conditions. When the tine distribution parameter is large, a positive value of e will tend to make the vehicle even more slender, as the center-body is becoming flatter as well. However, if the reverse is true, that is if D is large and e is negative, then the vehicle actually becomes more blunt. The large magnitude

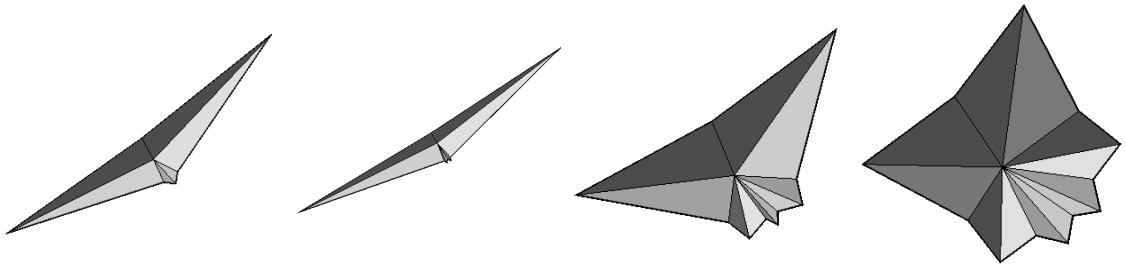

Figure 7.13: Optimal 3-, 4-, 5-, and 6-tine starbodies (high initial energy)

of D is necessary in order to create the large lifting surface; however, having the center-body become more eccentric in the vertical plane tends to increase the wave drag that the vehicle will experience because the cross-sectional area increases. The former scenario is found in the lower energy entry condition, where increased wave drag is not necessary to sufficiently decelerate, whereas the latter scenario is present when there is substantially more entry energy.

Next, while the slenderness ratio of the center-body was held constant, as discussed earlier, the overall ratio of the vehicle was not fixed, and varies dramatically. The length of all vehicles are of the same approximate magnitude, however their width is not. Note that $b_{\max}$ represents the widest tine. This value can therefore be used to determine the maximum dimension, for example, that might have to be contained in a launch vehicle faring or shroud. By this criterion, the six-tine solution is extremely favorable as it is capable of only marginally less lift with a value of $b_{\max}$ that is only one quarter as large as the four-tine solutions.

Finally, the trends of volumetric efficiency are as predicted by Figure 7.12a, except for three vs. four tine designs. The optimal three- and four-tine starbodies look almost identical, except for the addition of a second small tine on the underside. The four-tine version performs worse, however, as the extra tine on the lower surface adds very little to lift, but detracts in terms of extra surface area and therefore skin friction. In other cases however, the more volumetrically efficient the design, the less plane change capability.

7.2.2.3 Trajectory Analysis

In order to better understand the flight precision required for these trajectories, the eight starbodies referred to in the previous section were used to fully quantify the feasible space. As this is a conceptual study, there were no limitations placed on g-load or heat rate. In actual practice, these factors would limit the steepest possible entry condition; however, in the cases studied in this present work, only trajectory limited conditions are observered. The steepest flight path angle represents the one that would allow the vehicle to just avoid the buffer altitude of 15 km, described earlier. The shallowest entry condition is somewhat more benign, and would likely not be altered by other figures of merit in the same way.

The enclosed areas in Figure 7.14 show the range of trajectory parameters at which successful trajectory solutions exist. Each upper curve represents the steepest entry flight path angle that the vehicle could feasibly use, while the lower line indicates the shallowest angle for which the vehicle would not simply skip out of the atmosphere. At the far left of each area, the vehicle flies without any bank angle, and therefore is capable of a wider range of entry flight path angles. As the bank angle increases, more lift is diverted away from the flight plane and is no longer usable for overcoming an excessively shallow or steep entry. Eventually, the bank angle becomes so severe, that aero-capture is no longer possible. The vehicle does not have sufficient drag to decelerate without using lift to maintain a prolonged flight, and beyond the critical bank angle, there is not sufficient lift available to hold altitude.

Because the higher tine number designs have less lift capability, they do not have as wide of an entry corridor at small values of bank. Conversely, as they are closer to axi-symmetric, the application of a bank angle has less adverse effect, as they still have large lifting surfaces normal to the vertical direction after the

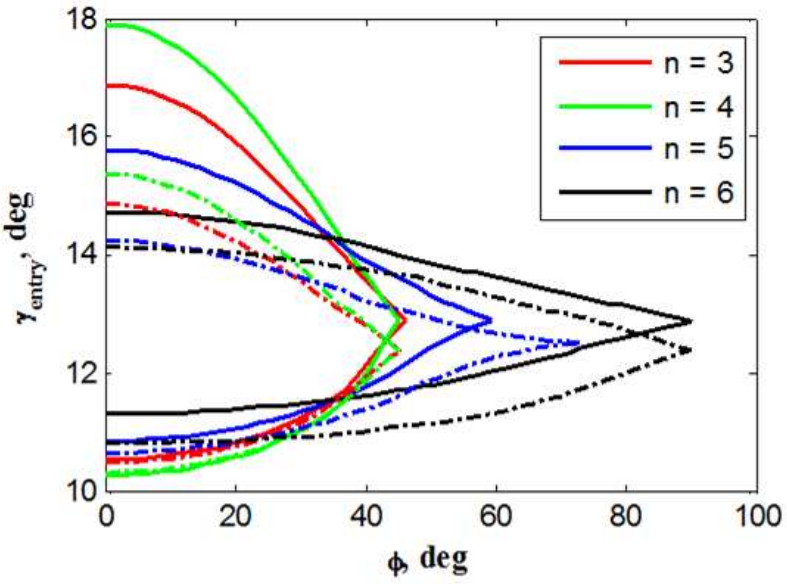

Figure 7.14: Entry Corridors for all values of bank angle. Solid lines correspond to high energy, $v_\infty = 6.32$ km^2/s^2, Dashed lines correspond to low energy, $v_\infty = 4.89$ km^2/s^2

rotation. The lower tine number designs resemble delta wing type aircraft, and are less capable of sustained, high-bank flight.

While the areas enclosed in Figure 7.14 represents the set of all possible entry and flight conditions, it does not indicate the effect on plane change. In order to understand that impact, Figures 7.15 - 7.22 display the plane change possible over the range of flight path angle and bank angle. At low levels of bank, the final inclination consistently increases; however, as larger values are reached, the relationship is more involved. The plane change increases more rapidly for shallow entry flight path angles. This is because the overall flight time increases for a successful aero-capture at these entry conditions. The vehicle remains at higher altitudes in less dense atmosphere, therefore deceleration occurs more slowly, and the vehicle has more time over which to increase inclination. In spite of this, for a given bank angle, the maximum plane change does not occur exactly at the shallowest entry flight path angle. There is a slight decrease at the most shallow angles. This

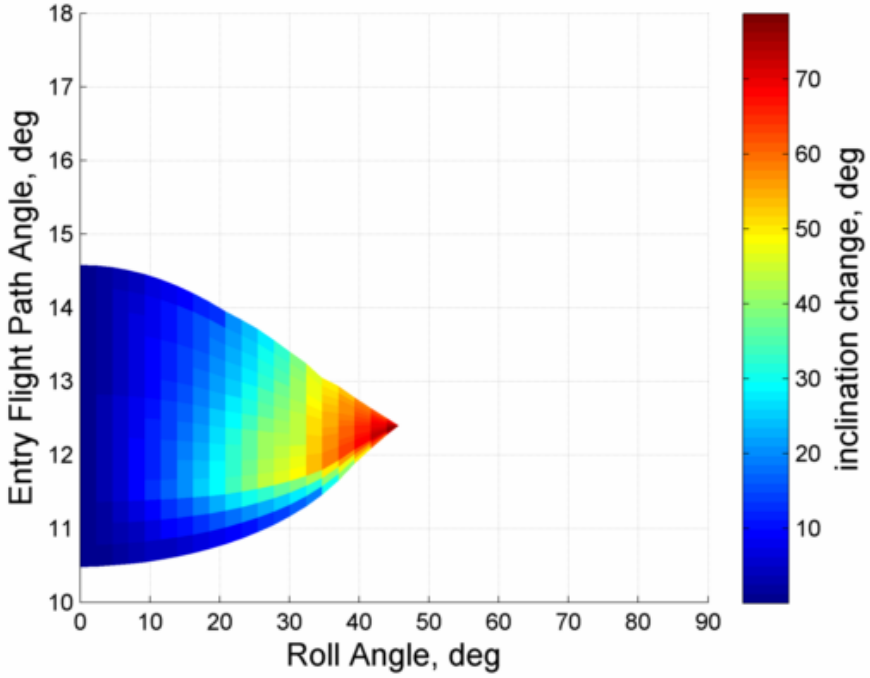

Figure 7.15: Inclination achievable as a function of entry flight path angle and roll angle for optimized 3-tine starbody with low initial energy ($v_\infty = 4.89$ km/s)

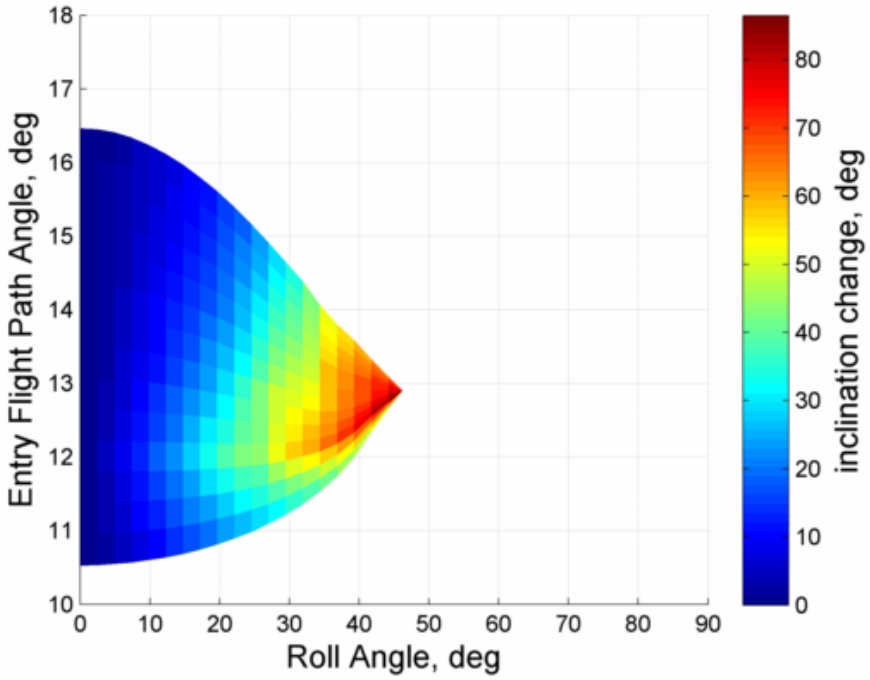

Figure 7.16: Inclination achievable as a function of entry flight path angle and roll angle for optimized 3-tine starbody with high initial energy ($v_\infty = 6.32$ km/s)

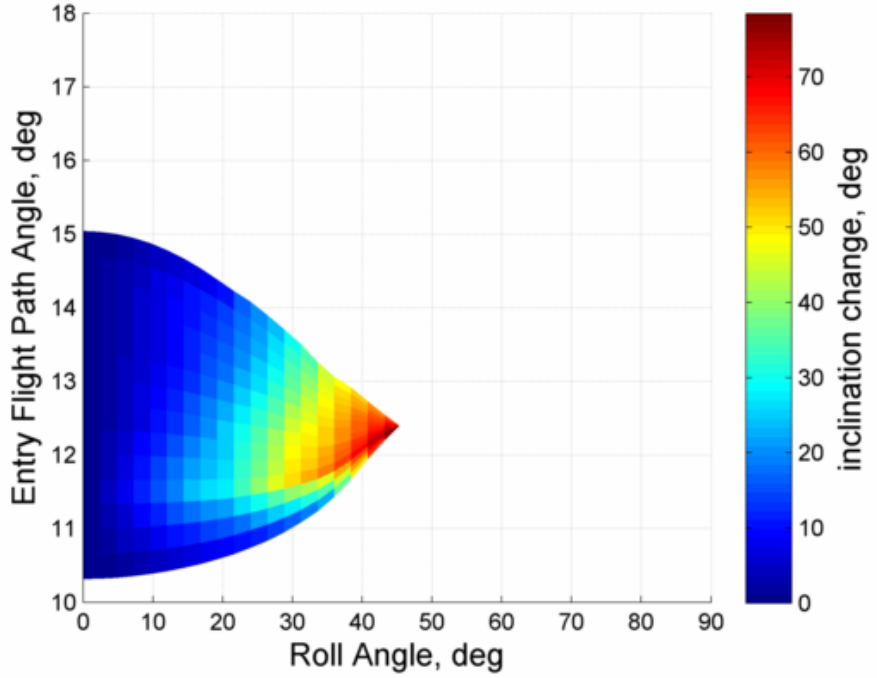

Figure 7.17: Inclination achievable as a function of entry flight path angle and roll angle for optimized 4-tine starbody with low initial energy ($v_\infty = 4.89$ km/s)

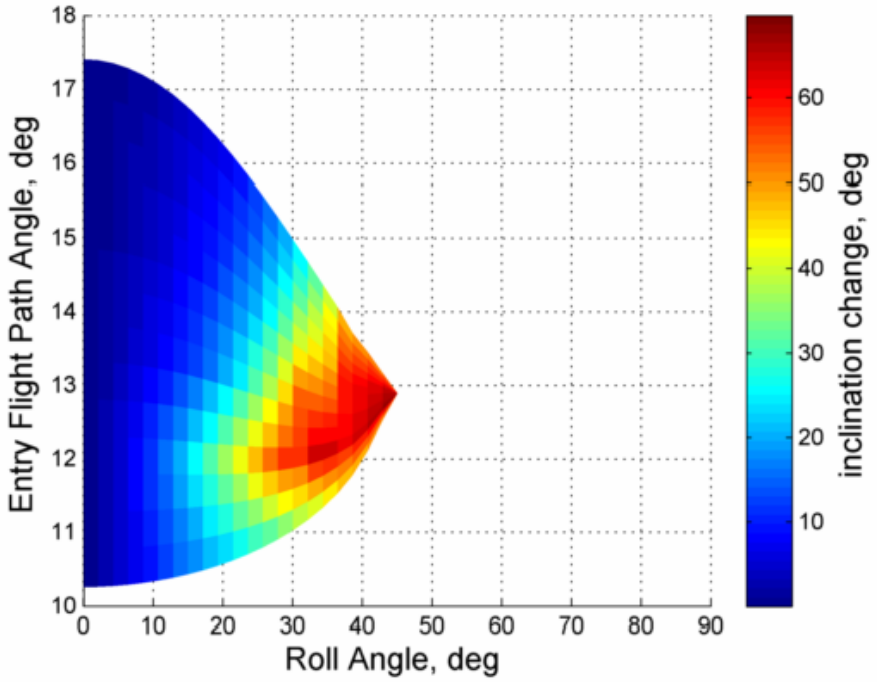

Figure 7.18: Inclination achievable as a function of entry flight path angle and roll angle for optimized 4-tine starbody with high initial energy ($v_\infty = 6.32$ km/s)

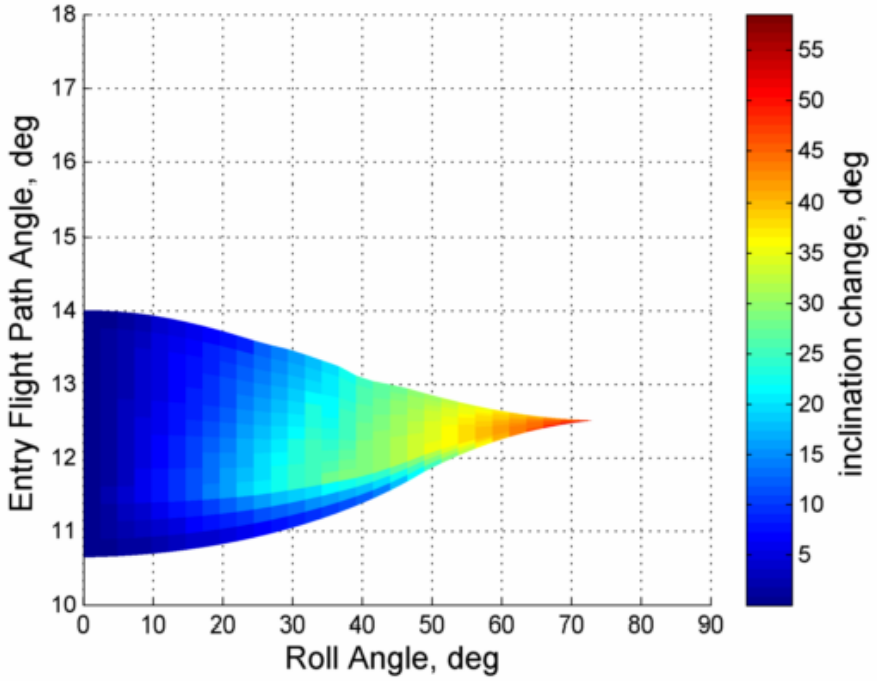

Figure 7.19: Inclination achievable as a function of entry flight path angle and roll angle for optimized 5-tine starbody with low initial energy ($v_\infty = 4.89$ km/s)

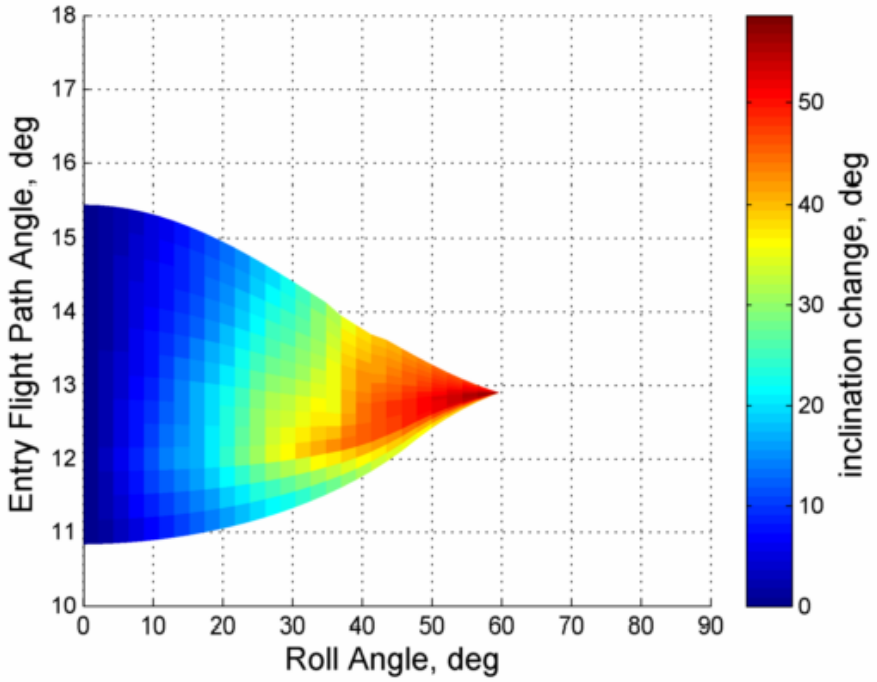

Figure 7.20: Inclination achievable as a function of entry flight path angle and roll angle for optimized 5-tine starbody with high initial energy ($v_\infty = 6.32$ km/s)

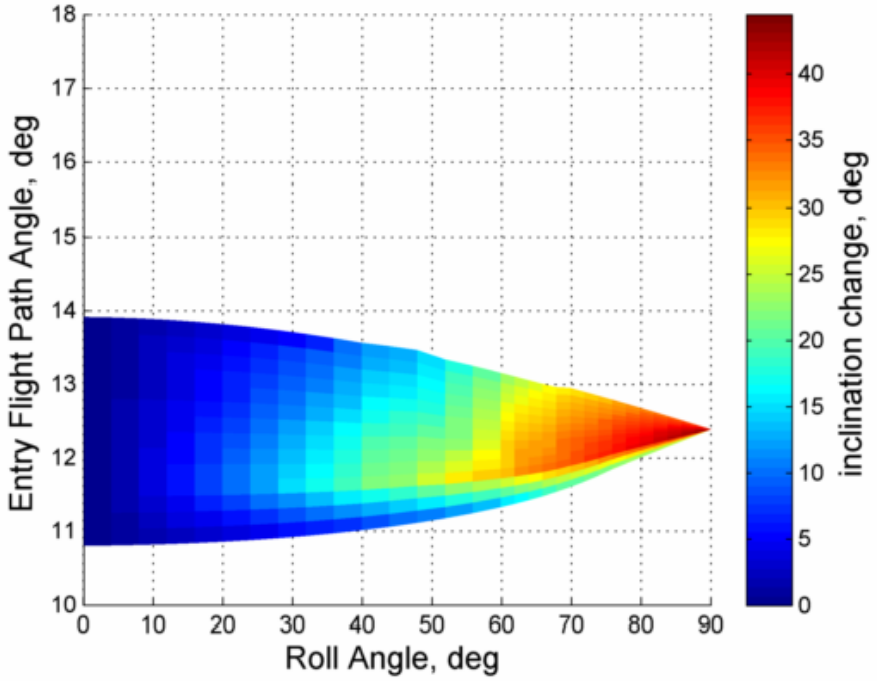

Figure 7.21: Inclination achievable as a function of entry flight path angle and roll angle for optimized 6-tine starbody with low initial energy ($v_\infty = 4.89$ km/s)

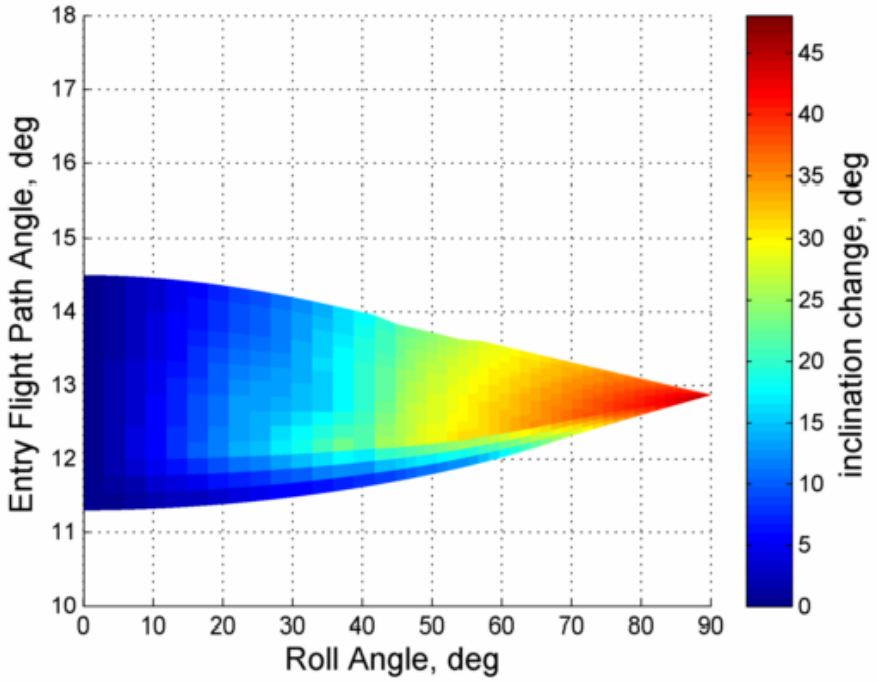

Figure 7.22: Inclination achievable as a function of entry flight path angle and roll angle for optimized 6-tine starbody with high initial energy ($v_\infty = 6.32$ km/s)

is a relic of the control system used, and is unlikely a universal trend. By entering at such a shallow angle, the nominal periapsis is too high to allow constant altitude flight. The vehicle uses lift to descend, however due to the weak gains in the control system, it drops farther than is necessary. Deceleration occurs more rapidly, and the overall flight time decreases compared to a slightly steeper entry

The greatest value of inclination is found at the maximum value of bank angle. This occurs at the intersection between the shallowest and the steepest entry flight path angle. As mentioned previously, this corresponds to the globally optimum set of trajectory parameters for the given shape. The location of the peak is crucially important, as the vehicle has absolutely no margin of error on entry conditions to achieve this outcome. While a given maximum value of plane change may be possible, a realistic mission design would likely target a lesser final inclination in order to increase the entry corridor. Luckily, near the peak, the gradient of the plane change is relatively small, and decreasing the bank angle slightly will not greatly decrease the final inclination.

7.2.2.4 Equivalent Δv

Table 7.10 shows a breakdown of the necessary Δv for three scenarios: the combined aero-assisted plane change with aero-capture as defined in this study, an aero-capture followed by a propellant burn to achieve the same inclination change, and a fully propellant-based combined capture and plane change scheme. When calculating the Δv required for an impulsive inclination change, the plane change values in the third column are used, which correspond to the maximum attainable with an aero-assisted aero-capture.

While the aero-assist does remove the significant majority of the needed Δv, a periapsis raise maneuver is still required in order to prevent an unwanted reentry. This requires a small velocity increment to circularize the orbit. The magnitudes of

Table 7.10: Δv required from propellant for different mission types. Savings yielded from aeroassist shown in parentheses

v_∞	n	Plane Change	Exoatmospheric Orbital Insertion and Plane Change	Aero-capture w/ Exoatmospheric Plane Change	Aero-capture w/ Aeroassisted Plane Change
4.89 km/s	3	78.77°	3.544 km/s	2.912 km/s (.631 km/s)	.113 km/s (3.431 km/s)
	4	78.46°	3.543 km/s	2.912 km/s (.631 km/s)	.113 km/s (3.431 km/s)
	5	49.70°	3.517 km/s	2.776 km/s (.741 km/s)	.115 km/s (3.402 km/s)
	6	44.48°	3.512 km/s	2.605 km/s (.907 km/s)	.107 km/s (3.405 km/s)
6.32 km/s	3	86.53°	4.636 km/s	2.908 km/s (1.727 km/s)	.102 km/s (4.534 km/s)
	4	79.73°	4.630 km/s	2.923 km/s (1.708 km/s)	.122 km/s (4.508 km/s)
	5	57.16°	4.610 km/s	2.904 km/s (1.706 km/s)	.130 km/s (4.480 km/s)
	6	45.00°	4.598 km/s	2.632 km/s (1.967 km/s)	.114 km/s (4.484 km/s)

each for all eight optimal shape/trajectories are as shown. There is little relationship between the inclination of the orbit and the magnitude of the necessary periapsis raise, it is mostly a function of the exiting flight path angle and the altitude flown when in the atmosphere.

The aero-assist maneuver shows dramatic reduction in propulsive Δv requirements compared to an impulsive only maneuver. In this case, the optimal maneuver is solved for, rather than assuming that the plane change would occur at the target circular radius of 400 km. Because the propellant required to change inclination decreases as orbital velocity decreases, it is typically optimal to perform the maneuver at a relatively high altitude even if the apoapse must be raised and lowered. In the scenario under consideration here, further propellant savings can be achieved by

incrementally inserting into the final circular orbit. First, a decelerating propellant burn occurs at the initial hyperbolic periapse of 400 km above the Martian surface. Enough Δv is applied in order to enter a captured orbit, with apoapse at some optimal altitude (the highest altitude was constrained to be one half of the radius of Mars' sphere of influence). At apoapse, the spacecraft performs the inclination change. Finally, after returning to periapse, the spacecraft uses one last maneuver in order to enter a circular orbit. Even with these improvements to a fully impulsive maneuver, this maneuver is extremely costly and it would serve mission designers well to avoid this.

The second category shows that a large velocity increment would be necessary in order to impart the plane change even if the vehicle had used aero-capture to decelerate from the hyperbolic entry conditions. Once again, the Δv for the inclination change was calculated for a propellant burn at some optimal altitude greater than 400 km. The propellant required to raise and lower apoapsis was also included.

Chapter 8

Aero-Gravity Assist Design

Gravity assist fly-bys have an important legacy in interplanetary space travel. For missions beyond Mars, it is often beneficial to depart from Earth and perform a series of gravity-assists around the inner planets before departing to the outer planets. In certain cases, the spacecraft can not be turned sufficiently in only one pass to reach the next planet in the sequence. In such cases, an aero-gravity assist (AGA) is likely worthy of consideration.

8.1 Maximum Performance

The present section examines the aero-gravity assist about Mars, Earth and Venus, using optimization methodologies to determine the maximum possible benefit achievable with the maneuver. In order to perform trajectory design, the feasible space of AGA performance must be identified. This is quantified by means of heliocentric velocity increase, $\Delta|v|$, turning angle, $\Delta\Theta$, and energy loss relative to the fly-by planet, C_3^+/C_3^-. The velocity change, $\Delta|v|$ is not the standard delta-v used to quantify velocity vector changes of impulsive maneuvers (see Equation 8.1), but instead the change in overall velocity magnitude before and after the maneuver (relative to the sun), as shown in Equation 8.2:

$$\Delta v = \vec{v}_f - \vec{v}_i \tag{8.1}$$

$$\Delta|v| = |v_f| - |v_i| \tag{8.2}$$

Quantified as such, the inclination change is not included in the overall gain or loss.

A wide range of entry conditions has been considered, characterized by approach velocity, v_∞^-, examining the possible $\Delta|v|$ as a function of the energy lost during the atmospheric pass. The orbital energy loss is not used directly but instead quantified by hyperbolic excess velocity before and after the maneuver. If we define $\xi \equiv v_\infty^+/v_\infty^-$, the relationship between energy loss and ξ is given by Equation 8.3:

$$\frac{\epsilon_f}{\epsilon_0} = \frac{(v_\infty^+)^2/2}{(v_\infty^-)^2/2} \Rightarrow \xi = \sqrt{\frac{\epsilon_f}{\epsilon_0}} \tag{8.3}$$

Such correlations are useful for designing AGA missions. In order to perform preliminary or even medium fidelity interplanetary trajectory design, an upper limit for AGA performance is required in the form of turning, $\Delta\Theta$, as a function of fly-by energy loss, ξ. Quantifying this relationship is the primary purpose of this section. In the following section, the maximum performances determined here will be used to perform spacecraft trajectory designs using AGA.

8.1.1 Study Parameters

The ranges of the various parameters used in this study are summarized in Table 8.1. The early chapters of this work provide more explanation on the significance of the values, and how they are used to model the engineering problem under review. This includes equations relating to the aerodynamics and the trajectory. The bank angle variation based control system used in this study is described in Section 5.2.2. The osculating cones methodology of developing hypersonic waveriders is used for geometry generation.

Table 8.1: Simulation and Optimization Options

Trajectory	Approach velocity, v_∞^-	6 km/s : 40 km/s
	Hyperbolic Velocity Fraction, ξ	.25 : .95
	γ_{entry}	10° : 14.5°
	α_{entry}	0° : 4°
Vehicle Properties	Mass	2500 kg
	Volume	25 m^3
Aerothermodynamics	Leading Edge Radius	0.01 : 0.1 m
Control System	Max Pitch Rate, q	0.25°/s
	Max Roll Rate, p	0.5°/s
Optimization	Population Size	1000
	Generations	10
	Minimum SQP Step Size	1e-12

8.1.1.1 Initial Conditions

For each optimization run, the vehicle is given a constant initial position and constant initial velocity magnitude, v_∞^-, at the edge of the planet's sphere of influence (see Figure 8.1). Because Figure 8.1 is not drawn to scale, the inbound and outbound paths appear to have steep angles relative to the sphere of influence. In reality, each would be almost exactly normal to the sphere of influence and pointing almost exactly towards or away from the center of the planet.

The direction of the initial velocity vector will vary slightly, allowing a range of atmospheric entry conditions. The optimization routine selects the flight path angle of entry, γ_{entry}, and from this design parameter, the necessary direction of the velocity is determined to ensure that the vehicle approaches the atmospheric boundary as selected. The value of γ_{entry} will vary, but to ensure consistent comparisons between trajectories, the location of entry to the sphere of influence will be the same for all trajectories.

In the heliocentric frame of reference, the vehicle is given an initial location such that the spacecraft's position vector relative to the planet is parallel to the planet's velocity vector. Using this definition, the vehicle lies in the ecliptic plane of

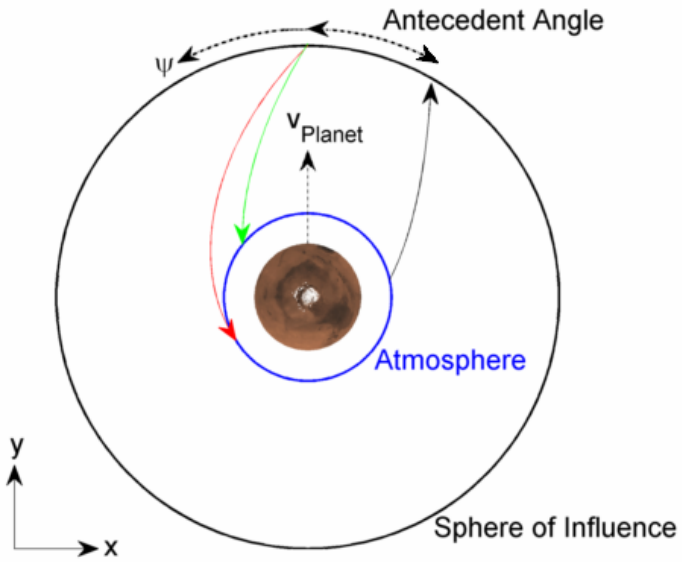

Figure 8.1: Initial conditions of spacecraft (not drawn to scale). Red and green curves correspond to shallow and steep atmospheric entry initial conditions, respectively

the spacecraft. For simplicity, it can be assumed that the maneuver occurs exactly at the vernal equinox, so that the planet velocity is almost entirely in the heliocentric $+y$-direction (see Section 5.3.3). Similarly, the relative position vector from the planet to the spacecraft at the initial conditions is in the heliocentric $+y$-direction. The initial spacecraft velocity vector is approximately in the ($-y$)-direction. The initial position of the spacecraft is converted into planet-centric coordinates for trajectory propagation.

Defining the initial conditions in this manner ensures that both the heliocentric velocity increase and turning angle are relevant. So long as the range of γ_{entry} is sufficiently small, the variation in the initial velocity vector direction will be negligible, as shown in Figure 8.2. The magnitude of $\Delta|v|$ for a pure gravity-assist is dependent on the approach direction, therefore, fixing the approach direction isolates changes to AGA performance only.

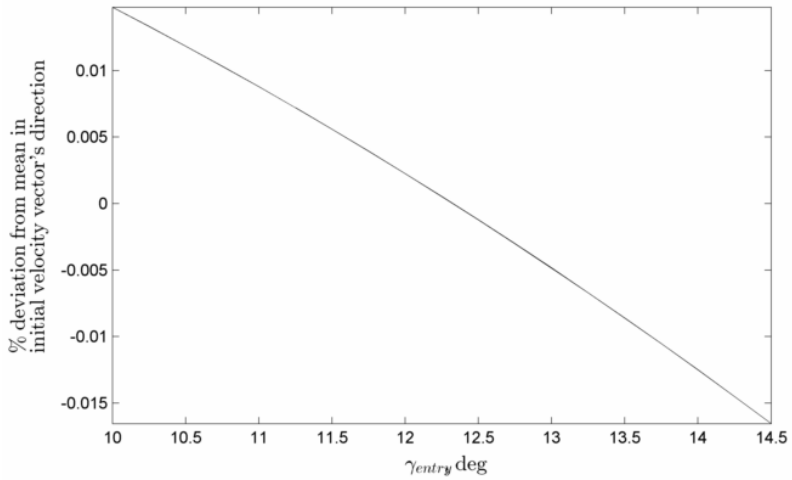

Figure 8.2: Variation of initial velocity vector direction for full range of γ_{entry} for $v_\infty^- = 20$ km/s

8.1.1.2 Optimization Formulation

From initial analysis, it was clear that the design space was nonlinear and, in places, non-continuous. A gradient based method would have difficulties with such a problem, therefore a global analysis method is preferred. A genetic algorithm is used to primarily parse the design space. Subsequently, a gradient based solver was used to further refine the results to ensure the necessary conditions were satisfied.

Both schemes use the turning angle (in inertial coordinates of the fly-by planet) before and after the maneuver as the objective function:

$$\min f = -\Delta|\Theta| = -(|\Theta_f| - |\Theta_i|) \tag{8.4}$$

Further, a constraint is placed on the value of ξ for a given optimization run. This serves to determine the maximum possible turning around the planet with a given approach and departure energy.

There should be a direct correlation between vehicle turning and velocity increase. This can be demonstrated by combining Equation 8.2 and the definition of

the sphere of influence, $v_{SOI} \approx v_\infty$:

$$\Delta|\boldsymbol{v}| = |\boldsymbol{v}_f| - |\boldsymbol{v}_i| = |\boldsymbol{v}_{\text{SOI}} + \boldsymbol{v}_{\text{Planet}}|_f - |\boldsymbol{v}_{\text{SOI}} + \boldsymbol{v}_{\text{Planet}}|_i \tag{8.5}$$

$$\Delta|\boldsymbol{v}| = |\boldsymbol{v}_\infty^+ + \boldsymbol{v}_{\text{Planet}}| - |\boldsymbol{v}_\infty^- + \boldsymbol{v}_{\text{Planet}}| \tag{8.6}$$

Define an angle, ψ, as the clockwise rotation from the spacecraft's approach vector and the heliocentric (-y)-direction as depicted in Figure 8.1. Then, the expression for the final velocity vector in terms of the initial velocity can be found using a rotation of $\Delta\Theta$:

$$\begin{aligned}\Delta|v| = &\left|\begin{bmatrix} \cos(\Delta\Theta+\psi) & -\sin(\Delta\Theta+\psi) & 0 \\ \sin(\Delta\Theta+\psi) & \cos(\Delta\Theta+\psi) & 0 \\ 0 & 0 & 1 \end{bmatrix}\begin{bmatrix} 0 \\ -v_\infty^+ \\ 0 \end{bmatrix} + \begin{bmatrix} 0 \\ v_{\text{Planet}} \\ 0 \end{bmatrix}\right| \\ &- \left|\begin{bmatrix} \cos(\psi) & -\sin(\psi) & 0 \\ \sin(\psi) & \cos(\psi) & 0 \\ 0 & 0 & 1 \end{bmatrix}\begin{bmatrix} 0 \\ -v_\infty^- \\ 0 \end{bmatrix} + \begin{bmatrix} 0 \\ v_{\text{Planet}} \\ 0 \end{bmatrix}\right|\end{aligned} \tag{8.7}$$

This expression also assumes that the maneuver is brief compared to the planet's orbit, thus the direction of the fly-by planet's velocity vector remains unchanged. This is a reasonable assumption, as gravity assist maneuvers take place on the scale of hours. Because the maneuver is theoretically confined to the ecliptic plane, omitting the ignored z-terms and using the definition of ξ to replace the magnitude of the final velocity yields the following simplification:

$$\Delta|v| = \left|\begin{bmatrix} v_\infty^- \xi sin(\Delta\Theta+\psi) \\ -v_\infty^- \xi cos(\Delta\Theta+\psi) + v_{\text{Planet}} \end{bmatrix}\right| - \left|\begin{bmatrix} v_\infty^- \sin(\psi) \\ v_{\text{Planet}} - v_\infty \cos(\psi)^- \end{bmatrix}\right| \tag{8.8}$$

With the initial conditions defined in the section above, the approach angle is zero:

$$\Delta|v| = \left|\begin{bmatrix} v_\infty^- \xi sin(\Delta\Theta) \\ -v_\infty^- \xi cos(\Delta\Theta) + v_{\text{Planet}} \end{bmatrix}\right| - \left|\begin{bmatrix} 0 \\ v_{\text{Planet}} - v_\infty^- \end{bmatrix}\right| \tag{8.9}$$

Equation 8.9 represents the general relationship for the AGA maneuver as established.

For a given v_∞^- and a fixed value of ξ, the only unfixed variable is $\Delta\Theta$. By inspection of this equation, it is maximized when $\Delta\Theta = 180°$. This is a physically reasonable result. Given vector summations, the greatest final heliocentric velocity that the spacecraft could have is if it departed parallel to the planet's velocity vector. Similarly, the least initial heliocentric velocity it could have (with a fixed value of v_∞^-) is if it approached the planet in the anti-parallel direction. In such a case, as the spacecraft approaches the GA or AGA maneuver, the spacecraft and the fly-by planet are moving directly towards one another. Gravitational and possibly aerodynamic forces bend the spacecraft's velocity vector such that it now moves in the same direction as the planet and with some excess velocity to spare.

In order to determine the actual theoretical maximum velocity increase, further simplifications can be made. First, let the turning angle be 180° as explained, and second assume that the maneuver was completed without any loss in v_∞. Setting $\xi = 1$ yields the following expression:

$$\Delta|v|_{\max} = (v_\infty + v_{\text{Planet}}) - (v_{\text{Planet}} - v_\infty) = 2v_\infty \tag{8.10}$$

While $\xi = 1$ is not possible for an AGA and $\Delta\Theta = 180°$ is unlikely for a pure gravity assist, Equation 8.10 provides a very useful limit. This limit will be used to scale the results found for possible velocity increment.

8.1.1.3 Genetic Algorithm

A genetic algorithm was employed using double precision genes, rather than encoding a binary genetic code for each population member. Instead of mutation by way of flipping bits, in this method, a mutation direction is randomly selected with weighting adaptively determined from the location of previous generation members within the design space. Next, a mutation step size is randomly chosen ensuring that it does not cross bounds and constraints. The psuedo-random mutation step method helps to ensure sufficient diversity within the population. Standard crossover techniques were used when mating genes by switching entire double precision design variables and direct transfer of a small number of elites following fitness evaluation of each generation.

A trade study was performed in order to determine the best options to use with the genetic algorithm, specifically the population size versus the number of generations. Three different scenarios were tested, keeping the total number of function evaluations roughly constant: a large population size (80) with a small number of generations (12); an average population size (30) with an average number of generations (30); or a small population size (12) with a large number of generations (80). It was found that the first scenario yielded the best results for this problem. It is certainly not a guarantee that the same relative results would be found when scaled up, however this provided for some quantitative reasoning for the values chosen (Population = 1000, Generations = 10).

8.1.1.4 Gradient Based Algorithm

A sequential quadratic programming (SQP) algorithm was implemented as the gradient based scheme. The initial guess is supplied as the best population found during the single objective genetic algorithm optimization. The first and

second derivatives are calculated at the initial guess and at each subsequent iteration using finite differencing. Although additional function evaluations are necessary to generate second order information, the number of iterations can often decrease as compared to a first order method, which reduces the overall number of function evaluations. At each iteration a subproblem is setup to find the search direction. Once the search direction is determined, a line search is performed in order to select the proper step size which will minimize the objective function along the search direction. With the search direction and step size determined, the next iteration's design point is calculated. This process is repeated until stopping criteria is reached. For this problem, the optimization was deemed complete when the norm of the step size was sufficiently small.

8.1.2 Results

Both of the optimization methods were instrumental in the overall solution, as improvement was made through generations and iterations in both. Once the stopping criteria was reached for all thirty five v_∞^- optimization runs for all three planets, over 2362500 function evaluations (distinct simulation runs) had been completed. This includes 1000 simulations per generation of the genetic algorithm, and roughly 500 cases for each iteration of the subsequent SQP algorithm. Once the best trajectory was found for a fixed value of ξ, the value of ϵ_{ascent} was varied to generate data for the full range of ξ conditions outlined in Table 8.1. The results are presented and discussed in this section.

The most important results of this section are shown in Figures 8.3, 8.5 and 8.7. These plots present the least amount of energy loss that would allow a given planetary fly-by turning angle at a given approach velocity. The maximum performance for a given turning angle and the associated minimum energy loss is important, as theoretically, any lesser amount of planetary turning is possible, simply using a

higher drag configuration vehicle. Presumably, each trajectory found in this study required the minimum drag configuration in order to complete the mission losing the least amount of energy as possible. A lesser drag configuration, capable of increased planetary turning, was not found to be feasible. However, a higher drag configuration should theoretically always be possible. Therefore, if the maximums are used as an upper limit on performance here, then subsequent trajectory design has a feasibility boundary.

In previous work,[75,81] an analytical correlation was used to determine the energy loss which would occur during a given aero-gravity assist fly-by:

$$\Theta = \Theta_{GA} + \sin^{-1}\left(\frac{1}{1+rv^2/\mu}\right) + \sin^{-1}\left(\frac{e^{2\Theta/(L/D)}}{1+rv^2/\mu}\right) \tag{8.11}$$

The data in these figures are an alternative, developed using optimization methods and removing assumptions about a constant flight altitude and a constant lift-to-drag ratio. Each data point used to generate these figures represents an AGA trajectory found during this study. On the other hand, Figures 8.4, 8.6 and 8.8 display the theoretical performance using Equation 8.11.

The trends in the pairs of plots corresponding to the same planet are identical, as the data used to populate the analytical charts was numerically extracted from the trajectories in the optimized charts. For example, in Figure 8.3, with an approach speed of $v_\infty^- = 20$ km/s, an AGA trajectory was found in which the ratio of energy before and after entry, C_3^+/C_3^-, was equal to .5 for a turning angle of 120°. The lift-to-drag ratio of this trajectory varies, as the vehicle varied its lift vector to maintain constant altitude. The maximum value of lift-to-drag ratio was extracted from this trajectory, as was the altitude at which the maximum L/D occurred. Then, using those values, Equation 8.11 was used to determine that analytically, it would be expected that 120° of turning would be possible with $C_3^+/C_3^- = .7$.

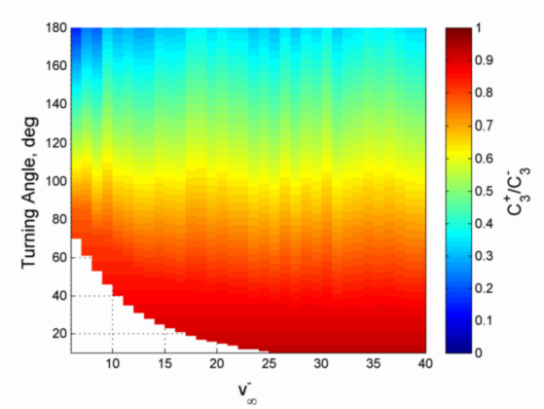

Figure 8.3: Maximum AGA performance for aero-gravity assist at Venus

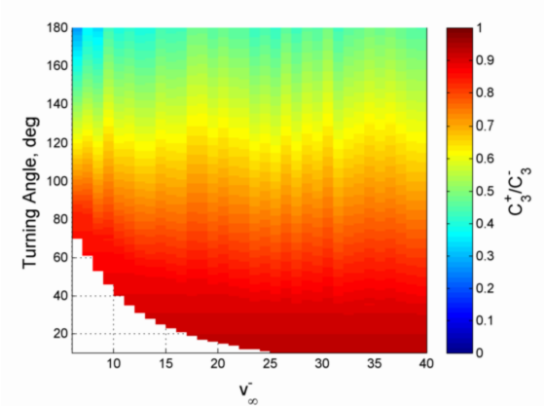

Figure 8.4: Analytic AGA performance for aero-gravity assist at Venus

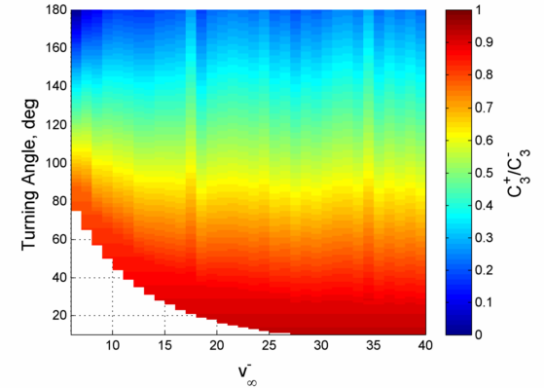

Figure 8.5: Maximum AGA performance for aero-gravity assist at Earth

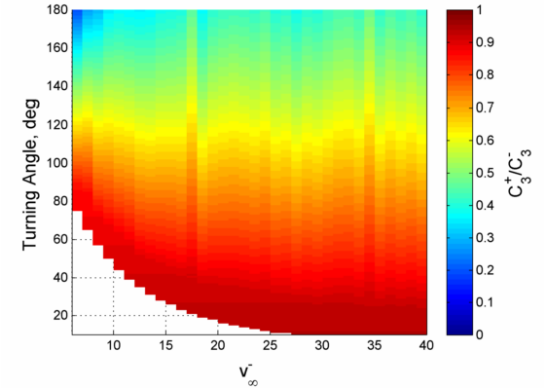

Figure 8.6: Analytic AGA performance for aero-gravity assist at Earth

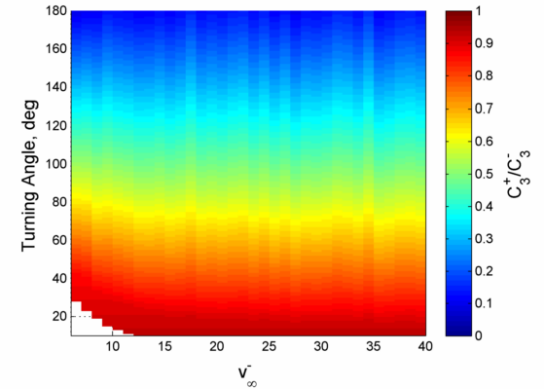

Figure 8.7: Maximum AGA performance for aero-gravity assist at Mars

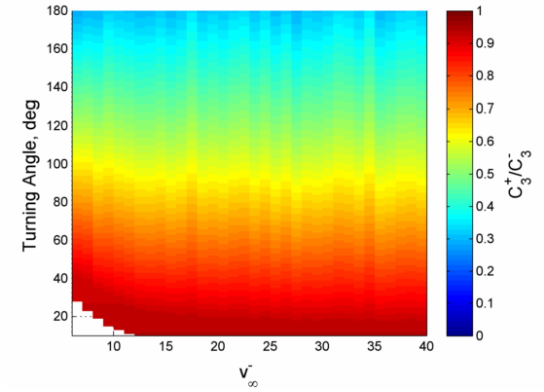

Figure 8.8: Analytic AGA performance for aero-gravity assist at Mars

Comparing the analytic data to the optimized data, a loss of 10% to 30% was found. This is attributable to two causes: inefficiency in the control system used and losses associated with ascent and descent. The vehicle does not fly at constant L/D in a real trajectory, and the lift vector must be varied in order to maintain a realistic constant altitude flight. This decreases the efficiency of the maneuver. A more sophisticated control system would likely be able to recover some of these losses. On the other hand, Equation 8.11 assumes that the entire maneuver occurs at a constant altitude. Beyond the slight variations associated with a real trajectory, this ignores the descent into the atmosphere and the ascent out. In these flight regimes, the waverider is far away from its on-design conditions, and are some of the least efficient portions of the flight path.

Note that each plot has a region where no trajectories were plotted in the lower left hand corners. These correspond to regions for which gravity assist alone would have sufficed, therefore AGA is not necessary or possible.

As has been suggested by previous work,[74] Venus was found to be the most promising for aero-assisted maneuvers, followed by Earth and then Mars. The atmospheric composition of each planet is capable of sustaining varying levels of aerodynamic performance and associated lift-to-drag ratios. Further, Earth and Venus are more massive planets, therefore they provide increased gravitational accelerations compared to Mars. This is seen both by the improved AGA performance, and with the larger GA only regions in the lower left hand corners.

The sinusoidal relationship between $\Delta|v|$ and $\Delta\Theta$ is displayed in Figures 8.9, 8.11 and 8.13. Each curve represents the relationship for a fixed value of v_∞^-. These curves, closely match the relationship predicted using simplifying assumptions in the derivation of Equation 8.9. If ξ were able to have a value of 1 for all of these trajectories, then the sinusoidal peaks would occur at $\Delta\Theta = 180^\circ$ and $\Delta|v|/\Delta|v|_{max} = 1$. It was expected that the amplitude would decrease from this theoretical maximum,

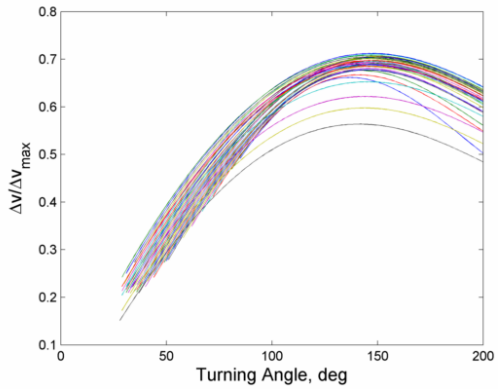

Figure 8.9: Variation in $\Delta|\boldsymbol{v}|$ with $\Delta\Theta$ about Venus. Note the amplitude decrease and the phase shift.

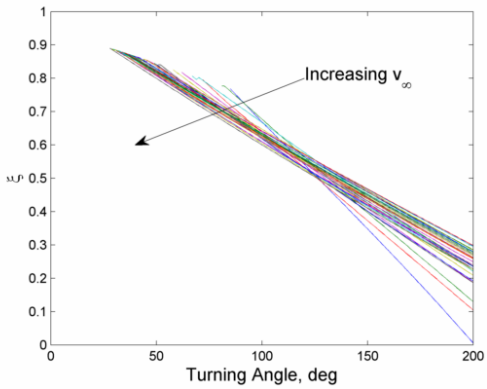

Figure 8.10: Hyperbolic velocity fraction required to achieve a given turning angle about Venus

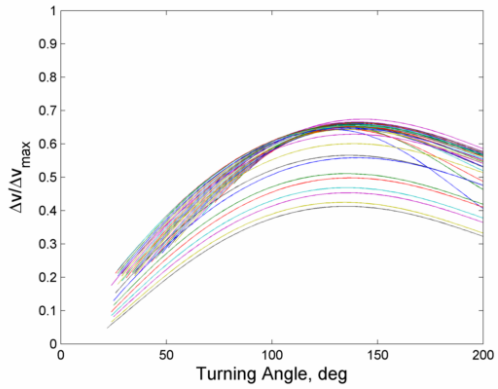

Figure 8.11: Variation in $\Delta|\boldsymbol{v}|$ with $\Delta\Theta$ about Earth. Note the amplitude decrease and the phase shift.

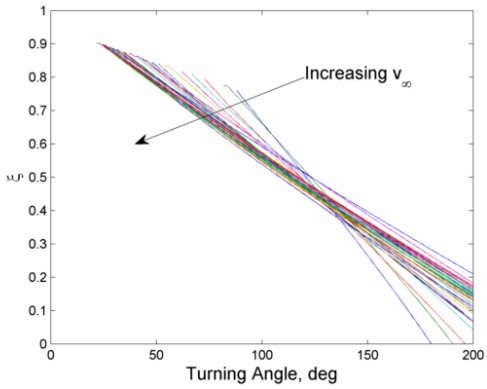

Figure 8.12: Hyperbolic velocity fraction required to achieve a given turning angle about Earth

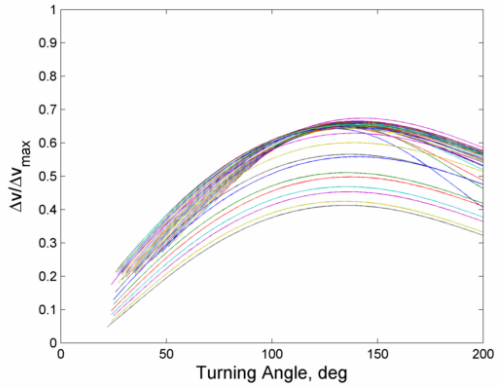

Figure 8.13: Variation in $\Delta|\boldsymbol{v}|$ with $\Delta\Theta$ about Mars. Note the amplitude decrease and the phase shift.

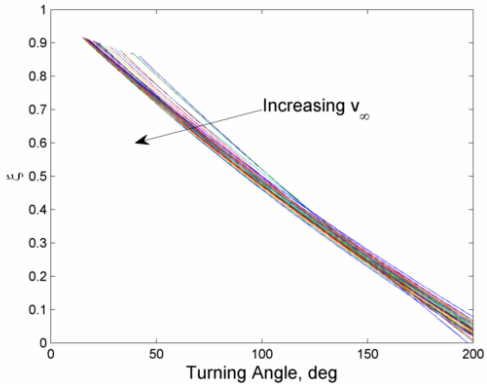

Figure 8.14: Hyperbolic velocity fraction required to achieve a given turning angle about Mars

as ξ cannot equal 1 for an aero-gravity assist mission which enters the atmosphere. As can be seen from the figures, the maximum velocity increases does not occur at 180° though. This may at first seem non-intuitive.

In order to explain the phase shift, first consider the rate at which ξ changes with $\Delta\Theta$ as shown in Figures 8.10, 8.12 and 8.14. These plots are a 2d, side view of the data presented in Figures 8.3, 8.5 and 8.7. The curves connect data points with constant v_∞^-. Each data point represents the necessary energy loss to achieve a given amount of turning during the cruise. The magnitude of the slope of the curve can be thought of as an energy loss rate, or the rate at which hyperbolic excess velocity is exchanged for increased turning around the fly-by planet. Recall that gravity and aero-gravity assists are promising because turning around a fly-by planet using gravitational forces can increase velocity relative to the Sun. The velocity increase as a function of turning is approximated by Equation 8.9. As explained previously, with fixed values of v_∞^-, ξ, and v_{Planet}, this equation is maximized for $\Delta\Theta = 180°$. Unfortunately, as shown in Figures 8.10, 8.12 and 8.14, ξ is itself a function of $\Delta\Theta$ as well.

Physically, as the turning angle nears 180°, the benefit of turning the spacecraft's velocity vector to be better aligned with the planet's velocity vector no longer outweighs the energy loss rate. For this reason, the peaks in Figures 8.9, 8.11 and 8.13 occur slightly *earlier* than what would be the geometrically predicted maximum of 180°. In terms of heliocentric velocity gain, it is more optimal to exit the atmosphere earlier than would allow departing the planet in the fully parallel direction.

Using the assumption of a planar maneuver, used to derive Equation 8.8, an estimation of the turning angle which maximizes heliocentric velocity increase can be made. No longer restricting the approach angle ψ to zero, even the theoretical maximum turning angle would no longer be 180°, as the angle which would leave

the vehicle parallel to the planet's velocity upon departure is instead 180°-ψ. First, modify Equation 8.8 with $\Delta\Theta' = \Delta\Theta + \psi$:

$$\Delta|v| = \left|\begin{bmatrix} v_\infty^- \xi sin(\Delta\Theta') \\ -v_\infty^- \xi cos(\Delta\Theta') + v_{\text{Planet}} \end{bmatrix}\right| - \left|\begin{bmatrix} v_\infty^- sin(\psi) \\ -v_\infty^- cos(\psi) + v_{\text{Planet}} \end{bmatrix}\right| \tag{8.12}$$

In order to calculate where the peak occurs, take the derivative of $\Delta|v|$ with respect to $\Delta\Theta$' and set it equal to zero:

$$\frac{d(\Delta|v|)}{d(\Delta\Theta')} = \frac{v_\infty^- \left[v_{\text{Planet}} \cos(\Delta\Theta + \psi)\frac{d\xi}{d\Delta\Theta'} + \xi(v_\infty^- \frac{d\xi}{d\Delta\Theta'} - v_{\text{Planet}} \sin(\Delta\Theta + \psi))\right]}{\sqrt{(v_\infty^-)^2\xi^2 + 2v_\infty^- v_{Mars}\xi \cos(\Delta\Theta + \psi) + v_{\text{Planet}}^2}} = 0 \tag{8.13}$$

or, more simply:

$$v_{\text{Planet}} \cos(\Delta\Theta + \psi)\frac{d\xi}{d\Delta\Theta'} + \xi(v_\infty^- \frac{d\xi}{d\Delta\Theta'} - v_{\text{Planet}} \sin(\Delta\Theta + \psi)) = 0 \tag{8.14}$$

The values shown thus far for $\Delta\Theta$, ξ, and ξ' (calculated numerically from Figures 8.10, 8.12 and 8.14) are independent of the value of ψ, therefore by simply varying ψ, using the data presented thus far in this section and solving for $\Delta\Theta$' in Equation 8.14, the value of $\Delta\Theta$ which maximizes Δv for any approach direction can be found without needing to simulate any additional trajectories.

Let the term 'antecedent angle' be defined as the angle by which the peak heliocentric velocity increase precedes the parallel direction (see Figure 8.1). For a given approach angle ψ, the antecendent angle is:

$$\text{antecedent angle} \equiv \pi - \Delta\Theta' = \pi - \psi - \Delta\Theta \tag{8.15}$$

The antecedent angle for various approach direction and speeds is presented in Figures 8.15 - 8.17. First, note that the curves are not defined for all approach angles, as there were not AGA trajectories found for all turning angles. The maximum

approach angle for which a given curve is defined, corresponds to the minimum turning angle for which data is available in Figures 8.3, 8.5 and 8.7.

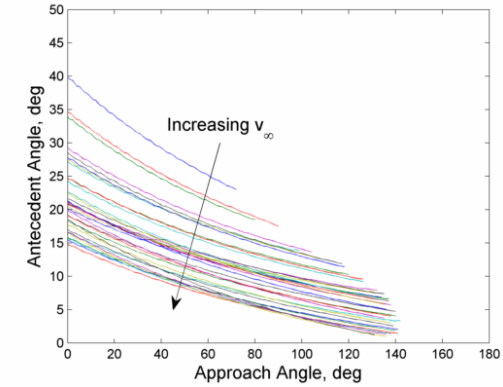

Figure 8.15: Planetary departure angle away from parallel to Venus' velocity vector which maximizes heliocentric velocity gain

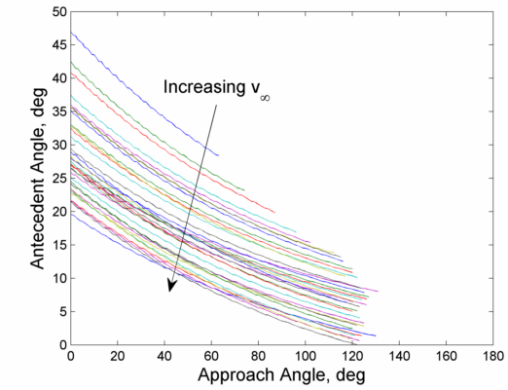

Figure 8.16: Planetary departure angle away from parallel to Earth's velocity vector which maximizes heliocentric velocity gain

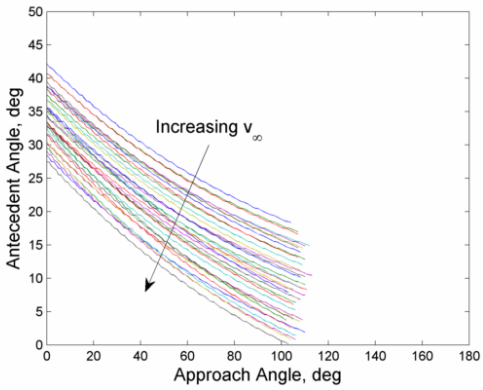

Figure 8.17: Planetary departure angle away from parallel to Mars' velocity vector which maximizes heliocentric velocity gain

Even though the value of $\frac{d\xi}{x\Delta\Theta}$ is roughly constant (the slope in Figures 8.10, 8.12 and 8.14), the antecedent angle is not at all constant. Again, the physical explanation for the presence of a non-zero antecedent angle is that the benefit of increased alignment between the spacecraft departure vector and the planet's velocity vector does not always outweigh the rate of hyperbolic excess velocity decay. It might be expected then, that the antecedent angle would be constant, regardless of

approach angle. It is not however, and there is a sinusoidal relationship.

The magnitude of the antecedent angle is very much a function of v_∞. As the approach energy decreases, the antecedent angle increases greatly, to as high as 45° in some cases. This phenomena occurs because as v_∞ decreases, there is less excess velocity that can be lost for the spacecraft to remain on an escape path. While increased turning is favorable for heliocentric velocity increase, it is not beneficial if the spacecraft can barely escape the fly-by planet.

The relatively large magnitude of the antecedent angles for many approach conditions underscores the need to factor energy loss rate into the detailed design of an AGA maneuver, as energy loss rate could be optimized over as well.

8.2 Mission Design Process

Adding even a single atmospheric entry to a series of fly-bys necessitates different design methods to generate the tour through the solar system as well as design a spacecraft capable of performing the hypersonic flight. In this section, a process is presented for designing all preliminary aspects of missions employing aero-gravity assists and resulting in a high fidelity, flyable trajectory. The overall objective is to have a trajectory which will take a spacecraft from Earth to some final destination. This is completed in three separate stages.

8.2.1 Phase Free Design

First, candidate planetary fly-by sequences are determined by considering a simplified version of the planets' orbits. Each is assumed to be on a perfectly circular Keplerian orbit around the Sun with zero inclination and radius equal to an average value of the planet's semi-major axis. Given these assumptions, the planet's phase around its orbit is not needed to consider departure from or arrivals

to that planet. For a given hyperbolic excess velocity, v_∞, varying the departure or approach angle from 0° to 360°, yields heliocentric orbits. Note that the orbit yielded from a departure angle of Φ is identical to those from a departure angle of $360 - \Phi$ or approach angles of Φ or $360 - \Phi$.

For each heliocentric orbit, certain parameters can be identified, including perihelion radius, orbital energy, and orbital period (when the orbit is not parabolic or hyperbolic). If two planets have individual pairs of departure angle and local v_∞, which yield the same heliocentric orbit, as defined by identical orbital energy and perihelion, then this orbit is a valid phase-free transfer orbit. As a means of identifying transfer orbits, Strange and Longuski developed a graphical method of searching for these routes using so-called Tisserand charts (see Figure 8.18).[128] The method was later updated to allow for aero-gravity assists as well as gravity assists by Johnson and Longuski.[78] Each curve on the Tisserand chart represents the locus of possible heliocentric orbital parameters by varying the departure angle from 0° to 360° with a fixed value of v_∞ relative to the planet. Therefore, any intersections represent a heliocentric orbit that would allow transfer between two different planets. The time of flight can be calculated by solving Kepler's problem for the four different combinations of departure and approach angle corresponding to a given intersection.

By moving along a single curve, from one intersection to another, a gravity assist is mapped out (see Figure 8.19). In some cases, the intersections along a single curve necessitate a turn around the planet from approach angle to departure angle which is too great to be completed in only one gravity assist fly-by. When considering gravity assist alone, these solutions are thrown out. When allowing for aero-gravity assists, the solution is considered, but the departure intersection must be moved to a curve with lower v_∞ (see Figure 8.20). The maximum gravity assist

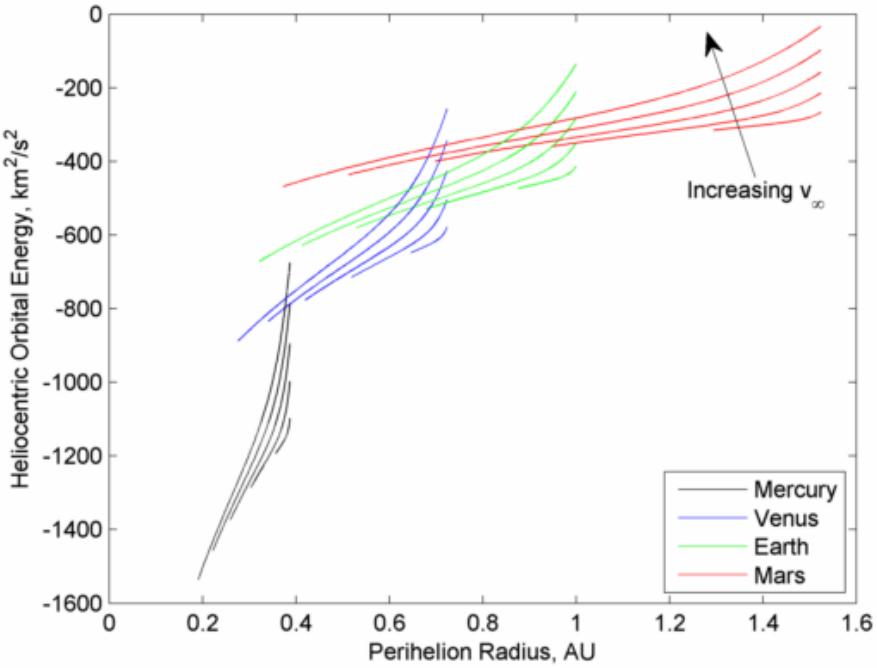

Figure 8.18: Tisserand chart for the inner planets. Curves shown for v_∞ = 1, 3, 5, 7, 9 km/s

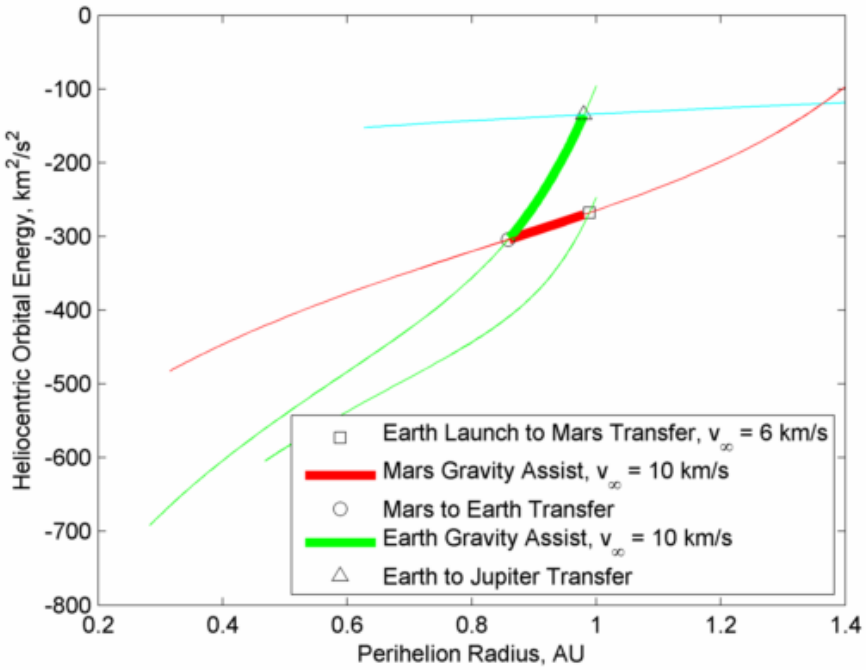

Figure 8.19: Tisserand Route for Earth to Jupiter using gravity assist only

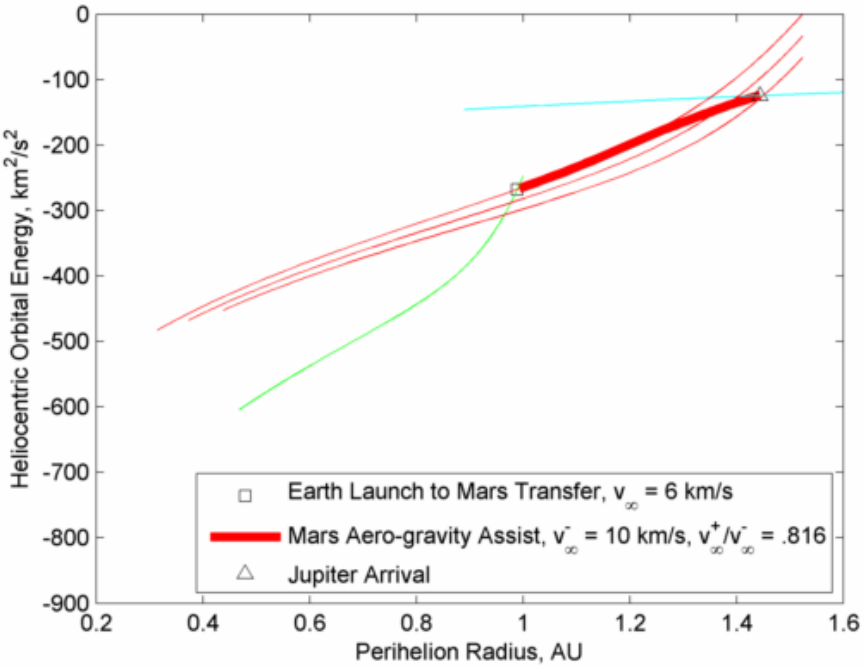

Figure 8.20: Tisserand Route for Earth to Jupiter using aero-gravity assist

only turning angle can be calculated using the following equation:

$$\Theta_{GA} = \pi - 2\cos^{-1}\left(\frac{1}{1-\frac{r_p v_\infty^2}{\mu}}\right) \tag{8.16}$$

where all values are relative to the fly-by planet, not the Sun. A reasonable minimum allowable r_p for the inner planets is 500 km above the surface and 5 times the radius of the planet for the outer planets.

In the case of an aero-gravity assist, determination of a maximum feasible turning angle is more complicated. In fact, where the present method of AGA design departs from previous work is the fidelity of the aero-gravity assist data. Rather than use an analytic trajectory model assuming a constant lift-to-drag ratio and ignoring the ascent and descent into the atmosphere, maximum AGA performance is calculated with hypersonic shape and trajectory optimization. To determine the turn possible in one AGA pass, and the associated loss in v_∞, data generated using

the method presented in Section 8.1 and shown in Figures 8.3, 8.5 and 8.7 is used. The color for a given combination of v_∞ and turning angle indicates the maximum possible departure hyperbolic velocity, or the maximum ratio C_3^+/C_3^-. Any data point on or below this surface indicates that the maneuver is possible, simply with an equally efficient or less efficient atmospheric flight. If the data point is below the mesh, then additional velocity must be lost to drag as compared to the optimal solution. In this first stage of design, only maximum performance is assumed. When lowering the outbound trajectory to a lower v_∞ line, a curve is followed equaling the optimal maneuver data.

It is important to note that the AGA performance data set is trajectory and aerodynamically constrained, but not aerothermally. Given uncertainties in both passive and active cooling technology, aerothermal concerns are better left as an objective, rather than a constraint.

Algorithm 1 explains the process of searching for phase free trajectories. First, each allowable fly-by planet is iterated over as are the allowable values of excess velocity, v_∞, and approach/departure angles, Φ. At each unique combination, the orbital period, perihelion radius and orbital energy are determined. These values are all stored and create the Tisserand chart (see Figure 8.18). Next, iterations move from the initial departure to the final destination by way of searching for intersections. The initial condition is the Tisserand curve matching the launch C_3 or v_∞ from Earth. All Tisserand curves which intersect the initial curve are found and cataloged. In the case of the initial departure, there is no arrival angle, so any departure angle is allowable. In subsequent fly-bys, feasibility must be checked against the maximum turning angle from Equation 8.16. If a given intersection point would require excessive turning from the previous intersection point for a gravity assist, then a solution is searched for along the maximum AGA Tisserand curve instead (see Figure 8.20). The process is repeated iteratively until one of three

Algorithm 1 Pseudocode of Phase Free Trajectory Design

select maximum v_∞
for planet = allowable fly-by body **do**
  for $v_\infty = 1 : v_{\infty,\max}$ **do**
    for $\Phi = 1^\circ : 360^\circ$ **do**
      $v = \begin{bmatrix} v_\infty \cos\Phi \\ v_\infty \sin\Phi \\ 0 \end{bmatrix} + \begin{bmatrix} 0 \\ v_{\text{Planet}} \\ 0 \end{bmatrix}$
      $r = \begin{bmatrix} r_{\text{Planet}} \\ 0 \\ 0 \end{bmatrix}$
      $\epsilon = \frac{v^2}{2} - \frac{\mu}{r}$ ▷ Calculate heliocentric energy
      $[a, e] = \text{Cartesian\_to\_Keplerian}(r, v)$
      $T = 2\pi\sqrt{\frac{a^3}{\mu}}$ ▷ Calculate period
      $r_p = a(1 - e)$ ▷ Calculate perihelion radius
    end for
  end for
end for
select destination planet
time of flight = 0
while current planet ≠ destination planet **do**
  for planet = allowable fly-by body **do**
    for $v_\infty = 1 : v_{\infty,\max}$ **do**
      look for intersections between Tisserand curves for (departure planet, departure v_∞) and (planet, v_∞)
      if intersection found **then**
        if arrival angle + maximum turn < departure angle **then**
          $\cos(\nu) = \frac{1}{e}\left(\frac{a(1-e^2)}{r} - 1\right)$ ▷ Calculate true anomaly
          $E = \frac{e+\cos(\nu)}{1+e\cos\nu}$ ▷ Calculate eccentric anomaly
          $M = E - e\sin(E)$ ▷ Calculate mean anomaly
          time of flight = time of flight + $T\frac{M}{2\pi}$
          update arrival angle
          departure planet = planet
          departure $v_\infty = v_\infty$
        end if
      end if
    end for
  end for
end while

stopping conditions: a maximum number of GA or AGA fly-bys has occurred, the total time of flight exceeds a maximum allowable, or until the desired destination planet is reached.

This phase free method is only an idealized, best case scenario, and real times of flight will be greater, or non-existent in certain cases. The trajectories found require all planets to be in an optimal position along their orbits when fly-by would occur. This is of course unlikely to be the case, but a phase free search is an important tool in suggesting promising planet sequences before searching for launch opportunities among the thousands of possible permutations of solar system bodies.

8.2.2 Launch Opportunity Search

With promising paths defined, the phasing of the planets is accounted for to determine launch opportunities to the planets using real ephemerides. Algorithm 2 and Figures 8.21 - 8.23 overview the steps involved in the process.

The overall launch window is discretized with a node every dt days (see Figure 8.21. The acceptable time of flight range to the first destination is as well, creating a grid. At each node location, Lambert targeting is used to search for conical solutions to connect the first and second planetary locations with the associated launch date and time of flight. Multi-revolution type I and II Lambert solutions are allowed. Spheres of influence are ignored, and gravity assists and aero-gravity assists are modeled as instantaneous changes of direction.

For a given conic trajectory connecting the first two planets, the spacecraft has a fixed arrival C_3. In the case of a gravity assist, the following departure C_3 must be identical. The Lambert problem must thus be solved in reverse. Conic arcs between the second and third planets are found iteratively, until a time of flight is found which requires the proper departure C_3. Again, multi-revolution type I and II Lambert solutions are allowed. If the destination planet of the iterative Lambert

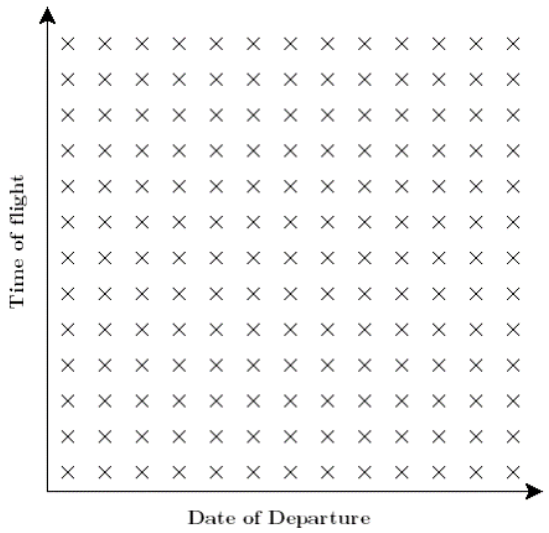

Figure 8.21: Launch opportunity search grid. A lambert arc from Earth to the first fly-by planet is searched for at each x.

solver is one of the inner planets (Mars, Earth, Venus, Mercury), then multiple planet revolution solutions are allowed as well. A similar solution method has been presented previously, and termed C_3 matching.[129] This process is repeated for each fly-by in the sequence until the ultimate destination planet has been reached.

When connecting each Lambert arc, maximum performance of both gravity-assist and aero-gravity assist is needed to determine feasibility. In the case of gravity assist, the maximum allowable angular difference between the in-bound and out-bound Lambert trajectories is again directly calculable using Equation 8.16.

When gravity-assist alone is infeasible, then AGA is considered. Once again, a solution is deemed viable by comparison with the maximum performance data in Figures 8.3, 8.5 and 8.7. Unlike in the phase-free design method, however, trajectories are not designed to require maximum AGA performance unless necessary. As the time of flight varies in the inverse Lambert solver described above, both the ratio of departure C_3 to approach C_3 and angular turn vary. This relationship is plotted in Figure 8.22 along with data reproduced from Figure 8.3. The trajectory solution chosen is the one which corresponds to the easiest aero-gravity assist, as defined by

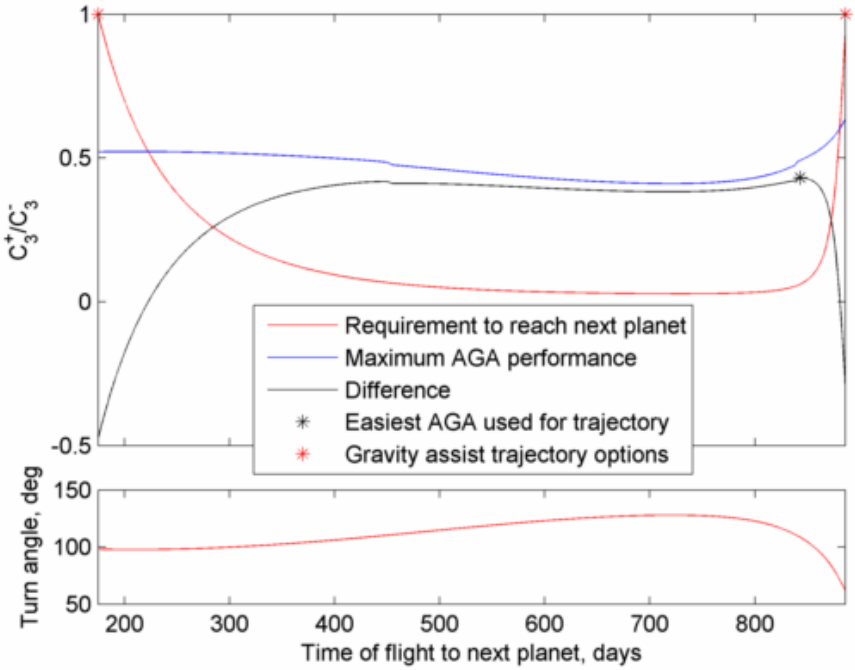

Figure 8.22: Aero-gravity assist selection criteria, the 'easiest AGA' method. Solution chosen which maximizes the difference between requirement and capability

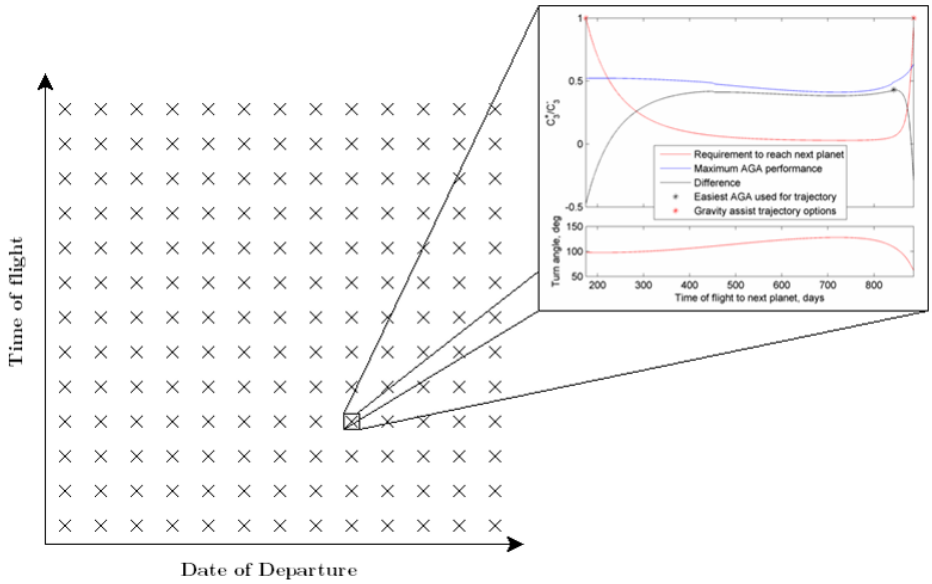

Figure 8.23: At each launch opportunity, sequentially search for gravity assist and aero-gravity assist options.

Algorithm 2 Pseudocode of Iterative Lambert Search

```
select maximum launch energy, C_{3,max}
select earliest and latest allowable launch dates, Date_0 and Date_F
select interval between launch searches, dt_1
select minimum and maximum time of flight to first fly-by, TOF_0 and TOF_F
select interval between time of flight, dt_2
time to destination = 0
for launch date = Date_0:dt_1:Date_F do
    for TOF = TOF_0:dt_2:TOF_F do
        [r_Dep, v_Dep] = EphemerisData(Earth, launch date)
        [r_Arr, v_Arr] = EphemerisData(Fly-by Planet 1, launch date + TOF)
        [v_Trans,Dep, v_Trans,Arr] = Lambert(launch date, TOF, r_Dep, r_Arr)
        C_3,Dep = [v_Trans,Dep − v_Dep]·[v_Trans,Dep − v_Dep]
        C_3,Arr = [v_Trans,Arr − v_Arr]·[v_Trans,Arr − v_Arr]
        if C_3,Dep < C_3,max then
            [r_Dep, v_Dep] = [r_Arr, v_Arr]
            dep. date = launch date + TOF
            C_3,Dep = C_3,Arr
            for planet = [Fly-By Planet 2,...,Destination Planet] do
                [v_Trans,Dep, r_Arr, v_Arr, TOF_new] =
                        C_3Matching(C_3,Dep, dep. date, EphemerisData, r_Dep)
                Θ = cos^{-1}( ([v_Trans,Arr − v_Dep]·[v_Trans,Dep − v_Dep]) / C_3,Arr )
                if Θ < Θ_max then
                    [v_Trans,Dep, v_Trans,Arr] = Lambert(dep. date, TOF_new, r_Dep, r_Arr)
                    C_3,Arr = [v_Trans,Arr − v_Arr]·[v_Trans,Arr − v_Arr]
                    C_3,Dep = C_3,Arr
                    [r_Dep, v_Dep] = [r_Arr, v_Arr]
                    dep. date = dep. date + TOF_new
                else
                    [v_Trans,Dep, r_Arr, v_Arr, TOF_new, C_3,Dep] =
                            AGA_Search(C_3,Arr, dep. date, EphemerisData, r_Dep)
                    [v_Trans,Dep, v_Trans,Arr] = Lambert(dep. date, TOF_new, r_Dep, r_Arr)
                    C_3,Arr = [v_Trans,Arr − v_Arr]·[v_Trans,Arr − v_Arr]
                    [r_Dep, v_Dep] = [r_Arr, v_Arr]
                    dep. date = dep. date + TOF_new
                end if
            end for
        end if
    end for
end for
```

the greatest magnitude between the two curves. Any point below the blue curve in Figure 8.22 is theoretically possible, but the further from this upper limit, the easier the aerodynamic design requirements on the AGA aero-shell as additional energy can be lost to drag. Note that the upper corners of the figure, where C_3^+/C_3^- equals 1, are the trajectory options selected for gravity assist alone, if the turning required was feasible without entering the atmosphere.

The final product of the launch opportunity search is a pork chop like plot, showing Earth departure C_3 values for all launch opportunities.

8.2.3 Optimization

The last stage of the AGA design process is to solve for real trajectories, by numerically propagating the entire flight from launch to arrival. This eliminates the minor inaccuracies associated with assuming entirely heliocentric Keplerian orbits. Further, a full trajectory propagation allows the atmospheric portion of any aero-gravity assists to be optimized.

An n-body simulation was created, accounting for the gravitational acceleration of every solar system body at each time step. Further, if or when the spacecraft entered a planetary atmosphere during the simulation propagation, then the multitude of hypersonic flight models described in previous chapters were invoked. A promising launch opportunity from the sequential Lambert solver is used as the starting guess for launch date and direction. The date, direction and energy of any impulsive maneuvers are the only trajectory inputs. The atmospheric flight models require a number of additional design parameters however, including those to define the aero-shell shape and the flight control law.

When performing interplanetary trajectory optimization, there are a number of objectives which could be maximized or minimized. These include time of flight, mass delivered, launch energy, or Sun-Earth angles. When including an atmospheric

fly-by, all of these objectives remain, but there are numerous additional potential objectives regarding the atmospheric trajectory alone, such as minimum heat load during AGA, maximum aero-shell volume, or minimum structural load.

8.3 Case Study of an Interstellar Probe

The end to end method of AGA interplanetary mission design is demonstrated by applying it to the construction of an interstellar probe trajectory. Each of the three stages were conducted and the results will be presented and discussed in the following sections. For comparison, the results will be evaluated in contrast to the baseline trajectories of previous studies of interstellar probes including those in Refs. 98 and 103.

8.3.1 Design Space

The design constants presented in Table 8.2 have great bearing on the overall results. The launch window was selected to provide a wide data set, without requiring infeasible calculation time. A similar criteria dictated the grid interval. An 8 day search algorithm is fine enough that it will be unlikely to altogether miss any launch opportunities, while being coarse enough to limit the computation time required. Admittedly, a finer grid would generate Lambert results which were closer to optimal.

Table 8.2: Case Study Parameters

Earliest Launch Date	01-Jan-2018
Latest Launch Date	31-Dec-2040
Grid search interval	8 days
Launch energy	154 km^2/s^2
Spacecraft Mass	1000 kg
Max v_∞ for AGA	40 km/s
Max AGA manuevers	2
Destination	200 AU

The allowable launch energy was selected for two important reasons: 1) along with the selected spacecraft mass, this is the expected capability of NASA's developing Space Launch System (SLS)[130] and 2) this was the maximum allowable C_3 in the solar sail to 200 AU trajectory study conducted in Ref. 103. This is an extremely high launch energy, but is likely necessary in order to limit flight time when attempting to escape the solar system!

The maximum allowable approach hyperbolic velocity was limited to 40 km/s. As the approach energy increases, the heat rate and heat load increase exponentially.[131] Even forecasting technology advancements, an atmospheric entry corresponding to $v_\infty > 40$ km/s is far-fetched. Minimizing the required entry speed is a promising objective that could be used in n-body optimization.

While there is good intuition to suggest that using only one AGA in a given trajectory is advisable, given the difficulty of the maneuver, a maximum of 2 per trajectory will be allowed in order to compare the results. Similarly, from an operational and human safety standpoint, it is unlikely that an aero-gravity assist will be performed at Earth. Again for completeness and comparison's sake, Earth will be fully included, along with more promising AGA bodies, Venus and Mars.

Finally, the destination is listed as simply 200 AU. At this stage of design, no attention was paid to the azimuth or declination of the departure vector to interstellar space. There are possibly certain scientific benefits for exiting the solar system in a particular direction, however the scientific community does not appear to currently have a consensus on what those directions might be. For this trajectory study, therefore, the departure angle will not be constrained.

8.3.2 Phase-Free Results

Thousands of different planet sequences were isolated and analyzed. As a means of observing the phase free results, see Figure 8.24. Each overlapped shaded

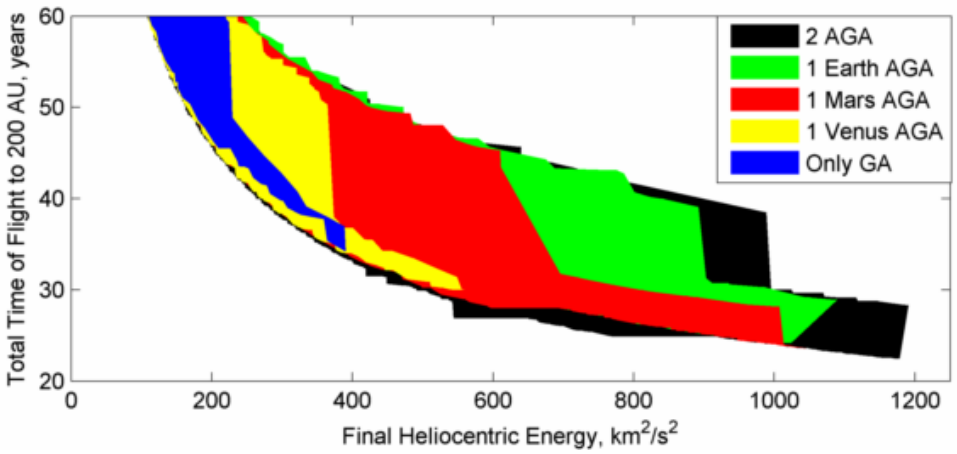

Figure 8.24: Relative phase free time of flight to interstellar space using AGA at different planets

region represents the area over which phase-free trajectories were found. The straightforward relationship between final heliocentric energy and the total time of flight is as expected. More importantly though, the data are presented in this way in order to demonstrate the relative size and shapes of each colored area. Immediately, the benefit of using aero-gravity assist is seen. Not only does the minimum time of flight decrease, but the range of trajectory options increases as well. For a given final energy, the diversity of routes increases for one AGA maneuver over gravity assist alone, or two AGA manuevers instead of just one.

The relative utility of a single aero-gravity assist maneuver around each of the inner planets carries information about the difficulties of the interstellar trajectory problem, the dissimilarities in the planets' physical characteristics, as well as design constraints. As seen in Figures 8.3, 8.7 and 8.7, Venus can sustain the most efficient AGA performance, followed by Earth and then Mars. This does not translate to fast interstellar trajectories, however. To understand, consider the trajectory routes presented in Table 8.3. This table does not contain exhaustive phase-free routes, but note that all AGA trajectories involve an atmospheric fly-by, sandwiched between two outer planet gravity assists. This would likely only be optimal in the case of an extremely long trajectory, such as one to 200 Astronomical Units away from the

Sun. The outer planet to AGA to outer planet flight sequence immediately favors Earth over Venus and Mars over both.

Although greater turning is possible with aero-gravity assist, the capability is not unlimited, and predicted waverider performance is often insufficient to complete a turn from Jupiter to Venus back to Jupiter, for example. A related issue is the relative velocities of the planets. Because the velocity of Venus is greater than Earth, relative velocity with an inbound spacecraft is more likely to surpass the 40 km/s limit. Further, as Venus is closer to the Sun, the spacecraft will be closer to its maximum, periapse velocity. These two factors explain why Venus does not have as rapid of a phase free trajectory option. If v_∞ had been allowed to go higher, more Venusian routes would be expected. The same comparisons apply to Earth as opposed to Mars, however, in this case, Earth's superior AGA capacity balances out its orbital limitations. The ideal phase free time of flight is nearly identical with Mars.

Due to the curvature of the relationship between heliocentric energy and time of flight, performing a second aero-gravity assist has less of a benefit than adding the first. As mentioned above, performing two AGA maneuvers in the same trajectory has many practical drawbacks, and now it is seen that there are limited benefits as well. At least in the case of an interstellar mission, phase free methodology suggests that one Earth or Mars AGA is as good as performing two (any combination of Venus, Earth and Mars was allowed).

Recall that the phase free method can be considered an ideal, best possible case. It is therefore not expected that with any combination of GA or AGA maneuvers that a trajectory will be found to 200 AU in less than 20 years. In one of the original proposals of a dedicated interstellar probe, Etchegaray[99] determined that a direct trajectory to 1000 AU could be completed in 50 years with nuclear powered electric propulsion. A rough calculation suggests that this corresponds to arriving

at 200 AU in under 15 years. There is no reason that the two methods could not be combined for an even greater boost, but on the basis of individual merits, nuclear electric rockets appear to hold more promise.

8.3.3 Launch Opportunities

With a substantial set of routes suggested, the iterative grid search algorithm along with ephemeris data from JPL's HORIZONS system examined real world feasibility. 75 different planet sequencings from Earth to 200 AU were tested. Table 8.3 lists the routes which had sub-60 year trajectories along with details of their fastest trajectory.

While the first stage of design was instrumental in proposing the 75 routes searched, the trends vary sharply from the predictions of Figure 8.24. First, the two best routes found were not for a two AGA trajectory, or even an Earth AGA, but for single Mars aero-gravity assists. The explanation for the lack of Earth and Venus trajectories is again the limit on maximum approach v_∞. Had this constraint been lifted, many more trajectories would likely be found. This helps to explain the dearth of low time of flight routes with two AGA maneuvers as well. Even though the AGA maneuver dissipates energy relative to the local planet, it picks up heliocentric energy during the manuever (as was shown in Figure 8.20). This means that subsequent fly-bys will likely be more energetic, and there is a greater chance that a subsequent AGA would need $v_\infty^- > 40$ km/s.

The lack of 2-AGA routes less than 40 years is also likely due to the increasing need for planets to be aligned in the correct location. With each additional planet added to the route, one more planet must be in a feasible location. AGA widens the range of acceptable phasing as compared to gravity assist alone, but it does become harder with each additional constraint.

While Table 8.3 shows the best version of each selected route, Figures 8.25 -

Table 8.3: Fastest potential AGA trajectories to interstellar space @ 200 AU

Route	Time of Flight		Launch		Arrival	
	Phase Free, years	Lambert, years	Date	C_3, km^2/s^2	Velocity, AU/year	Date
			No AGA			
EVVEJS	30.36	56.46	12-Sep-2029	90.07	4.19	28-Feb-2086
EJVVEJ	36.92	56.55	16-Jul-2034	152.54	4.22	01-Feb-2091
EVVEJN	33.23	58.10	27-Jul-2038	141.21	4.19	01-Sep-2096
EVVEJU	32.74	59.09	06-Jun-2034	78.79	4.58	09-Jul-2093
			Venus AGA			
EJEV$_{AGA}$N	25.85	43.96	11-Oct-2025	125.79	5.58	26-Sep-2069
EJEV$_{AGA}$J	24.38	44.76	16-Nov-2038	130.88	5.49	21-Aug-2083
EJV$_{AGA}$J	25.31	45.32	21-Apr-2032	125.63	4.74	18-Aug-2077
EJEV$_{AGA}$U	25.76	45.38	14-Dec-2028	92.23	5.30	01-May-2074
ESJV$_{AGA}$J	28.33	46.27	19-Aug-2032	151.37	4.98	28-Nov-2078
EJV$_{AGA}$JP	25.60	52.60	15-Oct-2038	143.60	5.00	29-Dec-2082
			Earth AGA			
EJE$_{AGA}$J	26.83	49.99	20-Oct-2037	136.97	4.33	17-Oct-2087
ESJE$_{AGA}$J	28.47	52.41	12-Oct-2034	142.16	4.39	10-Mar-2087
EJSE$_{AGA}$J	31.45	52.51	18-Sep-2037	148.35	5.83	26-Mar-2090
EJE$_{AGA}$JS	25.49	56.89	08-Jun-2023	149.79	4.75	29-Apr-2080
EJE$_{AGA}$JU	26.41	58.42	04-Aug-2035	122.48	4.57	03-Jan-2094
EJE$_{AGA}$JP	27.05	59.62	20-Oct-2037	137.63	3.55	03-Jun-2097
			Mars AGA			
EJM$_{AGA}$J	28.43	35.02	25-Jan-2018	129.36	6.87	02-Feb-2053
EJM$_{AGA}$N	30.79	36.63	30-Dec-2028	128.46	6.26	16-Aug-2065
EJM$_{AGA}$JN	27.97	43.31	13-Dec-2039	140.41	5.58	06-Apr-2083
EJM$_{AGA}$JP	29.25	44.27	04-Oct-2037	142.79	5.18	10-Jan-2082
ESJM$_{AGA}$J	30.23	47.11	14-Mar-2018	141.97	7.15	24-Apr-2065
ESJM$_{AGA}$JS	28.78	53.33	02-Dec-2038	139.98	5.99	01-Apr-2092
EJM$_{AGA}$JU	27.83	54.55	07-Oct-2038	139.72	4.74	24-Apr-2093
EJM$_{AGA}$JS	27.40	58.05	07-Jul-2022	152.11	4.74	26-Jul-2080
			2 AGA			
EJV$_{AGA}$E$_{AGA}$J	25.37	43.15	05-Dec-2039	98.54	5.76	30-Jan-2083
EJE$_{AGA}$V$_{AGA}$N	26.98	43.96	11-Oct-2025	125.79	5.58	26-Sep-2069
EJM$_{AGA}$E$_{AGA}$J	26.64	44.34	24-Nov-2038	152.47	5.56	30-Mar-2083
EJE$_{AGA}$V$_{AGA}$J	25.86	44.76	16-Nov-2038	130.88	5.49	21-Aug-2083
EJE$_{AGA}$M$_{AGA}$J	24.85	44.87	04-Apr-2020	101.11	5.43	17-Feb-2065
EJV$_{AGA}$M$_{AGA}$J	24.78	44.96	11-Feb-2030	123.26	5.31	29-Jan-2075
EJE$_{AGA}$V$_{AGA}$U	28.05	45.38	14-Dec-2028	92.23	5.30	01-May-2074
EJE$_{AGA}$V$_{AGA}$S	26.66	46.56	18-Sep-2037	107.84	4.92	10-Apr-2084
EJM$_{AGA}$V$_{AGA}$J	24.23	49.35	24-Nov-2038	153.18	4.37	01-Apr-2088
EJME$_{AGA}$V$_{AGA}$U	28.06	51.27	03-Feb-2030	97.88	4.89	11-May-2081
EJM$_{AGA}$E$_{AGA}$N	25.66	54.07	24-Nov-2038	152.47	4.57	19-Dec-2092
EJM$_{AGA}$V$_{AGA}$S	25.14	56.31	26-Sep-2037	94.55	3.92	19-Jan-2094

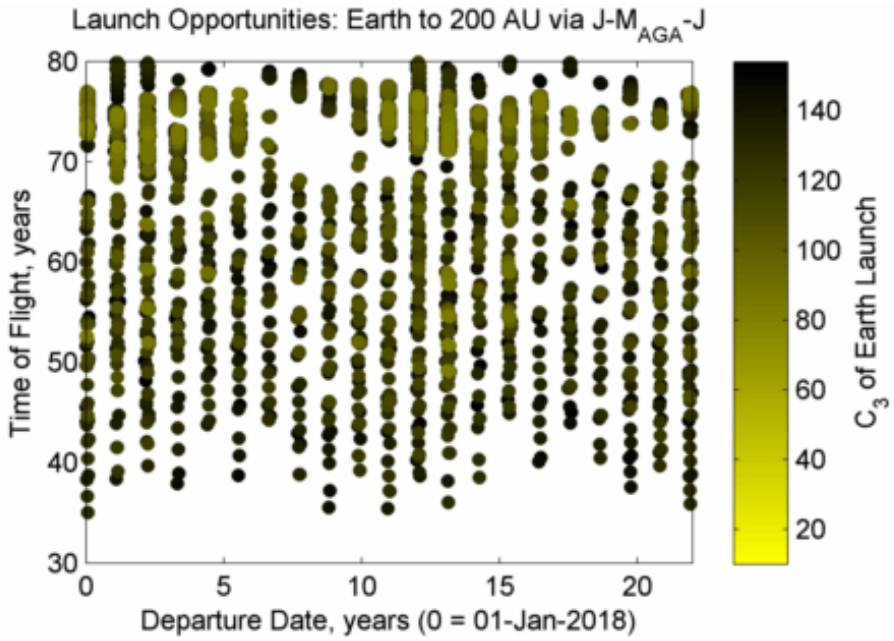

Figure 8.25: Launch opportunities and required energy for Earth, Jupiter GA, Mars AGA, Jupiter GA, 200 AU route

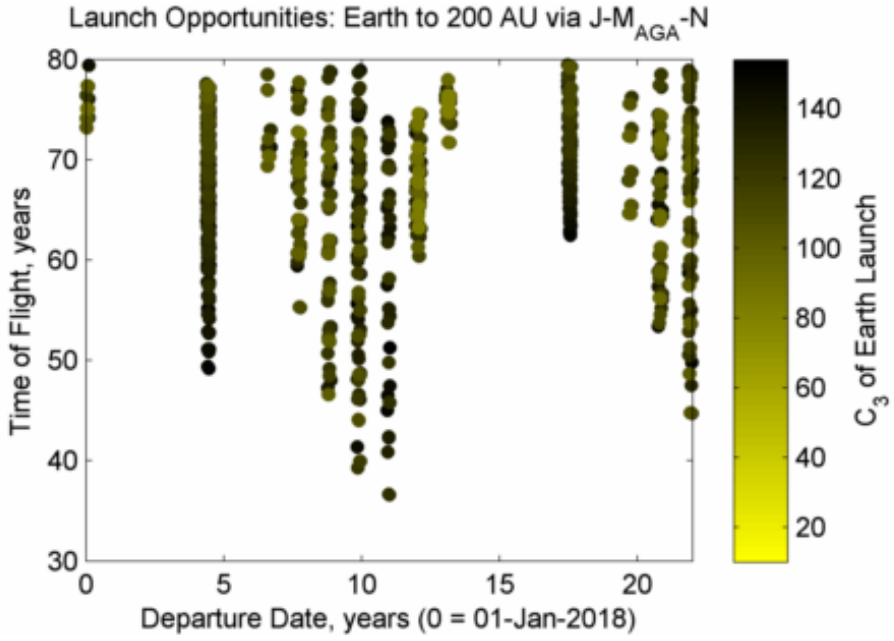

Figure 8.26: Launch opportunities and required energy for Earth, Jupiter GA, Mars AGA, Neptune GA, 200 AU route

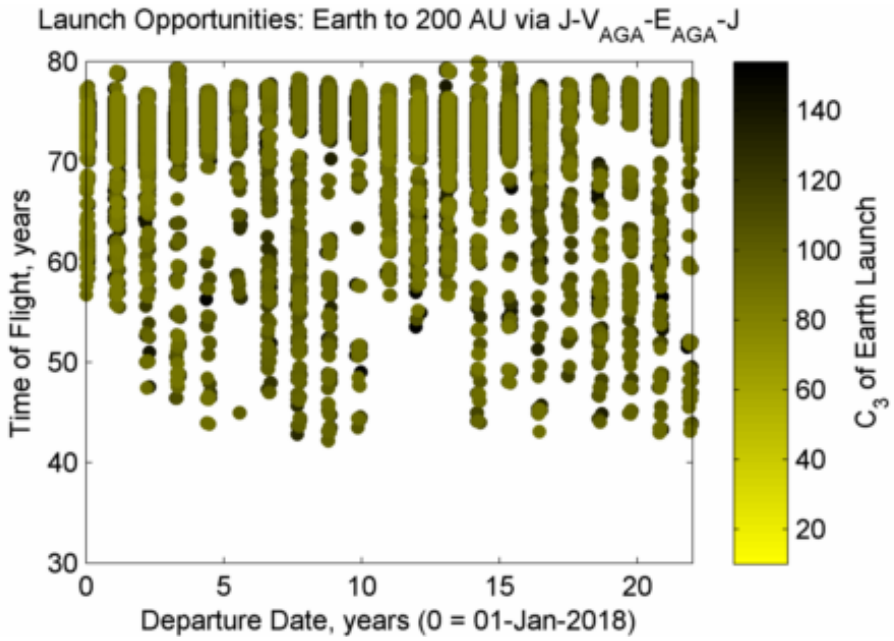

Figure 8.27: Launch opportunities and required energy for Earth, Jupiter GA, Venus AGA, Earth AGA, Jupiter GA, 200 AU route

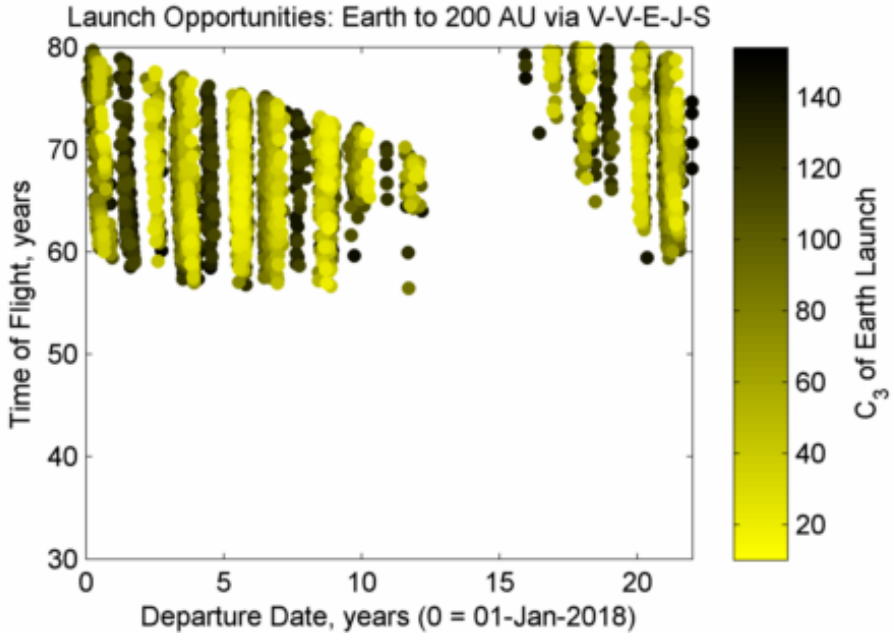

Figure 8.28: Launch opportunities and required energy for Earth, Venus GA, Venus GA, Earth GA, Jupiter GA, Saturn GA, 200 AU route

8.28 show the launch opportunities of the entire 22 year span for 4 promising routes. Appendix B shows the launch opportunities for all other routes with sub-60 year trajectories.

Figure 8.25 depicts the full launch energy plot for an E-J-M$_{AGA}$-J-interstellar trajectory. There are groups of trajectories found which repeat roughly every 12 or 13 months, so a mission could be carried out just about any year with only a slight penalty in overall time of flight or launch energy. This route is the most promising found in this case study. This route will be examined in more detail in the next Section.

Figure 8.26 also shows a route using a single Martian aero-gravity assist, but the phasing required is much less common, therefore only providing fast trajectories to interstellar space every 12 years. There is no discernible benefit in launch energy to this trajectory either, however it would allow a fly-by of seldom visited Neptune.

While a route faster than 40 years to 200 AU was not found using two AGAs, there are still benefits to using multiple in one mission, however. The increased energy gained from the additional AGA fly-by, reduces the launch energy requirements considerably (see Figure 8.27). Once again, there are launch windows every 12 to 13 months corresponding to the ability to rendezvous with Jupiter for the first leg of the journey.

Finally, a gravity assist only trajectory plot is presented in Figure 8.28. The initial planet in the sequence is Venus rather than Jupiter, so considerably less launch energy is required. There are consistent launch opportunities except for a gap in the early 2030s, however, the times of flight are very long. For reference on gravity assist only trajectories, the Voyager spacecraft recently escaped the solar system and will reach 200 AU roughly 54 years after launch. This 54 years includes an extremely fortuitous fly-by of both Jupiter and Saturn. Such phasing was not found in the 22 year window over which this case study comprises.

8.3.4 N-Body Optimization Design Criteria

The final stage of the case study is to perform an optimization of the trajectory in order to find a flyable route. An optimization of the Earth-Jupiter-Mars AGA-Jupiter-200 AU trajectory is performed.

In this stage of design, reaching 200 AU was used as a constraint, along with a minimum close approach of 10 planet radii for each fly-by body (Jupiter twice, in this case) and a close approach of the AGA fly-by body such that the atmosphere was entered. The second and third of these constraints may seem redundant, as the spacecraft wouldn't reach 200 AU without the fly-bys. However, in practice, these constraints proved necessary for guiding the numerical algorithm towards the feasible solution space.

Two competing and one independent objective functions were used to select trajectories: minimizing the surface integrated heating on the vehicle, maximizing volumetric efficiency and reducing the overall time of flight. Maximizing volume is seldom an effective objective when designing hypersonic vehicles, as it results in very long or very wide and very skinny designs. While the volume is large, much of it is in such slender regions of the vehicle that it is not particularly usable, and the increased surface area has a detrimental impact on aerodynamics. Instead, volumetric efficiency is used as a metric for usable volume (see Equation 6.5).

The optimization of an atmospheric flight vehicle and its flight trajectory are unavoidably complex. In order to increase the likelihood of finding optimal and feasible trajectories when co-optimized, the interplanetary propagation was kept relatively simple without any deep space maneuvers. The independent variables were:

- 10 osculating cone waverider geometry variables (see Section 3.4)
- 5 control system variables (see Section 5.2.2)

- 3 launch parameters (date, energy, direction)

In order to propagate the n-body simulation and select an optimal solution, a genetic algorithm was used. This allowed for a wider set of data for post-optimization analysis, however a gradient based method was briefly tested and seemed effective as well. This also allowed seeding the initial population with each of the local minima in Figure 8.25. For reference, the trajectory corresponding to the overall minima in Figure 8.25 is plotted in Figure 8.29. Note that at point 2 in the mission sequence, the spacecraft makes a turn to a highly elliptical orbit with an inclination of almost 90°, hence the appearance of a straight orbit line emanating away from the Sun at that point.

8.3.5 N-Body Optimization Results.

The best overall trajectory found during the genetic algorithm is presented in Figure 8.30. While it may look similar to the patched conic plot in Figure 8.29, the black curve was generated by a numerical propagation of a hypersonic waverider from Earth through the fly-by sequence and to 200 AU. A route was found that was two and a half years faster than the Lambert solution, at the price of launch energy much closer to the maximum allowable of 154 km^2/s^2. The spacecraft first launches to Jupiter and completes a turn backwards to enter a retrograde orbit. It slowly moves out to aphelion beyond Jupiter's orbit before swinging back in to complete the aero-gravity assist around Mars. After a 71.6° turn through the atmosphere, it passes through perihelion a few degrees below the ecliptic. It must enter an inclined orbit following the aero-gravity assist in order to allow Jupiter sufficient time to reach the final fly-by location. Following the second Jupiter gravity assist, the spacecraft turns as close to parallel to Jupiter's velocity as possible. The remaining coast to interstellar space constitutes the bulk of the time of the flight, requiring 27.5 of the 32.45 years.

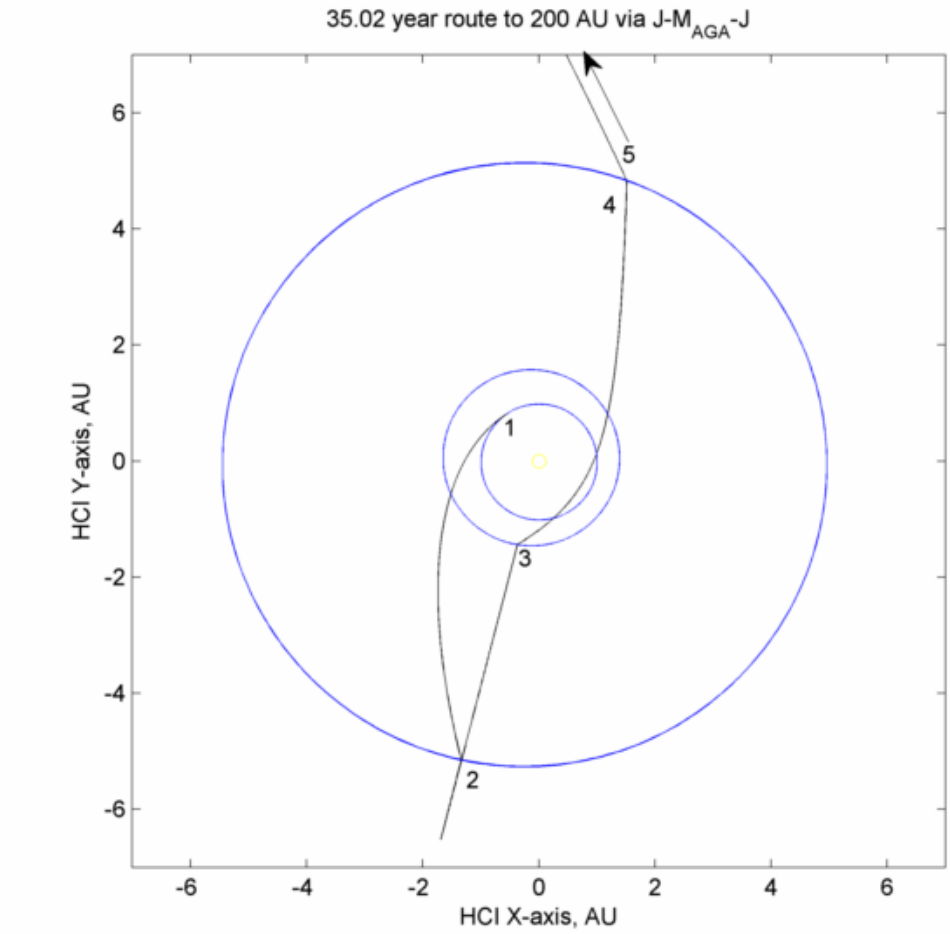

Mission Sequence

1. **Earth Launch:** 25-Jan-2018, $C_3 = 129.36$ km^2/s^2
2. **Jupiter Fly-by:** 25-Apr-2019, $C_3 = 242.52$ km^2/s^2
3. **Mars AGA:** 27-Dec-2023, $C_3^- = 873.37$ km^2/s^2, $\theta = 53.34^\circ$, $C_3^+/C_3^- = 0.62$
4. **Jupiter Fly-by:** 31-Oct-2024, $C_3 = 877.70$ km^2/s^2
5. **Arrival @ 200 AU:** 02-Feb-2053

Figure 8.29: 35.02 year route to 200 AU via J-M$_{AGA}$-J based on sequential Lambert arcs

The selection of a waverider geometry involves balancing aerodynamic performance, vehicle size and aerothermal load. These three objectives often compete, as they did in this case study. The aerodynamic performance was only indirectly represented by the constraint of meeting the trajectory requirements, but the other two were directly used as objective functions. As the vehicle shape becomes larger,

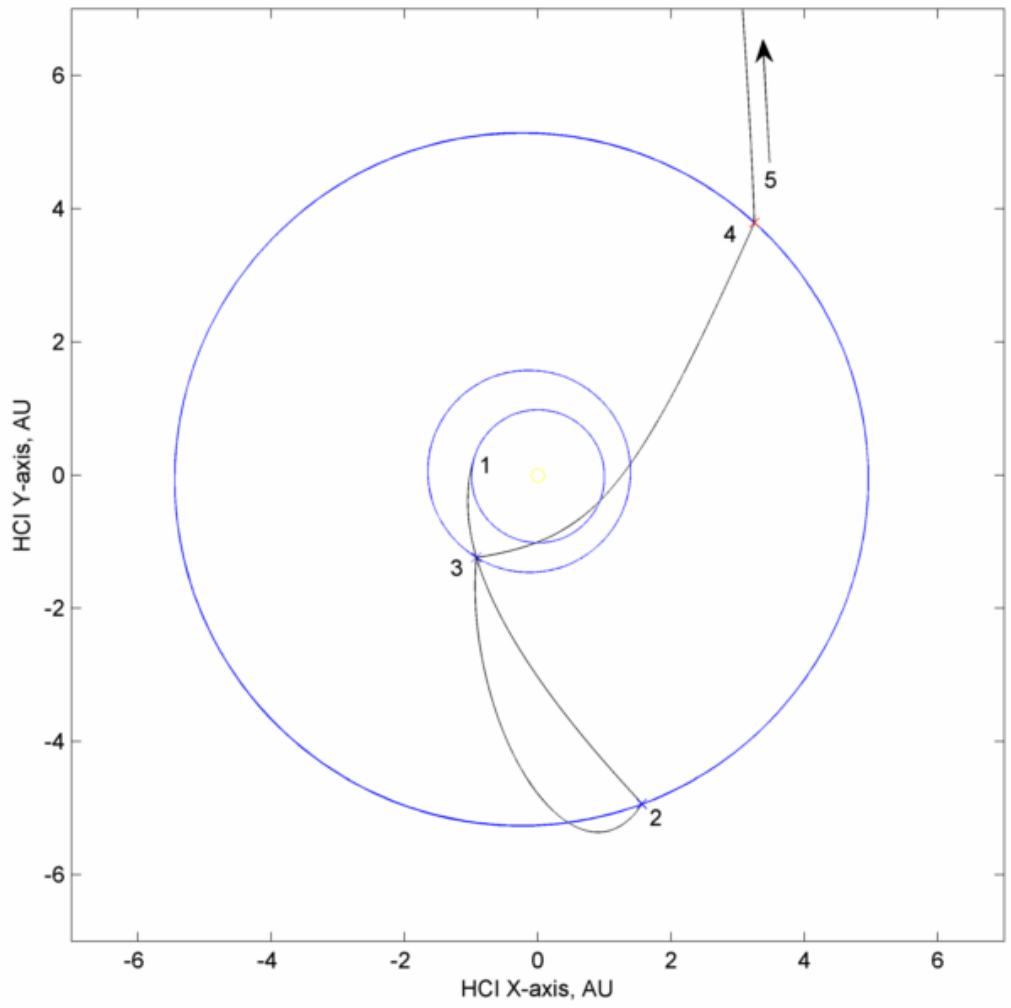

Mission Sequence

1. Earth Launch: 02-Mar-2031, C_3 = 152.8574 km^2/s^2
2. Jupiter Fly-by: 01-Apr-2032, r_p = 381273.62 km
3. Mars AGA: 27-Feb-2035, v_{entry} = 45.25 km/s, θ = 71.60°, v_{exit}/v_{entry} = .620
4. Jupiter Fly-by: 26-Dec-2035, r_p = 349596.95 km
5. Arrival @ 200 AU: 09-Aug-2063

Figure 8.30: 32.45 year route to 200 AU via J-M$_{AGA}$-J based on n-body simulation

and its volume increases relative to its surface area, it becomes less slender. This does not affect the stagnation heating rate, but it is negatively correlated with the integrated heat load over the entire surface (see Figure 8.31). As the vehicle volume increases, its frontal area increases. This strengthens the forebody shocks emanating from the leading edges. The pressure and temperature rise behind the leading shock

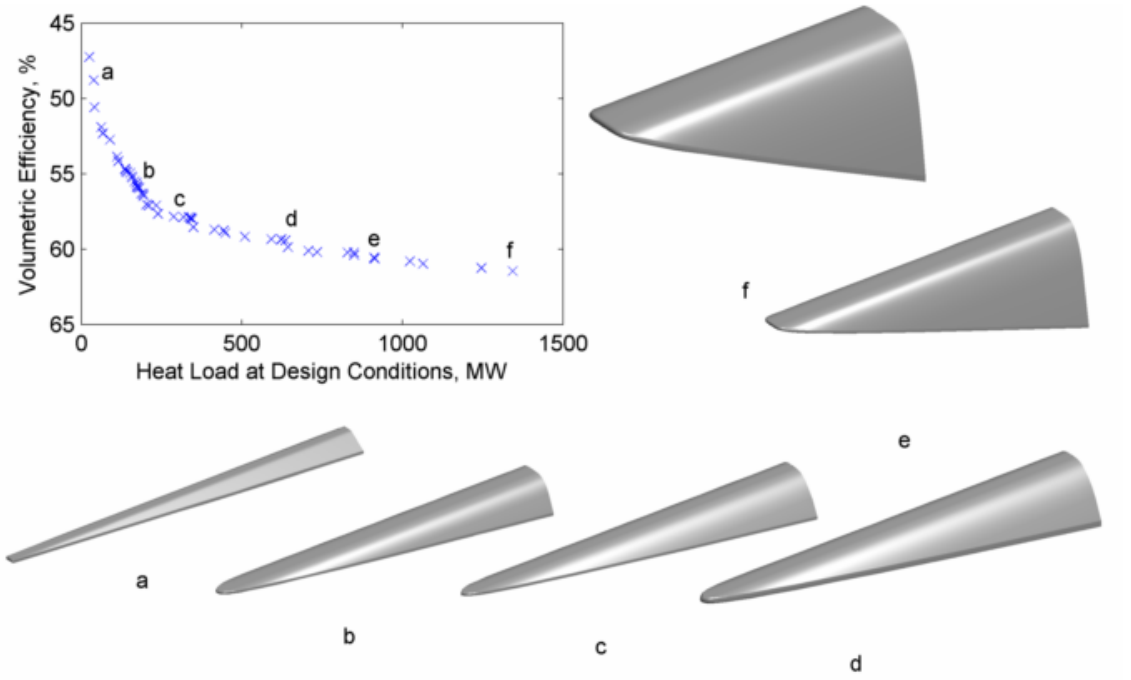

Figure 8.31: Pareto curve between competing objectives, minimizing the heat load and maximizing the volumetric efficiency

becomes greater. Limiting the stagnation point heating is accomplished trivially by increasing the leading edge radius, but this does not necessarily benefit the heating over the rest of the surface area.

Any multidisciplinary design requires optimizing competing objectives such as those shown in the pareto curve of Figure 8.31. As the vehicle becomes more slender, it would be harder and harder to package the spacecraft inside of the aeroshell. The converse is not viable either, however, as excessive heating will likely overwhelm even the most capable thermal protection system. For this study, the L2-norm optimum was chosen as the simplest trade-off. This equally weights the value of each objective.

More detail on the 160 second atmospheric portion of the optimal trajectory is shown in Figure 8.32 and the L2-norm optimal waverider is shown in Figure 8.33. The top chart shows the altitude profile from entry to exit, while the second shows both the velocity relative to Mars and the Mach number. The optimization

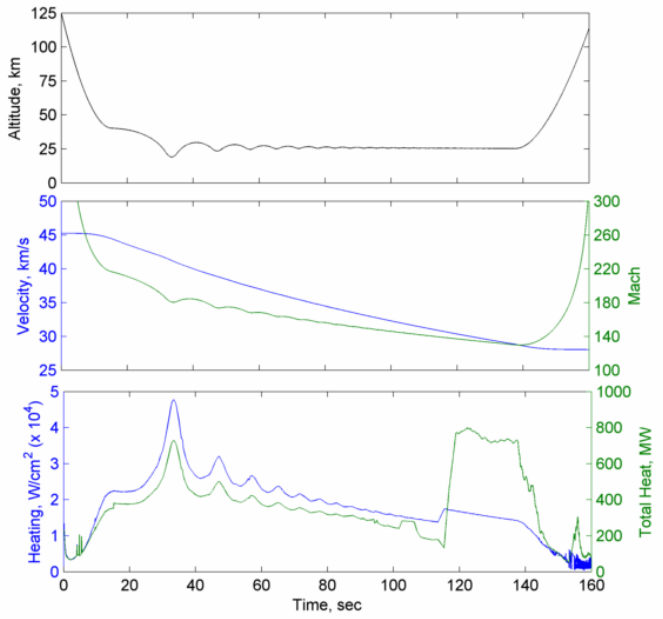

Figure 8.32: Time profiles during the atmospheric pass

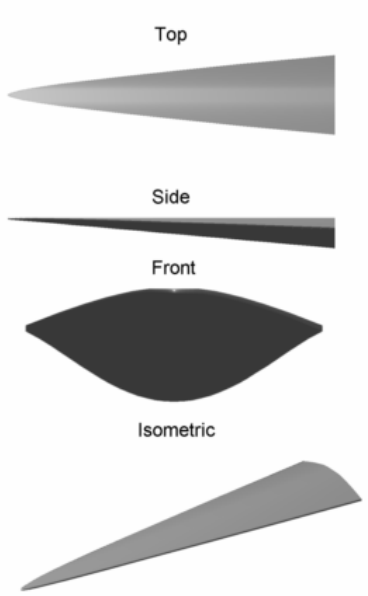

Figure 8.33: Optimal Waverider

routine selected a cruise at 26 km above the surface. The vehicle does not settle directly in at the cruise altitude, however. It has damped oscillations about the target altitude. This is because the final waverider had too slim of a drag profile, so in order to dissipate enough energy to reach the correct exit conditions (v_{exit} = 28.04 km/s), it needed to linger in the atmosphere for longer. The control system used is a simple feedback controller responding to the vertical velocity and the altitude of cruise. Unsurprisingly then, gains and exponents could be selected which result in oscillatory behavior as seen. There may be a more optimal vehicle with a slightly blunter forebody, resulting in slightly higher drag that would not require the oscillations. This would likely increase the integrated heat load though.

The extreme aerothermal environment is shown in the third time profile plot. In order to exit the atmosphere in the correct location, the vehicle needed to bank over and then pitch in order to turn. This is done at roughly constant altitude, so it is only visible in the heating chart, as the heat rate and load increase with angle-of-attack. For reference, the space shuttle had a peak heating of 113 W/cm^2 during

reentry.[110] This trajectory has a peak heating rate of 48,000 W/cm^2. While aero-gravity assist maneuvers will always require extreme flight speeds, due to the high launch energy and hyperbolic velocities resulting from preceding gas giant gravity assists, the atmospheric fly-bys associated with interstellar trajectories are particularly intense. In this case, the vehicle enters the Martian atmosphere traveling 45 km/s, cruises at over $M = 140$, and travels about 5600 km, or a little further than New York to London, in under three minutes.

Chapter 9

Conclusions

This chapter will discuss the many results found throughout this work and summarize the most important aspects of the findings.

9.1 Discussion

A series of investigations were conducted in order to analyze and improve many aspects of aero-assisted spacecraft missions. This includes the physical shape of the vehicle performing the maneuver, the trajectory flown, and the optimization schemes used to maximize both for certain design metrics.

One promising configuration of vehicle for performing aero-assisted missions is the asymmetric starbody waverider. A means of producing these shapes was described in detail. Using a limited set of parameters, these vehicle shapes can be generated for specific flight conditions. Three of these parameters are dedicated to increasing or decreasing the relative asymmetry of a given vehicle configuration. In Chapter 6, a specific flight condition was chosen and the design space was thoroughly examined. Each asymmetry parameter was found to have a different effect on the aerodynamic and stability performance of the waverider. Introducing an effective angle of attack to the vehicle gave dramatically improved static margin.

Next, a study was conducted numerically to analyze the tradeoffs between

various performance metrics of asymmetric starbody waveriders and osculating cone waveriders. It was found that small amounts of leading edge bluntness immediately have a strongly adverse effect on the lift-to-drag ratio. Volumetric efficiency is also unfavorably related to aerodynamic performance, as the highest-lifting waveriders are capable of holding the least payload. While the maximum heat load experienced by the waverider is inversely related to L/D, it was shown that the surface integrated heat rate is positively correlated with aerodynamic performance. Further, the flight conditions played a more crucial role in varying the aerothermal environment than did the waverider geometry. Trajectory design and optimization can limit the heating on a vehicle more effectively than slight variation in bluntness. The primary benefit of starbody waveriders for aero-assist missions is demonstrated by their improved stability characteristics. While few osculating cone waveriders were found to be statically stable in yaw, none were found to be statically stable in roll. Many starbody waveriders, on the other hand, were found to be naturally statically stable in the lateral directions. The next stage of design, including a reasonable set of control algorithms and control devices and a full dynamic analysis, will be needed to determine whether the improved stability behavior is sufficient to overcome the 10% reduction in L/D for starbody waveriders.

An optimization was executed to determine ideal parameters to design a starbody waverider which uses aerodynamics to decelerate from hyperbolic planetary approach velocity into a captured and highly inclined orbit. It was found that increasing the plane change of the combined maneuver to nearly a polar orbit is possible, however this has adverse effects on other important metrics such as heat rate. Any subsequent work in designing such a vehicle will need to consider expected structural and thermal limitations, as well as launch vehicle size and required payload volume in order to determine the maximum inclination possible given these other constraints. The overall entry corridors for such high-lift vehicles are quite

large and add significant flexibility to the mission design. While there appears to be an ideal set of entry conditions, the gradients of achievable plane change are relatively low near these peaks. While other trajectory design choices could be used to limit the needed propellant for a plane change maneuver when arriving at a destination planet, few would come close to offering similar benefits to the aero-assisted mission. The Δv savings by performing inclination change aerodynamically are immense, as high as 4.5 km/s in some cases.

When including aero-gravity assists into an interplanetary trajectory, an upper limit on performance is required in the form of minimum energy loss for a given turning angle around the planet. A study was first conducted using a combined stochastic and gradient based optimization method to quantify the relationship for Mars, Earth and Venus. The maneuvers were directly simulated, using the engineering level modeling techniques described. The maximum turning angle and velocity increment was identified for the entire breadth of usable approach velocities and energy dissipations. In addition to this performance database, much was learned about the maneuver itself. It was demonstrated that all phases of the trajectory are important to the final results, as at least 10%, and likely more of the analytical performance is lost due to the ascent and descent flight segments when the waverider is "off design" and the cruise control system not maintaining flight near maximum L/D. Further, it was demonstrated that for any energy depletion rate, there will be an optimal antecedent angle, less than the parallel direction, which maximizes the heliocentric velocity increment. This was not necessarily expected, but is reasonable as planetary alignment requires energy loss, and in certain cases the energy loss outweighs increased alignment.

Finally, an end-to-end methodology for designing interplanetary trajectories using aero-gravity assists was presented. The proposed approach uses three separate steps which directly feed into each other. The final product is a flyable trajectory

from Earth to the final destination, and a thorough dataset of alternate routes, launch opportunities and aeroshell designs. The first stage of design ignores the phasing of the planets in order to quickly parse the thousands of possible permutations of planet sequences. By making only a few simplifying assumptions, strong insight is gained into the problem under consideration. Also, the times of flight calculated are usable as a theoretical limit for the fastest possible transfer under the given study conditions (launch energy, maximum AGA entry speed, etc). The second stage of design 'brute forces' a trajectory by iterating over the entire launch window and acceptable times of flight (to the first planet). A simplifying assumption is made to model a gravity assist or aero-gravity assist as an instantaneous change in velocity direction (and magnitude for AGA). An iterative Lambert solver was described which works backwards to find acceptable times of flight which generate departure C_3 values that match the incoming hyperbolic orbit. A novel method was introduced to determine whether an AGA is possible to connect Lambert arcs and if so, what outbound lambert arc to select. The scheme was given the name the 'easiest AGA' method, as it attempts to find the AGA trajectory with the most margin for error in waverider performance. The third and final stage of the preliminary design process involved optimizing the overall interplanetary trajectory in one single orbit propagation from Earth to the final destination, including the atmospheric AGA flight. This allows co-optimizing the interplanetary trajectory, the aeroshell configuration and the hypersonic flight profile.

The AGA design method was demonstrated with an examination of a trajectory search for routes to a radial distance of 200 AU from the Sun. It was shown that even from a phase free standpoint, there is little benefit to using a second AGA maneuver in a single spacecraft trajectory. It was determined that if the atmospheric entry speed is going to be constrained, then for a heliocentric escape mission, AGA around Venus is likely ineffective. Two promising routes to inter-

stellar space were found with varying levels of launch availability when considering solar system ephemerides. When the overall time of flight is as long as an interstellar route, performing initial gravity assist maneuvers around the outer planets is actually beneficial. The fastest route using AGA to 200 AU demonstrated this, as trajectories as short as 35 years were found using sequential Lambert targeting to design a trajectory from Earth to Jupiter to Mars (AGA) to Jupiter to interstellar space. This would be a savings of 21 years over the fastest gravity assist only trajectory! When this trajectory was considered in detail and optimized using an n-body simulator including full atmospheric flight, the time of flight was lowered by two and a half years.

Unfortunately, the AGA performance required to make a relatively high speed trajectory such as an interstellar one, in terms of aero-thermal load, is somewhat pessimistic. While further thermal protection technology advancements will likely be required before the realization of aero-gravity assist in practice, the maneuver holds great promise to increase access to far away regions of space, both in and out of our solar system. Optimization methodology is a useful tool for providing a reasonable estimate of the limitations and capabilities of waverider performance for aero-assisted missions. Studies such as these continue to demonstrate that hypersonic waveriders are an encouraging means of flying higher and faster in the atmosphere of planetary bodies. Further and increasingly detailed numerical investigations into AGA and other aero-assist trajectories serve as a consistent reminder that innovative thinking can be used to solve even the most challenging problems presented by deep space exploration.

9.2 Summary of Contributions

In summary, the following contributions have been made to the state of the art:

- An entirely new method of generating asymmetric starbody waveriders was described. These novel shapes greatly extend the waverider design space. Vehicles can be designed which produce substantial lifting force, even at zero angle-of-attack. Using three discrete inputs, hypersonic waverider forms were presented which have greatly varied aerodynamic behavior and physical dimensions of length, width, volume and volumetric efficiency.

- Asymmetric starbody waveriders were compared to the better understood osculating cone family of waveriders. It was shown that starbody waveriders have significantly improved stability behavior, with only limited lift-to-drag penalty and similar aero-heating performance.

- This work presented the first study of a combined aero-capture and orbital plane change maneuver, in the form of a trajectory and vehicle shape optimization. The maximum expected delta-v savings were presented along with the waverider forms capable of completing the maneuver. A thorough trajectory analysis was also included describing the likely structural and dynamic pressure requirements. Up to 4.5 km/s of delta-v could be saved by capturing and changing orbit inclination using a planetary atmosphere rather than chemical rocket burns.

- By comparing aero-gravity assist simulations with analytical performance, the necessity of including ascent and descent performance and improving control systems was shown as a 10% to 40% loss from analytical predictions.

- A parameter termed the 'antecedent angle' was introduced with a description and explanation of why departing an aero-gravity assist in the parallel direction is not optimal for maximizing heliocentric velocity.

- This work was the first to describe and implement a method using aero-gravity

assist simulation data in conceptual and preliminary trajectory design of interplanetary missions.

- When performing an aero-gravity assist, it was explained why there are a near infinite number of outgoing trajectory solutions as compared to only one for a gravity assist. The "easiest aero-gravity assist" method was introduced and described as a promising means of choosing amongst the trajectory options.

- An atmospheric simulation and interplanetary trajectory propagation was combined inside the loop of a high fidelity interplanetary trajectory optimization. This created the first end-to-end trajectory design optimization in which the trajectory is numerically propagated from launch to its destination, including an atmospheric pass.

- This work examined the benefit of using an aero-gravity assist maneuver for an interstellar probe. It was shown that a time savings of over 21 years can be achieved with just one aero-gravity assist included amongst a series of planetary fly-bys.

Appendix A

Asymmetric Starbody Waveriders

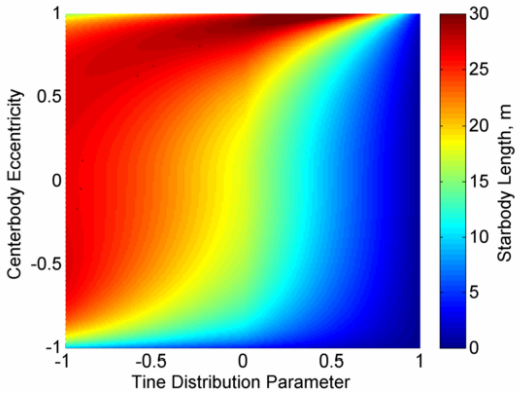

Figure A.1: Range of vehicle lengths for a 3-tined starbody with $\alpha_0 = 0.62$. $M = 18$, $h = 20$ km, in the Martian atmosphere.

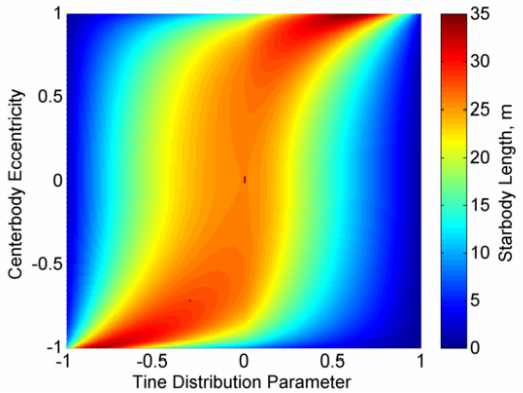

Figure A.2: Range of vehicle lengths for a 3-tined starbody with $\alpha_0 = 0$. $M = 18$, $h = 20$ km, in the Martian atmosphere.

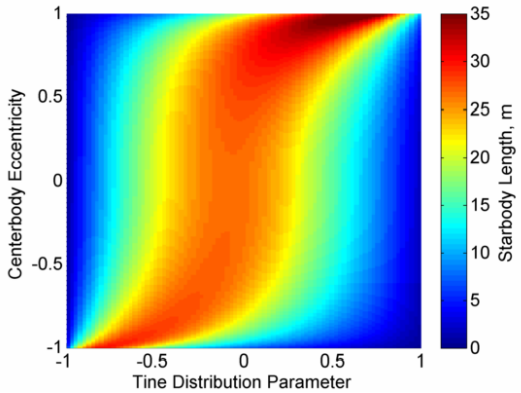

Figure A.3: Range of vehicle lengths for a 3-tined starbody with $\alpha_0 = -0.62$. $M = 18$, $h = 20$ km, in the Martian atmosphere.

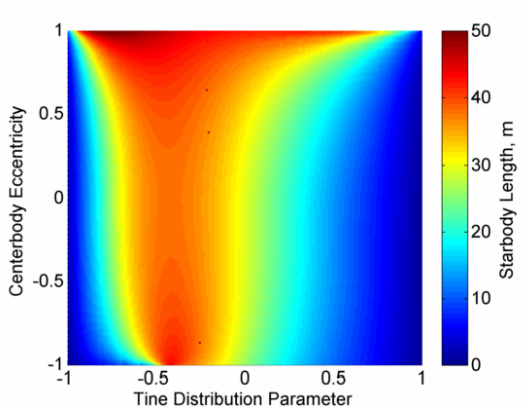

Figure A.4: Range of vehicle lengths for a 4-tined starbody with $\alpha_0 = 0.62$. $M = 18$, $h = 20$ km, in the Martian atmosphere.

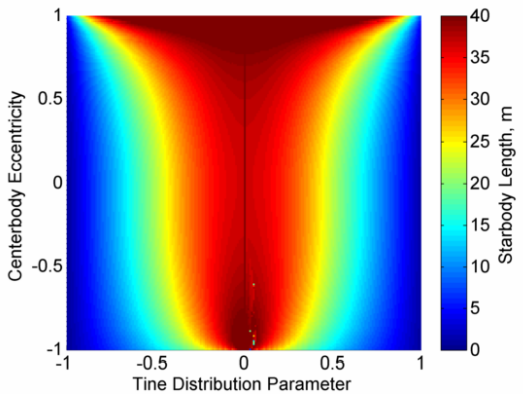

Figure A.5: Range of vehicle lengths for a 4-tined starbody with $\alpha_0 = 0$. $M = 18$, $h = 20$ km, in the Martian atmosphere.

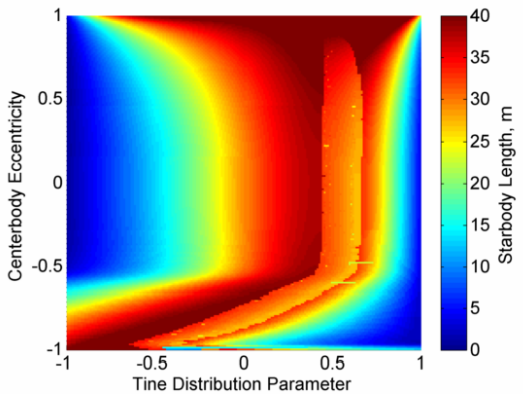

Figure A.6: Range of vehicle lengths for a 4-tined starbody with $\alpha_0 = -0.62$. $M = 18$, $h = 20$ km, in the Martian atmosphere.

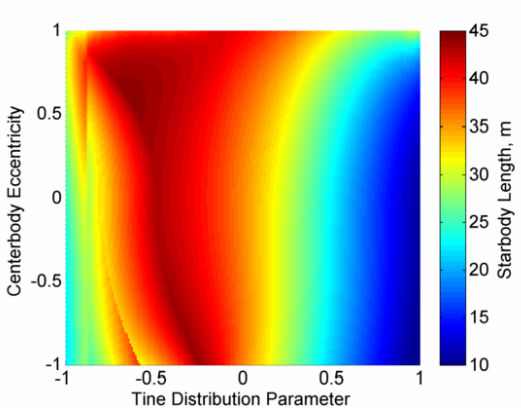

Figure A.7: Range of vehicle lengths for a 5-tined starbody with $\alpha_0 = 0.62$. $M = 18$, $h = 20$ km, in the Martian atmosphere.

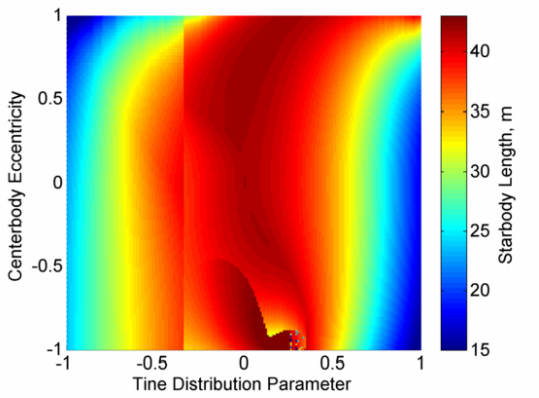

Figure A.8: Range of vehicle lengths for a 5-tined starbody with $\alpha_0 = 0$. $M = 18$, $h = 20$ km, in the Martian atmosphere.

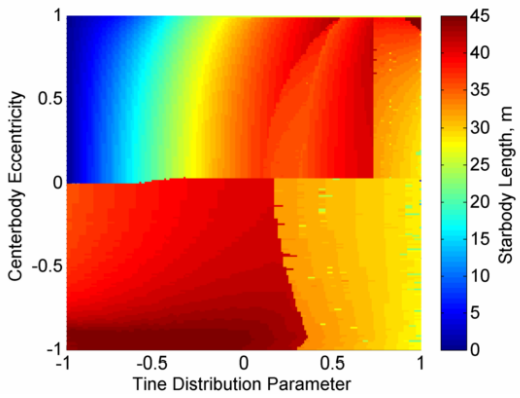

Figure A.9: Range of vehicle lengths for a 5-tined starbody with $\alpha_0 = -0.62$. $M = 18$, $h = 20$ km, in the Martian atmosphere.

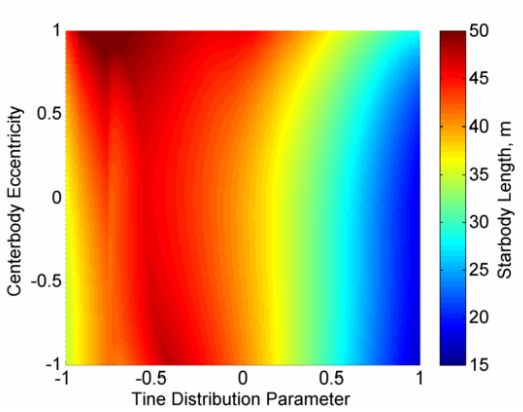

Figure A.10: Range of vehicle lengths for a 6-tined starbody with $\alpha_0 = 0.62$. $M = 18$, $h = 20$ km, in the Martian atmosphere.

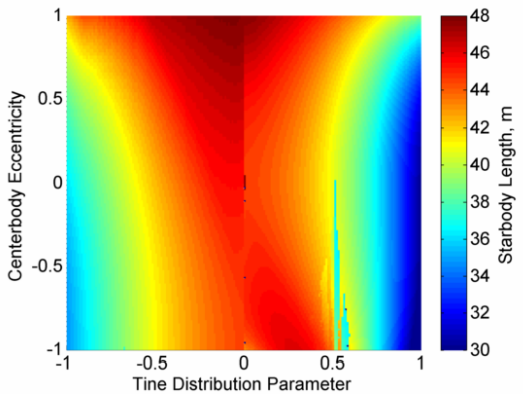

Figure A.11: Range of vehicle lengths for a 6-tined starbody with $\alpha_0 = 0$. $M = 18$, $h = 20$ km, in the Martian atmosphere.

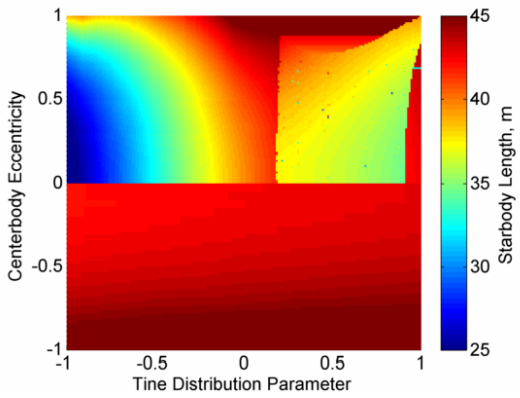

Figure A.12: Range of vehicle lengths for a 6-tined starbody with $\alpha_0 = -0.62$. $M = 18$, $h = 20$ km, in the Martian atmosphere.

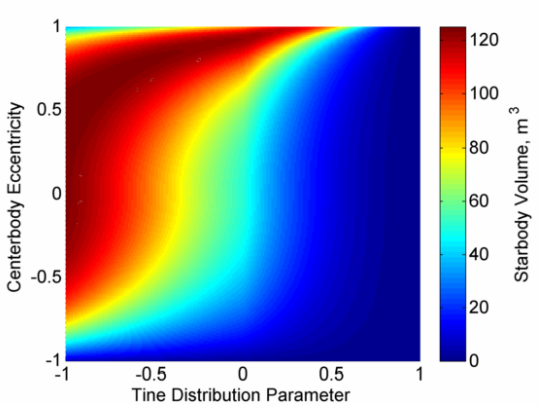

Figure A.13: Range of vehicle volume for a 3-tined starbody with $\alpha_0 = 0.62$. $M = 18$, $h = 20$ km, in the Martian atmosphere.

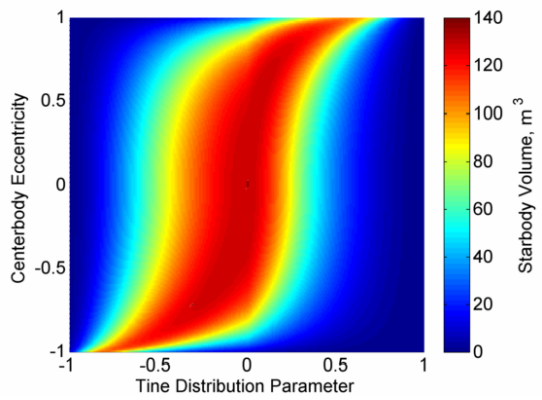

Figure A.14: Range of vehicle volume for a 3-tined starbody with $\alpha_0 = 0$. $M = 18$, $h = 20$ km, in the Martian atmosphere.

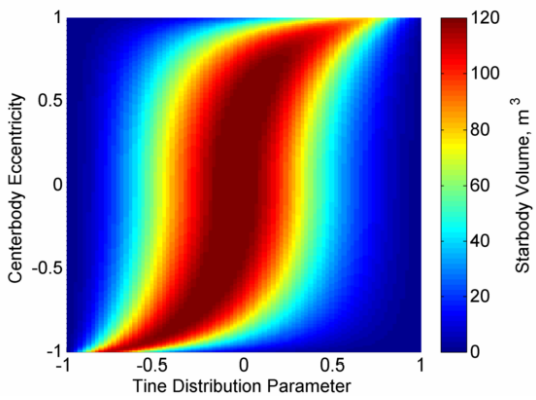

Figure A.15: Range of vehicle volume for a 3-tined starbody with $\alpha_0 = -0.62$. $M = 18$, $h = 20$ km, in the Martian atmosphere.

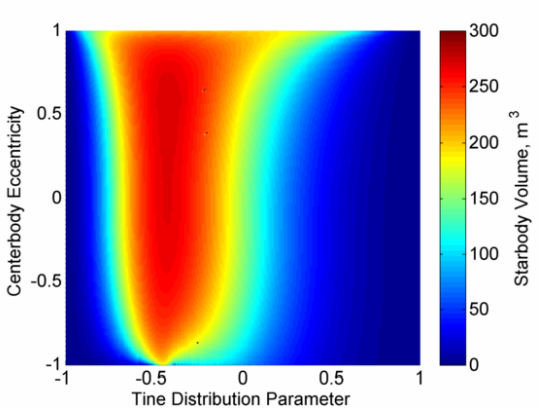

Figure A.16: Range of vehicle volume for a 4-tined starbody with $\alpha_0 = 0.62$. $M = 18$, $h = 20$ km, in the Martian atmosphere.

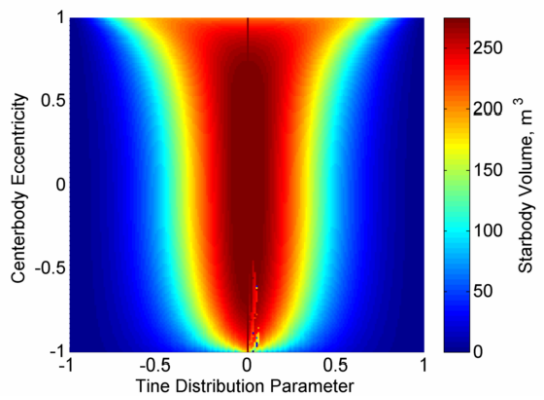

Figure A.17: Range of vehicle volume for a 4-tined starbody with $\alpha_0 = 0$. $M = 18$, $h = 20$ km, in the Martian atmosphere.

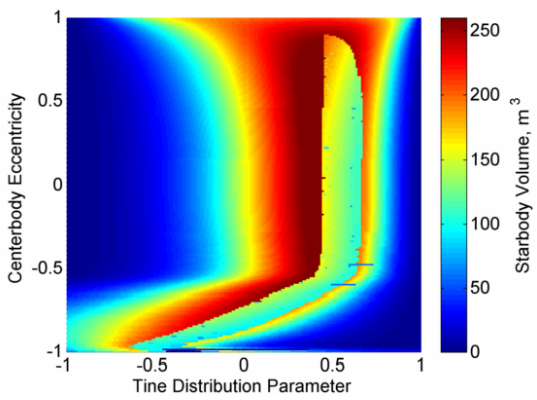

Figure A.18: Range of vehicle volume for a 4-tined starbody with $\alpha_0 = -0.62$. $M = 18$, $h = 20$ km, in the Martian atmosphere.

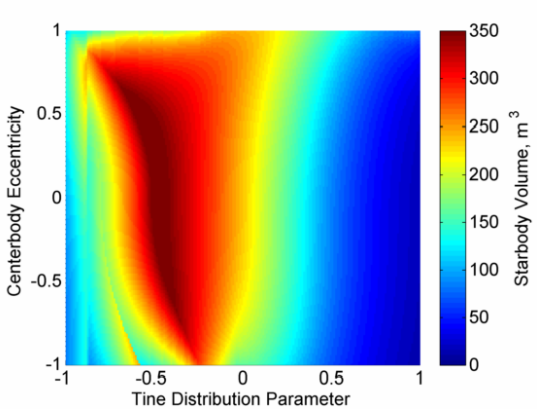

Figure A.19: Range of vehicle volume for a 5-tined starbody with $\alpha_0 = 0.62$. $M = 18$, $h = 20$ km, in the Martian atmosphere.

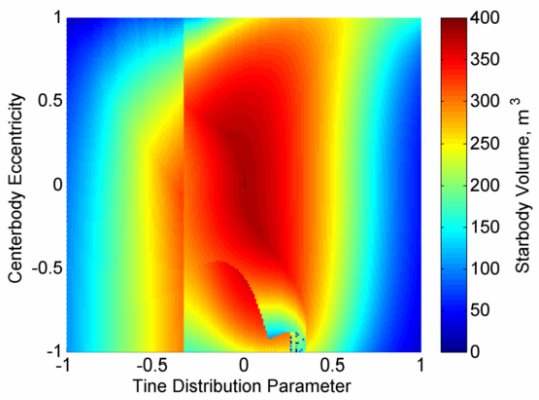

Figure A.20: Range of vehicle volume for a 5-tined starbody with $\alpha_0 = 0$. $M = 18$, $h = 20$ km, in the Martian atmosphere.

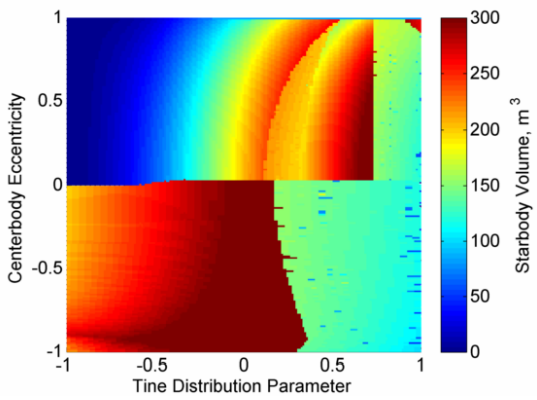

Figure A.21: Range of vehicle volume for a 5-tined starbody with $\alpha_0 = -0.62$. $M = 18$, $h = 20$ km, in the Martian atmosphere.

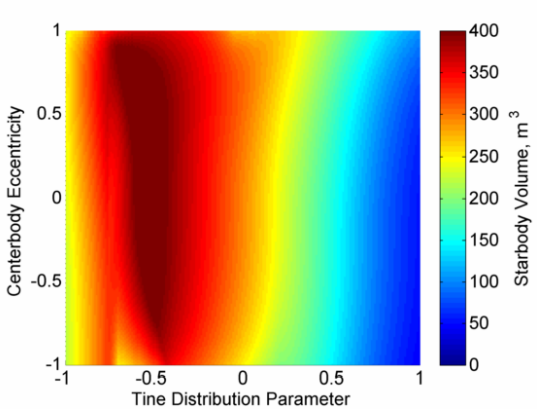

Figure A.22: Range of vehicle volume for a 6-tined starbody with $\alpha_0 = 0.62$. $M = 18$, $h = 20$ km, in the Martian atmosphere.

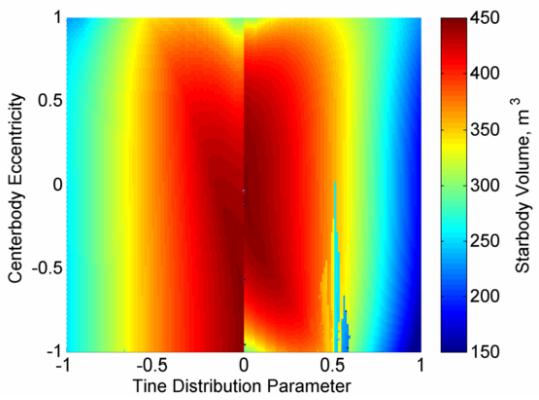

Figure A.23: Range of vehicle volume for a 6-tined starbody with $\alpha_0 = 0$. $M = 18$, $h = 20$ km, in the Martian atmosphere.

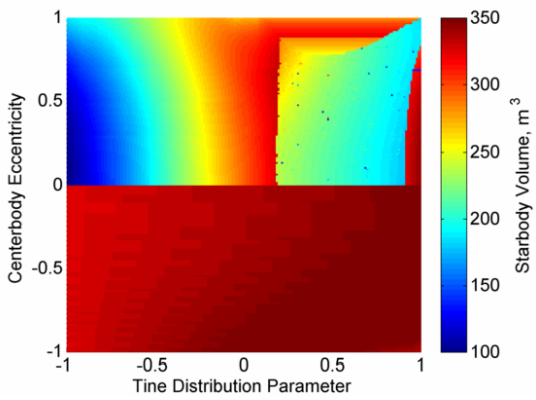

Figure A.24: Range of vehicle volume for a 6-tined starbody with $\alpha_0 = -0.62$. $M = 18$, $h = 20$ km, in the Martian atmosphere.

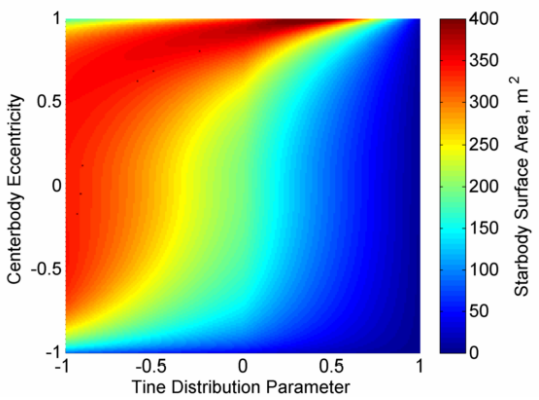

Figure A.25: Range of surface area for a 3-tined starbody with $\alpha_0 = 0.62$. $M = 18$, $h = 20$ km, in the Martian atmosphere.

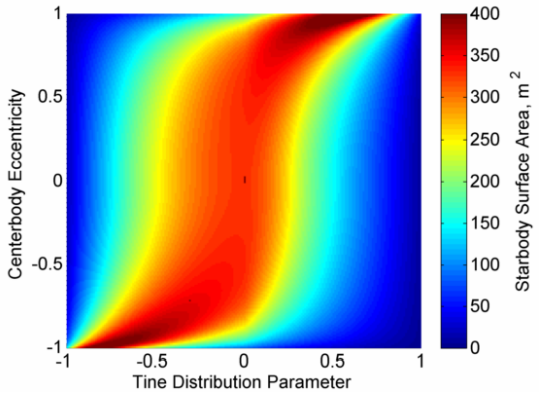

Figure A.26: Range of surface area for a 3-tined starbody with $\alpha_0 = 0$. $M = 18$, $h = 20$ km, in the Martian atmosphere.

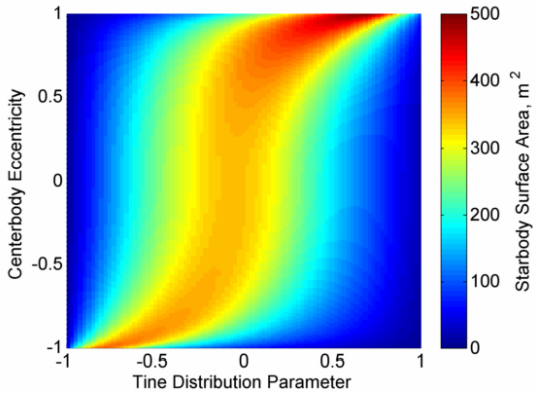

Figure A.27: Range of surface area for a 3-tined starbody with $\alpha_0 = -0.62$. $M = 18$, $h = 20$ km, in the Martian atmosphere.

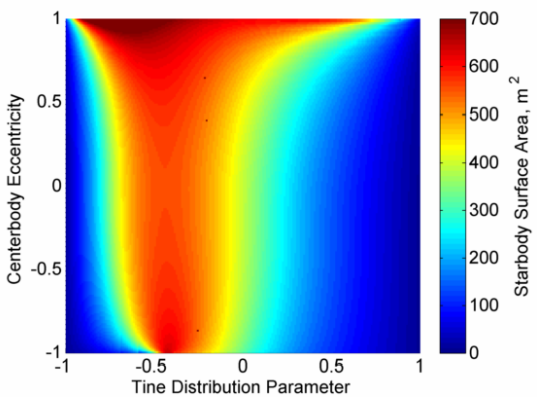

Figure A.28: Range of surface area for a 4-tined starbody with $\alpha_0 = 0.62$. $M = 18$, $h = 20$ km, in the Martian atmosphere.

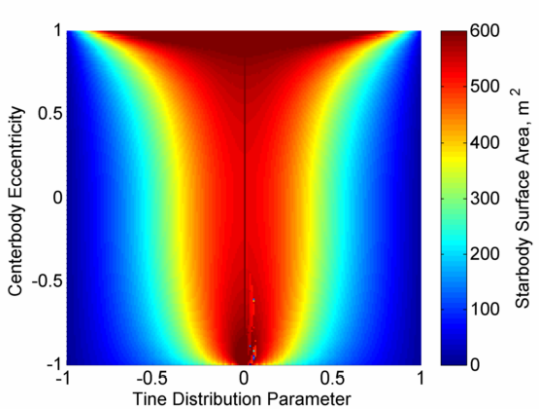

Figure A.29: Range of surface area for a 4-tined starbody with $\alpha_0 = 0$. $M = 18$, $h = 20$ km, in the Martian atmosphere.

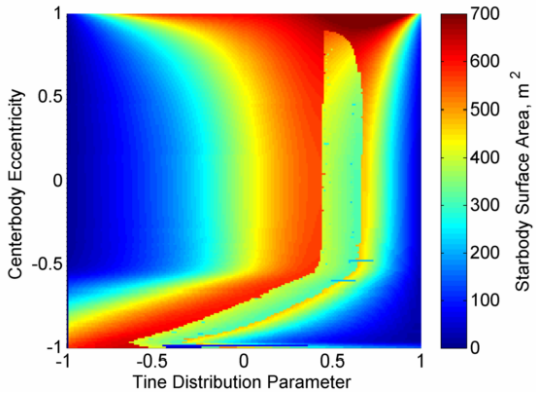

Figure A.30: Range of surface area for a 4-tined starbody with $\alpha_0 = -0.62$. $M = 18$, $h = 20$ km, in the Martian atmosphere.

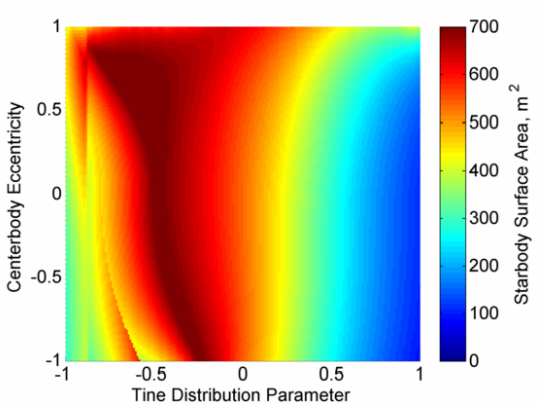

Figure A.31: Range of surface area for a 5-tined starbody with $\alpha_0 = 0.62$. $M = 18$, $h = 20$ km, in the Martian atmosphere.

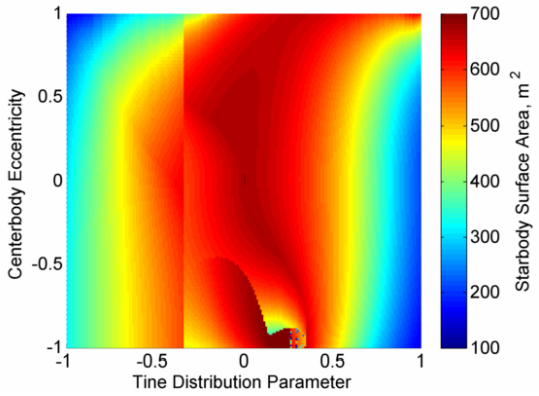

Figure A.32: Range of surface area for a 5-tined starbody with $\alpha_0 = 0$. $M = 18$, $h = 20$ km, in the Martian atmosphere.

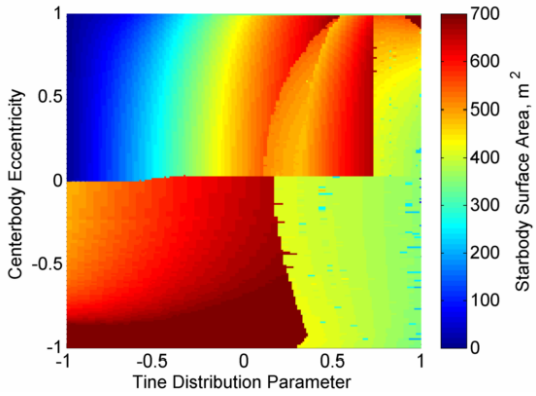

Figure A.33: Range of surface area for a 5-tined starbody with $\alpha_0 = -0.62$. $M = 18$, $h = 20$ km, in the Martian atmosphere.

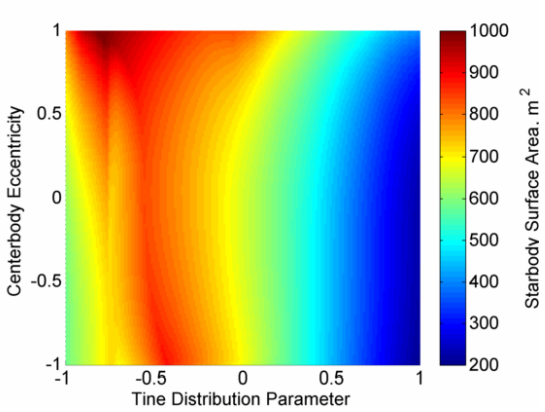

Figure A.34: Range of surface area for a 6-tined starbody with $\alpha_0 = 0.62$. $M = 18$, $h = 20$ km, in the Martian atmosphere.

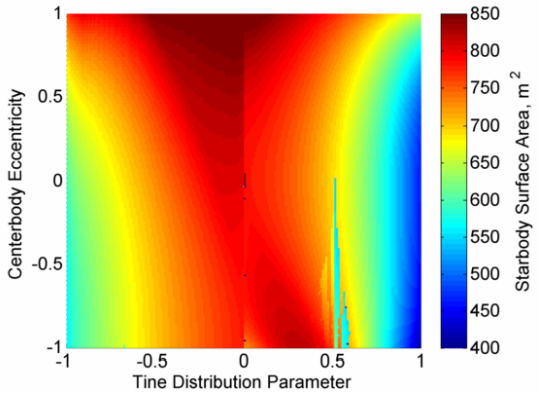

Figure A.35: Range of surface area for a 6-tined starbody with $\alpha_0 = 0$. $M = 18$, $h = 20$ km, in the Martian atmosphere.

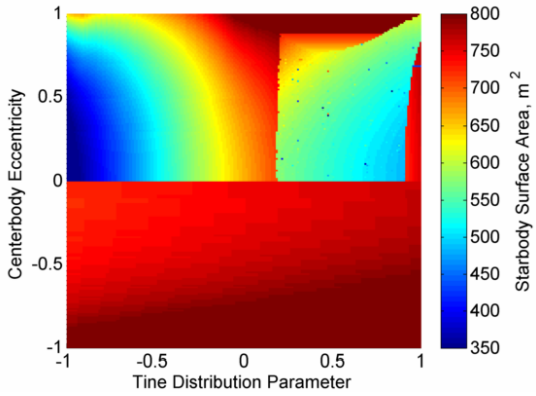

Figure A.36: Range of surface area for a 6-tined starbody with $\alpha_0 = -0.62$. $M = 18$, $h = 20$ km, in the Martian atmosphere.

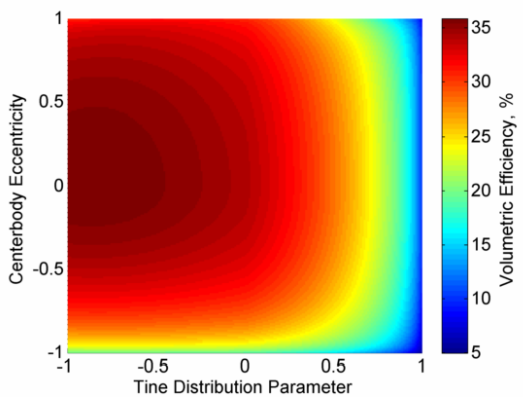

Figure A.37: Range of volumetric efficiency for a 3-tined starbody with α_0 = 0.62. M = 18, h = 20 km, in the Martian atmosphere.

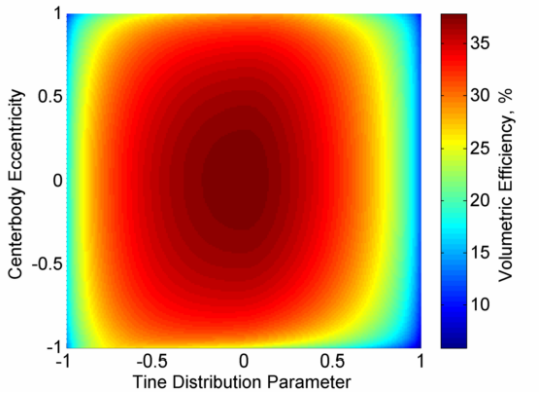

Figure A.38: Range of volumetric efficiency for a 3-tined starbody with α_0 = 0. M = 18, h = 20 km, in the Martian atmosphere.

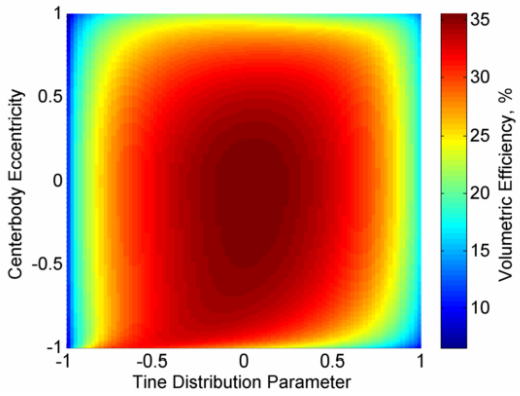

Figure A.39: Range of volumetric efficiency for a 3-tined starbody with α_0 = -0.62. M = 18, h = 20 km, in the Martian atmosphere.

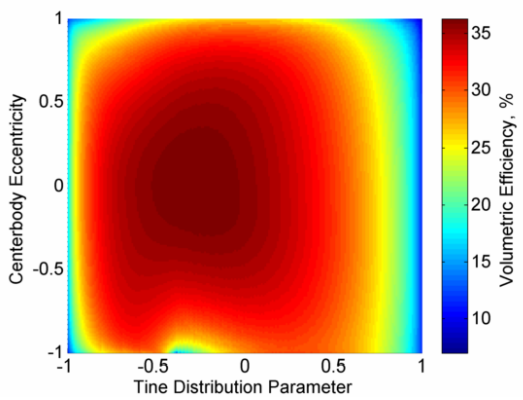

Figure A.40: Range of volumetric efficiency for a 4-tined starbody with α_0 = 0.62. M = 18, h = 20 km, in the Martian atmosphere.

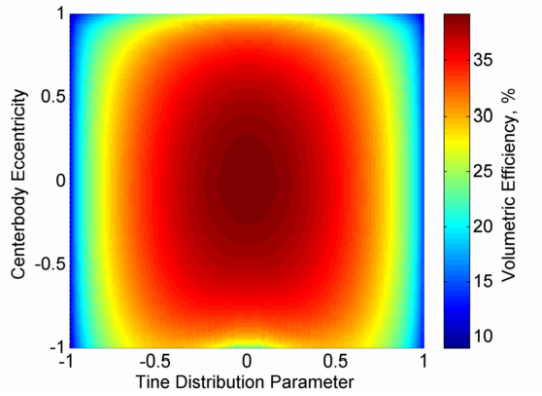

Figure A.41: Range of volumetric efficiency for a 4-tined starbody with α_0 = 0. M = 18, h = 20 km, in the Martian atmosphere.

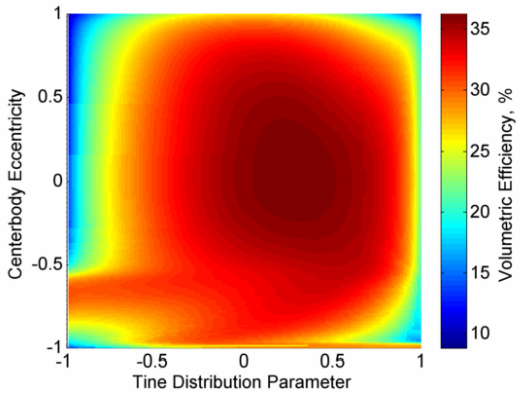

Figure A.42: Range of volumetric efficiency for a 4-tined starbody with α_0 = -0.62. M = 18, h = 20 km, in the Martian atmosphere.

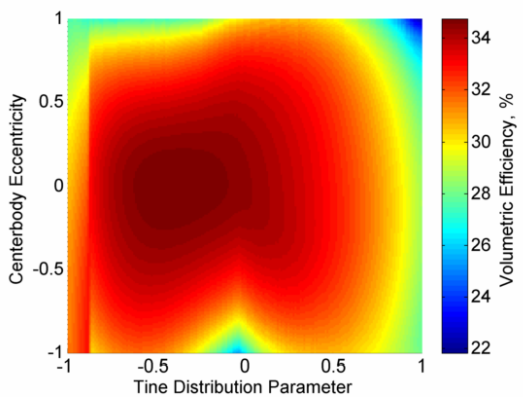

Figure A.43: Range of volumetric efficiency for a 5-tined starbody with α_0 = 0.62. M = 18, h = 20 km, in the Martian atmosphere.

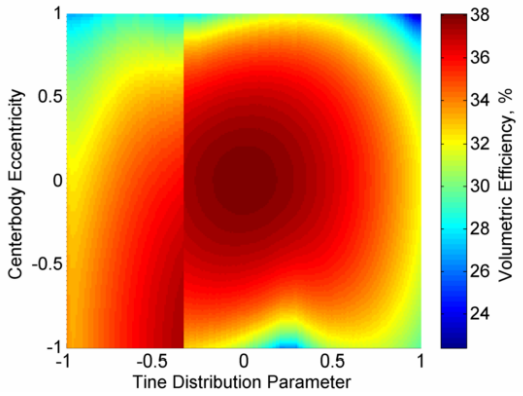

Figure A.44: Range of volumetric efficiency for a 5-tined starbody with α_0 = 0. M = 18, h = 20 km, in the Martian atmosphere.

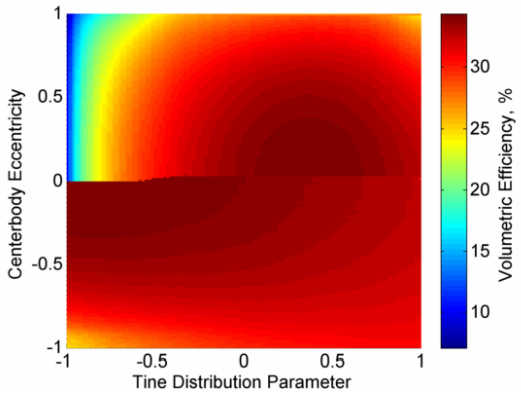

Figure A.45: Range of volumetric efficiency for a 5-tined starbody with α_0 = -0.62. M = 18, h = 20 km, in the Martian atmosphere.

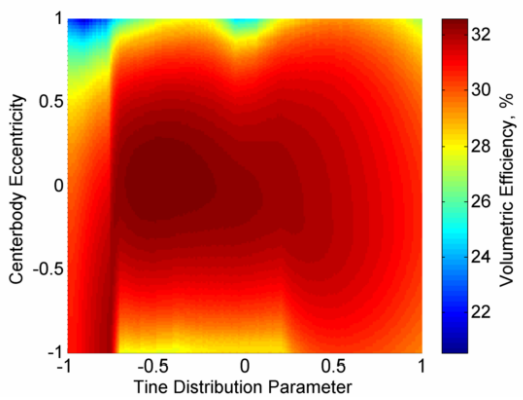

Figure A.46: Range of volumetric efficiency for a 6-tined starbody with α_0 = 0.62. M = 18, h = 20 km, in the Martian atmosphere.

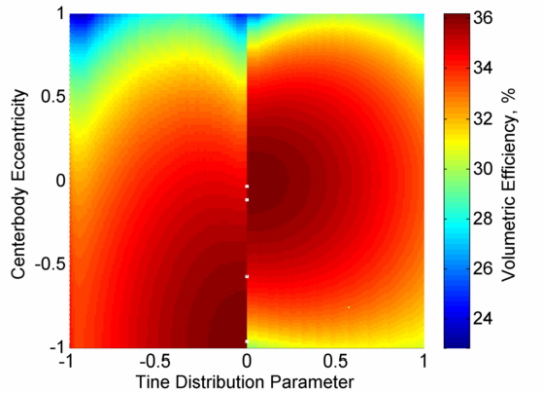

Figure A.47: Range of volumetric efficiency for a 6-tined starbody with α_0 = 0. M = 18, h = 20 km, in the Martian atmosphere.

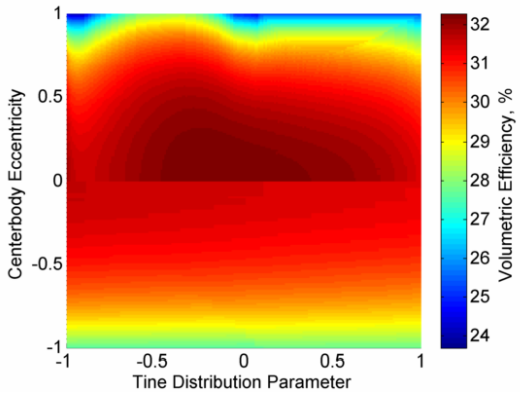

Figure A.48: Range of volumetric efficiency for a 6-tined starbody with α_0 = -0.62. M = 18, h = 20 km, in the Martian atmosphere.

Appendix B

Interstellar Launch Opportunities

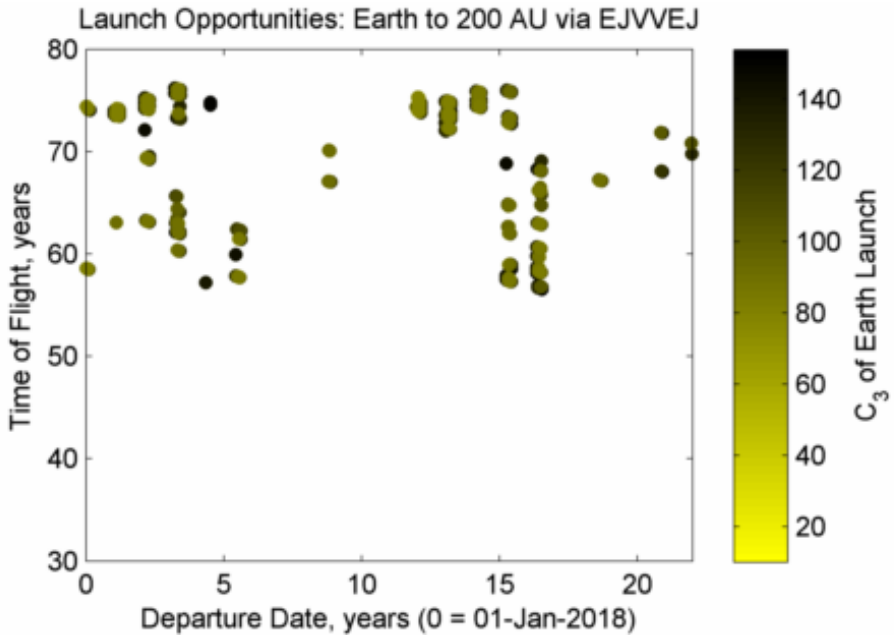

Figure B.1: Launch opportunities and required energy for Earth, Jupiter GA, Venus GA, Venus GA, Earth GA, Jupiter GA, 200 AU route

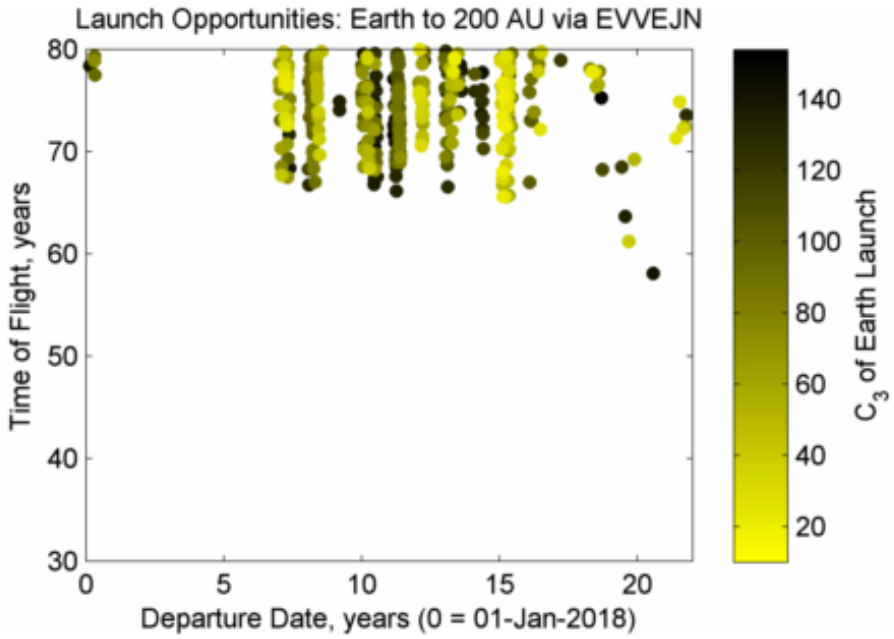

Figure B.2: Launch opportunities and required energy for Earth, Venus GA, Venus GA, Earth GA, Jupiter GA, Neptune GA, 200 AU route

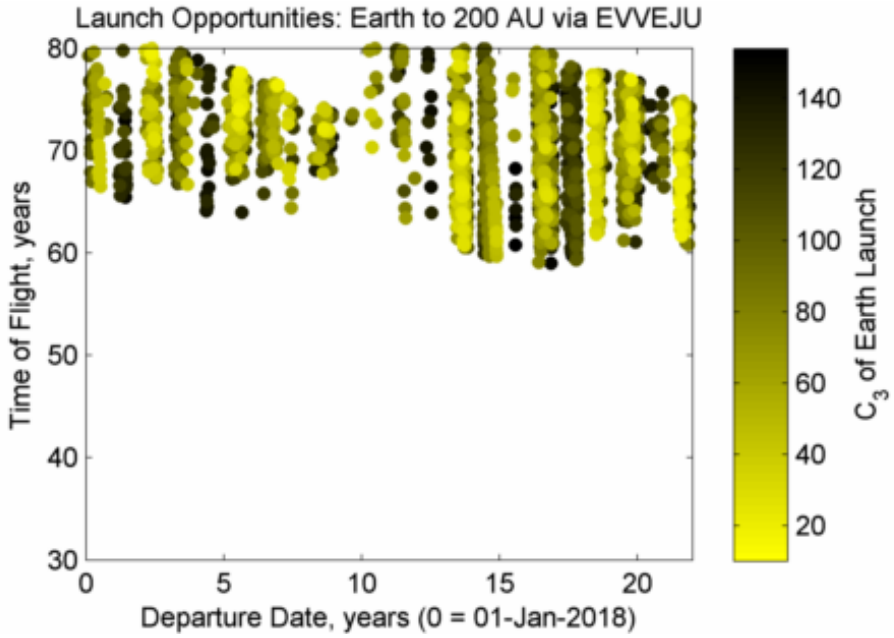

Figure B.3: Launch opportunities and required energy for Earth, Venus GA, Venus GA, Earth GA, Jupiter GA, Uranus GA, 200 AU route

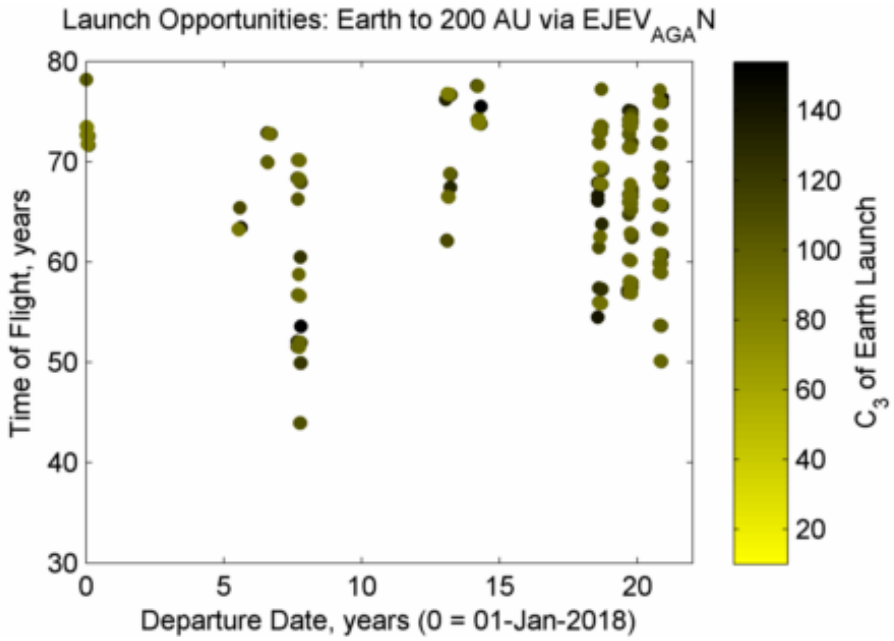

Figure B.4: Launch opportunities and required energy for Earth, Jupiter GA, Earth GA, Venus AGA, Neptune GA, 200 AU route

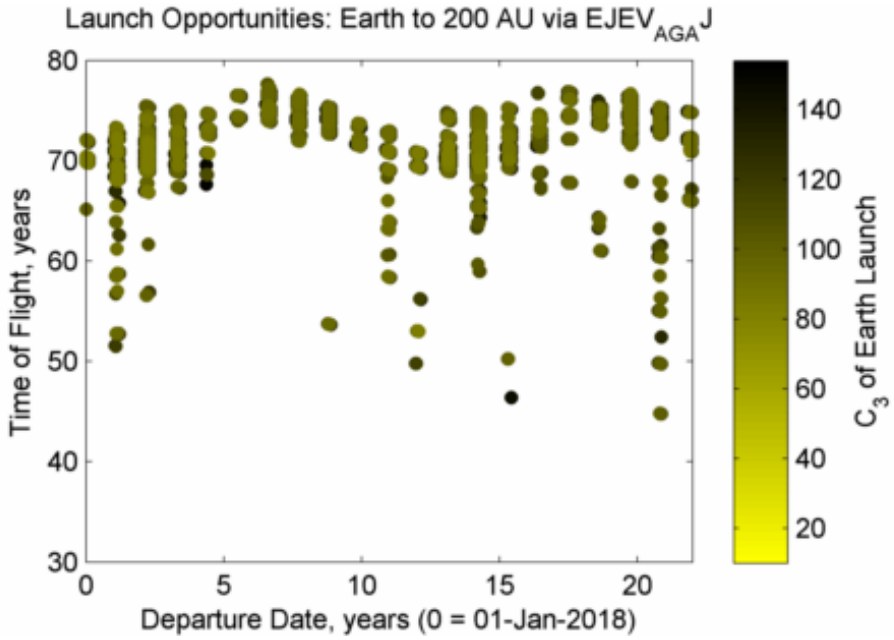

Figure B.5: Launch opportunities and required energy for Earth, Jupiter GA, Earth GA, Venus AGA, Jupiter GA, 200 AU route

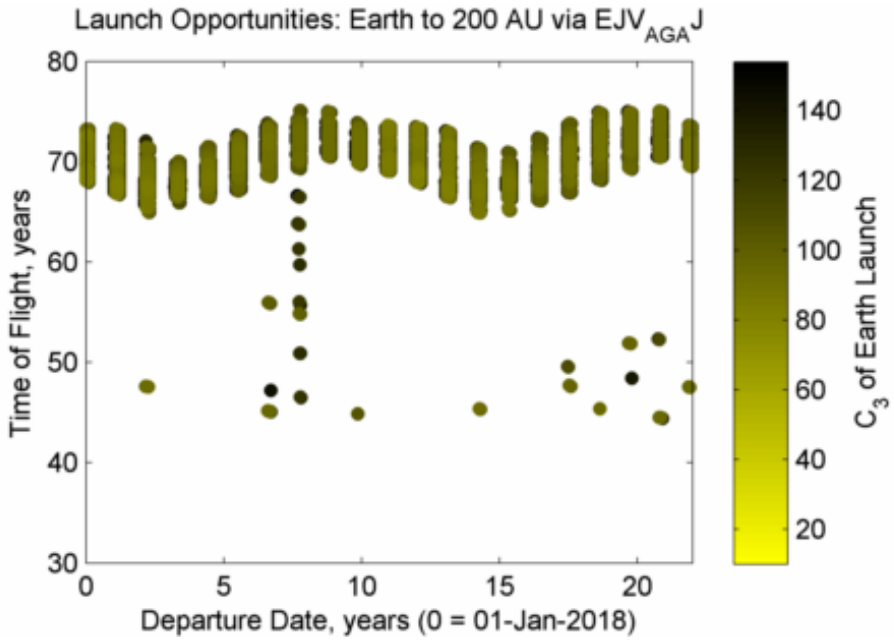

Figure B.6: Launch opportunities and required energy for Earth, Jupiter GA, Venus AGA, Jupiter GA, 200 AU route

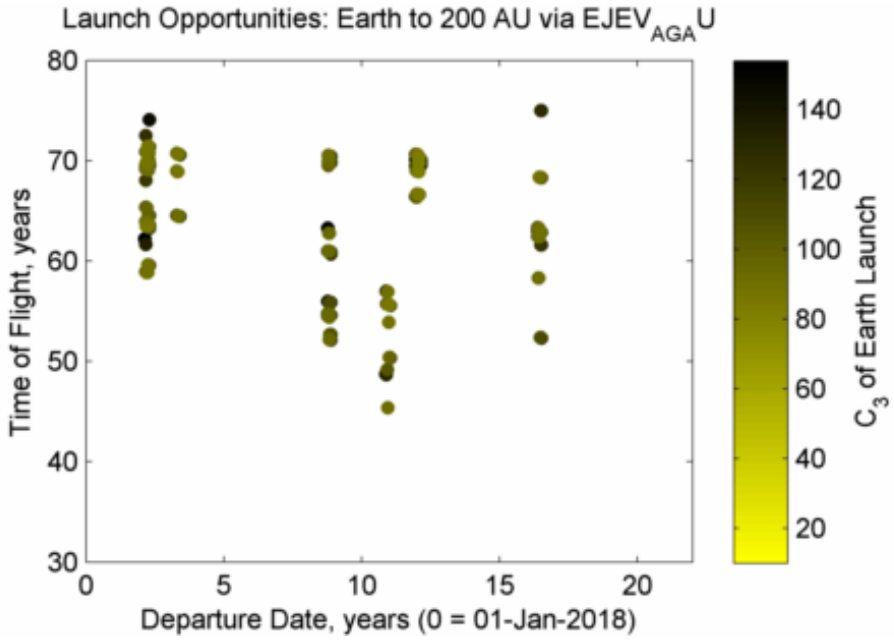

Figure B.7: Launch opportunities and required energy for Earth, Jupiter GA, Earth GA, Venus AGA, Uranus GA, 200 AU route

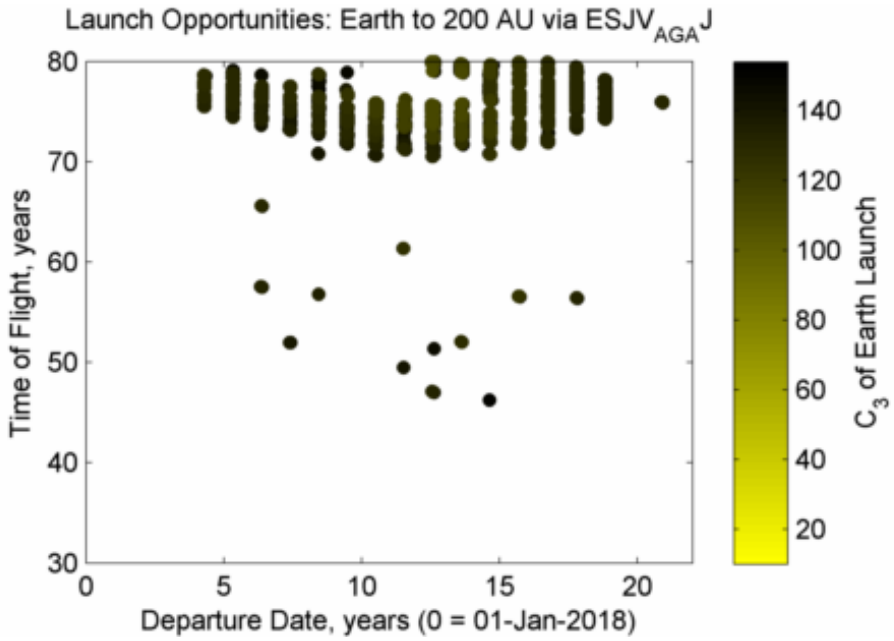

Figure B.8: Launch opportunities and required energy for Earth, Saturn GA, Jupiter GA, Venus AGA, Jupiter GA, 200 AU route

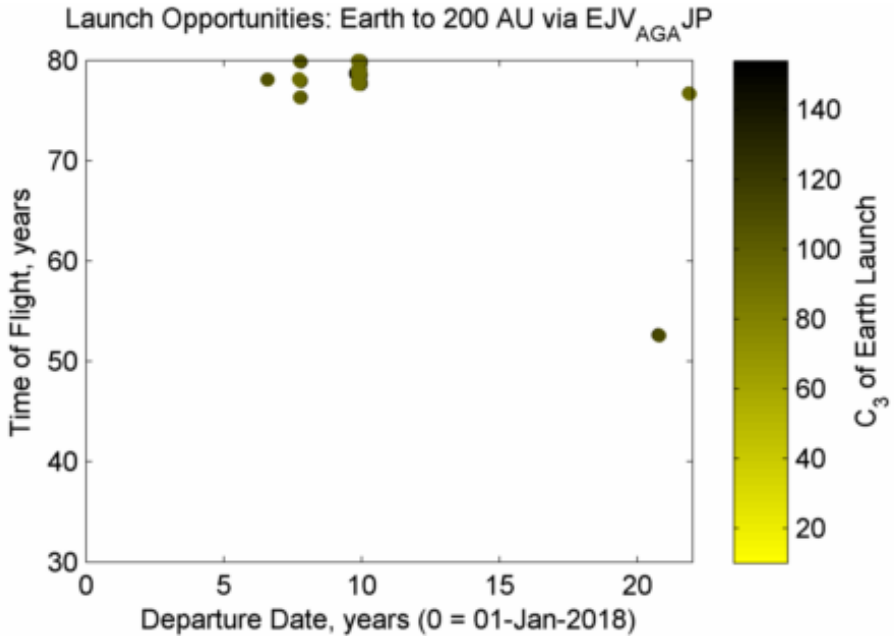

Figure B.9: Launch opportunities and required energy for Earth, Jupiter GA, Venus AGA, Jupiter GA, Pluto GA, 200 AU route

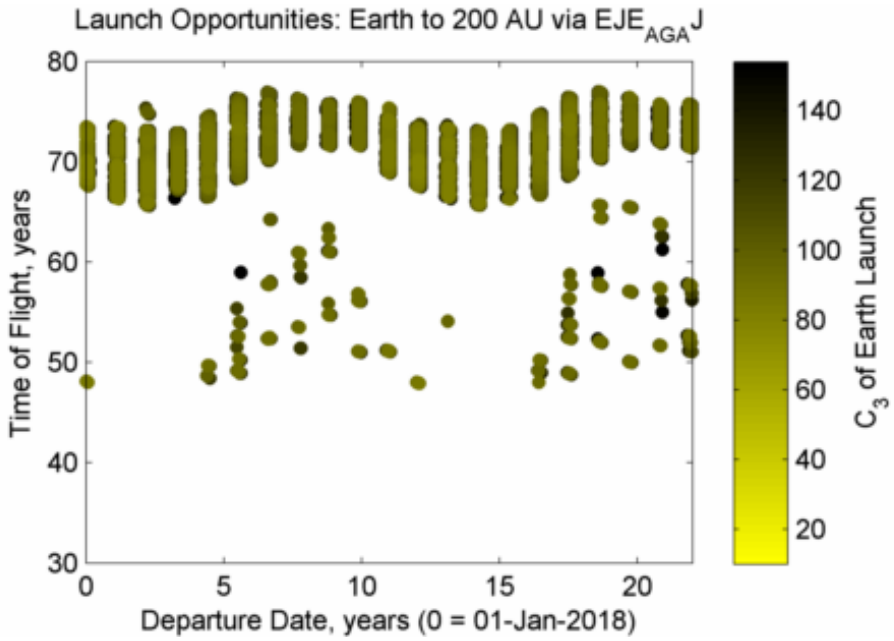

Figure B.10: Launch opportunities and required energy for Earth, Jupiter GA, Earth AGA, Jupiter GA, 200 AU route

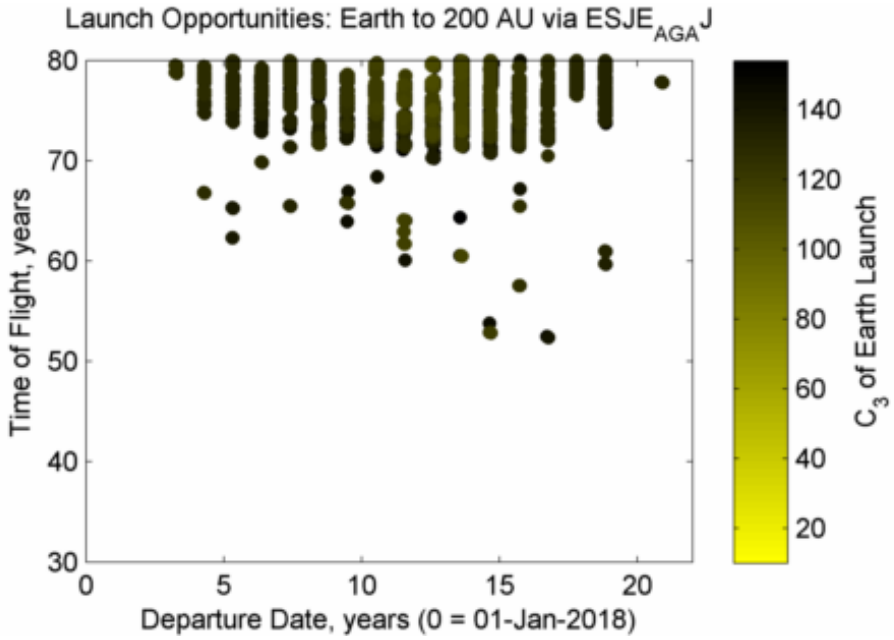

Figure B.11: Launch opportunities and required energy for Earth, Saturn GA, Jupiter GA, Earth AGA, Jupiter GA, 200 AU route

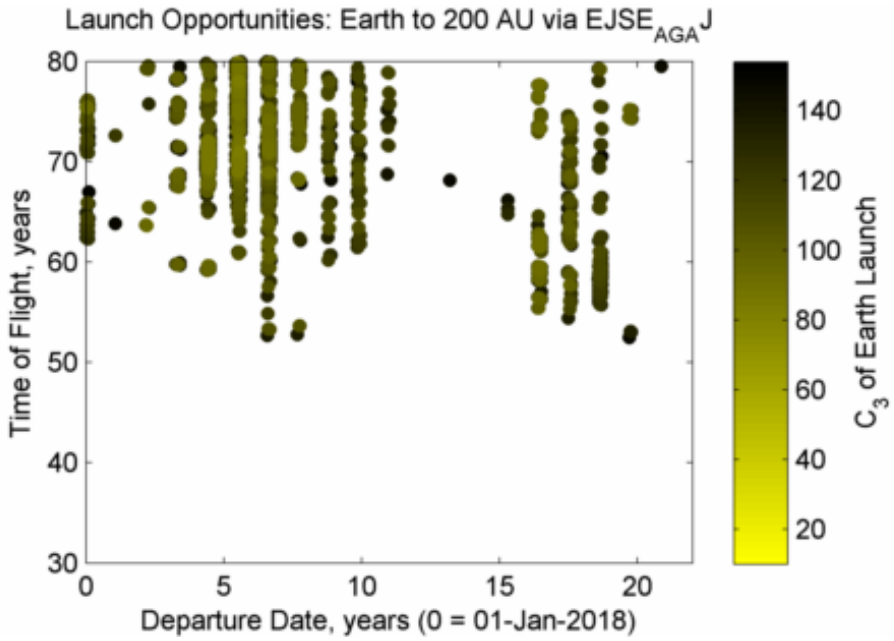

Figure B.12: Launch opportunities and required energy for Earth, Jupiter GA, Saturn GA, Earth AGA, Jupiter GA, 200 AU route

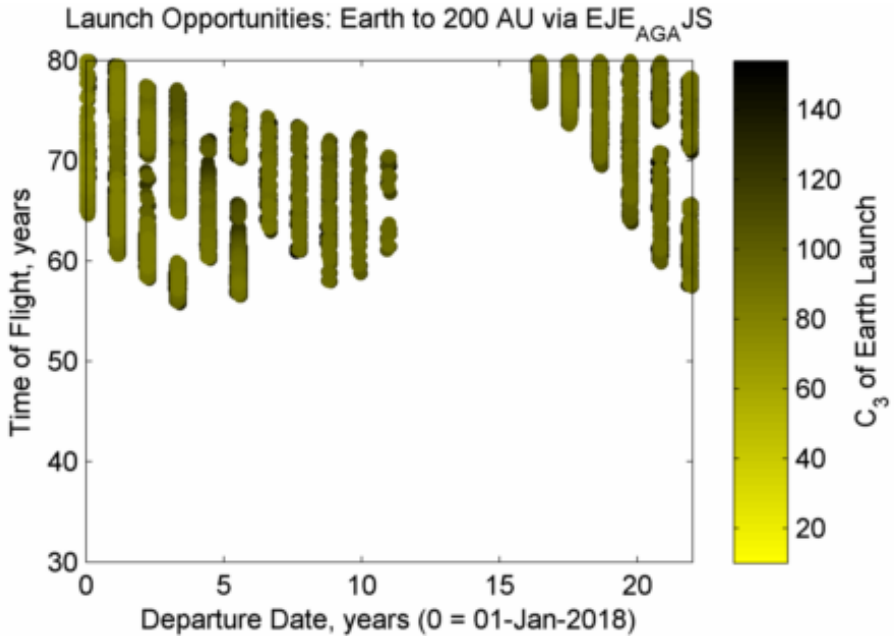

Figure B.13: Launch opportunities and required energy for Earth, Jupiter GA, Earth AGA, Jupiter GA, Saturn GA, 200 AU route

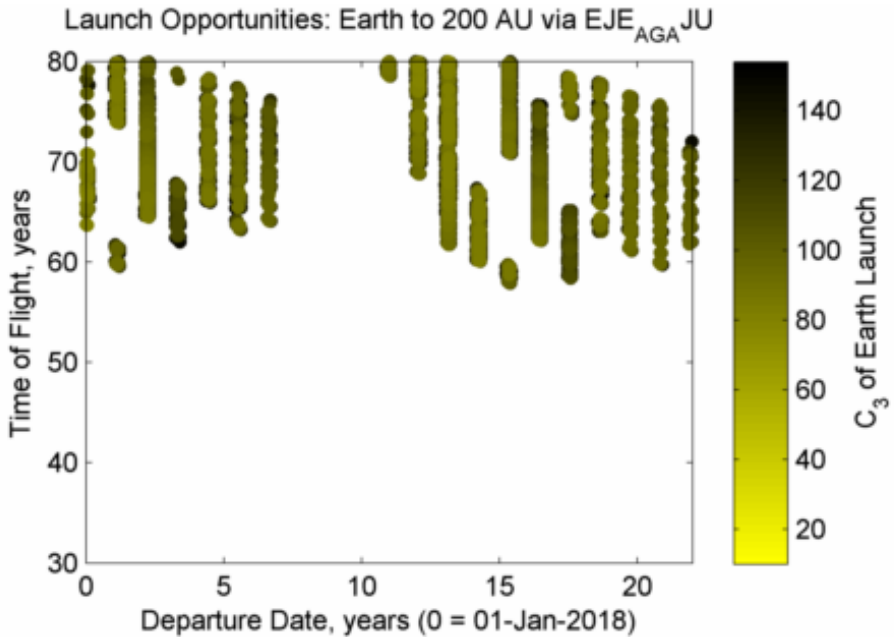

Figure B.14: Launch opportunities and required energy for Earth, Jupiter GA, Earth AGA, Jupiter GA, Uranus GA, 200 AU route

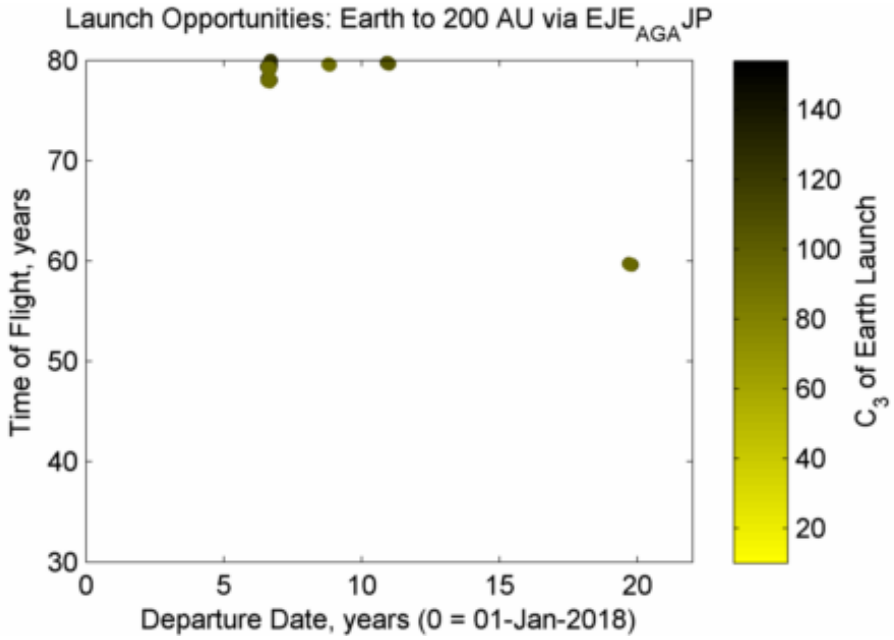

Figure B.15: Launch opportunities and required energy for Earth, Jupiter GA, Earth AGA, Jupiter GA, Pluto GA, 200 AU route

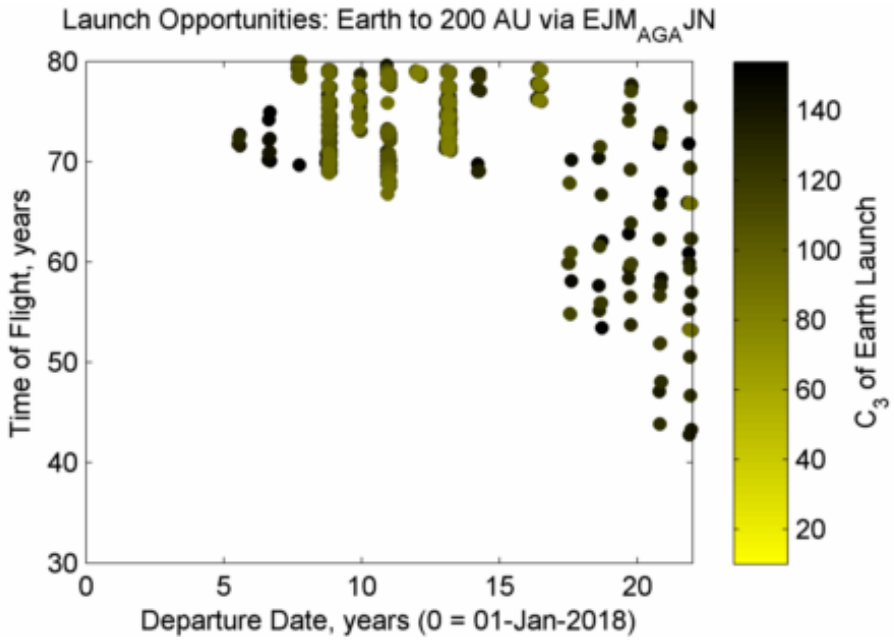

Figure B.16: Launch opportunities and required energy for Earth, Jupiter GA, Mars AGA, Jupiter GA, Neptune GA, 200 AU route

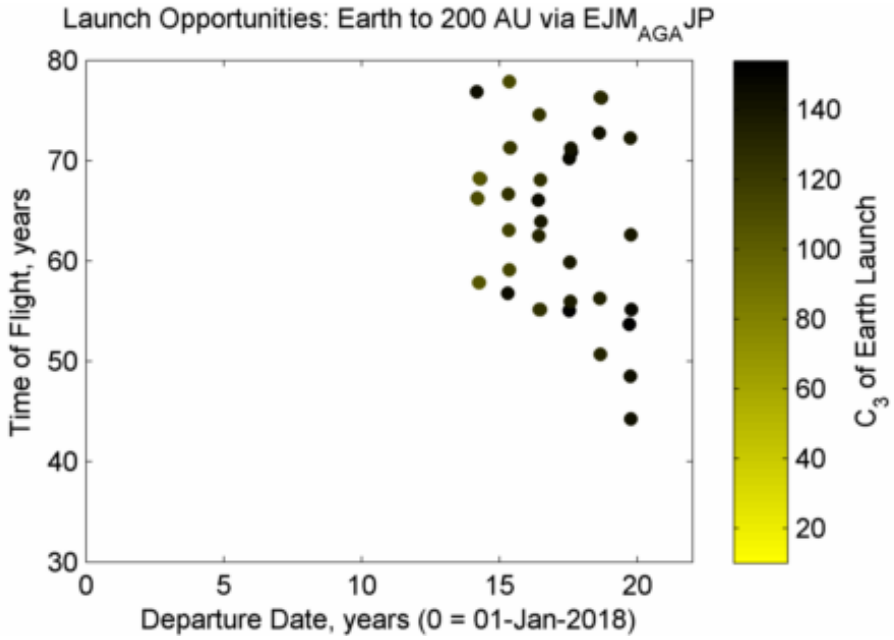

Figure B.17: Launch opportunities and required energy for Earth, Jupiter GA, Mars AGA, Jupiter GA, Pluto GA, 200 AU route

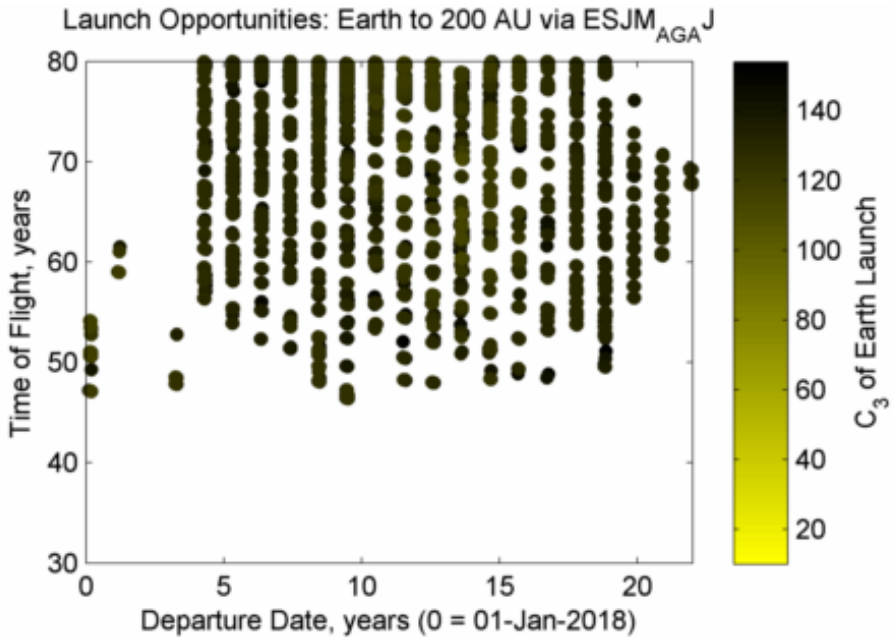

Figure B.18: Launch opportunities and required energy for Earth, Saturn GA, Jupiter GA, Mars AGA, Jupiter GA, 200 AU route

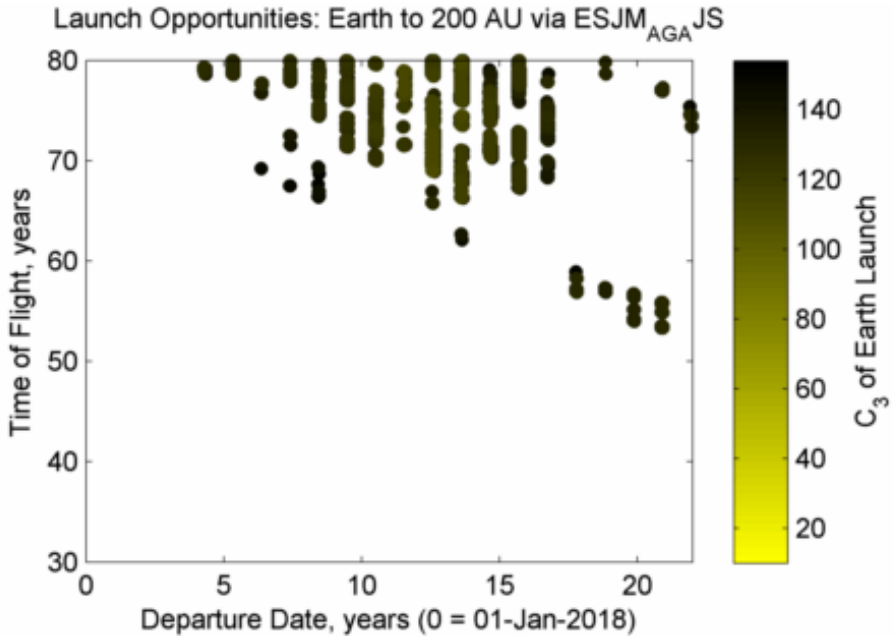

Figure B.19: Launch opportunities and required energy for Earth, Saturn GA, Jupiter GA, Mars AGA, Jupiter GA, Saturn GA, 200 AU route

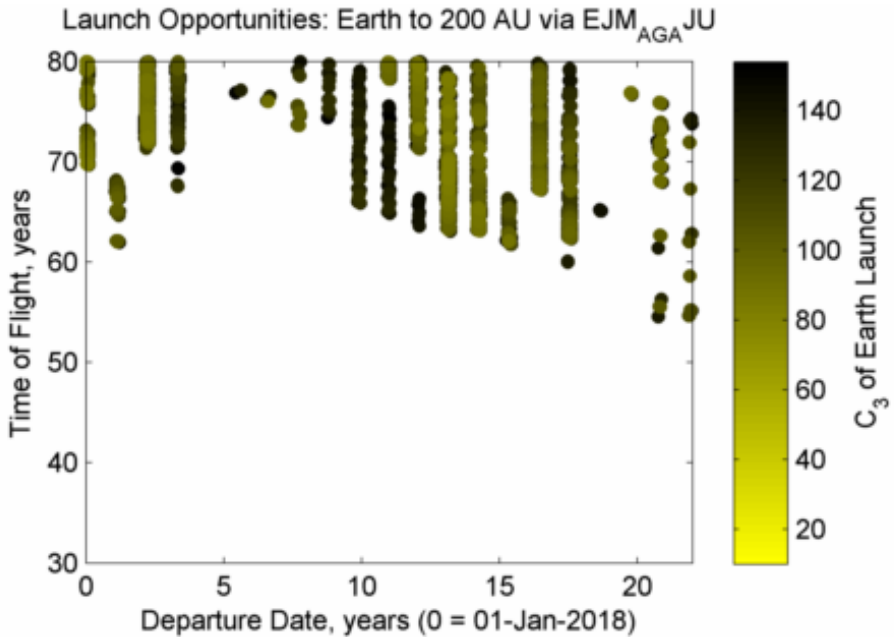

Figure B.20: Launch opportunities and required energy for Earth, Jupiter GA, Mars AGA, Jupiter GA, Uranus GA, 200 AU route

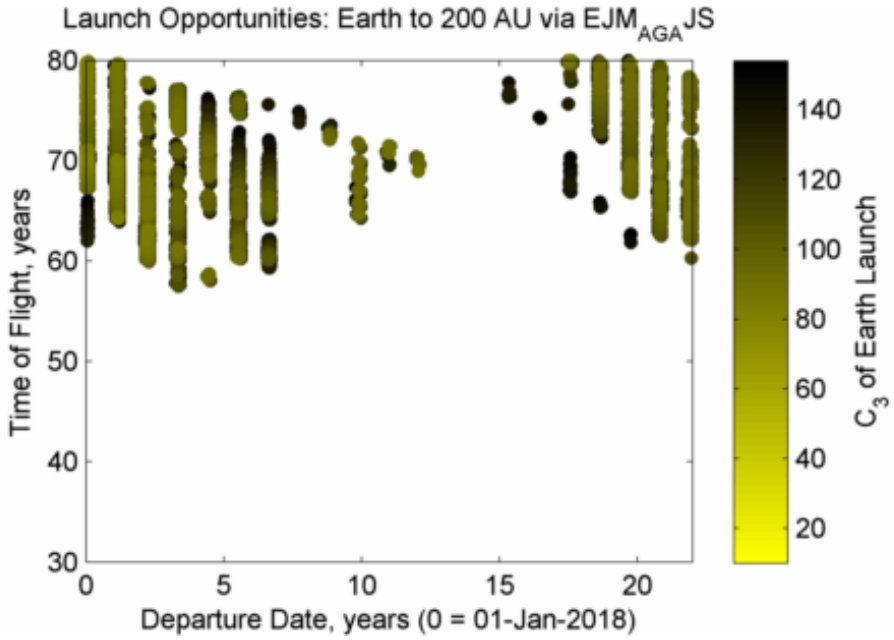

Figure B.21: Launch opportunities and required energy for Earth, Jupiter GA, Mars AGA, Jupiter GA, Saturn GA, 200 AU route

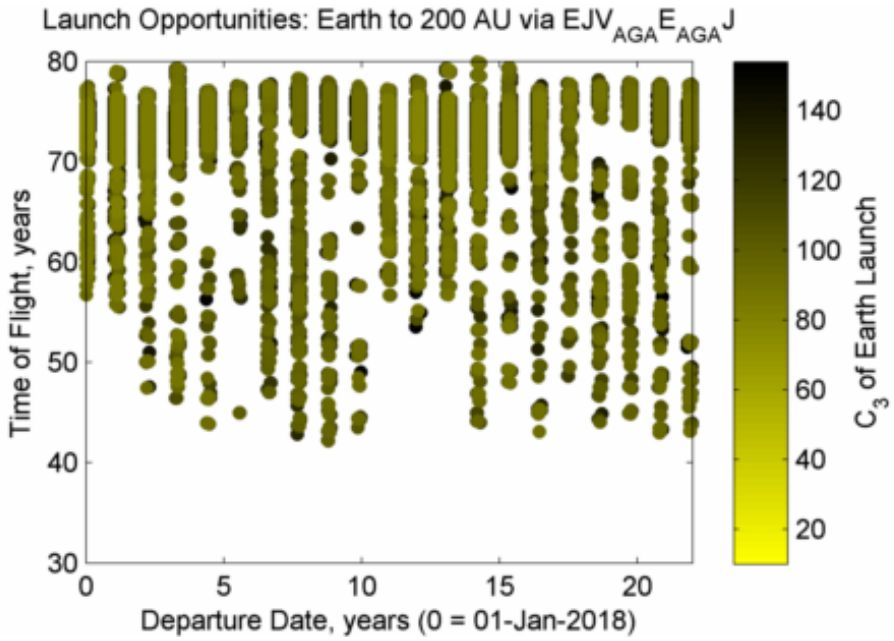

Figure B.22: Launch opportunities and required energy for Earth, Jupiter GA, Venus AGA, Earth AGA, Jupiter GA, 200 AU route

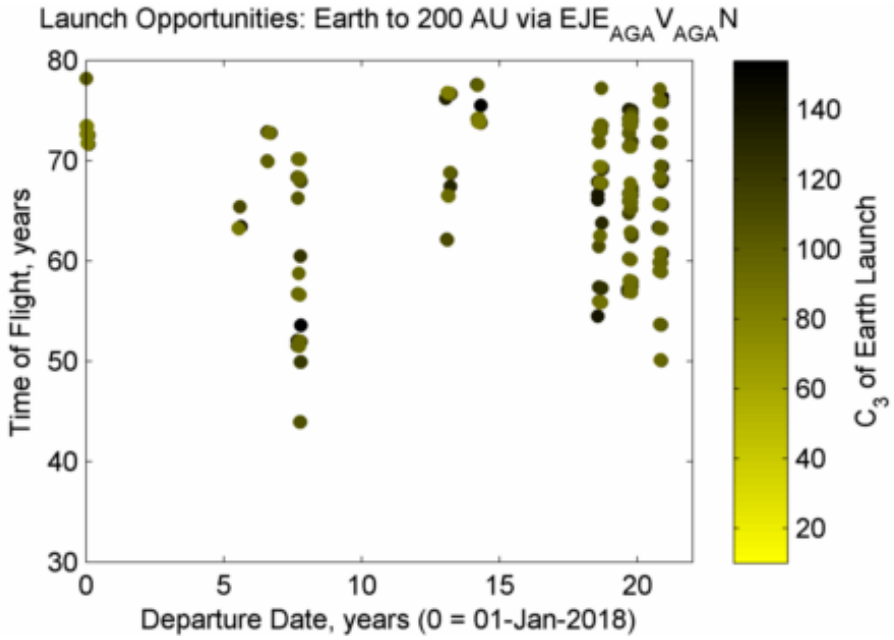

Figure B.23: Launch opportunities and required energy for Earth, Jupiter GA, Earth AGA, Venus AGA, Neptune GA, 200 AU route

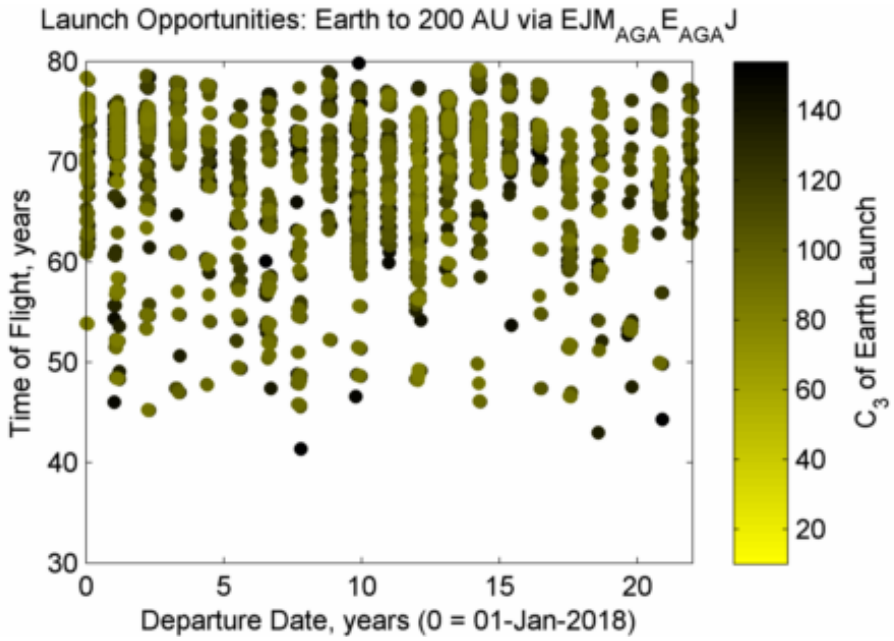

Figure B.24: Launch opportunities and required energy for Earth, Jupiter GA, Mars AGA, Earth AGA, Jupiter GA, 200 AU route

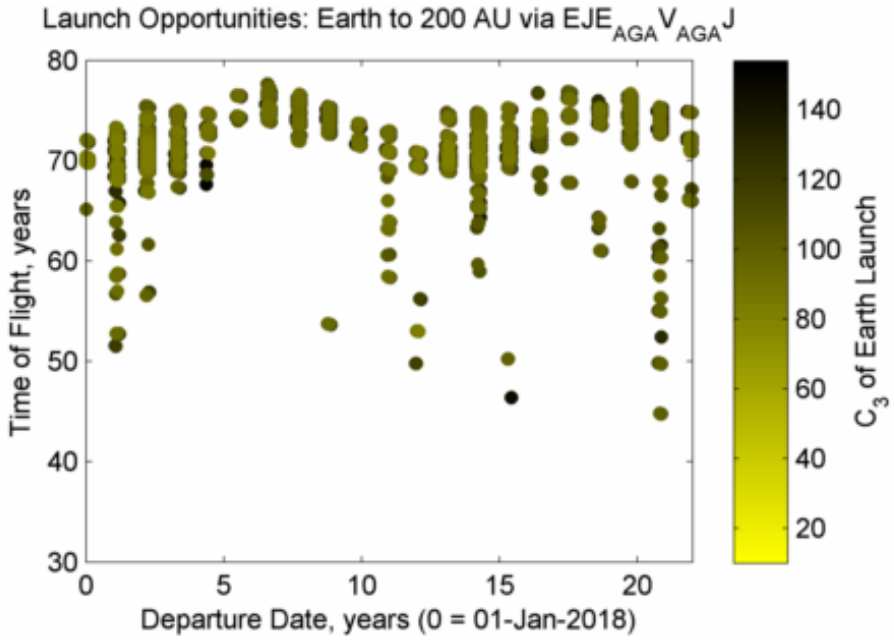

Figure B.25: Launch opportunities and required energy for Earth, Jupiter GA, Earth AGA, Venus AGA, Jupiter GA, 200 AU route

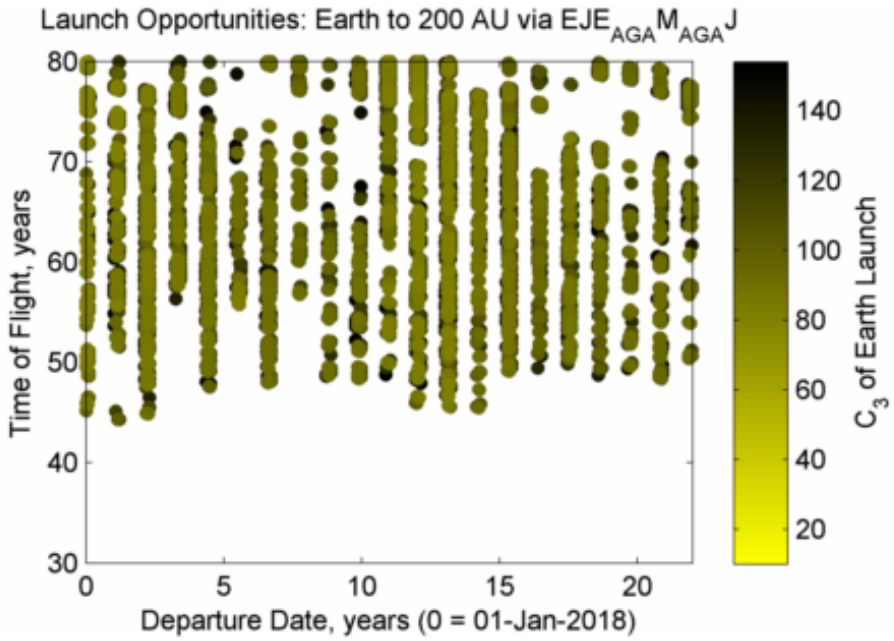

Figure B.26: Launch opportunities and required energy for Earth, Jupiter GA, Earth AGA, Mars AGA, Jupiter GA, 200 AU route

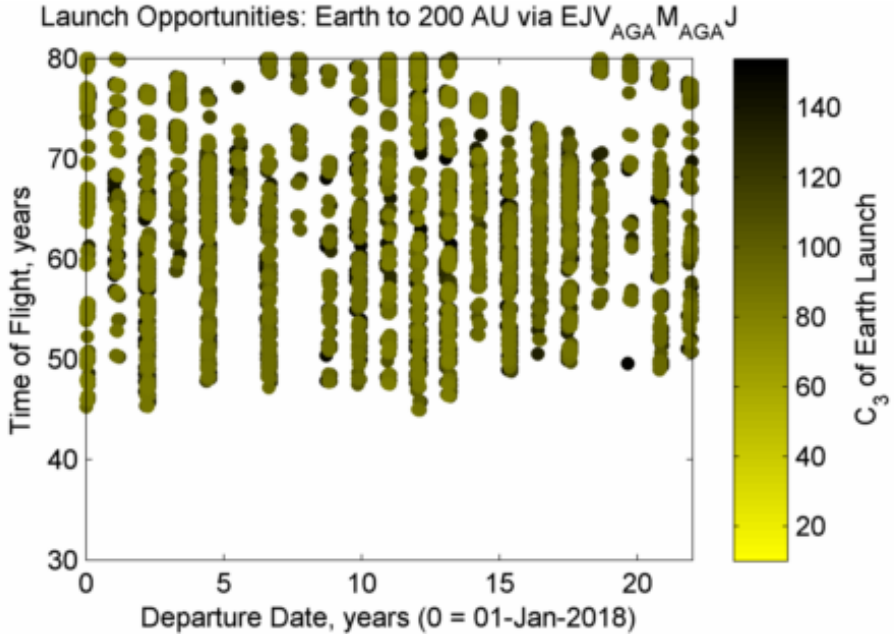

Figure B.27: Launch opportunities and required energy for Earth, Jupiter GA, Venus AGA, Mars AGA, Jupiter GA, 200 AU route

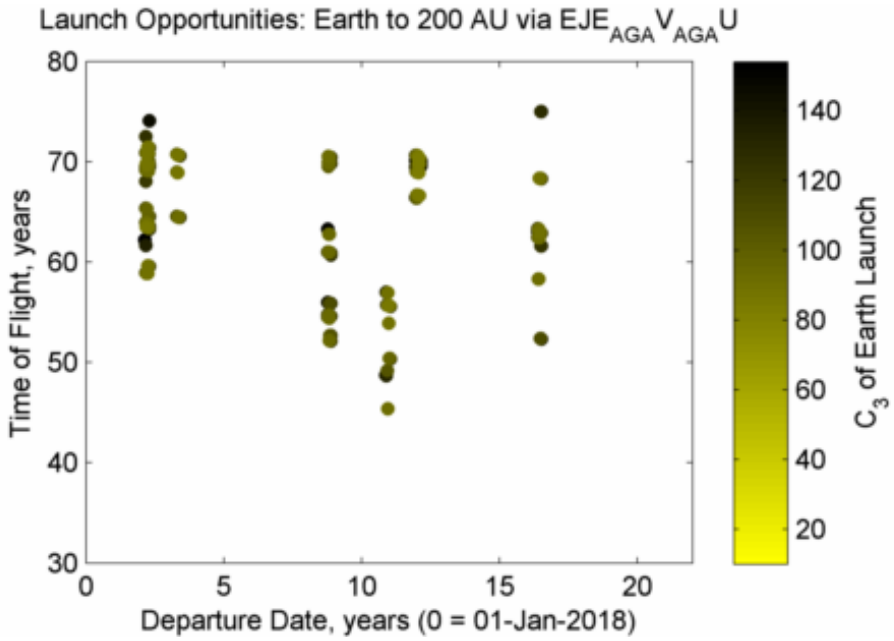

Figure B.28: Launch opportunities and required energy for Earth, Jupiter GA, Earth AGA, Venus AGA, Uranus GA, 200 AU route

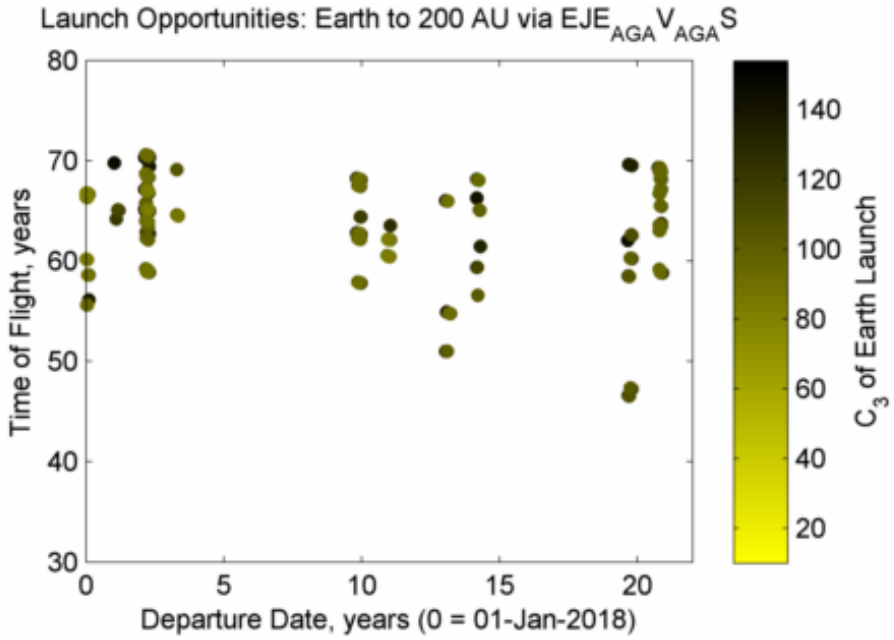

Figure B.29: Launch opportunities and required energy for Earth, Jupiter GA, Earth AGA, Venus AGA, Saturn GA, 200 AU route

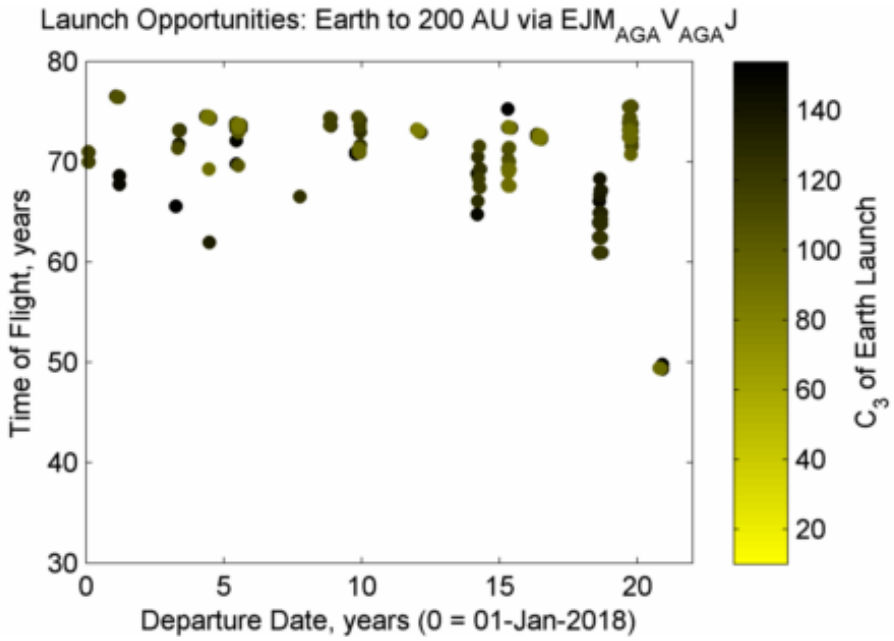

Figure B.30: Launch opportunities and required energy for Earth, Jupiter GA, Mars AGA, Venus AGA, Jupiter GA, 200 AU route

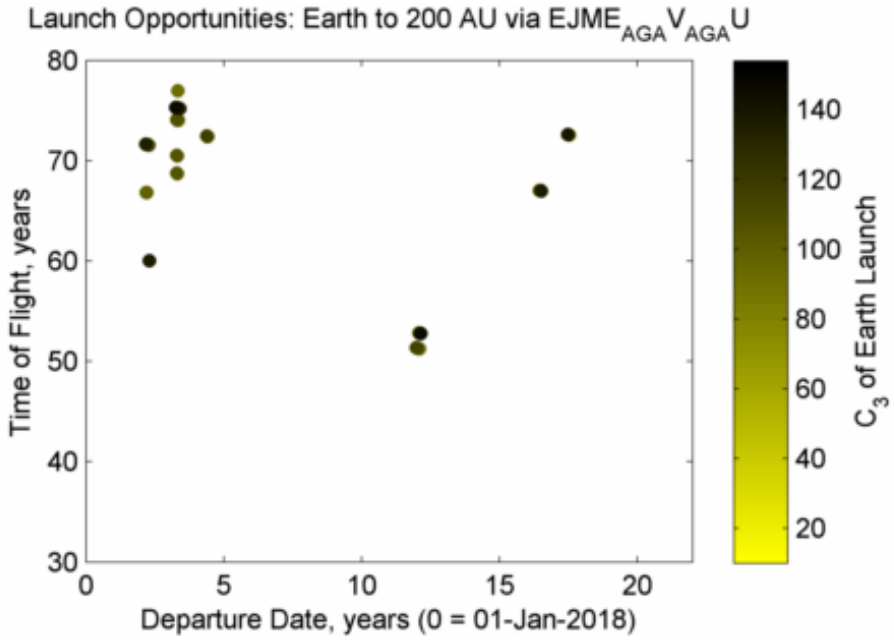

Figure B.31: Launch opportunities and required energy for Earth, Jupiter GA, Mars GA, Earth AGA, Venus AGA, Uranus GA, 200 AU route

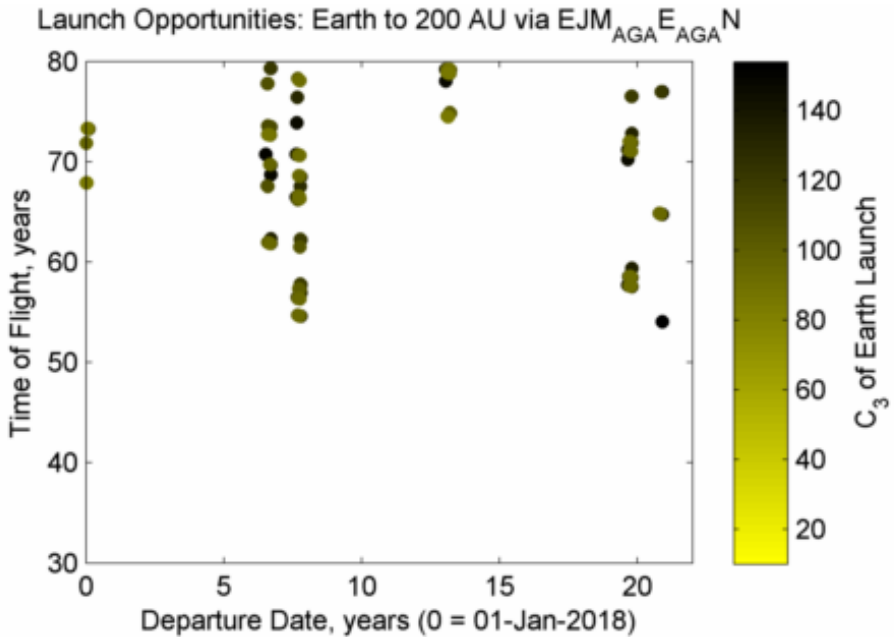

Figure B.32: Launch opportunities and required energy for Earth, Jupiter GA, Mars AGA, Earth AGA, Neptune GA, 200 AU route

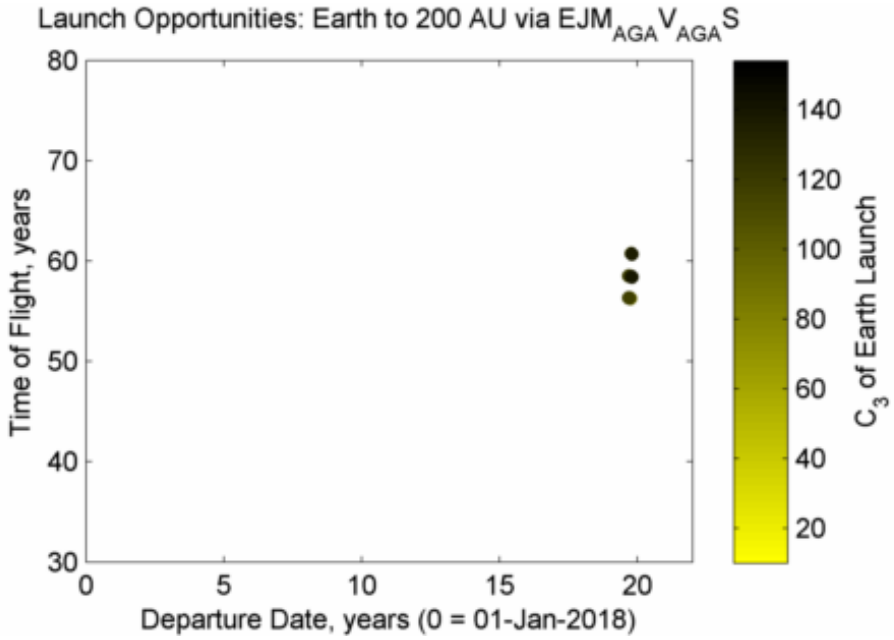

Figure B.33: Launch opportunities and required energy for Earth, Jupiter GA, Mars AGA, Venus AGA, Saturn GA, 200 AU route

References

[1] Talbert, T. and Green, M., "Space Technology Grand Challenges," December 2010 (accessed Nov 19th, 2014). `http://www.nasa.gov/offices/oct/strategic_integration/grand_challenges_detail.html`.

[2] Guo, Y. and Farquhar, R. W., "New Horizons mission design for the Pluto-Kuiper Belt mission," *Proceedings of the 2002 AIAA/AAS Astrodynamics Specialist Conference*, Aug 5-8, Monterey, CA, 2002.

[3] Spencer, D. A., Blanchard, R. C., Thurman, S. W., Braun, R. D., Peng, C.-Y., and Kallemeyn, P. H., "Mars pathfinder atmospheric entry reconstruction," *Proceedings of the 1998 AAS/AIAA Space Flight Mechanics Meeting*, Feb 9-11, Monterey, CA, 1998.

[4] Nonweiler, T., "Aerodynamic problems of manned space vehicles," *Journal of the Royal Aeronautical Society*, Vol. 63, No. 4, 1959, pp. 521–528.

[5] Nonweiler, T., "Delta wings of shapes amenable to exact shock-wave theory," *Journal of the Royal Aeronautical Society*, Vol. 67, No. 1, 1963, pp. 39–40.

[6] Townend, L., "On lifting bodies which contain two-dimensional supersonic flows," *RAE RN Aero 2675*, 1964.

[7] Jones, J., "A method for designing lifting configurations for high supersonic speeds using the flow fields of non-lifting cones," *RAE RN Aero 2674*, 1963.

[8] Jones, M. J., Moore, M. K., Pike, M. J., and Roe, M. P., "A method for designing lifting configurations for high supersonic speeds, using axisymmetric flow fields," *Ingenieur-Archiv*, Vol. 37, No. 1, 1968, pp. 56–72.

[9] Gonor, A., Kazakov, M., and Shvets, A., "Drag measurements on star-shaped body at M = 6 and 8," *Fluid Dynamics*, Vol. 3, No. 1, 1968, pp. 64–66, 10.1007/BF01016240.

[10] Pennelegion, L. and Cash, R., "Preliminary measurements in a shock tunnel, of shock angle and under-surface pressure related to a Nonweiler wing," *ARCoCP*, No. 684, 1962.

[11] Pike, J., "Experimental Results from Three Cone Flow Waveriders," *Hypersonic Boundary Layers and Flow Fields*, Vol. 30, 1968.

[12] Kipke, K., "Experimental investigations of waveriders in the Mach number range from 8 to 15," *Hypersonic Boundary Layers and Flow Fields*, Vol. 30, 1968.

[13] Squire, L. and Roe, P., "Off-design conditions for waveriders," RAE Technical Memorandum Aero 1168, 1969.

[14] Rasmussen, M. P. F., "Waverider configurations derived from inclined circular and elliptic cones," *Journal of Spacecraft and Rockets*, Vol. 17, No. 6, 1980, pp. 537–545.

[15] Rasmussen, M. and Clement, L., "Cone-derived waveriders with longitudinal curvature," *Journal of Spacecraft and Rockets*, Vol. 23, No. 5, 1986, pp. 461–469.

[16] Sobieczky, H., Dougherty, F., and Jones, K., "Hypersonic waverider design from given shock waves," *Proceedings of the First International Hypersonic Waverider Symposium*, 1990, pp. 17–19.

[17] Starkey, R. P. and Lewis, M. J., "Simple analytical model for parametric studies of hypersonic waveriders," *Journal of Spaceraft and Rockets*, Vol. 36, No. 4, 1999, pp. 516–523.

[18] Starkey, R. P. and Lewis, M. J., "Analytical off-design lift-to-drag-ratio analysis for hypersonic waveriders," *Journal of Spacecraft and Rockets*, Vol. 37, No. 5, 2000, pp. 684–691.

[19] Sabean, J. W., Lewis, M. J., Mee, D., and Paull, A., "Performance study of a power law starbody," *Journal of Spaceraft and Rockets*, Vol. 36, No. 5, 1999, pp. 646–652.

[20] Corda, S., "Star-body waveriders with multiple design mach numbers," *Journal of Spacecraft and Rockets*, Vol. 46, No. 6, 2009, pp. 1178–1185.

[21] Kim, B., Rasmussen, M., and Jischke, M., "Optimization of waverider configurations generated from axisymmetricconical flows," *Journal of Spacecraft and Rockets*, Vol. 20, No. 5, 1983, pp. 461–469.

[22] Bowcutt, K. G., *Optimization of hypersonic waveriders derived from cone flows, including viscous effects.* PhD thesis, University of Maryland, College Park, 1986.

[23] Bowcutt, K. G., Anderson, J. D., and Capriotti, D., "Viscous optimized hypersonic waveriders," *AIAA Paper 87-0272*, 1987.

[24] Corda, S. and Anderson, J. D., "Viscous optimized hypersonic waveriders designed from axisymmetric flow fields," *26th AIAA Aerospace Sciences Meeting*, Jan 7-9, Reno, NV, 1988.

[25] Mangin, B., Benay, R., Chanetz, B., and Chpoun, A., "Optimization of viscous waveriders derived from axisymmetric power-law blunt body flows," *Journal of Spaceraft and Rockets*, Vol. 43, No. 5, 2006, pp. 990–998.

[26] Foster, N. F., Dulikravich, G. S., and Bowies, J., "Three-dimensional aerodynamic shape optimization using genetic evolution and gradient search algorithms," *Proceedings of the 34th AIAA Aerospace Sciences Meeting and Exhibit*, Jan 15-18, Reno, NV, 1996.

[27] Starkey, R. P., Rankins, F., and Pines, D., "Coupled waverider/trajectory optimization for hypersonic cruise," *43rd AIAA Aerospace Sciences Meeting*, Jan 10-13, Reno, NV, 2005.

[28] Armellin, R., Lavagna, M., Starkey, R. P., and Lewis, M. J., "Aerogravity Assist Maneuvers: Coupled Trajectory and Vehicle Shape Optimization," *Journal of Spacecraft and Rockets*, Vol. 44, No. 5, 2007, pp. 1051–1059.

[29] Burt, J. M., Josyula, E., Ferguson, F., and Blankson, I. M., "Automated Aerodynamic Optimization for Lifting Hypersonic Vehicles at High Altitude," *50th AIAA Aerospace Sciences Meeting and Exhibit*, Jan 6-9, Nashville, TN.

[30] Ryan, K., *Robust Multi-Objective Optimization of Hypersonic Vehicles Under Asymmetric Roughness-Induced Boundary-Layer Transition*. PhD thesis, University of Maryland, College Park, 2014.

[31] Neville, A. G. and Candler, G. V., "Computational-Fluid-Dynamics-Based Axisymmetric Aeroshell Shape Optimization in Hypersonic Entry Conditions," *Journal of Spacecraft and Rockets*, 2014, pp. 1–13.

[32] Takashima, N. and Lewis, M. J., "Navier-Stokes computation of a viscous optimized waverider," *Journal of Spacecraft and Rockets*, Vol. 31, No. 3, 1994, pp. 383–391.

[33] Gillum, M. J. and Lewis, M. J., "Experimental results on a Mach 14 waverider with blunt leading edges," *Journal of Aircraft*, Vol. 34, No. 3, 1997, pp. 296–303.

[34] Kammeyer, M. E. and Gillum, M. J., "Design Validation Tests on a Realistic Hypersonic Waverider at Mach 10, 14, and 16.5 in the Naval Surface Warfare Center Hypervelocity Wind Tunnel No. 9," Tech. Rep. 93/198, DTIC Document NSWCDD, 1994.

[35] Burnett, D. W. and Lewis, M. J., "A re-evaluation of the waverider design process," *31st AIAA Aerospace Sciences Meeting*, Jan 4-7, Reno, NV, 1993.

[36] Drayna, T. W., Nompelis, I., and Candler, G. V., "Numerical simulation of the AEDC waverider at Mach 8," *25th AIAA Aerodynamic Measurement Technology and Ground Testing Conference*, Jun 5-8, San Francisco, CA, 2006.

[37] Norris, J. D., "Mach 8 High Reynolds Number Static Stability Capability Extension Using a Hypersonic Waverider at AEDC Tunnel 9," *25th AIAA Aerodynamic Measurement Technology and Ground Testing Conference*, Jun 5-8, San Francisco, CA, 2006.

[38] Chauffour, M., *Shock-Based Waverider Design With Pressure Corrections and Computational Simulations*. Masters Thesis, University of Maryland, College Park.

[39] Vanhoy, D. and Jones, E., "Low-speed wind tunnel testing of a Mach 6 viscous optimized waverider," *International Hypersonic Waverider Symposium*, College Park, MD, 1990.

[40] Bauer, S., Covell, P., Forrest, D., and McGrath, B., "Preliminary Assessment of a Mach 4 and Mach 6 waverider," *International Hypersonic Waverider Symposium*, College Park, MD, 1990.

[41] Ohta, T., Miyagawa, T., and Matsuzaki, R., "Experimental study of cone-derived waveriders at Mach 5.5," *Journal of Spaceraft and Rockets*, Vol. 34, No. 4, 1997, pp. 445–448.

[42] Miller, R. W., Argrow, B. M., Center, K. B., Brauckmann, G. J., and Rhode, M. N., "Experimental verification of the osculating cones method for two waverider forebodies at Mach 4 and 6," *36th AIAA Aerospace Sciences Meeting*, Jan 12-15, Reno, NV, 1998.

[43] Liao, J.-R., Isaac, K. M., Miles, J. B., and Tsai, B.-J., "Navier-Stokes simulation for cone-derived waverider," *AIAA journal*, Vol. 30, No. 6, 1992, pp. 1521–1528.

[44] Cockrell, C. E., "Interpretation of waverider performance data using computational fluid dynamics," *Journal of Aircraft*, Vol. 31, No. 5, 1994, pp. 1095–1100.

[45] Hui, W. H., "Stability of oscillating wedges and caret wings in hypersonic and supersonic flows.," *AIAA Journal*, Vol. 7, No. 8, 1969, pp. 1524–1530.

[46] Rasmussen, M., "Stability derivatives for hypersonic waveriders according to Newtonian theory," *AIAA Atmospheric Flight Mechanics Conference*, Aug 7-9, Baltimore, MD, 1995.

[47] Lighthill, M. J., "Oscillating airfoils at high Mach number," *Journal of the Aeronautical Sciences*, Vol. 20, No. 6, 1953, pp. 402–406.

[48] Tarpley, C. and Lewis, M. J., "Stability derivatives for a hypersonic caret-wing waverider," *Journal of Aircraft*, Vol. 32, No. 4, 1995, pp. 795–803.

[49] v. Eggers Rudd, L. and Pines, D. J., "Integrated Propulsion Effects on Dynamic Stability and Control of Hypersonic Waveriders," *36th AIAA/ASME/SAE/ASEE Joint Propulsion Conference*, Jul 16-19 Huntsville, AL, 2000.

[50] Keshmiri, S., Colgren, R., and Mirmirani, M., "Six-DOF modeling and simulation of a generic hypersonic vehicle for control and navigation purposes," *AIAA Guidance, Navigation and Control Conference*, Aug 21-24, Keystone, CO, 2006.

[51] Bolender, M. A., "An overview on dynamics and controls modelling of hypersonic vehicles," *Proceedings of the American Control Conference*, Jun 10-12, St. Louis, MO, 2009, pp. 2507–2512.

[52] Mooij, E., "Characteristic Motion of Re-entry Vehicles," *AIAA Atmospheric Flight Mechanics Conference*, Aug 19-22, Boston, MA, 2013.

[53] Yin, L.-L., Huang, Y.-m., Sun, C.-Z., Jia, J., and Yang, Y., "Improved Dutch Roll Approximation for Hypersonic Vehicle," *Sensors and Transducers*, Vol. 173, 2014, pp. 28–33.

[54] Anderson, J. D., *Hypersonic and High Temperature Gas Dynamics.* AIAA, 2000.

[55] Vanmol, D. O. and Anderson, J. D., "Heat Transfer Characteristics of Hypersonic Waveriders with an Emphasis on the Leading Edge Effects," *NASA CR 189586*, 1992.

[56] Blosser, M. L., Blankson, I. M., Schwoerke, S., Brunson, D., and Hagseth, P., "Wing leading-edge design concepts for airbreathing hypersonic waveriders," *Journal of Aircraft*, Vol. 32, No. 2, 1995, pp. 307–312.

[57] Mason, W. and Lee, J., "Aerodynamically blunt and sharp bodies," *Journal of Spacecraft and Rockets*, Vol. 31, No. 3, 1994, pp. 378–382.

[58] O'Brien, T. F. and Lewis, M. J., "Power law shapes for leading-edge blunting with minimal shock standoff," *Journal of Spaceraft and Rockets*, Vol. 36, No. 5, 1999.

[59] Santos, W. F. and Lewis, M. J., "Aerothermodynamic performance analysis of hypersonic flow on power law leading edges," *Journal of Spaceraft and Rockets*, Vol. 42, No. 4, 2005, pp. 588–597.

[60] Silvester, T. and Morgan, R., "Computational hypervelocity aerodynamics of a caret waverider," *40th AIAA/ASME/SAE/ASEE Joint Propulsion Conference and Exhibit.*

[61] London, H. S., "Change of satellite orbit plane by aerodynamic maneuvering," *Journal of the Aerospaces Sciences*, Vol. 29, No. 3, 1962, pp. 323–332.

[62] Roessler, M., "Optimal aerodynamic-propulsive maneuvering for the orbital plane change of a space vehicle.," *Journal of Spacecraft and Rockets*, Vol. 4, No. 12, 1967, pp. 1678–1680.

[63] Hull, D., Giltner, J., Speyer, J., and Mapar, J., "Minimum energy-loss guidance for aeroassisted orbital plane change," *Journal of Guidance, Control, and Dynamics*, Vol. 8, No. 4, 1985, pp. 487–493.

[64] Hull, D. G., McClendon, J. R., and Speyer, J. L., "Improved aeroassisted plane change using successive approximation," *Journal of the Astronautical Sciences*, Vol. 36, No. 1/2, 1988, pp. 89–101.

[65] Mease, K. D. and Vinh, N. X., "Minimum-fuel aeroassisted coplanar orbit transfer using lift-modulation," *Journal of Guidance, Control, and Dynamics*, Vol. 8, No. 1, 1985, pp. 134–141.

[66] Abd El-Salam, F., "Optimization out-of-orbit plane changes using aeroassisted maneuvers," *Applied Mathematics and Computation*, Vol. 170, No. 2, 2005, pp. 1303–1313.

[67] Lu, P. and Vinh, N. X., "Minimax optimal control for atmospheric fly-through trajectories," *Journal of Optimization Theory and Applications*, Vol. 57, No. 1, 1988, pp. 41–58.

[68] Kuo, T.-S., Chern, J.-S., and Hsu, F.-K., "Optimal aeroassisted orbital plane change with heating-rate constraint," *Journal of Guidance, Control, and Dynamics*, Vol. 13, No. 1, 1990, pp. 186–189.

[69] Mazzaracchio, A., "Thermal Protection System and Trajectory Optimization for Orbital Plane Change Aeroassisted Maneuver," *Journal of Aerospace Technology and Management*, Vol. 5, No. 1, 2013, pp. 49–64.

[70] Miele, A., "The 1st John V. Breakwell Memorial Lecture: Recent advances in the optimization and guidance of aeroassisted orbital transfers," *Acta Astronautica*, Vol. 38, No. 10, 1996, pp. 747 – 768.

[71] Randolph, J., "Aero-Gravity-Assist Trajectory Analysis for Starprobe," Jet Propulsion Lab., Pasadena, CA. Internal Memoranda 312182-5-981, 1982.

[72] Anderson, J. D., Ferguson, F., and Lewis, M., "Hypersonic waveriders for high altitude applications," *29th AIAA Aerospace Sciences Meeting*, Jan 7-10, Reno, NV, 1991.

[73] Rault, D. F., "Aerodynamic characteristics of a hypersonic viscous optimized waverider at high altitudes," *Journal of Spacecraft and Rockets*, Vol. 31, No. 5, 1994, pp. 719–727.

[74] Anderson, J. D., Lewis, M. J., Kothari, A. P., and Corda, S., "Hypersonic waveriders for planetary atmospheres," *Journal of Spacecraft and Rockets*, Vol. 28, No. 4, 1991, pp. 401–410.

[75] Lewis, M. J. and McRonald, A. D., "Design of hypersonic waveriders for aeroassisted interplanetary trajectories," *Journal of Spacecraft and Rockets*, Vol. 29, No. 5, 1992, pp. 653–660.

[76] McRonald, A. D. and Randolph, J. E., "Hypersonic maneuvering for augmenting planetary gravity assist," *Journal of Spacecraft and Rockets*, Vol. 29, No. 2, 1992, pp. 216–222.

[77] Randolph, J. E. and Mcronald, A. D., "Solar system 'fast mission' trajectories using aerogravity assist," *Journal of Spacecraft and Rockets*, Vol. 29, No. 2, 1992, pp. 223–232.

[78] Johnson, W. R. and Longuski, J. M., "Design of aerogravity-assist trajectories," *Journal of Spacecraft and Rockets*, Vol. 39, No. 1, 2002, pp. 23–30.

[79] Sims, J. A., Longuski, J. M., and Patel, M. R., "Aerogravity-assist trajectories to the outer planets," *Acta Astronautica*, Vol. 35, 1995, pp. 297–306.

[80] Sims, J. A., Longuski, J. M., and Patel, M. R., "Aerogravity-assist trajectories to the outer planets and the effect of drag," *Journal of Spacecraft and Rockets*, Vol. 37, No. 1, 2000, pp. 49–55.

[81] Bonfiglio, E. P., Longuski, J. M., and Vinh, N. X., "Automated design of aerogravity-assist trajectories," *Journal of Spacecraft and Rockets*, Vol. 37, No. 6, 2000, pp. 768–775.

[82] Lohar, F. A., Mateescu, D., and Misra, A., "Optimal atmospheric trajectory for aero-gravity assist," *Acta Astronautica*, Vol. 32, No. 2, 1994, pp. 89–96.

[83] Lohar, F. A., Misra, A. K., and Mateescu, D., "Optimal atmospheric trajectory for aerogravity assist with heat constraint," *Journal of Guidance, Control, and Dynamics*, Vol. 18, No. 4, 1995, pp. 723–730.

[84] Lohar, F. A., Misra, A. K., and Mateescu, D., "Optimal aero-gravity assist with heliocentric plane change," *Acta Astronautica*, Vol. 38, No. 4, 1996, pp. 445–456.

[85] Lavagna, M., Povoleri, A., and Finzi, A., "Interplanetary mission design with aero-assisted manoeuvres multi-objective evolutive optimization," *Acta Astronautica*, Vol. 57, No. 2, 2005, pp. 498–509.

[86] Armellin, R., Lavagna, M., and Ercoli-Finzi, A., "Aero-gravity assist maneuvers: controlled dynamics modeling and optimization," *Celestial Mechanics and Dynamical Astronomy*, Vol. 95, No. 1-4, 2006, pp. 391–405.

[87] Casoliva, J., Lyons, D. T., Wolf, A. A., and Mease, K. D., "Robust guidance via a Predictor-Corrector algorithm with drag tracking for aero-gravity assist maneuvers," *AIAA guidance, Navigation and control conference and exhibit*, Aug 18-21, Honolulu, HI, 2008.

[88] Lyons, D. T., Sklyanskiy, E., Casoliva, J., and Wolf, A. A., "Parametric Optimization and Guidance for an Aerogravity Assisted Atmospheric Sample Return From Mars and Venus," *AIAA guidance, Navigation and control conference and exhibit*, Aug 18-21, Honolulu, HI, 2008.

[89] Mazzaracchio, A., "Flight-Path Angle Guidance for Aerogravity-Assist Maneuvers on Hyperbolic Trajectories," *Journal of Guidance, Control, and Dynamics*, 2014, pp. 1–11.

[90] Cruz, M., "The aerocapture vehicle mission design concept," *Conference on Advanced Technology for Future Space Systems, Hampton, VA*, 1979, pp. 195–201.

[91] Knittel, J. M., Lewis, M. J., and Yu, K. H. *18th AIAA/3AF International Space Planes and Hypersonic Systems and Technologies Conference*, Sep 24-28, Tours, France, 2012.

[92] Vinh, N. X., Johnson, W. R., and Longuski, J. M., "Mars aerocapture using bank modulation," *AIAA/AAS Astrodynamics Specialist Conference*, Aug 14-17, Denver, CO, 2000.

[93] Whitmore, S. A., Banks, D. W., Andersen, B. M., and Jolley, P. R., "Direct-entry, aerobraking, and lifting aerocapture for human-rated lunar return vehicles," *Proceedings of the 44th AIAA Aerospace Sciences Meeting and Exibit*, Jan 11-13, Reno, NV, 2006.

[94] Armellin, R. and Lavagna, M., "Multidisciplinary optimization of aerocapture maneuvers," *Journal of Artificial Evolution and Applications*, 2008.

[95] Lockwood, M. K., "Titan aerocapture systems analysis," *AIAA Paper 2003-2799*, 2003.

[96] Lockwood, M. K., "Neptune aerocapture systems analysis," *AIAA Atmospheric Flight Mechanics Conference and Exhibit*, 2004, pp. 16–19.

[97] Wright, H. S., Oh, D. Y., Westhelle, C. H., Fisher, J. L., Dyke, R. E., Edquist, K. T., Brown, J. L., Justh, H. L., and Munk, M. M., "Mars Aerocapture Systems Study,"

[98] Nock, K. T., "TAU - A Mission to a Thousand Astronomical Units," *19th AIAA/DGLR/JSASS International Electric Propulsion Conference*, May 11-13, Colorado Springs, CO, 1987.

[99] Etchegaray, M. I., "Preliminary Scientific Rationale for a Voyage to a Thousand Astronomical Units," JPL Publication 87-17, 1987.

[100] Mewaldt, R. A. and Liewer, P. C., "An Interstellar Probe Mission to the Boundaries of the Heliosphere and Nearby Interstellar Space," *AIAA Space 2000 Conference and Exposition*, Sep 19-21, Long Beach, CA, 2000.

[101] Wallace, R. A., Ayon, J. A., and Sprague, G. A., "Interstellar probe mission/system concept," *2000 IEEE Aerospace Conference Proceedings*, Mar 20-25, Big Sky, MT, 2000, pp. 385–396.

[102] Johnson, L. and Leifer, S., "Propulsion options for interstellar exploration," *36th AIAA/ASME/SAE/ASEE Joint Propulsion Conference*, Jul 16-19 Huntsville, AL, 2000.

[103] Fiehler, D. I. and McNutt, R. L., "Mission design for the innovative interstellar explorer vision mission," *Journal of Spaceraft and Rockets*, Vol. 43, No. 6, 2006, pp. 1239–1247.

[104] Tarpley, C., *The optimization of engine-integrated hypersonic waveriders with steady state flight and static margin constraints*. PhD thesis, University of Maryland at College Park, 1995.

[105] Anderson, J. D., *Modern compressible flow: with historical perspective*. McGraw Hill Higher Education, 1990.

[106] Mascitti, V. R., "A closed-form solution to oblique shock-wave properties," *Journal of Aircraft*, Vol. 6, No. 1, 1969, pp. 66–66.

[107] McBride, B. J. and Gordon, S., "Computer program for calculation of complex chemical equilibrium compositions and applications: II. Users manual and program description," *NASA reference publication 1311*, 1996.

[108] Taylor, G. and Maccoll, J., "The air pressure on a cone moving at high speeds," *Proceedings of the Royal Society of London A: Mathematical, Physical and Engineering Sciences*, Vol. 139, No. 838, 1933, pp. 278–297.

[109] Lees, L., "Hypersonic flow," *Fifth International Aeronautical Conference*, Institute of the Aeronautical Sciences, Los Angeles, CA.

[110] Bertin, J. J., *Hypersonic aerothermodynamics*. AIAA, 1994.

[111] Probstein, R. F. and Bray, K. N., "Hypersonic Similarity and the Tangent-Cone Approximation for Unyawed Bodies of Revolution," *Journal of the Aeronautical Sciences*, Vol. 22, No. 1, 1955, pp. 66–68.

[112] White, F. M. and Corfield, I., *Viscous fluid flow*. McGraw-Hill New York, 3 ed., 2006.

[113] Laboratory, J. P., "HORIZONS Web Interface," 2015.

[114] Laskar, J., "Secular terms of classical planetary theories using the results of general theory," *Astronomy and astrophysics*, Vol. 157, 1986, pp. 59–70.

[115] Observatory, U. N., "Approximate Sidereal Time," 2015.

[116] Justus, C., Duvall, A., and Keller, V. W., "Atmospheric Models for Aerocapture Systems Studies," *AIAA Atmospheric Flight Mechanics Conference*, Aug 16-19, Providence, RI, 2004.

[117] Justus, C. G. and Johnson, D., "The NASA/MSFC Global Reference Atmosphere Model-1999 Version," *NASA Technical Memo 209630*, 1999.

[118] Justus, C. G. and Johnson, D., "Mars Global Reference Atmospheric Model 2001 Version (Mars-GRAM 2001): Users Guide," *NASA Technical Memo 210961*, 2001.

[119] Justh, H. L., Justus, C., and Keller, V. W., "Global Reference Atmospheric Models, Including Thermospheres, for Mars, Venus, and Earth," *AIAA/AAS Astrodynamics Specialist Conference and Exhibit*, Aug 21-24, Keystone, CO, 2006.

[120] Kliore, A., Moroz, V., and Keating, G., "The Venus International Reference Atmosphere," *Advances in Space Research*, Vol. 5, No. 11, 1985, pp. 1–304.

[121] Justus, C. G. and Braun, R. D., "Atmospheric Environments for Entry, Descent and Landing (EDL)," *5th International Planetary Probe Workshop*, June 23-29, Bordeaux, France.

[122] Kinney, D. J., "Aero-thermodynamics for conceptual design," *42nd AIAA Aerospace Sciences Meeting and Exhibit*, Jan 5-8, Reno, NV, 2004.

[123] Bowles, J. V., Huynh, L. C., Hawke, V. M., and Jiang, X. J., "Mars Sample Return Mars Ascent Vehicle Mission and Technology Requirements," *NASA Technical Memo 216620*, 2013.

[124] Tarpley, C., *The optimization of engine-integrated hypersonic waveriders with steady state flight and static margin constraints*. PhD thesis, University of Maryland at College Park, 1995.

[125] Bogacki, P. and Shampine, L. F., "A 3 (2) pair of Runge-Kutta formulas," *Applied Mathematics Letters*, Vol. 2, No. 4, 1989, pp. 321–325.

[126] Lewis, M. J., "The use of hypersonic waveriders for aero-assisted orbital manoeuvring," *Journal of the British Interplanetary Society*, Vol. 46, 1993, pp. 11–20.

[127] Korzun, A. M., Dubos, G. F., Iwata, C. K., Stahl, B. A., and Quicksall, J. J., "A concept for the entry, descent, and landing of high-mass payloads at Mars," *Acta Astronautica*, Vol. 66, No. 7, 2010, pp. 1146–1159.

[128] Strange, N. J. and Longuski, J. M., "Graphical Method for Gravity-Assist Trajectory Design," *Journal of Spacecraft and Rockets*, Vol. 39, No. 1, 2002, pp. 9–16.

[129] Longuski, J. M. and Williams, S. N., "Automated design of gravity-assist trajectories to Mars and the outer planets," *Celestial Mechanics and Dynamical Astronomy*, Vol. 52, No. 3, 1991, pp. 207–220.

[130] Creech, S. D., "Game Changing: NASA's Space Launch System and Science Mission Design," *Proceedings of the 2013 IEEE Aerospace Conference*, Mar 2 - 9, Big Sky, MT, 2013.

[131] Knittel, J. M., Lewis, M. J., and Yu, K. H., "Optimization of a Martian Aero Gravity Assist," *2014 AIAA Science and Technology Symposium*, Jan 13-17, National Harbor, MD, 2014.